Calcium isotope insight into the global carbon cycle

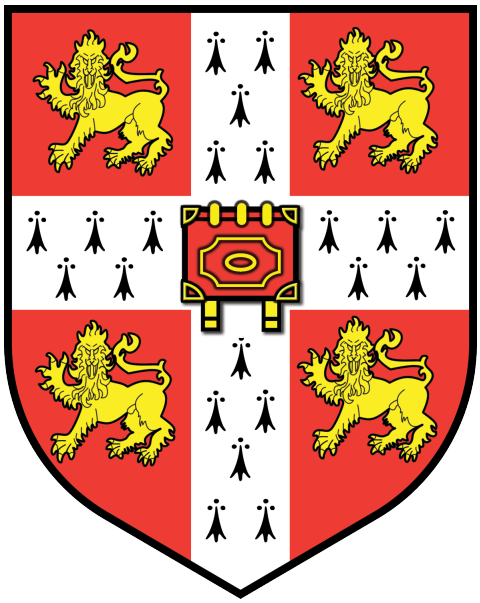

Harold John Bradbury
Jesus College, Cambridge

September 2017

This dissertation is submitted for the degree of Doctor of Philosophy

Declaration

This dissertation is the result of my own work and includes nothing which is the outcome of work done in collaboration except as declared in the Preface and specified in the text. It does not exceed the page limit and is not substantially the same as any work that has been or is being submitted to any university for any degree, diploma or other qualification.

Harold J Bradbury

Abstract

Over the course of my PhD, I developed the analytical capability to measure calcium isotopes at the University of Cambridge and analyzed calcium isotopes in a range of fluids and minerals in modern and past environments. After discussing my methodological development, I report my work in the glacial precursor to the Dead Sea. Here, the calcium isotope composition of aragonite varies synchronously with lake level fluctuations over the last 70,000 years. My numerically reconstructed lake calcium budget led me to conclude that 20,000 years ago, the Dead Sea was wetter than modern conditions, rather than colder and drier, as had previously been proposed. The primary focus of my PhD research was understanding the sedimentary sink for carbon. The formation of authigenic carbonate in marine sediments is caused by the microbial degradation of organic matter. I used pore fluid measurements and a numerical model to identify zones of authigenic carbonate precipitation. This knowledge was then combined with an understanding of the microbial processes that occur beneath the seafloor to determine the link between microbial activity and authigenic carbonate formation. Two processes, sulfate reduction and the anaerobic oxidation of methane were determined to be the main drivers of authigenic carbonate precipitation. In order to assess the importance of the carbon isotope signal imparted by each of the two identified processes, I created Artificial Neural Networks to predict the areal extent of authigenic carbonate precipitation and the dominant microbial process driving the precipitation. My ANNs identified that 37% of the modern seafloor is precipitating authigenic carbonate, which leads to a flux of $1.2*10^{12}$ moles of carbon per year, of which 88% is due to the anaerobic oxidation of methane, and 12% is due to sulfate reduction. This represents 2-3% of the modern global carbon deposition, however I was able to show that this would be significantly higher in the geological past when ocean conditions were vastly different to how they are today. Finally, I conclude by proposing that some variations in the global carbon cycle in the past can be explored by linking marine calcium concentrations to authigenic carbonate formation and the flux of alkalinity from the seafloor.

Acknowledgements

First and foremost, I would like to thank my supervisor, Dr Alexandra Turchyn, for guiding my research, challenging my ideas and providing me with invaluable encouragement throughout my PhD. Sasha remained eternally supportive, not only in my academic, but also my sporting endeavours. I enjoyed the countless individual and group meetings, and the numerous discussions that were had over the past four years. I have learnt so much from Sasha on so many levels; I am endlessly grateful for both the supervision and trust that was placed in me that allowed me to develop and grow through my time at Cambridge.

I would like to thank Dr Gilad Antler, Dr Andrea Erhardt and Dr Sambuddha Misra for providing me with a wealth of guidance and advice; I would not have developed into the geochemist I am today without their invaluable assistance. Furthermore, I would like to thank the numerous members of the Ocean Biogeochemistry group (Xiaole, Jenny, Florence, Beth, Nick, Chin-Yik and Jo) for the countless conversations in the lab, offices and group meetings.

I would like to acknowledge the support of my family. They have provided invaluable emotional and moral support throughout my undergraduate and postgraduate degrees. As the fourth, and final, sibling at Cambridge University, a 12-year period of a Bradbury studying at Jesus College is finally coming to an end; there were some big shoes to fill!

I would finally like to thank Hetty, who has both helped and motivated me through finishing my PhD. I'm exceptionally appreciative for the hours of proofreading and encouragement that has helped me through the final stint.

Table of Contents

List of Figures

CHAPTER 1

INTRODUCTION

1.1 The carbon cycle

The long-term, or geological, carbon cycle refers to the cycling of carbon between Earth's surface and its interior. As such, the geological carbon cycle comprises the input of carbon from the lithosphere through volcanoes and metamorphism of carbon-bearing rocks, and the removal of carbon from the surface, dominated by the deposition of carbon-bearing minerals (both remnant organic carbon and carbonate minerals) on the ocean floor (Berner, 1992; Berner, 2003).

Changes in the sources and sinks of carbon to Earth's surface are traditionally tracked using the carbon isotope composition of deposited carbonate minerals and rocks. With some assumptions, the relative proportions of the two carbon sinks (carbonate-mineral carbon and remnant organic matter) can be determined by using a known carbon isotope fractionation factor for the formation of organic carbon and assuming an isotopically homogenous, and static, source of carbon to Earth's surface (Equation 1.1, Figure 1.1 – Knoll et al., 1986).

$$\delta^{13}C_{in} = \delta^{13}C_{org}f_{org} + \delta^{13}C_{carb}(1 - f_{org})$$

EQUATION 1.1

where $\delta^{13}C_{in}$, $\delta^{13}C_{org}$ and $\delta^{13}C_{carb}$ are the carbon isotopic compositions of the input (from the mantle), the organic carbon buried and the carbonate minerals respectively. The fraction of total carbon burial as either carbonate or organic carbon (f_x) is defined such that $f_{org} + f_{carb} = 1$.

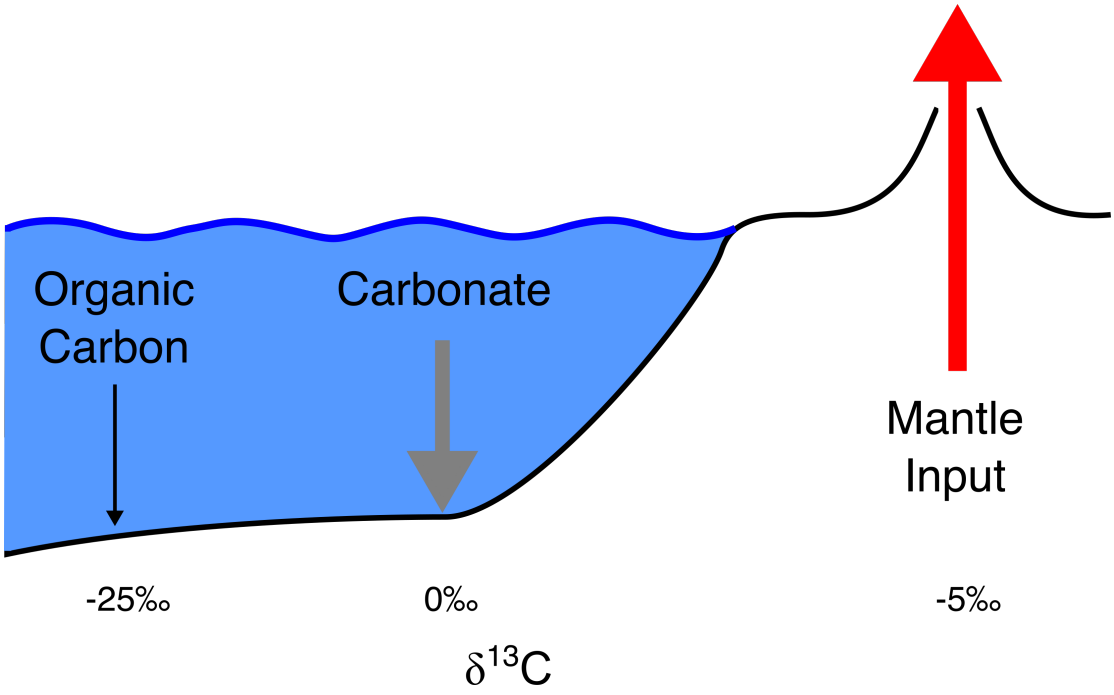

FIGURE 1.1: SIMPLIFIED GEOLOGICAL CARBON CYCLE, ARROW THICKNESS REPRESENTS THE UNDERSTOOD FRACTION OF ORGANIC CARBON AND CARBONATE DEPOSITED (BERNER, 2003)

Over the course of Earth history, the carbon isotope composition of carbonate minerals ($\delta^{13}C_{carb}$) has varied and these variations are largely interpreted as changes in relative amount of burial of organic carbon and carbonate-mineral carbon, f_x (Equation 1.1). Organic carbon is depleted in ^{13}C relative to the dissolved inorganic carbon (DIC) from which it is derived. As such, when there is fractionally more organic carbon burial (or less carbonate mineral burial) the remaining DIC in seawater will become enriched in ^{13}C, and when there is less organic carbon burial the remaining DIC will be enriched in ^{12}C.

On a broad scale, over Earth history, the $\delta^{13}C_{carb}$ has varied more-or-less around 0‰. With the assumption that the carbon isotope composition of organic matter ($\delta^{13}C_{org}$) is 25‰ lower than carbonate carbon due to the carbon isotope fractionation associated with organic carbon production (Figure 1.1), and assuming a global carbon input ($\delta^{13}C_{in}$) of mantle carbon (-5‰, Hayes et al., 1999; Schrag et al., 2013) suggests an 80:20 ratio for the deposition of carbonate minerals and organic carbon (Figure 1.2 - Berner, 2009).

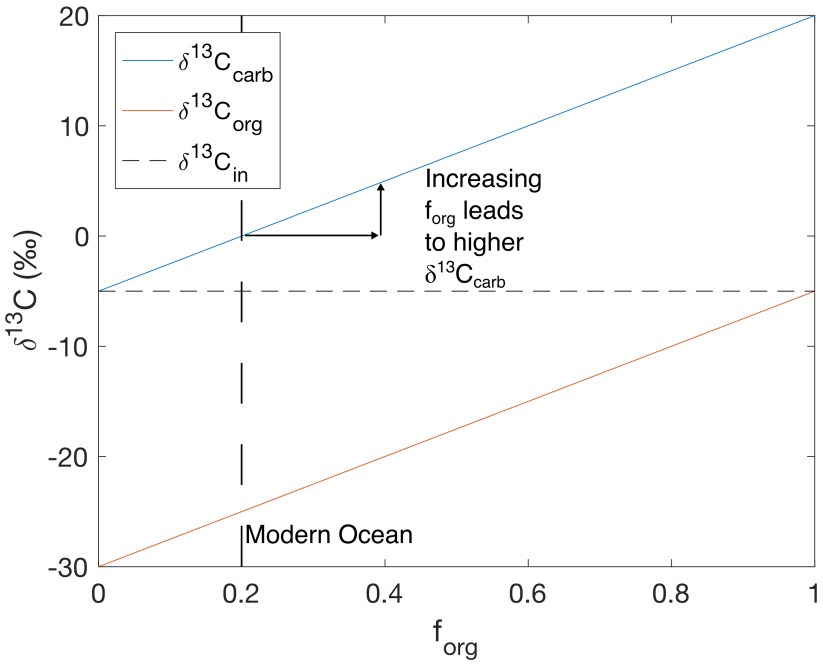

FIGURE 1.2: RELATIONSHIP BETWEEN $\delta^{13}C$ OF CARBONATE AND ORGANIC CARBON DEPOSITED RELATIVE TO THE FRACTION OF ORGANIC CARBON BURIAL

This model for 'one input and two outputs' for the geological carbon cycle is, however, an oversimplification for many reasons. Not least of these is that carbonate minerals continue to grow and react as they are deposited and buried, so what lands at the bottom of the ocean is not representative of what is ultimately removed from Earth's surface environment. Within sediments the oxidation of organic carbon occurs due to a series of microbial reactions using a sequence of terminal electron acceptors: oxygen, manganese, nitrate, iron, sulfate (Froelich et al., 1979). This oxidation of organic carbon produces DIC. This DIC can diffuse back to the ocean above through the network of pore fluids. However, if there is enough aqueous calcium, and the chemical conditions are right, the DIC can precipitate as calcium carbonate minerals and remain in the sediment. Throughout this thesis, I will refer to "authigenic carbonate", or "sedimentary carbonate", to discuss this process.

The net effect of authigenic carbonate precipitation is to transform deposited organic carbon into inorganic, mineralized, carbonate carbon within marine sediments. This transfer, or sink swap, of carbon from organic carbon to carbonate carbon is not a significant process today because the modern

oceans are oxic, and oxic respiration lowers pH and precludes the precipitation of calcium carbonate (Soetaert et al., 2007). However, it has been suggested that this sedimentary carbonate formation may be a larger process in the global carbon cycle at points in Earth history when the oceans were largely anoxic and authigenic carbonate may have more readily formed (Higgins et al., 2009; Schrag et al., 2013). If globally significant, authigenic carbonate would be an additional carbon sink within the simple carbon isotope mass balance shown in Figures 1.1 and 1.2, and given in Equation 1.1; Authigenic carbonate, forming from oxidized organic carbon, has far more ^{12}C in it than standard ocean carbonate minerals (Schrag et al., 2013).

There have been many past studies on the formation of authigenic carbonate and carbonate cements in marine sediments (Swart, 1979; Swart et al., 1989; Swart and Burns, 1990; Berner, 1992; Milliman, 1993; Schrag et al., 1995; Melim et al., 1995; Swart and Melim, 2000; Melim et al., 2002; Berner, 2003; Swart and Eberli, 2005; Teichert et al., 2009; Higgins et al., 2009; Schrag et al., 2013; Swart et al., 2014; Fantle and Tipper, 2014; Sun and Turchyn, 2014; Teichert et al., 2014; Swart, 2015). However there has been much debate into where and how the carbonate forms below the seafloor (Irwin et al., 1977; Hein et al., 1979; Bohrmann et al., 1998; Stakes et al., 1999; Lein, 2004; Arndt et al., 2006; Schrag et al., 2013; Blättler et al., 2015). Much of this thesis will explore the question of where and how authigenic carbonate forms, and how significant this authigenic carbonate might be over geological time. The rest of this introduction will discuss the impact that microbial respiration can have on the carbonate saturation state in sedimentary pore fluids, before introducing calcium isotope ratios and their application within this thesis.

1.2 Microbial respiration

Below the seafloor, the chemistry of the pore fluids, that is the fluids between the grains of sediment, can evolve from their original seawater composition by a variety of chemical and biological processes. The main process in the upper part of the sediment column that influences the chemistry of pore fluid is the

microbially-mediated oxidation of organic matter (Irwin et al., 1977; Curtis, 1978; Froelich et al., 1979). Below the sediment-water interface, the oxidation of organic carbon occurs aerobically with oxygen, however this process and the rate of diffusion of oxygen from the seawater into the seafloor leads to the presence of anaerobic conditions often close to the sediment-water interface, it has been estimated that 75% of the seafloor is anoxic within 50cm of the sediment-water interface (Froelich et al., 1979; Wang and Van Cappellen, 1996). Once oxygen has been consumed, remaining organic matter can be oxidised using a series of electron acceptors. The energy released during these reactions determines the order in which the electron acceptors are used (Froelich et al., 1979). Nitrate reduction, or denitrification is the next most energetically favourable electron acceptor, before manganese and iron reduction. Below the zone of iron reduction is the zone of microbial sulfate reduction then the zone of methanogenesis (Froelich et al., 1979; Berner, 1980). These reactions are summarised in Table 1.1 along with the Gibbs free energy changes associated with each reaction (Froelich et al., 1979).

TABLE 1.1: ZONES OF MICROBIAL RESPIRATION

Electron acceptor	Zone	$\Delta G^{0'}$ (kJ/mole glucose)
O_2	Zone of Aerobic Respiration	-3190
MnO_2	Manganese Reduction Zone	-3090
HNO_3	Nitrate Reduction Zone	-3030
Fe_2O_3	Iron Reduction Zone	-1410
SO_4^{2-}	Sulfate Reduction Zone	-380
Fermentation	Zone of Methanogenesis	-350

Due to the low concentration of oxygen, nitrate, manganese and iron within seawater (and thus sediments), the zones of aerobic respiration, manganese reduction, nitrate reduction and iron reduction are generally very condensed near the top of the sediment column. However the concentration of sulfate is high in seawater (28mM), and as such microbial sulfate reduction generally

dominates the modern marine oxidation of organic carbon (Kasten and Jørgensen, 2000) (Figure 1.3).

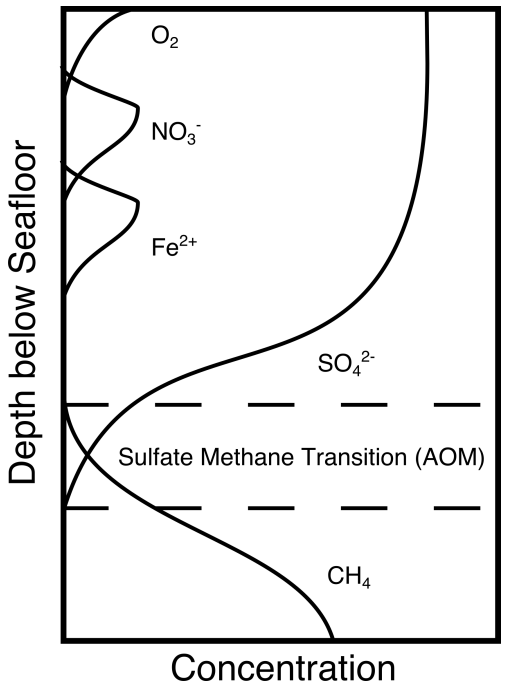

FIGURE 1.3: CONCENTRATION OF ELECTRON ACCEPTORS WITH DEPTH BELOW THE SEAFLOOR (FROELICH ET AL., 1979)

Organic carbon that escapes oxidation via microbial sulfate reduction can, below the zone of sulfate depletion, be converted into methane. Methane will diffuse up in the sediment column, and when it encounters sulfate, it is typically anaerobically oxidized, reducing the sulfate. The zone of anaerobic methane oxidation (AOM) was first identified from pore fluid profiles, although the mechanism for the anaerobic oxidation of methane was initially unknown as it is not an energetically favourable redox reaction (Martens and Berner, 1974; Barnes and Goldberg, 1976). Further research demonstrated that a consortia between sulfate reducing bacteria and methane oxidizing archaea are involved in AOM (Hoehler et al., 1994; Hinrichs et al., 1999; Boetius et al., 2000; Orphan et al., 2001). It has more recently been shown that some archaea can perform AOM without sulfate-reducing bacteria, suggesting that the bacteria-archaea consortia may not always be required (Milucka et al., 2012). Both microbial sulfate reduction and AOM involve the reduction of sulfate by microbes, however, in this thesis, when I discuss microbial sulfate

reduction I am referring to the reduction of organic matter by microbes using sulfate, rather than the reduction of methane by microbes using sulfate (AOM).

One of the main conundrums in the understanding of AOM is that although the sulfate reduction zone is above the zone of anaerobic methane oxidation, when methane is present, geochemical evidence suggests all of the sulfate is reduced through AOM rather than organiclastic microbial sulfate reduction, which should be more energetically favourable (Kasten and Jørgensen, 2000; Sivan et al., 2007). This geochemical evidence includes sulfate concentrations profiles at sites where there is AOM occurring that display a linear decrease to the methane-sulfate transition zone (Sivan et al., 2007). If microbial sulfate reduction were occurring above this zone, the profile should exhibit an exponential decay. Throughout this thesis, I assume that where there is methane at a particular location, all sulfate is reduced through AOM, although this is a simplification of an extremely complex system (Antler et al., 2014).

All of the above processes alter the chemistry of the pore fluids in different ways and, as such help determine where in the sediment pile authigenic carbonate may precipitate. The majority of deep-ocean sediments are bathed in bottom water that is undersaturated with respect to calcium carbonate. We can define the saturation state for calcium carbonate using $\Omega_{Calcite}$, which is the concentrations of calcium and bicarbonate ions in the fluid over the solubility product of carbonate at *in situ* pressure, temperature and salinity conditions:

$$\Omega_{Calcite} = \frac{[Ca^{2+}]_{sol} \times [CO_3^{2-}]_{sol}}{K_{sp}^*}$$

EQUATION 1.2

where $[X]_{sol}$ denotes the concentration in solution, while K_{sp}^* is the solubility product of calcium carbonate at the *in situ* conditions of temperature, salinity and pressure. When $\Omega>1$ the fluid is said to be super-saturated with respect to calcium carbonate minerals, favouring precipitation whereas when $\Omega<1$ the

fluid is said to be under-saturated, favouring dissolution. The concentration of calcium within the pore fluid is mainly determined by the calcium concentration of the seawater (10.4mM today) and amended by processes in sediments that consume or release calcium such as dissolution or precipitation of carbonate minerals and ion exchange with clay minerals within the sediments or reaction with the underlying basalt (Gieskes, 1975; McDuff and Gieskes, 1976; Gieskes and Lawrence, 1981). The concentration of the carbonate ion is controlled by the production of carbonate alkalinity, which occurs mainly during microbial sulfate reduction and methanogenesis (Equations 1.3 & 1.4, below), and the pH of the solution. The alkalinity of a solution is the capacity of a solution to neutralize an acid, and is equivalent to the stoichiometric sum of the bases in the solution. Within seawater, bicarbonate and carbonate ions are present in higher concentrations than other bases, which means that carbonate alkalinity is approximately equal to the total alkalinity (Zeebe and Wolf-Gladrow, 2001). As such, in this thesis, I will use alkalinity and DIC (dissolved inorganic carbon) in the same way although recognising this is an over simplification. The main reason why I will discuss alkalinity rather than DIC is that alkalinity is easier to measure (by titration), and hence, has been reported far more widely than DIC in a range of environments.

$$2CH_2O + SO_4^{2-} \rightarrow 2HCO_3^- + H^+ + HS^-$$

EQUATION 1.3

$$CH_4 + SO_4^{2-} \rightarrow HCO_3^- + HS^- + H_2O$$

EQUATION 1.4

Microbial sulfate reduction can be coupled to a wide range of organic carbon compounds, rather than simply glucose, as described in Equation 1.3. The different possible carbon electron donors lead to the creation of differing quantities of alkalinity and H^+ (Table 1.1, Gallagher et al., 2012) .

TABLE 1.1: THE AFFECT ON THE pH AND THE DIC OF A SOLUTION DURING SULFATE REDUCTION WITH DIFFERENT ELECTRON ACCEPTORS

Electron donor	Chemical Equation	DIC/ mole donor	H^+ eq/ mole donor	pH change
Hydrogen	$4H_2 + SO_4^{2-} \rightarrow HS^- + OH^- + 3H_2O$	0	-0.25	Increase
Formate	$4CHO_2^- + SO_4^{2-} + H_2O \rightarrow 4HCO_3^- + HS^- + OH^-$	1	-0.25	Increase
Acetate	$C_2H_3O_2^- + SO_4^{2-} \rightarrow 2HCO_3^- + HS^-$	2	0.00	Increase
Glycolate	$4C_2H_3O_3^- + 3SO_4^{2-} \rightarrow 8HCO_3^- + 3HS^- + H^+$	2	0.25	Decrease
Lactate	$2C_3H_5O_3^- + 3SO_4^{2-} \rightarrow 6HCO_3^- + 3HS^- + H^+$	3	0.50	Decrease
Alkane (e.g. propane)	$2C_3H_8 + 5SO_4^{2-} \rightarrow 6HCO_3^- + 5HS^- + 2H_2O + H^+$	3	0.50	Decrease
Ethanol	$2C_2H_6O + 3SO_4^{2-} \rightarrow 4HCO_3^- + 3HS^- + 2H_2O + H^+$	2	0.50	Decrease
Glyoxalate	$2C_2HO_3^- + SO_4^{2-} + 2H_2O \rightarrow 4HCO_3^- + HS^- + H^+$	2	0.50	Decrease
Lactate (incomplete)	$2C_3H_5O_3^- + SO_4^{2-} \rightarrow 2HCO_3^- + 2C_2H_3O_2^- + HS^- + H^+$	1	0.50	Decrease
Xylose	$2C_5H_{10}O_5 + 5SO_4^{2-} \rightarrow 10HCO_3^- + 5HS^- + 5H^+$	5	2.50	Decrease

Although all the reactions in table 1.1 show bicarbonate ions being produced through microbial sulfate reduction, in general dissolved inorganic carbon is present as bicarbonate ions, dissolved carbon dioxide and carbonate ions. The relative proportion of these three species is determined by the pH of the solution. As the pH of the solution increases, the chemical equilibrium between the carbonic acid, the bicarbonate, and the carbonate ions shifts towards the carbonate ion, as the carbonic acid and bicarbonate both dissociate releasing H^+ ions to the solution. Conversely when the pH of the solution is lower (with more H^+ within the solution), the equilibrium shifts towards carbonic acid. At higher pH there is more bicarbonate and carbonate

ions within the solution than there would be with a similar DIC concentration at a lower pH. This can be visualised using a Bjerrum plot (Figure 1.4).

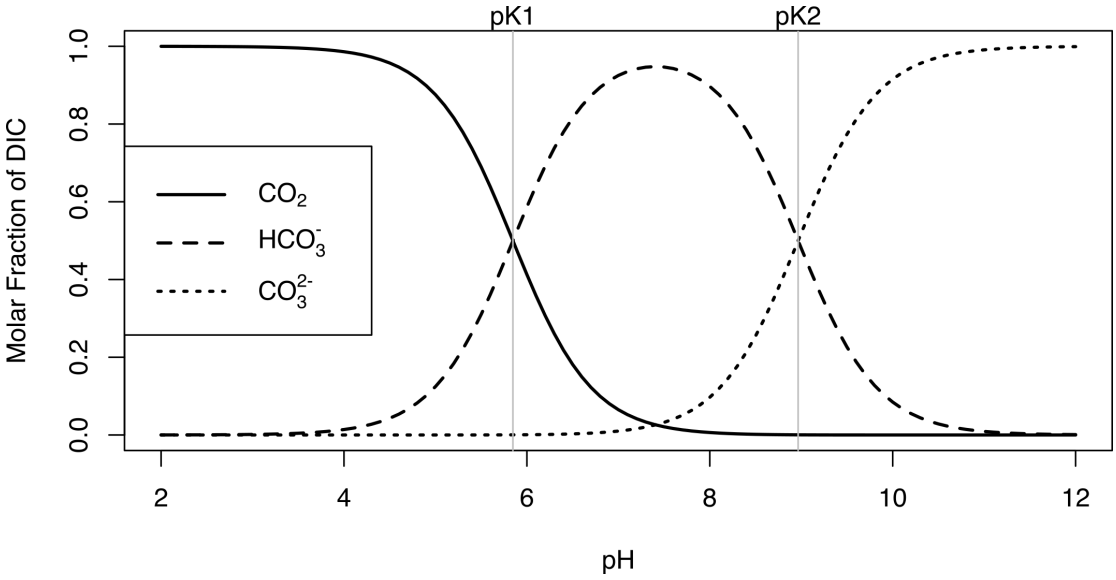

FIGURE 1.4: BJERRUM PLOT OF THE pH DEPENDANT SPECIATION OF CARBONATE AT T=25^{O}C, S=35 AND P=1ATM.

As microbial activity produces alkalinity and can either produce or consume protons, both alkalinity and pH can vary at different depths within the sediment depending on the type of sediment and the nature of the organic material. Thus, a combined view must be used to assess the probability of carbonate formation.

The general processes of microbial sulfate-reduction and AOM both produce bicarbonate ion, leading to an increase in alkalinity. An increase in the concentration of bicarbonate increases the saturation state of calcium carbonate when sulfate is reduced. However, as also shown in Table 1.1, this reduction of sulfate can also release protons (H^+), which reduces the pH. Therefore, for microbial sulfate reduction to drive authigenic carbonate precipitation, another chemical reaction must consume protons to increase the pH of the pore fluids to make sure enough of the DIC is available as carbonate ions. There are multiple possible chemical reactions that could lead to an increase in pH including bacterial iron reduction, manganese reduction, anaerobic oxidation of methane (AOM) or the formation of pyrite (FeS_2) (Arndt et al., 2006; Soetaert et al., 2007; Chatterjee et al., 2011; Arndt et al., 2013).

Pyrite precipitation can occur within the sulfate-reduction zone through two potential chemical reactions (Equations 1.5 & 1.6), both of which release hydrogen (gas), and lead to an increase in pH (Rickard, 1975).

$$Fe^{2+} + HS^{-} \rightarrow FeS + H_2S \rightarrow FeS_2 + H_2$$

EQUATION 1.5

$$Fe^{2+} + HS^{-} \rightarrow Fe(SH)_x + H_2S \rightarrow FeS_2 + H_2$$

EQUATION 1.6

The release of hydrogen gas may also be important as it can also be respired by sulfate reducing bacteria in the place of organic carbon (Rickard, 1975).

The anaerobic oxidation of methane occurs at the sulfate-methane transition zone and both drives an increase in pH towards ~7.9 and releases bicarbonate ions, increasing the alkalinity (Soetaert et al., 2007). For every mole of sulfate reduced during the anaerobic oxidation of methane only a mole of bicarbonate is produced (Equation 1.4). A further complication however is that the sulfate-methane transition zone occurs below the sulfate reduction zone (Figure 1.3), which means that the alkalinity is already high before the zone of anaerobic methane oxidation.

Most authigenic carbonate should be ^{12}C-enriched because the DIC from which it derives originates from the oxidation of organic matter (Schrag et al., 2013). However, the $\delta^{13}C$ of DIC within sediments can vary by up to 40‰ due to the oxidation or subsequent fermentation of organic carbon (Figure 1.5, Sivan et al., 2007) and given the complications highlighted above, it remains unclear at which depth the largest amount of authigenic carbonate is precipitating (Teichert et al., 2009). Although the net flux of calcium within pore fluids has been used to quantify the total amount of authigenic carbonate precipitating in the modern ocean, these studies do not tell us the depth distribution of authigenic carbonate precipitation within the sediment column (Anderson et al., 2013; Sun and Turchyn, 2014).

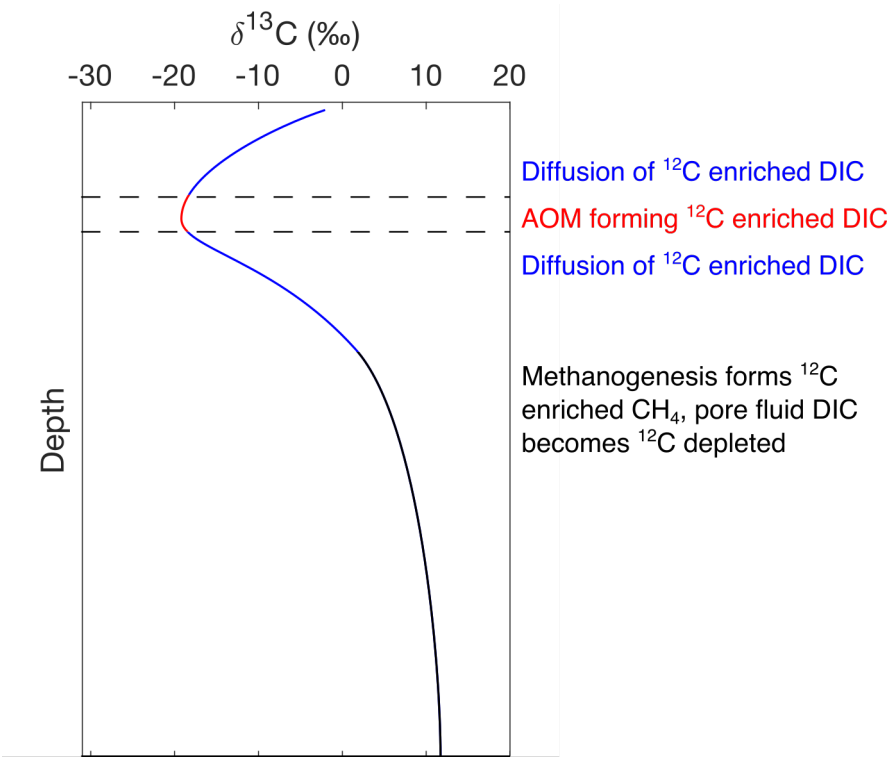

FIGURE 1.5: MAIN PROCESSES AFFECTING THE δ^{13}C OF THE DIC IN SEDIMENT WITH HIGH ORGANIC MATTER AND LOW CARBONATE CONTENT

The depth distribution of the authigenic carbonate precipitation is of key importance in determining the impact that authigenic carbonate precipitation can have on the global carbon cycle. The isotopes of calcium (one of the stoichiometric constituents of calcium carbonate) provide a unique insight into the precipitation of authigenic carbonate.

1.3 Calcium isotopes

Calcium has 5 stable isotopes (^{40}Ca, ^{42}Ca, ^{43}Ca, ^{44}Ca and ^{46}Ca) and ^{48}Ca is considered stable due to its long half-life (6.4×10^{19} years). The stable isotope composition of calcium is reported as the ratio of the two most abundant isotopes ^{44}Ca (2.09%) to ^{40}Ca (96.94%) using delta notation in common with many other stable isotopes systems.

$$\delta^{44}Ca_{sample} = \left(\frac{\left({}^{44}Ca/{}^{40}Ca \right)_{sample}}{\left({}^{44}Ca/{}^{40}Ca \right)_{reference}} - 1 \right) \times 1000$$

EQUATION 1.7

Calcium isotopes are measured relative to multiple different reference standards (Equation 1.7). Some of the earliest work on calcium isotopes used calcium fluoride (CaF_2) to represent Bulk Silicate Earth or ultrapure calcium carbonate standards (Russell et al., 1978; Jungck et al., 1984). More recent work uses four different reference standards, NIST 915A, NIST 915B, Bulk Silicate Earth and modern seawater (Zhu and Macdougall, 1998; Heuser et al., 2002; Gussone et al., 2003; Fantle and DePaolo, 2007; Heuser and Eisenhauer, 2008). In this thesis, I report calcium isotope ratios relative to Bulk Silicate Earth, which can be converted to other scales as discussed in Chapter 2 (Figure 1.6).

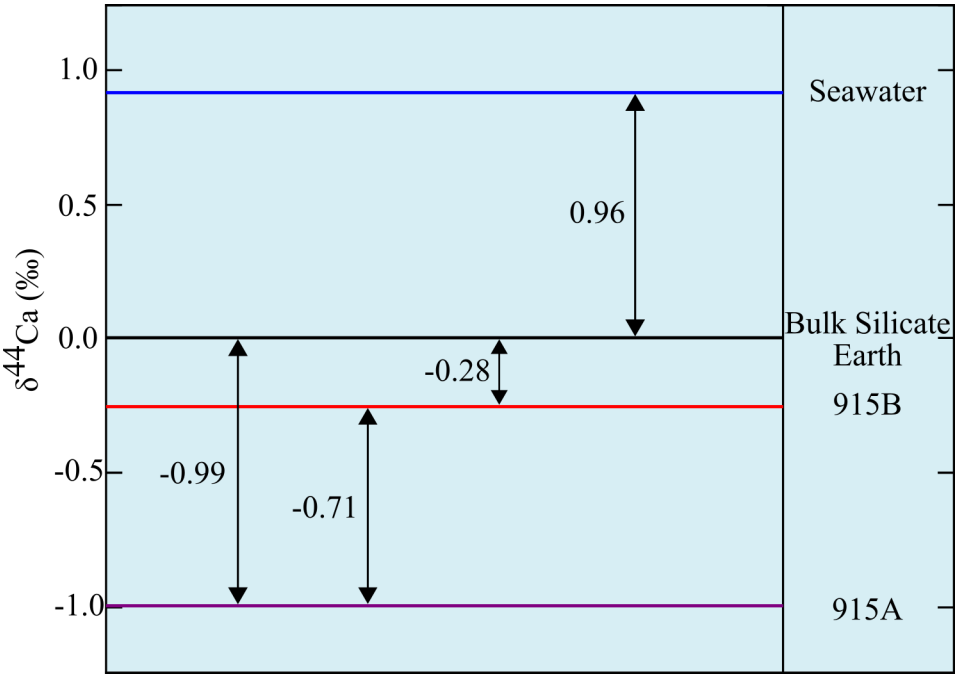

FIGURE 1.6: CONVERSION BETWEEN BULK SILICATE EARTH, SEAWATER, 915A AND 915B

The application of calcium isotopes to study sedimentary carbonate dissolution, precipitation, and recrystallization has been pioneered over the

last 15 years (Heuser et al., 2002; Gussone et al., 2003; DePaolo, 2004; Lemarchand et al., 2004; Gussone et al., 2005; Fantle and DePaolo, 2007; Tang et al., 2008a; Teichert et al., 2009; Fantle and Tipper, 2014; Brazier et al., 2015). Measurements of calcium isotopes in the natural environment have been useful for elucidating silicate versus carbonate source rock weathering (Zhu and Macdougall, 1998; De La Rocha and DePaolo, 2000; Schmitt et al., 2003; Fantle and DePaolo, 2005; Blättler et al., 2011; Brazier et al., 2015; Jacobson et al., 2015), the biological pathways of calcification (Gussone et al., 2003; Böhm et al., 2006; Nielsen et al., 2012b), and the burial and recrystallization of carbonate minerals when measured in deep-sea sediments and fluids (Fantle and DePaolo, 2007; Teichert et al., 2009; Turchyn and DePaolo, 2011; Fantle and Higgins, 2014). Calcium isotope ratios have also been used to study the reaction of groundwater with carbonate and silicate rocks along its flow path (Skulan et al., 1997; Skulan and DePaolo, 1999; Reynard et al., 2010; Fantle and Tipper, 2014) and to elucidate changes in the calcium budgets of lakes (Nielsen and DePaolo, 2013; Oehlerich et al., 2015).

During the precipitation of calcium carbonate from fluid there is an apparent calcium isotope fractionation between the solid and the formation fluid of between -2‰ to 0‰ depending on the temperature, stoichiometry, mineralogy and ionic strength of the solution; the direction of the calcium isotope fractionation, with the ^{40}Ca in the solid, suggests kinetic isotope fractionation (De La Rocha and DePaolo, 2000; Gussone et al., 2003; Marriott et al., 2004; Fantle and DePaolo, 2005; Gussone et al., 2005; Fantle and DePaolo, 2007; Tang et al., 2008b; Teichert et al., 2009; Gussone et al., 2011; Tang et al., 2012; Nielsen et al., 2012a; Fantle, 2015). During this calcium isotope fractionation, ^{40}Ca is preferentially incorporated into the carbonate mineral, with the remaining fluid enriched in ^{44}Ca. The magnitude of this calcium isotope fractionation is precipitation-rate dependent. The effect of the saturation state and stoichiometry of the solution has also been shown to be important in driving the calcium isotope fractionation during precipitation to an equilibrium or kinetic limit (Nielsen et al., 2012a).

Previous work has suggested that a kinetic calcium isotope effect dominates during high rates of mineral precipitation and an equilibrium calcium isotope effect dominates at low rates of mineral precipitation, particularly true for carbonate minerals but believed to be true for most calcium-bearing minerals (Gussone et al., 2003; Gussone et al., 2005; Fantle and DePaolo, 2007). It has also been suggested that by increasing solution oversaturation with respect to the mineral of interest, which in theory should increase the precipitation rate, the system will approach a kinetic limit (for example –1.6‰ for aragonite - Lemarchand et al., 2004; Nielsen et al., 2012). In practice, most biogenically precipitated carbonate in the ocean is around 1.4-1.5‰ lower in $\delta^{44}Ca$ than the global ocean, suggesting fast precipitation rates and a kinetic control on the calcium isotope composition. There has been an attempt to attribute a changing calcium isotope fractionation factor during carbonate precipitation quantitatively to temperature:

$$1000\times \ln \alpha = -1.9 + 0.017\times T(℃)$$

EQUATION 1.8

DePaolo (2011) furthered this by suggesting that the apparent temperature dependence of calcium isotope fractionation is due to changes in relative sizes and growth rates of calcite, which vary with both salinity, pH, and temperature (Zuddas and Mucci, 1998; DePaolo, 2011). Therefore, there is a general consensus that the calcium isotope fractionation factor during carbonate precipitation is temperature dependent, although the mechanism remains unclear.

The calcium isotope fractionation during other calcium-bearing minerals, such as gypsum, is less well studied. A series of experiments have suggested that in gypsum the fractionation is between 0.8 and 2.25‰ (Hensley, 2006; Harouaka et al., 2014; Blättler and Higgins, 2014; Harouaka et al., 2016). The work of Harouaka et al. (2014) suggested that this calcium isotopic fractionation factor depends on the crystal face of gypsum growth, specifically

that lower calcium isotopic fractionation occurs when the gypsum precipitation occurs on the 010 face of the crystals. This is due to the fact that calcium can attach to the 010 faces without completely desolvating, leading to lower calcium isotope fractionation. Precipitation primarily occurs on the 010 faces during rapid precipitation leading to tabular crystals relative to higher relative precipitation on the 011 and 110 faces, which produces acicular crystals (Harouaka et al., 2014).

During carbonate mineral dissolution there is no known calcium isotope fractionation; as such the released calcium has the same $\delta^{44}Ca$ as the solid (Fantle and DePaolo, 2007; Gussone et al., 2009; Turchyn and DePaolo, 2011). Multiple studies have shown that when there is calcium isotope equilibrium between carbonate minerals and aqueous calcium, that the equilibrium fractionation factor is close to unity; this means that in fluid-limited systems like sedimentary pore fluids, the aqueous calcium approaches the $\delta^{44}Ca$ of the carbonate solids over a length scale proportional to the rate that the carbonate minerals are recrystallizing (Fantle and DePaolo, 2007; DePaolo, 2011; Turchyn and DePaolo, 2011; Nielsen et al., 2012a; Fantle, 2015). In clay and organic-rich sediments, carbonate minerals recrystallize slower, which is manifest by the $\delta^{44}Ca$ of the pore fluid staying out of isotopic equilibrium with, or at a different $\delta^{44}Ca$ to, the solid carbonate (Turchyn and DePaolo, 2011). In theory by tracking the $\delta^{44}Ca$ in pore fluid of clay and organic-rich sites during the sedimentary precipitation of authigenic carbonate, there will be an enrichment of the heavier ^{44}Ca isotope in the pore fluid, as the light ^{40}Ca goes into the solid (Teichert et al., 2009). The pore fluid enrichment in ^{44}Ca during authigenic carbonate precipitation has previously been shown in sedimentary pore fluids in other settings (Teichert et al., 2005; Henderson et al., 2006).

One emerging new tool that I will also apply in this thesis is the use of the range of $\delta^{44}Ca$ in various minerals in different environments to investigate the fluid chemistry from which the minerals precipitated. The $\delta^{44}Ca$ of different calcium-bearing minerals has been shown to reflect the ratio of $Ca:HCO_3$ or

$Ca:SO_4$ of the precipitating fluid (Blättler and Higgins, 2014; Blättler et al., 2017). This approach was first applied to the $Ca:SO_4$ ratio in evaporate minerals, before being applied to the $Ca:HCO_3$ ratio in carbonate minerals (Blättler and Higgins, 2014; Blättler et al., 2017). During the precipitation of a calcium-bearing mineral, if calcium concentrations are higher than sulfate (in the case of gypsum) or bicarbonate (in the case of carbonate minerals) then all sulfate or bicarbonate in the solution is fully depleted, while calcium in the solution only is partially depleted: the final solution in this scenario contains some calcium, but no sulfate or bicarbonate. It has been shown experimentally that the higher the fraction of the total calcium in the solution that precipitates, the larger the range in $\delta^{44}Ca$ observed in the calcium-bearing mineral, as the later minerals will precipitate from a fluid with a highly evolved $\delta^{44}Ca$ due to Rayleigh distillation (Blättler and Higgins, 2014). This means that when multiple samples from the precipitated fluid are measured, some of the measured $\delta^{44}Ca$ will represent the original fluid composition (plus the calcium isotope fractionation factor), whereas other measured $\delta^{44}Ca$ will record the solid $\delta^{44}Ca$ precipitated from a highly isotopically evolved fluid. In contrast, if the range of $\delta^{44}Ca$ in the calcium-bearing mineral is low, it suggests that calcium was not sufficiently depleted to fully express calcium isotope fractionation during mineral precipitation, and hence all of samples are precipitating from a fluid with a relatively similar calcium isotope composition. Thus far, this emerging tool has been applied to pure carbonate or evaporite sequences but not to any stratigraphic intervals that contain both, as I will do in this thesis.

In summary, calcium isotopes have a wide variety of potential and current applications, ranging from the determination of calcium carbonate precipitation and dissolution in sediments to elucidating the fluid chemistry that carbonates form from. It is these applications I will be focussing on during this thesis.

1.4 Thesis objectives

The objective of this dissertation was to improve the understanding of the sedimentary carbon sink utilising calcium isotope measurements through three projects.

1.4.1 Thesis roadmap

The remaining chapters within this thesis include the analytical development, numerical modelling, laboratory and field data studies that were undertaken throughout my PhD. I start by discussing the development of the measurement of calcium isotopes at the University of Cambridge and several case studies that were undertaken to validate my method development (Chapter 2). In Chapter 3, the measurement of calcium isotopes is applied to two calcium-bearing minerals in a hyper-saline lake to study the regional hydrological cycle over the last 70kyr. Chapter 4 contains the study of the calcium isotope ratios of subsurface pore fluids, and how they can be applied to constrain the precipitation of authigenic carbonate. The knowledge gained in Chapter 4 is applied on a global scale in Chapter 5, with the implications of temporally changing authigenic carbonate precipitation being discussed. Finally, I will conclude the thesis with a summary of the insights gained into the global carbon cycle throughout this PhD.

CHAPTER 2

METHODOLOGICAL DEVELOPMENT FOR THE SEPARATION OF CALCIUM AND MEASUREMENT OF $\delta^{44}Ca$

2.1 Introduction

To measure calcium isotopes at the Department of Earth Sciences at the University Cambridge, method development for both the separation and isolation of calcium from samples and the subsequent measurement of calcium isotopic ratios was needed. At the start of my PhD, we had recently acquired a Thermo Scientific Dionex ICS 5000+ high performance ion chromatography (HPIC) system and a Thermo Scientific Triton Plus thermal ionisation mass spectrometer (TIMS) for the cation separation and isotope analysis, respectively. A large part of the start of my PhD was developing, testing and implementing the methods for these instruments. The decision was taken early on to use an automated HPIC to separate calcium from other elements in the matrix; this is in contrast with the use of a traditional, manual, gravity column. One of the great advantages of using HPIC for column chemistry is the speed at which samples are processed; a single sample takes 30 minutes for complete separation, relative to several hours on a gravity column (Russell et al., 1978; Russell and Papanastassiou, 1978; Schmitt et al., 2009). Furthermore, the HPIC allows for the continuous measurement of concentrations during the separation, which improves the isolation of the calcium from the matrix. This continuous measurement allows for variable collection windows, which is especially important in the presence of different matrices, which changes the elution time of the ions. Once the calcium was isolated from the other cations it was dried down and loaded onto the TIMS for isotope analysis. Additionally, the HPIC system allowed the lab

to routinely measure concentrations of various cations and anions, which we now use in a wide variety of applications.

In this chapter, I will detail the method development and data validation procedure for the data in my thesis. The method development can be divided into three parts:

1. Separating calcium from other cations within solutions (using HPIC)
2. Analysis of the calcium isotope ratios on the TIMS
3. Developing a calcium double spike for separation and isotope analysis

Finally, I present three case studies of small projects I did toward the start of my PhD to verify the analytical methods I developed.

2.2 Calcium separation using the Dionex (HPIC)

Ion-exchange chromatography separates ions in an aqueous solution that have differential charge and ionic radius, based on their affinity to a charged ion exchanger. The sample is placed in a column filled with an ion exchanger, or resin, and the cations or anions within the solution bind to the ion exchanger/resin. An eluent is then run through the column, which replaces the ions that were previously bound to the column. This process causes the ions to elute from the ion exchanger/resin in a predictable order, depending upon their affinity to the ion exchanger and their solubility in the eluent. Traditionally, ion-exchange chromatography has been used to quantify the concentration of different ions in various aqueous samples. However, if the separated ions can be collected, it can also serve as a means for isolating one ion from a mixed-ionic solution (Schmitt et al., 2009). It was this latter application I sought to develop. When developing ion-exchange chromatography, the first step is to calibrate the column and eluent strength to get the desired peak separation for different ions, so the order of elution of the ion of interest is clear, and to make sure there is no co-elution with other ions in the matrix.

In an automated Ion Chromatography system, the sample is run through the column continuously and the conductivity of the resulting eluent is measured. The conductivity of the eluent is evaluated with respect to time, and the area under each peak (representing a specific ion in a well-calibrated system) is calculated. The area measured under the peak can be used, when compared to a calibration line of known standards, to calculate the concentration or amount of each ion within the measured solution.

In this thesis, I measured the concentrations of cations in a variety of matrices, and isolated calcium from the other cations within various solutions. To do this a Dionex ICS 5000+ High Performance Ion Chromatography unit was used. The Dionex ICS 5000+ runs at a pressure of 2000-2400psi, allowing for much faster separation than a traditional gravity-based ion-exchange setup (Schmitt et al., 2009). The Dionex HPIC system runs at a higher pressure than previous IC systems; the high pressure is required due to the smaller particle size within the columns (5.5um), which increases the backpressure on the system. The smaller particle size provides significant performance advantages including more efficient peaks, improved speed, and chromatographic resolution. At 2000psi and a column temperature of 40^{o}C it takes 30 minutes to separate the major cations from one another regardless if the matrix is seawater or freshwater (Figure 2.1). A chromatogram from a diluted six-cation standard, which contains: Lithium 50mg/L, Sodium 200mg/L, Ammonium 400mg/L, Potassium 200mg/L, Magnesium 200mg/L and Calcium 1000mg/L is shown in Figure 2.1.

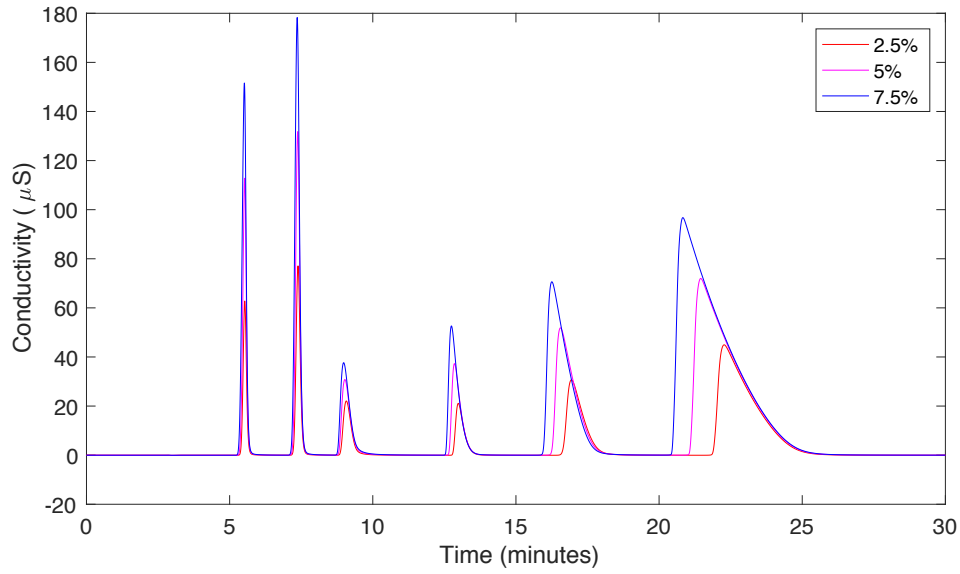

FIGURE 2.1: CHROMATOGRAM DISPLAYING THE RELATIVE PEAK SIZE AND SHAPE FOR 2.5-7.5% DILUTIONS OF A SIX CATION STANDARD. WITH THE INCREASING CONCENTRATION OF THE MEASURED STANDARD THE CORRESPONDING PEAKS BECOME BOTH TALLER AND WIDER.

For my thesis, separating calcium from other major ions within a sample was important to minimise possible interference effects and limit extraneous material being loaded into the mass spectrometer. Initially, a time window was determined in which calcium eluted off the column, and by collecting the eluent during this time period the calcium ions were isolated. The disadvantage of this method was that the elution time of the calcium depends upon the matrix of the solution and its ionic strength. As can be seen in Figure 2.2, the greater the injection volume of sample, the earlier the calcium elutes from the column. This can also be seen in Figure 2.1, where the changing peak size and shape can be observed with a change in the ionic strength of the solution. A larger peak size means that the time window to collect the calcium has to be longer than the peak length to account for the varying peak position (with varying ionic strength of the solution). This wide time window led to the collection of upwards of 10ml of eluent, which made the subsequent evaporation of the sample tedious. In order to improve this problem and to remove the need for a large time window, I developed a method to trigger the collection of calcium when the peak was first detected. This was

accomplished by using a change in peak slope to determine when the calcium first started eluting from the column and when sample collection should begin.

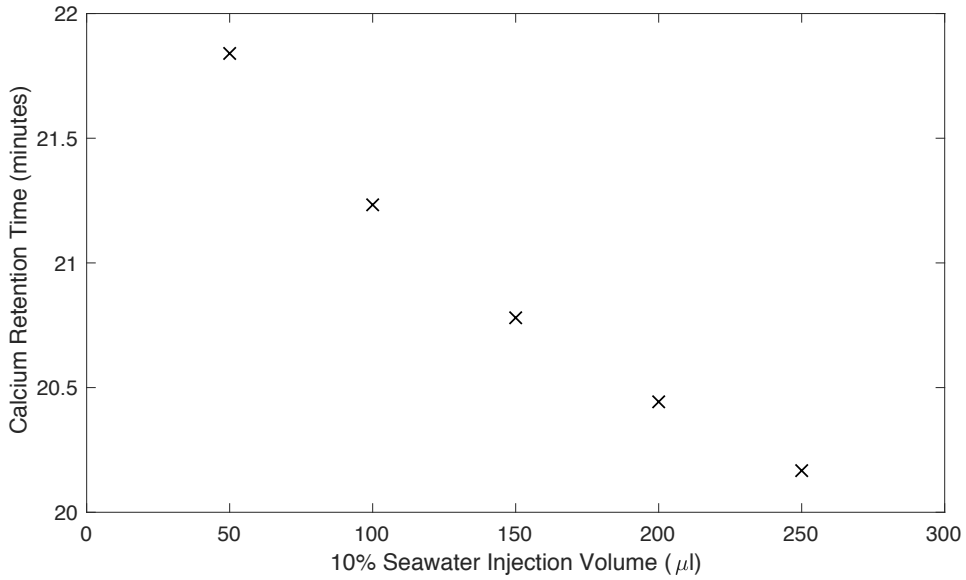

FIGURE 2.2: CHANGES IN THE CALCIUM PEAK RETENTION TIME WITH INCREASING VOLUME OF LOADED SEAWATER. AS THE VOLUME OF SEAWATER LOADED ON THE COLUMN INCREASES THE PEAK RETENTION TIMES DECREASE.

One of the major challenges in isolating the calcium using HPIC was trying to achieve near to 100% recovery. There is calcium isotopic fractionation occurring within ion-exchange columns, with the lighter isotopes preferentially retained by the column resin (Russell and Papanastassiou, 1978). If 100% recovery is achieved then this calcium isotope fractionation does not matter. However, if there is non-total recovery then a double spike must be added to correct for isotopic fractionation on the column (see Section 2.4). In order to quantify the recovery of calcium from the Dionex HPIC, the eluent from several collection cycles was subsequently measured for its calcium concentration. The average recovery of calcium from the peak detection method was 88% (n=3). Part of the difficulty with achieving total recovery was the tailing effect of doubly charged ions such as calcium and magnesium due to their higher affinity for the column resin. The tailing effect was also greater at higher ionic strength, and many of the samples in this thesis were at higher ionic strength (Figure 2.1).

The column capacity for the CS16 column that was used in the Dionex ICS5000+ was 8.4 mEq/column. There are four major cations in seawater: sodium, potassium, magnesium and calcium (see Table 2.1)

TABLE 2.1: THE FOUR MAJOR CATIONS WITHIN SEAWATER.

Ion	mEq/L	g/L
Na^+	479	11.02
Mg^{2+}	109	1.31
Ca^{2+}	21	0.42
K^+	10	0.39

As shown in the above table (Table 2.1), there is a total equivalent value of 619mEq/L in seawater. This suggests 13.6ml of seawater could run through the column before every binding site in the column was occupied with a cation from seawater. However, previous studies have shown that maximum ionic separation is achieved with columns run below 1% of total capacity (Russell and Papanastassiou, 1978); this suggests a maximum of 136µl of seawater could be analysed. There are 57µg of calcium within 136µl of seawater. Only 4 µg of calcium, compared with the 57 µg available, is required for a single measurement of the calcium isotopic ratio, which demonstrates that there is greater than an order-of-magnitude more capacity on the column with which to separate calcium when seawater is the matrix.

I tested the ionic separation with a range of seawater concentrations, from 1% to 10%. The asymmetry of the peak shapes in Figure 2.3 is clearly shown relative to the more symmetric peak shapes in Figure 2.1. As the ionic strength of the solution increases, the peak tailing effect, as discussed earlier, increases the length of time take from the individual elements to elute from the column. The method was setup so that the separation between magnesium and calcium was large enough to compensate for the decrease in peak separation with solutions of higher ionic strength. For the collection of potassium or magnesium the eluent strength would have to be altered to

adjust for the peak tailing affect, as it leads to some co-elution at higher ionic strength (10% and above).

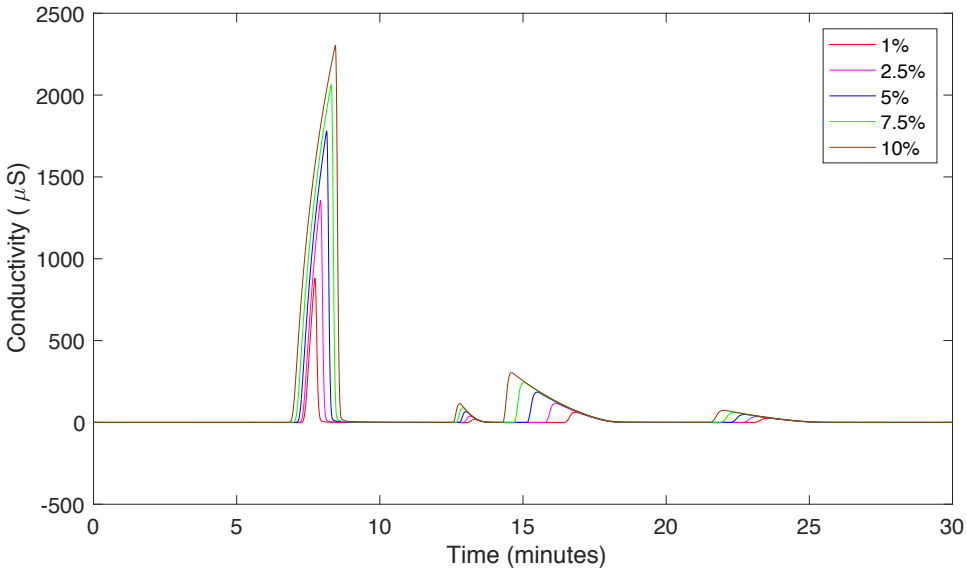

FIGURE 2.3: CHROMATOGRAM DISPLAYING THE PEAK ASYMMETRY ASSOCIATED WITH SEAWATER CONCENTRATIONS RANGING FROM 1-10% IAPSO ATLANTIC SEAWATER.

At first, 100% seawater samples were attempted through the HPIC, but, as shown in Figure 2.4, the area measured beneath the calcium peaks were variable and the peak area was lower than expected, particularly at higher volumes of seawater. This was due to the occurrence of a high baseline when running these samples, which meant all the calcium within the sample was not being measured. In Figure 2.4, this is shown by the gradient for 100% seawater and 10% seawater that was diluted in ultrapure water. For the same volume of seawater, the measured calcium area is higher in all of the samples that were diluted relative to the undiluted seawater for volumes greater than 5µl. Post-dilution, the area of the calcium was then comparable a single element calcium standard within the rated error of the Dionex system (1-2%).

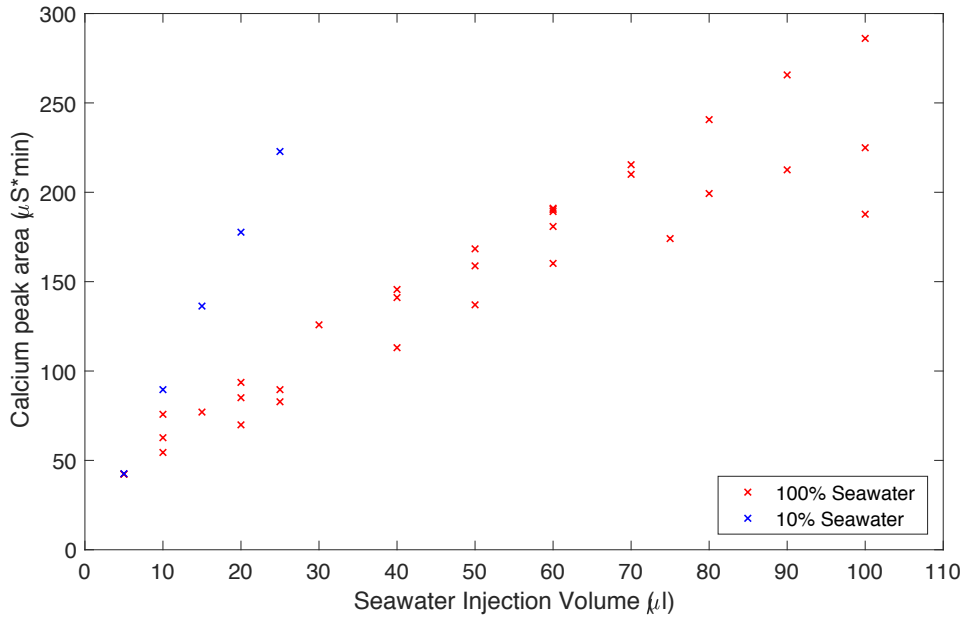

FIGURE 2.4: THE RELATIONSHIP BETWEEN THE VOLUME OF SEAWATER LOADED ON THE COLUMN AT 10 AND 100% CONCENTRATION. THE 10% SEAWATER CONSISTENTLY RECORDS A HIGHER PEAK AREA ABOVE 5µL THAN THE 100% SEAWATER. AS THE VOLUME OF 100% SEAWATER INCREASES THE ERROR ON A SINGLE MEASUREMENT INCREASES.

Another potential concern when separating the calcium from the other major ions within the samples, as well as during sample preparation was the potential for contamination during the procedure. In order to minimise potential contamination, all chemistry was undertaken using acid-cleaned Teflon vials, pipette tips and bottles, as well as using single or doubly distilled Nitric and Hydrochloric acids. In order to assess the potential for contamination, a full procedural blank was run. This procedure was conducted by placing 1ml of distilled 1M Nitric acid in an acid-cleaned Teflon beaker, which was then evaporated using the standard hot plate. The residue was then dissolved in a 0.5% Nitric acid solution and loaded onto the Dionex. As the calcium concentration was below the detectable limit on the Dionex a window of collection was defined in order to collect any calcium within the solution. Finally, the solution was evaporated, re-dissolved in a dilute nitric acid solution and measured on the Agilent ICP-OES. This gave a measured procedural blank of 96ng of calcium. When compared to the total collection of

4.4μg of calcium for a single sample for the TIMS this represents approximately 2% of the collected calcium and as such, can be neglected.

2.3 Calcium isotope measurement using the Triton

Thermal Ionisation Mass Spectrometry (TIMS) involves the heating of an element of interest from a single element solution loaded on a narrow filament, which produces a beam of ions. The beam is then focussed using electrostatic lenses, separating the beams by mass and measuring the individual beams using either a single Faraday cup or multi-collector array. TIMS have been widely used since the 1960s and the measurement of calcium isotopes using TIMS has been developed since the late 1970s (c.f. Fantle and Bullen, 2009). The early measurements of calcium isotopes either measured calcium over a small mass range ^{40}Ca to ^{44}Ca or using multiple static measurement steps (Price et al., 1990; Fletcher et al., 1997; Skulan et al., 1997). Improvements in instrumentation, such as the introduction of the later generations of multi-collector TIMS such as the ThermoFisher Triton and Triton Plus, have allowed for the measurement of the different calcium isotopes, in a dynamic mode, with high precision (Fantle and Bullen, 2009). The Triton Plus contains 9 faraday cups, with the central cup being fixed in position.

The most common alternative to the TIMS, when measuring calcium isotopes, is the use of a multi-collector inductively coupled plasma mass spectrometer (MC-ICP-MS). The main issue with the use of the MC-ICP-MS is the isobaric interference between ^{40}Calcium and ^{40}Argon due to the presence of argon gas in the plasma torch. When measuring calcium isotopes on an MC-ICP-MS, the isotope ratio that is measured is $\delta^{44/42}$Ca, which is then corrected assuming mass-dependent fractionation to a reported $\delta^{44/40}$Ca. In contrast, ^{40}Ca is measured directly on the TIMS. $\delta^{44/42}$Ca is approximately half the magnitude of $\delta^{44/40}$Ca due to the lower mass difference between ^{42}Ca and ^{44}Ca, as such the ~2‰ variation observed in the natural system $\delta^{44/40}$Ca is ~1‰ in $\delta^{44/42}$Ca. The errors measured using TIMS and ICP-MS are similar (~0.1‰ 2σ),

however, post conversion from $\delta^{44/42}Ca$ to $\delta^{44/40}Ca$, the error on the ICP-MS makes up approximately a fifth of the natural variation. Thus, TIMS is uniquely suited to measure calcium isotopes particularly at high resolution.

2.3.1 Cup setup and decay

Due to the significant mass difference between ^{40}Ca and ^{48}Ca (20%), the dispersion of the beams by the magnet is wider than the Faraday cups can accommodate. As such, a dynamic mode is required to measure the complete range of calcium isotopes if this is required. There have been many different cup configurations and dynamic modes using multi-collector mass spectrometers for calcium (Fantle and Bullen, 2009).

TABLE 2.2: THE TWO CONFIGURATIONS THAT ARE USED FOR THE MEASUREMENT OF ^{40}CA TO ^{48}CA ON THE TIMS.

Config.	Step	L4	L3	L2	L1	C	H1	H2	H3	H4
A	1		40Ca	41K		42Ca	43Ca	44Ca		
	2	42Ca			44Ca					48Ca
B	1			40Ca	41K	42Ca	43Ca	44Ca		
	2	42Ca			44Ca					48Ca

I originally modified the Triton Plus using configuration A as detailed in Table 2.2. Due to the high relative proportion of calcium that occurs as ^{40}Ca (97%) the main beam is significantly larger than the other beams that are measured. During the initial operation of the Triton Plus, the samples were run at between 20 and 40V so as to reduce the internal errors that often occur during the measurements of the smaller beams. The ^{40}Ca was measured using a $10^{10}\Omega$ resistor, whereas all the other masses were measured using $10^{11}\Omega$ resistors. The $10^{11}\Omega$ resistors show a 3-fold decrease in the signal to noise ratio over the $10^{10}\Omega$ resistor, but when running the beams of 20+V this is

inconsequential, and the $10^{11}\Omega$ resistor leads to a faster degradation of the faraday cup (Schiller et al., 2012).

When running at these high voltages, the calcium beam tended to decay over the course of analysis. The Triton Plus corrects for this automatically by heating the evaporation filament between blocks, but this leads to varying isotope ratios during the run. Also when running at 20-40V on ^{40}Ca, the large beam size lead to rapid degradation of the Faraday cup liner. As the carbon liner in the Faraday cup degraded, the sensitivity for measuring the beam decreased, which caused the measured isotope ratios to gradually shift to higher values; the machine measures that there is less ^{40}Ca relative to ^{44}Ca (Figure 2.5).

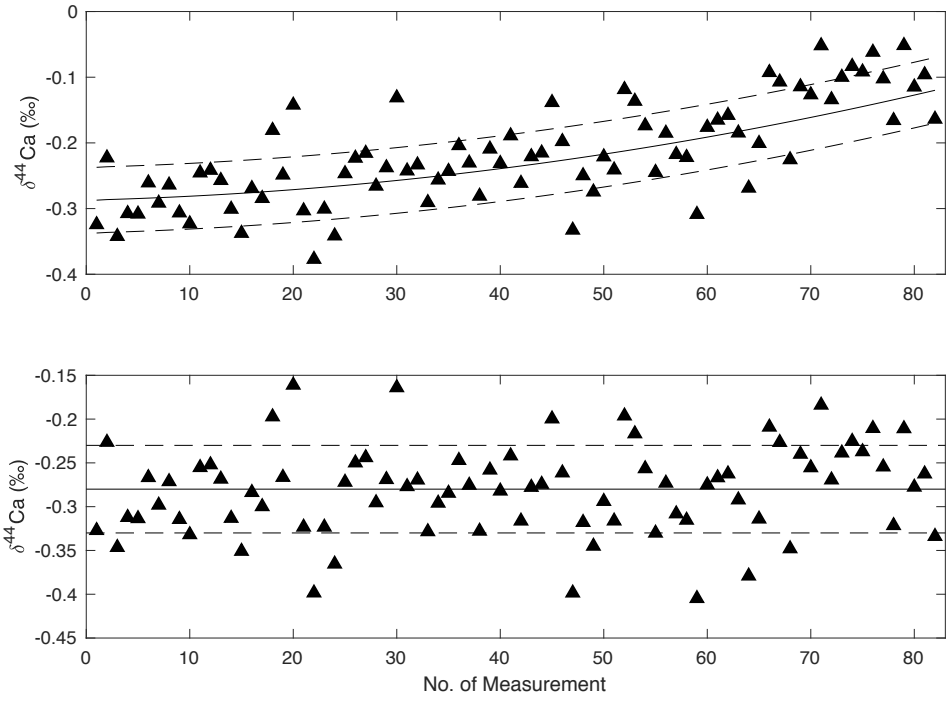

FIGURE 2.5: THE 9-MONTH REPRODUCIBILITY OF THE MEASURED NIST 915B. THE LOWER FIGURE HAS BEEN CORRECTED FOR THE DRIFT THAT IS CAUSED BY THE DEGREDATION OF THE SENSITIVITY OF THE FARADAY CUP MEASURING ^{40}CA. THE DASHED LINES REPRESENT 1σ OF THE EXTERNAL ERROR. THE 9-MONTH 2σ OF THE MEASURED 915B IS 0.1‰.

The degradation of the liner also led to an increase in the external error measured by the standards over time (Figure 2.5). Due to the degradation of

the cup, I developed the second configuration (B, Table 2.2). This configuration avoided the use of the L3 cup, which measures the ^{40}Ca beam in configuration A. By measuring ^{40}Ca in a different cup, the $\delta^{44}Ca$ could be measured using both configurations, which allowed for an assessment of the degradation of the L3 cup. When the difference between L2 and L3 became greater than 0.25‰ the L3 cup was replaced.

2.3.2 Calcium loading and activators

During the initial few months where I was analysing a 40V beam of ^{40}Ca, I noticed that due to the high voltage inter-block heating was required during the later part of the measurements (Figure 2.6). This inter-block heating could lead to shifts in the isotopic ratios, and as such I decided to try using an activator to see if the beam could be stabilised for the course of a run without the automated increase in the temperature of the evaporation filament.

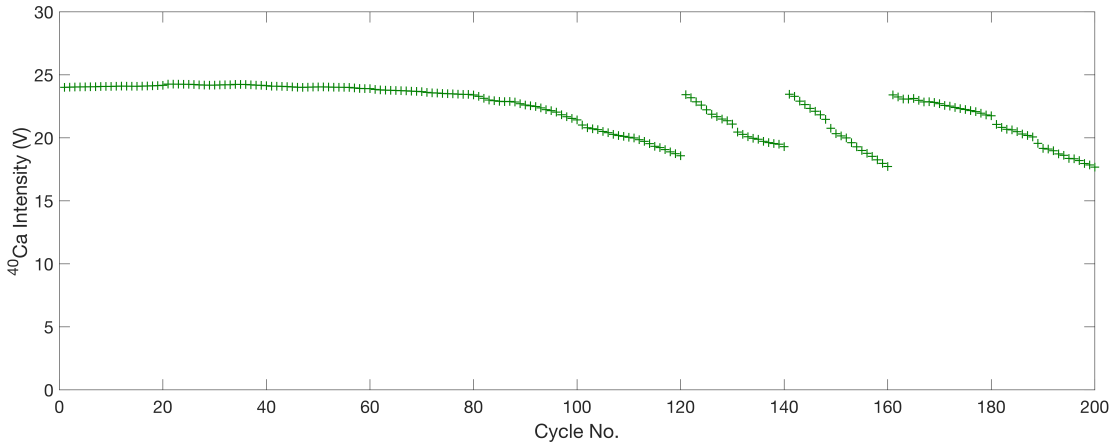

FIGURE 2.6: DEGRADATION OF THE SIGNAL INTESITY MEASURED ON ^{40}CA THROUGH A RUN. INTERBLOCK HEATING OCCURS AT CYCLES 120, 140 AND 160.

Conceptually, with an activator, calcium would evaporate from the filament at a higher temperature. In a double filament assembly (Figure 2.7), such as on the Triton Plus, this means that the difference between the evaporation and ionisation temperatures is reduced, leading to a more stable beam. Two activators have been reported in the literature: TaO_5 when using a tantalum filament assembly and H_2PO_4 when using a rhenium filament assembly (Birck,

1986; Zhu and Macdougall, 1998; Skulan and DePaolo, 1999; Heuser et al., 2002; Fantle and Bullen, 2009).

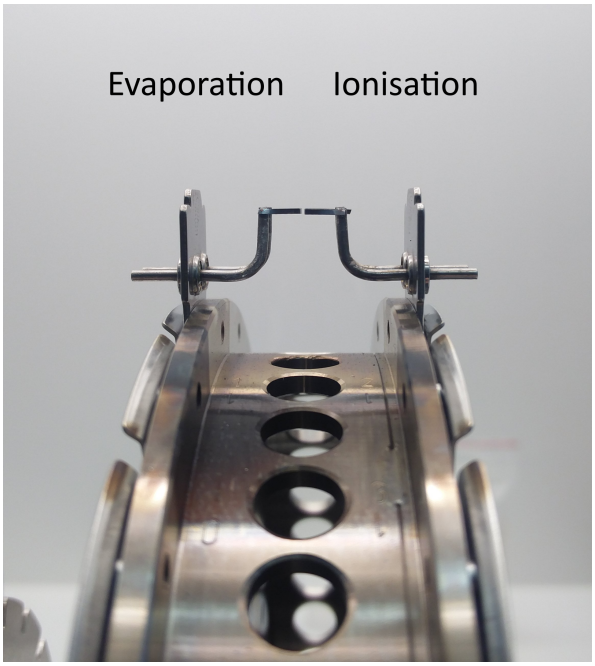

FIGURE 2.7: THE DOUBLE FILAMENT ASSEMBLY. THE SAMPLE WAS LOADED ON THE EVAPORATION FILAMENT. DURING MEASUREMENTS THE IONISATION FILAMENT WAS HEATED TO 2800mA - 1400^{O}C (AS MEASURED ON A PYROMETER), AND THE EVAPORATION FILAMENT WAS HEATED TO AROUND 2000mA.

There is a wide variety of loading protocols for the different activators, ranging from mixing the activator into the samples pre-loading, to using a “sandwich” or “melange” method: loading a small quantity of the activator before and after loading the sample onto the filament (Birck, 1986; Zhu and Macdougall, 1998). There is no consensus in the literature about which method is preferable, with different laboratories sticking with their own proven method (Fantle and Bullen, 2009; Boulyga, 2010). I loaded the activator on top of the dried down sample on the filament. Once we had switched to the loading of the phosphoric acid after the samples a stable, or slightly increasing beam could be measured on most samples and hence we were able to start running the samples at lower intensities of 5-10V on ^{40}Ca (Figure 2.8). With the lower ^{40}Ca intensity I could use a $10^{11}\Omega$ resistor, which led to an improvement in the internal error.

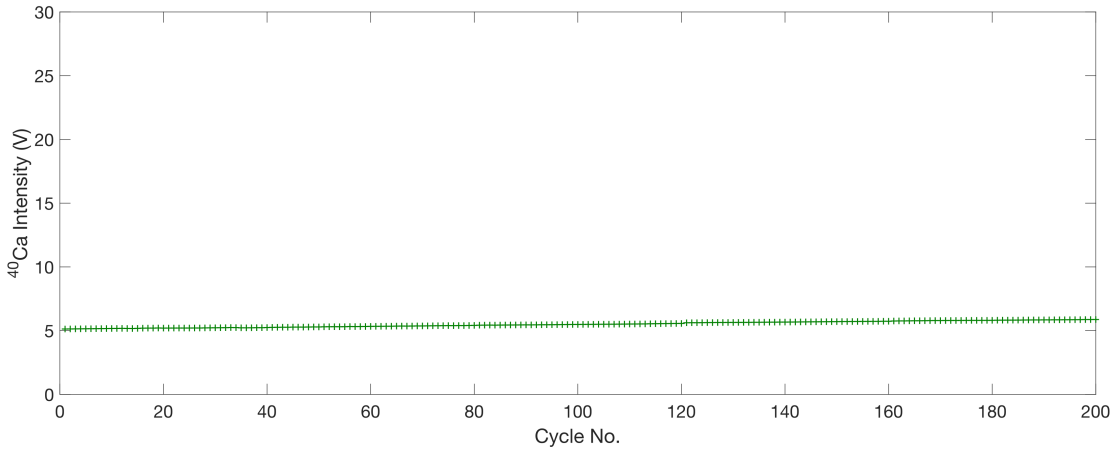

FIGURE 2.8: BEAM STABILITY WHEN USING PHOSPHORIC ACID AS AN ACTIVATOR OVER A SINGLE MEASUREMENT.

When loading the calcium onto the rhenium filament, the calcium had to be concentrated in the centre of the filament to minimize potential reservoir effects (Fantle and Bullen, 2009). Reservoir effects occurred if the calcium is loaded thinly across the length of the filament. When there were two or more reservoirs on the filaments, these reservoirs could evaporate and ionize at different times during a measurement. The difference in the relative proportions of the measured isotopes from these two reservoirs can generate extreme fluctuations in the spike-corrected isotopic ratios if there is a significant change in the proportion of one reservoir relative to another. This effect has previously been discussed in great detail (Hart and Zindler, 1989; Fantle and Bullen, 2009). In order to minimize the potential for reservoir effects, solid separated calcium samples were dissolved in 1µl of 2M HNO_3, and loaded in 0.25-0.3µl increments onto a preheated (0.7A) rhenium filament. Between each increment, heating the filament at a constant current of 0.7A dried the pure calcium solution. When the calcium was loaded the filament current was increased to 1A to ensure complete evaporation before 0.5µl of H_2PO_4 was loaded as an activator. This was then also evaporated at 1amp, and once the phosphoric acid had dried the filament was gradually heated to around 2.1-2.3A until it briefly glowed. This process ensures total evaporation of moisture from the filament.

The quantity of calcium loaded onto the filaments affects the measured isotope ratios in several ways. The lower the amount of calcium loaded on the filament, the higher the proportional impact a minor contaminant will have on the measured ratios. In theory, the larger the sample the easier it is to achieve a stable ion beam during the measurement and when the beam strength is higher, the measured internal errors on the TIMS will be lower. As such, a range of calcium sample sizes was attempted. When >10µg of calcium was loaded on the filaments, the calcium formed an irregular residue on the filament. Due to the calcium protruding from the surface of the evaporation filament, the ionisation filament had to be inserted with a greater separation, which led to inconsistent results when measured. When loading large samples (>10ug) it was found that the samples were much more likely to 'spread' during the loading, causing a greater risk of reservoir effects as discussed earlier.

2.3.3 Heating and measurement protocol

In order to measure the $\delta^{44}Ca$ of a sample the samples had to be heated slowly to achieve a stable beam. The evaporation and ionisation filaments were heated at rates of 150mA/minute and 100mA/minute to ~2800mA and 2000mA respectively. The ^{40}Ca beam was then auto-tuned after resetting the X-Symmetry and Z-Focus to 0. The Evaporation filament was then heated at a rate of 50mA/minute until a stable beam of between 5 and 10V was reached. The sample was then auto-tuned again. The heating process took around 30 minutes per sample.

The measurement routine consisted of 10 blocks of 20 cycles, where each cycle measured both of the steps: ^{40}Ca to ^{44}Ca and ^{42}Ca to ^{48}Ca. Peak centring on ^{40}Ca and ^{44}Ca beams and lens focusing was conducted at the beginning of each measurement. Between every second block, lens focussing occurred. The total measurement routine took 1.5 hours to complete.

2.3.4 Interference effects

There are several potential isobaric interferences that can affect the measurement of calcium isotopes. The most obvious isobaric interference is with potassium, and ^{40}K cannot be measured directly. In order to limit the effect of isobaric interferences with potassium, ^{41}K was measured during the initial heating of the sample, and also during the measurement of the isotope ratios. I observed that, when there was potassium in the sample, it was released during the initial heating of the sample, typically around 1000^{o}C, and by the start of the measurement acquisition, the ^{41}K beam size was below $1*10^{-3}$V on a $10^{11}\Omega$ resistor. The ratio of $^{40}K/^{41}K$ in nature is $1.734*10^{-3}$. As such there would need to be a beam of around 1V on a $10^{11}\Omega$ resistor on ^{41}K before a measureable correction for potassium would be required (Heuser et al., 2002).

During the separation of cations using either a manual or automated column setup, the two closest ions that behave most similarly to calcium are magnesium and strontium. Magnesium oxide ($^{24}Mg^{16}O^{+}$) can interfere with ^{40}Ca and doubly charged strontium (^{84}Sr, ^{86}Sr & ^{88}Sr) can interfere with ^{42}Ca, ^{43}Ca and ^{44}Ca. These interferences cannot be monitored like the potassium interference. Hence, in order to assess the potential for interference caused by magnesium and strontium I spiked NIST 915B with single element solutions of magnesium and strontium of varying concentrations. The NIST 915B was spiked with solution of 5, 50 and 500ng of magnesium and strontium separately as well as the same weights with both elements added. The results are shown in Figure 2.9, with each added element increasing in weight from left to right.

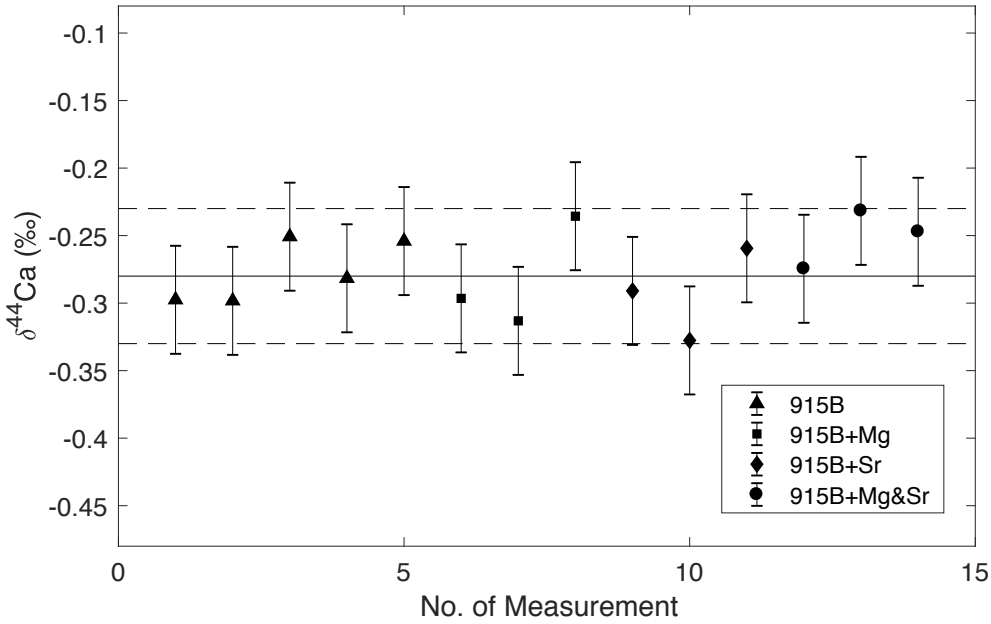

FIGURE 2.9: NIST 915B STANDARDS COMPARED TO SPIKED NIST 915B WITH MAGNESIUM AND STRONTIUM. PURE NIST 915B IS REPRESENTED BY TRIANGLES, NIST 915B WITH MAGNESIUM IS REPRESENTED BY SQUARES, NIST 915B WITH STRONTIUM IS REPRESENTED BY DIAMONDS, AND NIST 915B SPIKED WITH BOTH MAGNESIUM AND STRONTIUM IS REPRESENTED BY CIRCLES. IN THE SPIKED STANDARDS THE QUANTITY OF THE MAGNESIUM AND STRONTIUM INCREASES FROM LEFT TO RIGHT: 5NG, 50NG AND 500NG. AS ALL OF THE STANDARDS AND SPIKED SAMPLES FALL WITHIN 1σ (DASHED LINES) OF THE LONG TERM NIST 915B STANDARD VALUE (SOLID LINE) IT IS CLEAR THAT THERE IS NO ISOBARIC INTERFERENCE FROM MAGNESIUM AND STRONTIUM.

Figure 2.9 suggests that there is no variation in the measured δ^{44}Ca of NIST 915B, as all of the spiked standards fall both within 2σ of the 5 measured NIST 915Bs from the same turret and within the 1σ long-term reproducibility measured on NIST 915B.

2.4 Double spike

Compston and Oversby (1969) first developed the double spike method to allow for the correction of isotopic fractionation during the preparation and measurement of lead isotopes. The principles used in their seminal paper have since been applied to multiple isotopic systems, including iron, calcium, and strontium amongst others. The double-spike technique requires the

element of interest to have four or more stable (or quasi-stable) isotopes. Two of the isotopes in the system are then artificially increased by the addition of a pre-prepared double spike of known ratio. Assuming that the element only undergoes mass-dependant fractionation during sample separation and preparation, an exponential law can be applied to the measured ratios to correct for any isotope fractionation or loss during the column chemistry or measurement on the TIMS (Russell et al., 1978; Hart and Zindler, 1989; Fantle and Bullen, 2009). Using the TIMS, the exponential law has been shown to describe the fractionation better than either a linear or Rayleigh fractionation (Russell et al., 1978). The exponential law takes the form:

EQUATION 2.1

$$R_{fractionated} = R_{unfractionated} \left(\frac{m_i}{m_j}\right)^p$$

where R is the ratio of two isotopes (*i* and *j*), m_I is the mass of the nuclide *i*, and *p* describes the degree to which a measured ratio is fractionated relative to the unfractionated value (Russell et al., 1978; Fantle and Bullen, 2009).

As calcium has a large range of stable isotopes there are many possible double spike combinations, which can be used to correct for calcium isotope fractionation during sample preparation. The choice of double spike has been discussed extensively in the literature, for the most recent overview see Rudge et al. (2009) and the references therein. The most commonly used double spike when measuring calcium is ^{42}Ca and ^{48}Ca (Russell et al., 1978; Russell and Papanastassiou, 1978; Boulyga, 2010), although there have also been recently studies using ^{43}Ca/^{46}Ca as well as ^{42}Ca/^{43}Ca (Fletcher et al., 1997; Lehn et al., 2013). There have been several papers discussing which double spikes provide the lowest errors (Gopalan et al., 2006; Fantle and Bullen, 2009; Rudge et al., 2009). A 42/48 double spike has several potential advantages:

- The mass range from ^{42}Ca to ^{48}Ca is the largest, and hence shows the greatest variability due to mass dependant fractionation.

- ^{42}Ca and ^{48}Ca are the third and fourth most abundant stable isotopes after ^{40}Ca and ^{44}Ca, which makes the purification process less expensive.
- By running in a dynamic mode due to the wide mass range in measured isotopes, the Faraday cup degradation caused by the large ^{40}Ca beam is decreased.
- 42/48 double spike is shown theoretically to have the lowest error estimates using the Double Spike Toolbox (Rudge et al., 2009).

However, there are also some disadvantages:

- The dynamic mode, which is required due to the aforementioned mass range, doubles the length of time taken for a single measurement.
- It has been suggested that by using a smaller mass range in the double spike (such as 42/43) the ratios will fractionate more coherently minimizing deviation of machine fractionation from the theoretical exponential law (Gopalan et al., 2006).

In our laboratory group, we made the decision that the advantages outweighed the potential disadvantages, and the 42/48 double spike was chosen. However, I have also created and calibrated a 42/43 double spike in order to compare the errors from two of the main options within our TIMS, as there is no consensus in the literature.

When creating a double spike the individual isotopes of interest are purchased (either from Oak Ridge National Laboratory-America or Isoflex-Russia). The isotopes for our first double-spike were purchased from ORNL, whereas when purchasing the isotopes for the second generation of the double spike we found that Isoflex offered a wider range of purities, and, as such, were more cost effective for our requirements.

There is an association between the rarity of the isotope in the natural system and the purity of the purchased isotope. When the natural abundance is low, the purification process is relatively more challenging, leading to a lower purity in the purchased sample. The single calcium isotopes were purchased as

calcium carbonate, and the first step upon receiving was to dessicate the powder until the measured weight stabilises. During this process the weight often decreases by up to 30% due to water release. When the weight of the calcium carbonate was measured accurately, the spike was then dissolved in double distilled 2% HNO_3 to a gravimetrically determined concentration of 1mM, calculated from the reported purity of the purchased isotopes. The composition of the single spikes was then assessed relative to their stated purity on the TIMS using multiple samples of the pure solution loaded as described above. Once the purity was determined, the molecular weight was recalculated and thus the concentration of calcium within the pure isotope solutions. Once this was accomplished, the two single isotopic solutions could be mixed to the predetermined ratio. A ratio of 1:1 for ^{42}Ca:^{48}Ca was used following the work conducted at UC Berkeley and others (Skulan and DePaolo, 1999; De La Rocha and DePaolo, 2000; DePaolo, 2004), which is close to the optimum ratio of 3:2 as suggested by Rudge et al., (2009). Measuring multiple samples of the mixed solutions allowed me to determine the ratio of ^{42}Ca to ^{48}Ca within the double spike. Finally, the double spike was calibrated by measuring a series of analytical standards (NIST 915A, NIST 915B and OSIL Atlantic Seawater). The power value within the exponential law, which is determined by instrumental fractionation, was set using this calibration (Equation 2.1).

In order to calculate the original composition from a spiked sample, an iterative procedure is followed, which corrects for the fractionation using an exponential law (Equation 2.1) by comparing the 42/48 ratio in the measured sample to the 42/48 ratio in the spike. This process is summarised in Figure 2.10 (Rudge et al., 2009).

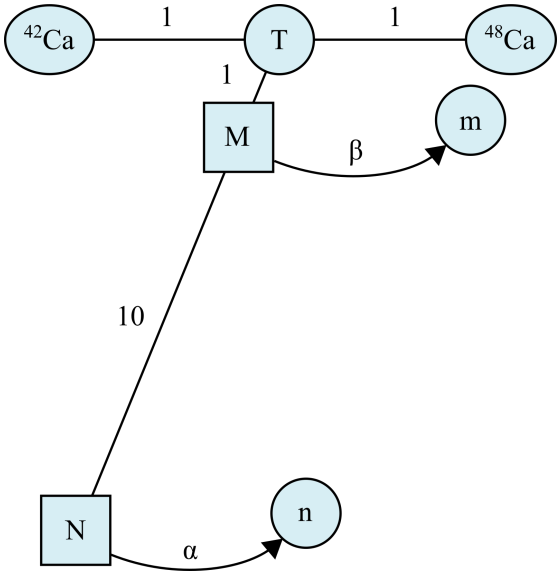

FIGURE 2.10: A SCHEMATIC DIAGRAM OF THE DOUBLE SPIKE TECHNIQUE (ADAPTED FROM RUDGE ET AL., 2009). THE SINGLE SPIKES ^{42}CA AND ^{48}CA ARE MIXED AT A RATIO OF 1:1 TO MAKE THE DOUBLE SPIKE WITH A KNOWN 42/48 RATIO (T). THE DOUBLE SPIKE IS THEN MIXED WITH THE NATURAL STANDARD (OR SAMPLE) (N) AT A RATIO OF 1:10 TO CREATE THE MIXTURE (M). THE MIXTURE FRACTIONATES WITH A FRACTIONATION FACTOR OF β TO FORM m, WHICH IS MEASURED. THE FRACTIONATION FACTOR α REFLECTS THE MASS FRACTIONATION THAT OCCURS IN NATURE. THE DOUBLE SPIKE INVERSION USES THE MEASURED COMPOSITIONS OF n, m AND T TO CALCULATE THE UNKNOWN β, M AND N.

Originally I conducted the spike subtraction using the average of all 200 cycles of data reported by the TIMS by using an Excel spreadsheet. The averaging in this method meant that shifts in the ratios were not easily observed and consequently the external error was higher than expected. This approach also limited the analysis that could be conducted on individual samples, particularly in identifying reservoir effects. In order to improve this, I ran the spike-subtraction iterative procedure on averages from each individual block (20 cycles) using an updated Excel spreadsheet. This decreased the external errors, and by plotting the spike-subtracted ratios it was clear if the ratios had shifted during the run. However, the internal errors were still larger that I initially expected due to the averaging occurring within each individual block. Finally, to improve the internal errors as well as the external errors the spike-subtraction iterative procedure was run on each individual cycle using a Matlab script, which could be run on a batch of exported ASCII data files from

the TIMS. This method is the most robust as it becomes clear if there were any reservoir effects, it also decreases the internal error on the measurement as it allows for the exclusion of individual cycles post spike subtraction (Figure 2.11).

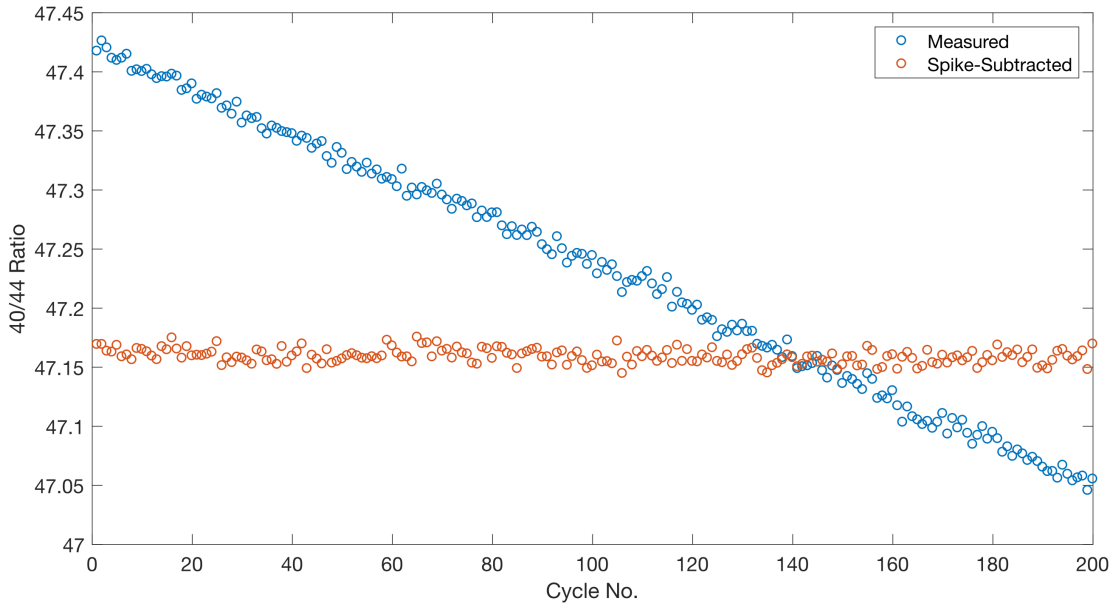

FIGURE 2.11: MEASURED AND SPIKE-SUBTRACTED 40/44 RATIOS USING THE MATLAB SCRIPT

2.5 Case studies

While much of the first two years of my PhD were spent establishing, calibrating, and developing the separation of calcium and measurement of calcium isotope ratios, I was involved in several side projects that served to test and refine the method development and validate the method procedures. Three of these are described here.

2.5.1 Comparison of separation on the Dionex vs. Column

One of the first tasks when setting up the Dionex for fraction collection was to assess whether the collection of calcium from the Dionex led to a calcium isotopic offset relative to the collection of calcium using the traditional approach of gravity columns. As such, I ran a variety of carbonate samples

from the Nama Group, Namibia (Late Proterozoic) through both a traditional gravity column setup using Bio-Rad AG50W-X8 resin and through HPIC. The goal of the HPIC was to separate strontium and other trace elements from the calcium. The samples were analysed for calcium isotopes over a period of several months, and have recently been re-run and checked, in preparation for publication. The first half of the samples were run using a 42/48 double spike acquired from Berkeley. The second half of the samples was run using Cambridge double-spike 1, and I have recently run a further replicate with the latest generation of the Cambridge double-spike (2). There were no differences in the measured $\delta^{44}Ca$ of the samples using the different spikes, which shows the validity of the double-spike calibration discussed in section 1.4.

The gravity columns were created from cut down 1ml pipettes with a reservoir size of 2ml and with a 20µm PE frit installed. They were filled to just below 1ml with slurried AG50W-X8 resin. The columns were pre-cleaned using 2ml of 4M HCl, 6M HNO_3, 4M HCl and water, before being preconditioned with 1.5M HNO_3. The columns had a flow rate of approximately 1ml/hour. The sample was loaded and then eluted with 1.5M HNO_3. The columns were calibrated by measuring the concentration of the ions eluting off the column using the Dionex. The calibration was setup to collect 100% of the calcium and maximise the separation of calcium from magnesium and strontium, whilst at the same time minimising the time taken to complete the column chemistry.

Initially a series of twelve carbonate powders from the Pre-Cambrian Nama Group (Namibia) were dissolved in 5% ultrapure acetic acid. An aliquot containing 12µg of calcium was then spiked at a ratio of 10:1 (sample to spike) with the double spike and dried. The dried sample was re-dissolved in 1.5M HNO_3 and separated using the calibrated gravity columns. The collected calcium was loaded in triplicate, with three separate filaments loaded with 4ug.

Another aliquot from the dissolved carbonate powders containing 4-8µg of calcium was then spiked, dried down and the re-dissolved in 0.5% HNO_3 before being separated using the Dionex HPIC system. The 4µg of the collected calcium was loaded per filament either singularly (n=6) or in duplicate (n=6). The measured sample data is shown graphically in Figure 2.12, where the $\delta^{44}Ca$ from the Dionex and the column separations are compared on the left, and the Berkeley and Cambridge double-spikes on the right.

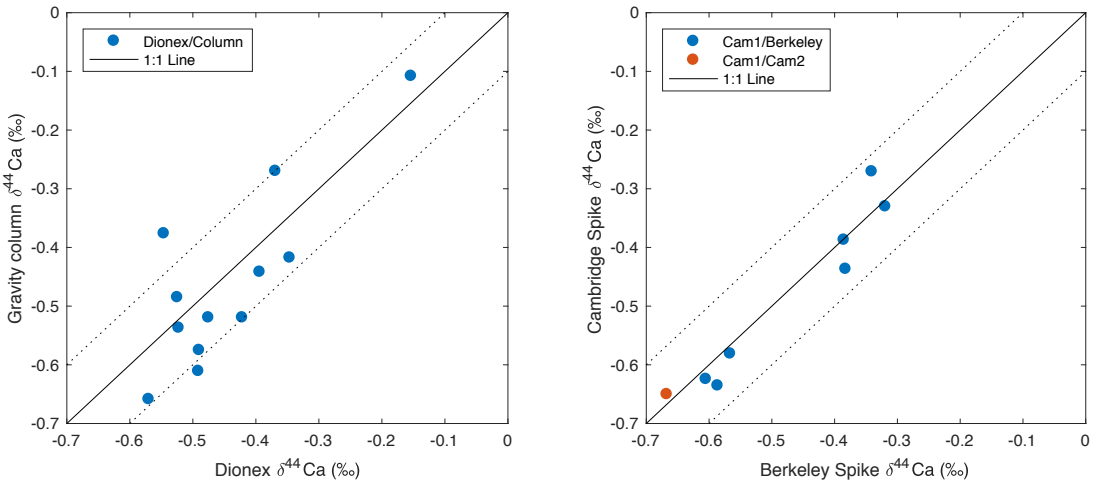

FIGURE 2.12: CROSS PLOTS OF THE TWELVE SAMPLES RUN ON THE DIONEX AND COLUMNS (N=12 R^2=0.65) AND THE 8 SAMPLES COMPARED USING DIFFERENT CALCIUM 42/48 (N=8 R^2=0.88) DOUBLE SPIKES. FOR THE SINGLE COMPARISON OF THE TWO GENERATIONS OF THE CAMBRIDGE DOUBLE SPIKES CAMBRIDGE 1 IS ON THE Y AXIS AND CAMBRIDGE 2 ON THE X AXIS. THE DOTTED LINES REPRESENT THE LONG TERM 2σ OF THE MEASUREMENT OF CALCIUM ISOTOPES.

As previously discussed the long-term 2σ of 915B is 0.1‰ (Figure 2.5). In Figure 2.13, all but one of the averages from the column samples and the Dionex sample fall within this error, with the average absolute offset of the column and Dionex samples being 0.08‰. The average difference between the column and Dionex samples is 0.02‰, which is well within the long-term error (2σ). The single outlier could be due to contamination during the loading of the sample, or possible reservoir effects during the running as previously described. As there is no consistent offset in the $\delta^{44}Ca$ of the measured

samples after separation using the traditional column setup or the Dionex HPIC system, I consider this a validation of the HPIC method for calcium separation.

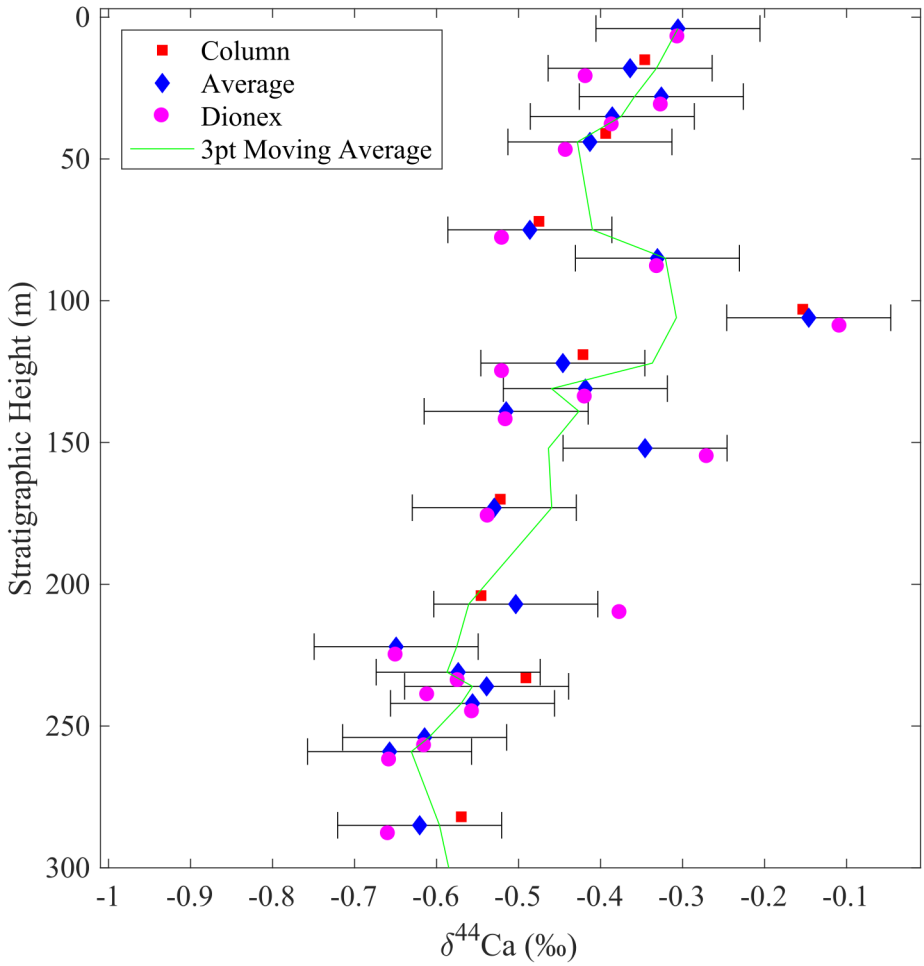

FIGURE 2.13: $\delta^{44}Ca$ OF CARBONATE SAMPLES FROM THE NAMA GROUP, WHERE EACH SAMPLE IS PLOTTED AT THE STRATIGRAPHIC HEIGHT WITHIN THE SEDIMENT COLUMN. THE AVERAGE VALUE IS THE MEAN FROM ALL MEASURED REPLICATES OF EACH SAMPLE (DIAMONDS), WHEREAS THE COLUMN AND DIONEX (SQUARE AND CIRCLE RESPECTIVELY) VALUES FOR EACH STRATIGRAPHIC HEIGHT REPRESENT THE MEAN OF REPLICATES RUN USING EACH METHOD. THE ERROR BARS REPRESENT THE LONG TERM 2σ OF NIST 915B. THERE IS NO CONSISTENT OFFSET SHOWING THAT THERE IS NO ISOTOPIC IMPACT AFTER SEPARATION OF CALCIUM USING THE DIONEX HPIC RELATIVE TO GRAVITY COLUMNS.

2.5.2 Inter-laboratory cross calibration

To assess the validity of our calcium isotope measurements on samples as well as standards, two studies have been undertaken where samples have been analysed both here and in another laboratory that routinely measures calcium isotope ratios.

As discussed in the earlier section on the measurement of calcium isotopes within this chapter (section 2.3), the two main ways to measure calcium isotopes are TIMS or MC-ICP-MS. In order to compare the data collected using the TIMS method as well as the automated separation using the Dionex it was decided to compare samples to another laboratory that used a similar HPIC system with the isotope measurement conducted on an MC-ICP-MS. The Higgins Lab at Princeton University was one of the first laboratories in the world to setup the automated cation separation using HPIC, which they use in the measurement of magnesium, calcium and potassium isotopes.

Six marine pore fluids from Site 1003, which is located on the middle slope of the Great Bahama Bank at 480mbsl, were measured in full procedural triplicate after separation on the Dionex at Cambridge (Higgins et al., 2018). The results shown in Figure 2.14 demonstrate that for the samples (n=6) five are within the error of the samples measured after separation on the HPIC on the Neptune MC-ICP-MS at Princeton University, with the average offset for all samples of 0.07‰. The reproducibility of the MC-ICP-MS method in the study has a reported 2σ 0.16‰, so the error on the samples is within both this error and the 2σ of our measurement of $\delta^{44}Ca$ (0.1‰).

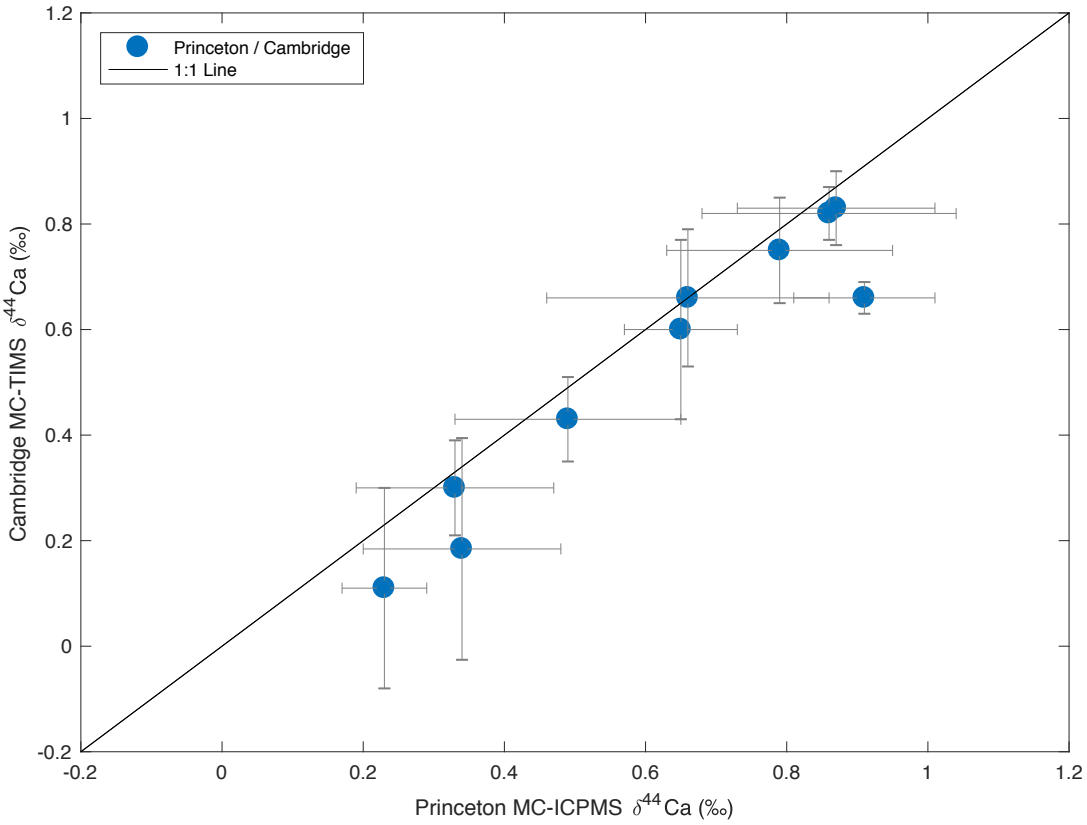

FIGURE 2.14: CROSS PLOT OF THE δ^{44}Ca OF PORE FLUIDS FROM SITE 1003, MEASURED AT PRINCETON (X AXIS) AND CAMBRIDGE (Y AXIS). THE ERROR BARS REPRESENT THE 2σ FROM TRIPLICATES.

In the second study to calibrate calcium isotope analysis between laboratories, speleothem calcium carbonate was measured using my procedure at Cambridge and also after manual column separation on a Neptune MC-ICP-MS at Ruhr-Universität Bochum (Figure 2.15). For the measured samples (n=5) the average absolute offset was 0.1‰ compared to the 2σ of 0.12‰ on the measured samples using the MC-ICP-MS method.

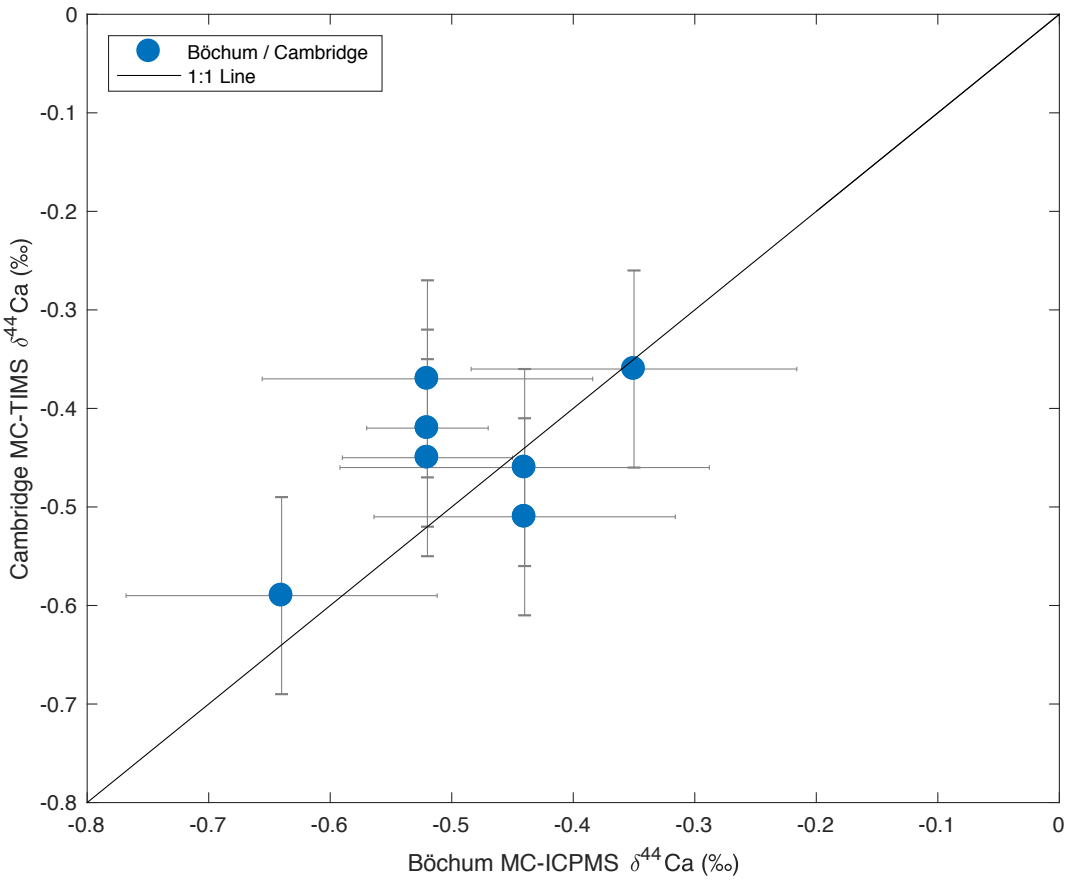

FIGURE 2.15: CROSS PLOT OF THE $\delta^{44}Ca$ OF SPELEOTHEM SAMPLES, MEASURED AT BÖCHUM UNIVERSITÄT (X AXIS) AND CAMBRIDGE (Y AXIS). THE ERROR BARS REPRESENT THE 2σ FROM TRIPLICATES ON THE BÖCHUM DATA AND THE LONG-TERM 2σ OF 915B AT CAMBRIDGE.

Standards have also been measured to cross compare the $\delta^{44}Ca$ measured with the reported values in the literature, with the long-term value of NIST915B (0.28‰ ± 0.1‰ [n=83] v. 0.28‰), NIST915A (-0.99‰ ± 0.1‰ [n=9] v. -1.01‰) and IAPSO seawater (0.96‰ ± 0.1‰ [n=8] 0.99%). The results of these inter-laboratory calibrations and repeated measurement of standards gave confidence to the procedural methods I had set up at Cambridge.

2.5.3 Calcium isotopes in bacterially mediated carbonate

The final case study that was required to assess the validity of our method for our calcium isotope measurements was to observe the fractionation of calcium isotopes during the precipitation of calcium carbonate. There has been much research into the isotopic fractionation of calcium during the

precipitation of calcium carbonate, as discussed in the introduction, which gives a wide range of calcium isotope fractionation factors under a range of experimental and natural conditions (De La Rocha and DePaolo, 2000; Gussone et al., 2003; Marriott et al., 2004; Fantle and DePaolo, 2005; Gussone et al., 2005; Fantle and DePaolo, 2007; Tang et al., 2008a; Teichert et al., 2009; Gussone et al., 2011; Tang et al., 2012; Nielsen et al., 2012a; Fantle, 2015). Authigenic carbonate precipitation occurs when calcium from seawater combines with bicarbonate, often produced by microbial processes within the seafloor. As such, I was interested in seeing if I could replicate this process under laboratory conditions, in order to observe the fractionation of calcium isotopes during precipitation from microbially-produced alkalinity. The two processes thought to drive authigenic carbonate precipitation in sediments, as discussed in the introduction are microbial sulfate reduction and the anaerobic oxidation of methane. Sulfate reduction by sulfate reducing bacteria, often occurs close to the seafloor in porefluids that are chemically similar to seawater. The anaerobic oxidation of methane is primarily coupled to sulfate reduction in marine sediments (Martens and Berner, 1974; Barnes and Goldberg, 1976; Reeburgh and Heggie, 1977; Hoehler et al., 1994) and is utilised by a consortia of archaea and bacteria (Hinrichs et al., 1999; Boetius et al., 2000; Orphan et al., 2001; Orphan et al., 2002; Niemann et al., 2006), although it has recently been shown that some archaea are able to perform AOM without sulfate reducing bacteria (Milucka et al., 2012).

Microbial sulfate reduction occurs in anoxic conditions so there were two possible methods to achieve this in a laboratory study: batch reactors or a chemostat. In a batch reactor setup, the solution composition is set at the start of the experiment and then evolves through the experimental run time. In a chemostat the chemical conditions of the solution are kept constant by the addition of reactants throughout the experiment. In order to mimic the natural marine sedimentary environment it was determined that a batch reactor would be more appropriate as the concentrations of multiple constituents of the pore fluids change with depth in the sediment column.

The first trials were conducted using the common sulfate-reducing bacteria *Desulfovibrio desulfuricans*, which has been extensively used in laboratory studies on sulfate-reducing bacteria, and is commonly found on the seafloor (Postgate and Campbell, 1966; Bryant et al., 1977; Abdollahi and Wimpenny, 1990; Marschall et al., 1993; Okabe et al., 1995). This strain of bacteria was cultivated using an artificial media: DSMZ media 63. Several electron donors were used as food sources for the bacteria to compare growth rates, with initial tests being conducted on lactate, ethanol and glucose. It was found that lactate promoted the fastest growth, followed by ethanol, and finally glucose, which took several weeks to reach the stationary phase relative to lactate, which took several days. However, these three electron donors led to a decrease in pH during the growth of bacteria, as H^+ ions were released. The decrease in pH during the bacteria growth led to the undersaturation of carbonate minerals due to the decrease in carbonate and bicarbonate ion concentrations. In order to precipitate carbonate, the pH must be above the "critical pH" of 7.2 (Soetaert et al., 2007). Following the work of Gallagher et al. (2012) the electron donor formate was tried as it had been shown that the consumption of H^+ during the oxidation of formate led to an increase in the pH. In order to replicate seawater conditions several sodium chloride concentrations were tested, all of which led to the inhibition of growth. Hence, it was determined that although this species of sulfate-reducing bacteria is common on the seafloor, the commercially available strain could not grow in seawater.

The sulfate-reducing bacteria *Desulfovibrio bizertensis* was then chosen as it has recently been isolated from marine sediments off the coast of Tunisia (Haouari et al., 2006). A seawater based medium was created using IAPSO Atlantic seawater based on the aforementioned DSMZ medium 63. By using the combination of a seawater-based media and formate as the electron donor, the carbonate saturation state (as calculated using PHREEQC 3.0 with the Pitzer database) increased over the course of the experiments. During the experiments a number of variables were measured including the calcium concentrations, alkalinity, pH and $\delta^{44}Ca$ of the fluid (Figure 2.16).

The bacteria grew rapidly over the first 3 days after inoculation of the medium, although it took around 10 days for the alkalinity to reach its peak. Calcite was supersaturated within 3 days and had reached a saturation index of 2 by day 5, although geochemical indication of carbonate precipitation didn't occur until day 11. During the precipitation of carbonate the $\delta^{44}Ca$ of the fluid increased from an initial value of 0.8‰ to a maximum of 1.3‰. The $\delta^{44}Ca$ of the fluid decreased to 1.1 in the days after the initial precipitation, which could be due to recrystallization of the initial carbonate, or the transformation of the carbonate from an initial amorphous precipitate to a more stable form.

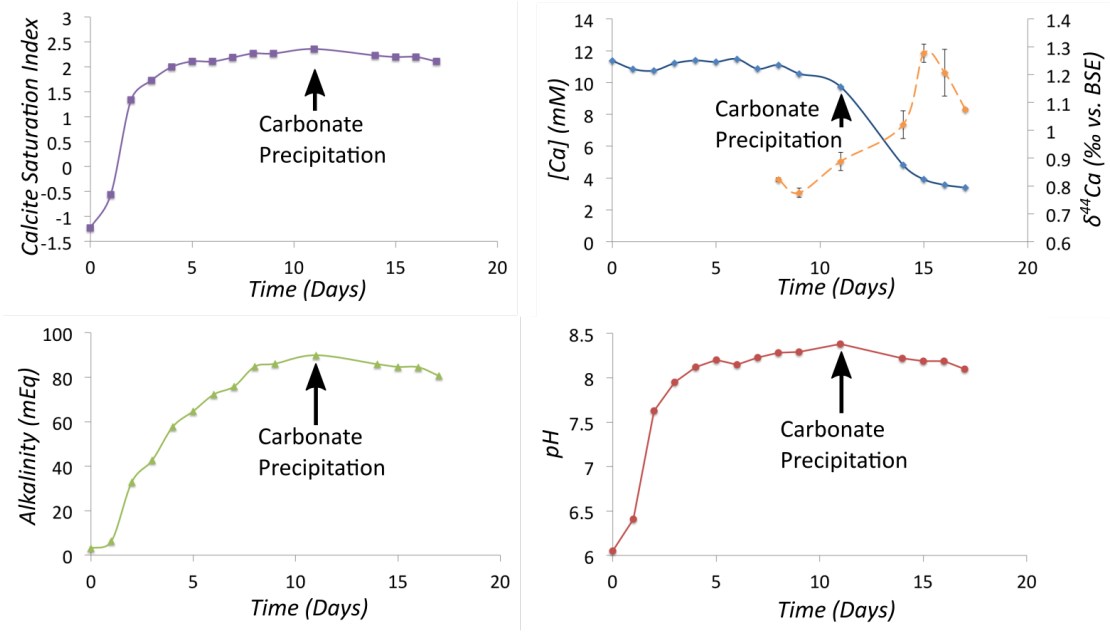

FIGURE 2.16: CHANGES IN SOLUTION CHEMISTRY OVER 17 DAYS OF CULTURING *DESULFOVIBRIO BIZERTENSIS* IN A BATCH REACTOR WITH FORMATE AS AN ELECTRON DONOR AND A SEAWATER BASED MEDIUM (FURTHER DETAILS IN TEXT).

The calcium isotope fractionation factor (α) can be calculated by comparing the $\delta^{44}Ca$ of the fluid with the remaining fraction of calcium in the exponential equation:

EQUATION 2.2

$$R = R_0 f^{\alpha-1}$$

where R is the isotope ratio (44/40), R_0 is the isotope ratio at the starting calcium concentration, f is the fraction of calcium remaining in the fluid and α is the fractionation factor.

By plotting the data from these experiments, I demonstrate that the calcium isotope fractionation factor that best fits the data is 0.99960, which equates to a solid-fluid offset of -0.4‰ (Figure 2.17).

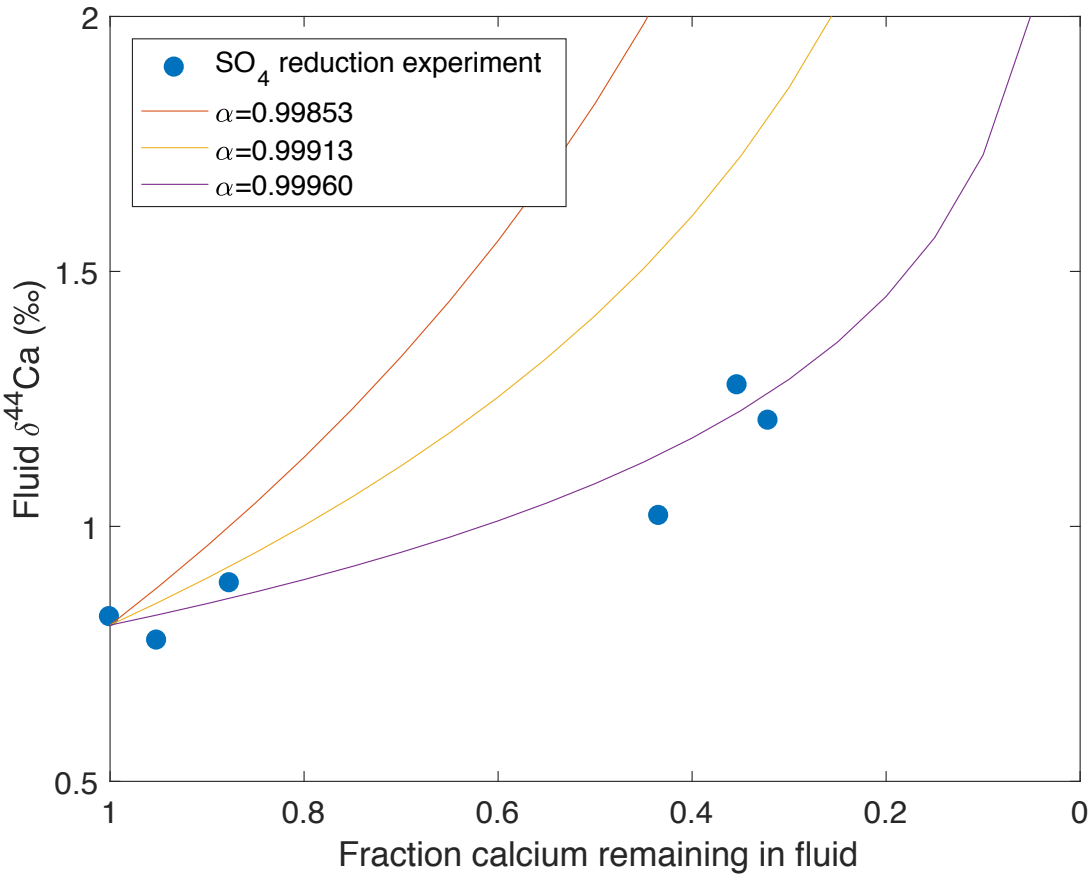

FIGURE 2.17: RAYLEIGH FRACTIONATION PLOTS FOR THE $\delta^{44}Ca$ OF THE FLUID RELATIVE TO THE FRACTION OF CALCIUM REMAINING IN THE FLUID. α=0.99853 AND α=0.99913 ARE THE CALCULATED FRACTIONATION FACTORS OF ARAGONITE AND CALCITE RESPECTIVELY AT 25^{o}C (GUSSONE ET AL., 2005).

This calcium isotope fractionation of -0.4‰ is lower than the calculated solid-fluid calcium isotope fractionation at 25^{o}C of aragonite and calcite of -1.47‰ and -0.87‰ respectively using the temperature controls on calcium isotope fractionation described by Gussone et al. (2005). This data suggested that the precipitated mineral was not aragonite or calcite or that the microbially induced carbonate precipitation has a unique calcium isotope fractionation

factor compared to abiotic precipitates. Although my research in this thesis moved to other projects, a second student in our group continues to work with the pure cultures and found that often the primary precipitate is monohydrocalcite. One possibility is that -0.4‰ is the calcium isotope fractionation associated with the precipitation of monohydrocalcite at 25^{o}C.

Exploration of these three case studies established the validation of the methods used to measure calcium isotope ratios throughout this thesis. The case studies also provided an underlying basis for my initial understanding of calcium isotopes in both carbonate minerals and during bacterially mediated carbonate precipitation. This was applied throughout my PhD, and was essential groundwork for the studies I subsequently performed which are reported in the following three chapters of this thesis.

CHAPTER 3

MASS BALANCE OF THE LAST GLACIAL LAKE LISAN FROM THE δ^{44}CA OF WATER AND SEDIMENTS IN THE DEAD SEA BASIN

3.1 Introduction

Calcium isotopes have been applied to a wide range of geological systems as previously discussed. To explore a range of processes in a natural environment, in this chapter, I will investigate the calcium isotope composition of two calcium-bearing minerals, aragonite and gypsum, in the glacial precursor to the Dead Sea. The aim of this chapter is to examine the importance of the factors that will have affected the isotopic composition of the minerals during their formation. I will use a numerical box-model to explore the effect of changing lake water levels on the calcium isotope composition of the aragonite and gypsum over the last glacial.

The Dead Sea Basin is a pull-apart basin that forms an elongated morpho-tectonic depression, the deepest continental depression on Earth (Quennell, 1958; Garfunkel and Ben-Avraham, 1996). Cliffs and steep slopes representing tectonic escarpments bound both sides of the 150 km long and 15-25 km wide Dead Sea graben (Figure 3.1). During the Quaternary, a series of lacustrine water bodies developed and then desiccated in the Dead Sea Basin in response to regional changes in the hydrology (Neev and Emery, 1967; Stein, 2001; Waldmann et al., 2007; Torfstein et al., 2009). As the valley is located on the boundary between the Saharo–Arabian deserts and the Mediterranean regional climatic zone, its hydrological budget is very sensitive to temporal and spatial shifts in the location of these climate zones. Reconstructing past hydrological changes in the Dead Sea Basin watershed from the lacustrine sediment records provides unequivocal information on

regional climate conditions, and is moreover, a key to link global climate change dynamics with regional climatic variability.

Studies of the limnological history of the Dead Sea Basin lakes have resulted in a relatively well established knowledge base, including the reconstruction of an absolute lake level curve for the last 70 ka (Bartov et al., 2002; Bartov et al., 2003; Bookman et al., 2006; Migowski et al., 2006; Torfstein et al., 2013b).

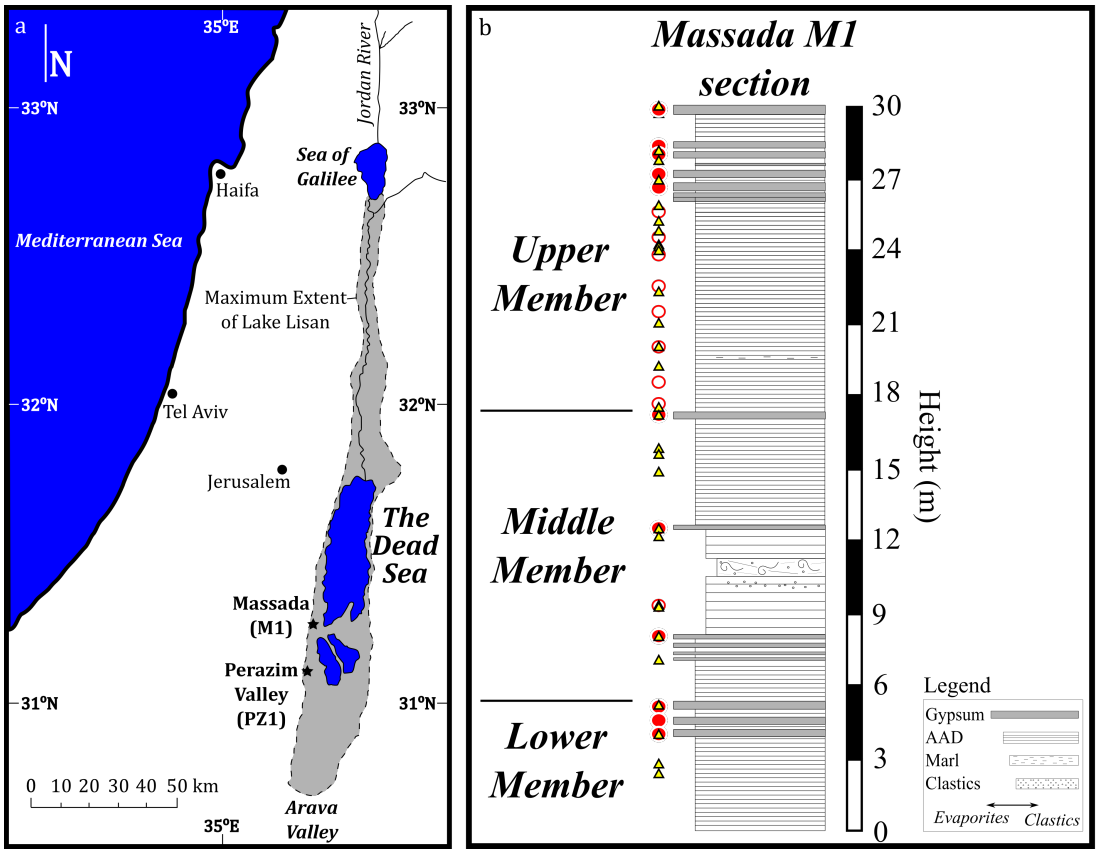

FIGURE 3.1: (A) LOCATION MAP. (B) STRATIGRAPHIC COLUMN FOR THE MASSADA M1 SECTION, WITH THE STRATIGRAPHIC LOCATION OF THE MEASURED SAMPLES: RED CIRCLES, EMPTY RED CIRCLES AND YELLOW TRIANGLES REPRESENT PRIMARY GYPSUM, SECONDARY GYPSUM AND ARAGONITE, RESPECTIVELY.

The processes driving the water budget and hence the lake level curve are nonetheless still debated. It is generally argued that the water level of the Dead Sea and its glacial predecessor, Lake Lisan, reflects the volume of incoming freshwater, such that glacial high water levels represent extremely wet conditions in the Levant (Stein et al., 1997; Enzel et al., 2003; Haase-Schramm et al., 2004; Enzel et al., 2008; Torfstein et al., 2008; Frumkin et al.,

2011; Torfstein et al., 2013b; Rohling, 2013). By contrast, other studies argued for a dry (and cold) glacial cycle in the Levant (Bar-Matthews et al., 1997; Shea, 2003; Robinson et al., 2006; Shea, 2008; Lisker et al., 2010; Miebach et al., 2017). To date, this controversy has not been unequivocally resolved, mainly because of the difficulties involved in accurately reconstructing the water-mass balance of previous cycles of the lake. Here, I approach this issue by using the calcium isotopic composition of evaporate minerals (aragonite, primary and secondary gypsum) through the Lisan Formation, the sedimentary sequence deposited from Lake Lisan to construct a numerical model that links between evaporation processes and the regional water flux, providing robust constraints on lake water volumes.

I will discuss the factors that impact the $\delta^{44}Ca$ of three calcium-bearing evaporite minerals: aragonite, primary gypsum and secondary gypsum. Thes study of the $\delta^{44}Ca$ of the three minerals offers a unique opportunity to constrain both the temporal variation in the calcium budget and changes in the $Ca:SO_4$ and $Ca:HCO_3$ ratios of the last glacial Lake Lisan brine. The results are integrated into in a numerical model that quantitatively constrains the hydrological budget of the Dead Sea Basin during the last glacial cycle.

3.1.1 Geological-limnological background

The Dead Sea and its predecessors are considered to be “amplifier lakes” because they are terminal and exhibit intense lake level fluctuations in response to regional climate variability (Street-Perrott and Roberts, 1983; Machlus et al., 2000). Lake Lisan spanned between the Sea of Galilee in the north and Hazeva in the Arava Valley to the South (Figure 3.1). During its Last Glacial Maximum highstand, Lake Lisan’s water level (~160 meters below sea level; mbsl) was more than 250 meters higher relative to the average Holocene lake level (~400 mbsl), with correspondingly larger water volumes (Stein et al., 1997; Stein, 2001; Bartov et al., 2002; Torfstein et al., 2009). These differences reflect the significantly more positive water balance that existed in the Dead Sea watershed during the last glacial relative to present.

The Lisan Formation contains a significant quantity of annually precipitated primary aragonite (rather than calcite, due to the high Mg/Ca ratio in the lake brine; (Katz, 1973)), which allowed direct radiocarbon and U–Th dating (Stein et al., 1997; Haase-Schramm et al., 2004). Absolute dating of several sedimentary sequences across the Dead Sea Basin yielded a basin-wide unified age model for Lake Lisan and its deposits (Torfstein et al., 2013a).

Intervals of positive water balance in Lake Lisan triggered the onset of long term meromictic conditions, which were characterized by the deposition of alternating aragonite and detritus (AAD) laminae (Machlus et al., 2000, Marco et al., 1996), whereby silty to clay-sized detritus laminae precipitated following winter flooding of the lake. These incoming freshwaters were enriched in bicarbonate, calcium and sulfate ions relative to the lake Ca-chloride brine (Stein et al., 1997). The bicarbonate ions precipitated as aragonite shortly after their introduction to the lake, while the sulfate gradually accumulated until gypsum saturation was reached. At that point, gypsum grazing from the mixolimnion was initiated. Subsequently, the sinking gypsum crystals dissolved in the anoxic monimolimnion, where gypsum under saturation existed due to microbial sulfate reduction. During negative water budget intervals, the freshwater supply into the lake decreased, reducing the amount of precipitating aragonite (Stein et al., 1997). Under a more extreme negative water balance, the water column overturned and mixed, resulting in massive precipitation of primary gypsum (Stein et al., 1997; Torfstein et al., 2005).

The Massada M1 Section, our main study site, is located on the foothills of the Massada archaeological site (Figure 3.1). The section is ~30 m thick, and its base is located at 374 mbsl, overlying the interglacial Samra Formation (Waldmann et al., 2007). The Massada section is divided into three Members (Machlus et al., 2000) (Figure 3.1). The Lower Member is 5.6m thick, deposited between ~70-58.5ka (Torfstein et al., 2013a), is primarily composed of an AAD sequence that is capped by three prominent gypsum layers. This Member represents a relatively high stand lake that declines ca. 61ka, resulting in massive gypsum deposition. The Middle Member (58.5-39.7ka) is

~11.4 m thick and is relatively enriched with clastic sediments, whose grain size ranges between fine sand and pebbles, that alternate AAD packages and occasional gypsum layers. An ~8kyr depositional hiatus separates the Middle and Upper Members. The Upper Member (31-14.5 ka) is comprised of a ~9 m thick sequence of AAD capped by a ~2 m thick primary gypsum unit. An additional ~2 m thick unit of AAD and gypsum caps the Upper Member (Stein, 2001; Bartov et al., 2003; Haase-Schramm et al., 2004). Stratigraphically, the Holocene Ze'elim Formation caps the Lisan Formation.

The sedimentology and geochemical composition of the Lisan Formation provides an important regional paleo-climatological archive that records orbital- and millennial- timescale climate fluctuations in the Levant (Neev and Emery, 1967; Begin et al., 1974; Katz et al., 1977; Ken-Tor et al., 2004; Torfstein et al., 2005; Bookman et al., 2006; Migowski et al., 2006; Torfstein et al., 2008; Torfstein et al., 2009).

3.1.2 Paleoclimate in the Lisan catchment

The late Pleistocene is characterised by a rapid changes in global climatic conditions, which are recorded extensively in deep-sea marine cores and polar ice records (Shackleton, 1967; Dansgaard et al., 1993; Andersen et al., 2004). Over the past two decades much progress has been made in addressing the dearth of research into the impact of these climatic changes on continental regions (Bartov et al., 2003).

Speleothems provide an excellent record for paleoclimate in the region due to the prevalence of carbonate bedrock and hence, karstic topography. There is evidence of continuously growing speleothems throughout the late Pleistocene from the west of Israel near the Eastern Mediterranean, which has been used to suggest there has been no extreme aridity over this period (Frumkin et al., 1999; Bar-Matthews et al., 2000; Ayalon et al., 2002; Bar-Matthews et al., 2003). Speleothems within the Soreq Cave, which is located to the west of Jerusalem, has been extensively studied (Bar-Matthews et al., 1997; Matthews et al., 2000; Bar-Matthews et al., 2000; Ayalon et al., 2002;

Vaks et al., 2003; Bar-Matthews et al., 2003; Affek et al., 2008 etc.). A combination of carbon and oxygen isotopes and the D/H ratio within the speleothems within the Soreq Cave led to the conclusion that the Eastern-Mediterranean was cooler during the last glacial period (Bar-Matthews et al., 1997; Matthews et al., 2000). This cooling reduced the volume and intensity of storms in the region, which, in turn, reduces the transfer of water from the Eastern-Mediterranean to the Lisan catchment.

Other studies in the area have focussed on the impact that the North Atlantic Heinrich and Dansgaard-Oeschger events had on the East-Mediterranean and the Lisan catchment (Schramm et al., 2000; Stein, 2001; Bartov et al., 2003; Haase-Schramm et al., 2004). These studies correlated rapid lake level drops in Lake Lisan with the Heinrich events. Low levels of precipitation over the Lisan catchment, which were caused by an influx of cooler water into the Mediterranean leading to lower evaporation from the Mediterranean, resulted in the lake level drops (Bartov et al., 2003). Recently, it has been proposed that the rapid lake level drops during Heinrich events could be due to exceptionally high wind speeds leading to increased evaporation (Rohling, 2013).

3.2 Methods

3.2.1 Sample selection

The M1 section was sampled (Figure 3.1) by carving out field blocks typically about 10x10x10 cm^3 in size from the cliff face (Figure 3.2). These were wrapped in plastic coating to avoid disintegration and taken to the lab where aragonite or gypsum were carefully scraped off the field block, in order to achieve clean mineral separation for the final sample powder. Water samples were collected from the Dead Sea (En Gedi shore) and Sea of Galilee (Karei-Deshe shore) directly into 100mL centrifuge tubes. The Dead Sea brine was stored at room temperature to avoid halite crystallization, and the Sea of Galilee samples were kept refrigerated until analysis. Prior to analysis, the

aqueous samples were filtered to remove suspended particles using Millipore 0.2µm syringe-filters. A separate aliquot of each of the aqueous samples was run after acidification with nitric acid to ensure there was no carbonate precipitation in the samples during transit.

FIGURE 3.2: THE SAMPLED CLIFF FACE AT THE MASSADA SECTION

3.2.2 Analytical methods

The three calcium-bearing minerals were identified through hand specimen examination, and dissolution in water if aragonite and gypsum needed to be separated. In general aragonite is found as layers within the AAD, and primary gypsum is composed of thick tabulate layers of gypsum (Neev and Emery, 1967; Stein et al., 1997). Secondary gypsum is found as disseminated gypsum crystals in several layers within the section, and is easily identified relative to the massive of interlaminated primary gypsum deposits (Stein et al., 1997). Approximately 500mg of powdered bulk aragonite and primary gypsum was extracted by scraping into glass vials taking care to avoid contamination from the any adjacent detrital, or gypsum laminae. Secondary gypsum was crushed gently, and then individual crystals of gypsum were picked and ground to a fine powder. Approximately 25µg of aragonite or 44µg of gypsum were weighed into Teflon screw-top vials and dissolved in 100µL 6M HNO_3. The samples were then spiked and separated on the Dionex and analysed for calcium isotope ratios as described in Chapter 2.

Oxygen and carbon isotopes analyses were conducted on carefully scraped and separated aragonite laminae, after rinsing in deionized, ultrapure, water. The isotope ratios were measured using a Thermo Scientific GasBench II equipped with a CTC auto sampler coupled to a Thermo Finnigan MAT253 in the Godwin Laboratory, University of Cambridge.

3.2.3 Modelling methods

I used a calcium 2-box model to explore changes in the lake calcium cycle over glacial–interglacial cycles as recorded by the calcium isotope composition of aragonite and primary gypsum. The model uses the same principles as the model previously developed by Nielsen and DePaolo (2013). The box model is based on the mass balance equation:

$$\frac{\partial M}{dt} = \sum_{inputs} F_{inputs} - \sum_{outputs} F_{outputs}$$

EQUATION 3.1

Where M is mass of calcium, F is the flux and t is time.

The total quantity of calcium in the surface box (M^{Ca}_{sb}) is determined by the sum of the input fluxes (rivers, groundwater and mixing with the deep box) and output fluxes (aragonite and primary gypsum precipitation):

$$\frac{\partial M_{sb}^{Ca}}{dt} = F_{riv} + F_{gw} + F_{mix} - F_{sed} = F_{riv} + F_{gw} + F_{mix} - F_{arag} - F_{gyp}$$

EQUATION 3.2

Previous studies have suggested that there is negligible net gypsum deposition in Lake Lisan during highstand stages. Although gypsum could have precipitated in the surface during highstands due to some mixing of the upper and lower water bodies, this gypsum would largely have been dissolved as it sank through the under-saturated lower brine, and the sulfate would then be reduced to sulfide, which precipitated as sedimentary sulfide minerals (Stein et al., 1997; Torfstein et al., 2005). This explains why negligible primary gypsum is found in the AAD layers and most is concentrated in the larger gypsum beds. Therefore, I initiate my model at highstand and treat the massive primary gypsum deposition and lake overturn as a perturbation to the system that allows the surface water to exceed gypsum saturation and generate the thick gypsum beds (Katz et al., 1977; Stein et al., 1997; Bartov et al., 2002; Torfstein et al., 2005; Torfstein et al., 2008). In contrast, the precipitation of aragonite is controlled by the freshwater input due to the supply of bicarbonate ions (Stein et al., 1997).

The calcium isotopic composition can then be modelled alongside the calcium concentration mass balance by adding the terms for the isotopic ratios of the inputs and outputs:

$$M_{lw}\frac{\partial R_{sb}}{dt} = F_{riv}[Ca_{riv}](\mathrm{R}_{riv} - \mathrm{R}_{lw}) + F_{gw}[Ca_{gw}](\mathrm{R}_{gw} - \mathrm{R}_{lw}) + F_{mix}[Ca_{mix}](\mathrm{R}_{mix} - \mathrm{R}_{lw}) - F_{sed}(R_{sed} - R_{lw})$$

EQUATION 3.3

Hence the surface box water composition becomes:

$$\frac{\partial \delta_{sb}}{dt} = \frac{1}{M_{lw}}\big(F_{riv}[Ca_{riv}](\delta_{riv} - \delta_{lw}) + F_{gw}\big[Ca_{gw}\big]\big(\delta_{gw} - \delta_{lw}\big) + F_{mix}[Ca_{mix}](\delta_{mix} - \delta_{lw}) - (F_{arag} \times \varepsilon_{arag})\big)$$

EQUATION 3.4

Where, $\delta_{lakewater}, \delta_{riv}, \delta_{gw}, \delta_{mix}$ and δ_{arag} are the $\delta^{44}Ca$ of the lake, rivers, groundwater, brine and deposited aragonite, respectively, and ε_{arag} is the calcium isotope fractionation factor associated with precipitation of aragonite.

The volume of water within the lake needs to be considered so that precipitation of gypsum can be triggered after overturning when the water volume reaches a critically low level. The approach of Rohling (1999; 2013) is followed to calculate the evaporative losses from the lake:

$$E_{lowS} = -\rho_a LCV(q_s - rq_a)1.26 \times 10^{-2}$$

EQUATION 3.5

where E_{lowS} is the evaporation from a low salinity lake, ρ_a is the density of air at mean lake level pressure (1.2 kg m^{-3}), L is the latent heat of vaporization in J kg^{-1} at surface-water temperature in °C (2500.83–2.34*T_s), C is the exchange coefficient (1.15*10^{-3}), V is the wind speed in m s^{-1}, r is the relative humidity between 0 and 1, q_s is the saturation vapour pressure at surface-water temperature T_a and q_a is the saturation vapour pressure at air temperature (10m above lake surface). The values for q are calculated using the formula:

$$q = (\frac{m_v}{m_d})e_{sat}(p - e_{sat})^{-1}$$

EQUATION 3.6

where m_v/m_d is the ratio between the molecular weight of water vapour and dry air, p is the pressure at mean sea level (1.012*10^5Pa) and e_{sat} (Pa) is:

$$e_{sat} = 10^2 e^{55.17 - 6803(T+273.15)^{-1} - 5.07\ln(T+273.15)}$$

EQUATION 3.7

In order to address the influence of high salinity, the E_{lowS} is corrected by (1-0.0015*S) (Salhotra et al., 1985; Rohling, 2013). The salinity was previously considered to be proportional to the volume of the lake (Rohling, 2013), however due to the stratified nature of the lake within this model the salinity is taken to be three during periods of lake stratification when evaporation occurs from the low salinity surface layer (Stein et al., 1997) and proportional to the dilution of the brine volume during lake overturn events when the lake composition becomes uniformly hyper-saline.

The terms for wind-speed, lake-surface temperature and air temperature were assumed to be in direct proportion to the Dansgaard-Oeschger (D–O) cycles recorded in the Greenland ice-core $\delta^{18}O$ (Dansgaard et al., 1993; Grootes et al., 1993). A non-dimensional scaling coefficient that imposes fluctuations in proportion with D–O cycles was calculated following Rohling (2013): $f=(\delta_{NG}-\delta_{NGmod})/\delta_{NGrange}$. δ_{NG} is the $\delta^{18}O$ from the NGRIP record (Andersen et al., 2004) at each time step, δ_{NGmod} is the modern value of Greenland ice and $\delta_{NGrange}$ is the range between the minimum glacial $\delta^{18}O$ and δ_{NGmod}. The non-dimensional scaling coefficient f was then applied to wind-speed, air temperature and sea-surface temperature using a formulation such as: $V=V_{mod}+f\Delta_V$ where V_{mod} is modern wind-speeds in the Dead Sea Basin ($4ms^{-1}$), Δ_V is the total glacial-interglacial amplitudes of change in wind speed (1.1; See Rohling (2013) for further details). The total glacial-interglacial temperature difference (Δ_T) is assumed to be $-7.5^{o}C$ (Rohling, 2013).

The volume of water lost at each time point from the lake due to evaporation (F_{evap}) is calculated by multiplying the evaporative flux and the surface area.

The riverine and groundwater fluxes are then calculated by using the previously determined input ratio for rivers to ground water of 61:39 (Stein et al., 1997) and comparing F_{evap} to the changing lake volume each year calculated from a hypsometric curve (Bartov et al., 2003).

The surface box is modelled as follows for the water volume and the deep brine box is held at a constant size during highstand conditions.

$$\frac{\partial Water_{sb}}{\partial t} = (F_{riv} + F_{groundwater}) - F_{evap}$$

EQUATION 3.8

The flux of aragonite out of the system depends on the concentration of calcium within the lake a time t:

$$F_{arag_t} = \frac{M_{Ca_t} / volume_t}{M_{Ca_{t0}} / volume_{t0}} (F_{arag_{t0}})$$

EQUATION 3.9

During the overturn of the lake, leading to gypsum oversaturation and precipitation, the two boxes are combined. When the lake level rises again, water column stratification is triggered, leading to cessation of the primary gypsum precipitation. The model was run for 55kyr with a time step of 1 year. The model is summarised in Figure 3.3.

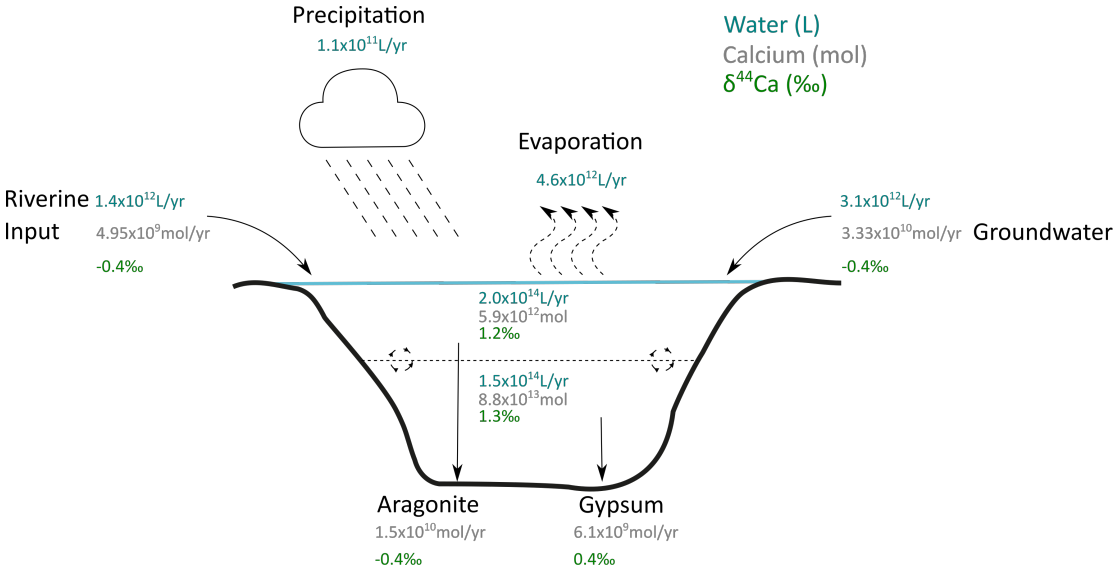

FIGURE 3.3: SUMMARY DIAGRAM OF THE TWO-BOX MODEL CONSISTING OF THE AVERAGE FLUXES AND RESERVOIR SIZES.

3.3 Results

3.3.1 Calcium isotopes

Calcium isotope analyses were performed on primary gypsum, secondary gypsum, and aragonite deposited between 70-14 ka (Figure 3.4). The primary gypsum $\delta^{44}Ca$ ranges between 0.17‰ and 0.48‰ with one sample that caps the thickest gypsum unit in the section displaying a much higher value at 0.71‰. There is no systematic trend in the gypsum $\delta^{44}Ca$ composition with time over the interval studied. I also report two high resolution transects of $\delta^{44}Ca$ across the largest beds of primary gypsum and observe a similar $\delta^{44}Ca$ range (LL_006, LL_038 – Table 3.1).

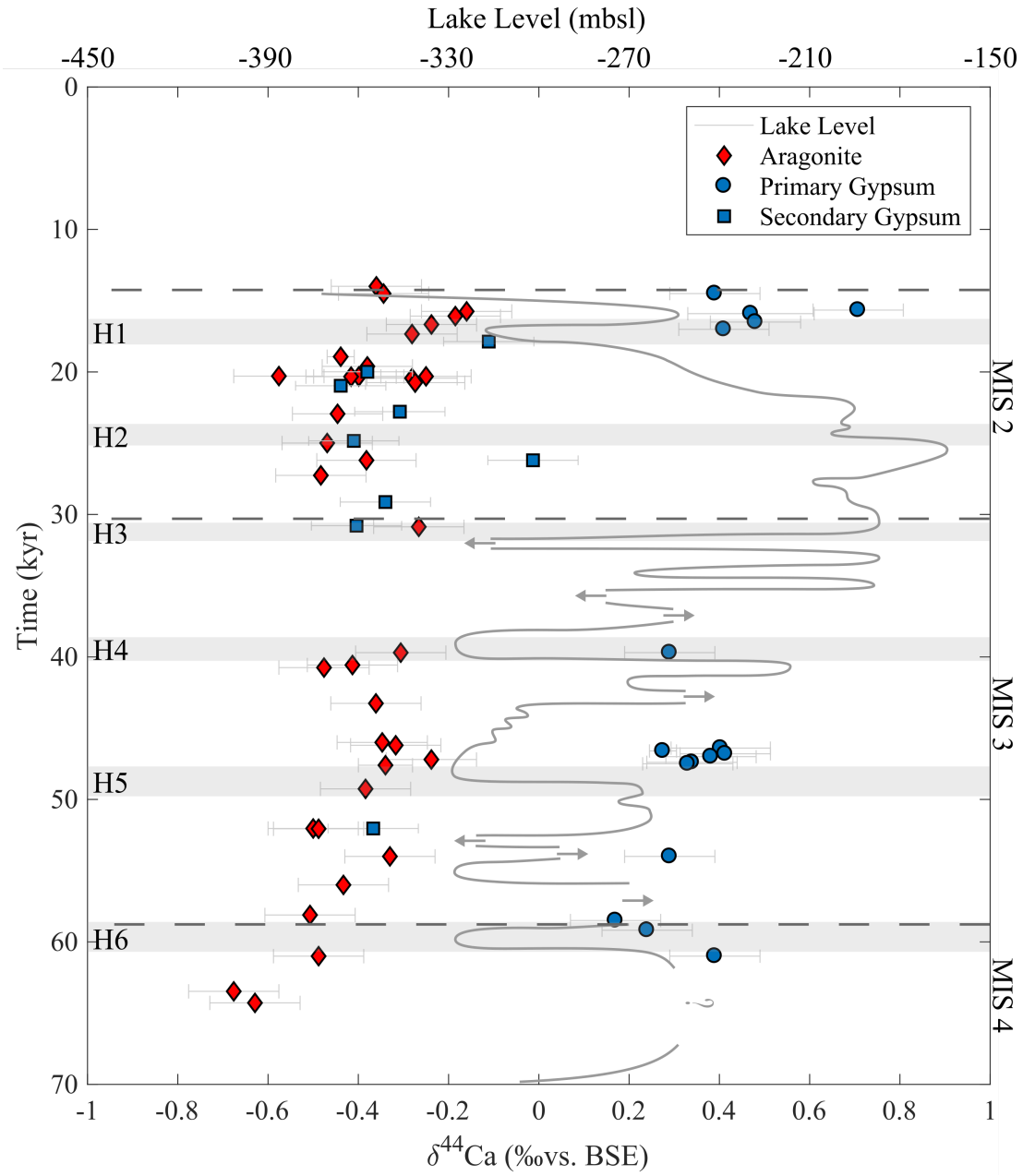

FIGURE 3.4: SECULAR EVOLUTION OF $\delta^{44}Ca$ OF ARAGONITE, PRIMARY AND SECONDARY GYPSUM FROM THE MASSADA SECTION. GREY RECTANGLES MARK THE TIMING OF NORTH ATLANTIC HEINRICH EVENTS, CORRESPONDING TO ABRUPT LAKE LEVEL DROPS TYPICALLY ASSOCIATED WITH MASSIVE GYPSUM PRECIPITATION. LAKE LEVEL FROM TORFSTEIN ET AL. (2013)

In contrast, the secondary gypsum has a much lower $\delta^{44}Ca$, ranging from –0.44‰ to –0.01‰, with an average $\delta^{44}Ca$ of –0.3‰ (Figure 3.4). Similar to the primary gypsum there are no clear temporal trends within the secondary gypsum. Aragonite $\delta^{44}Ca$ ranges from –0.68‰ to –0.16‰, with the bulk of the

$\delta^{44}Ca$ around –0.4‰. A transgressional unconformity between 40 and 31ka accounts for the data paucity over this time period (Torfstein et al., 2013b).

Five consecutive aragonite laminae within each of two 10x10x10cm^3 blocks of 'AAD' were sampled to assess the homogeneity of the samples and to investigate the possibility of annual variations in the $\delta^{44}Ca$ composition of the aragonite. One of the sets of aragonite layers ranges between –0.51‰ and –0.22‰ whereas the other ranges from –0.40‰ to –0.15‰ (Figure 3.5). Modern water samples from the Dead Sea and the Sea of Galilee were measured as described above and averaged 0.45‰ and 0.76‰, respectively (n=2, 2σ=0.02).

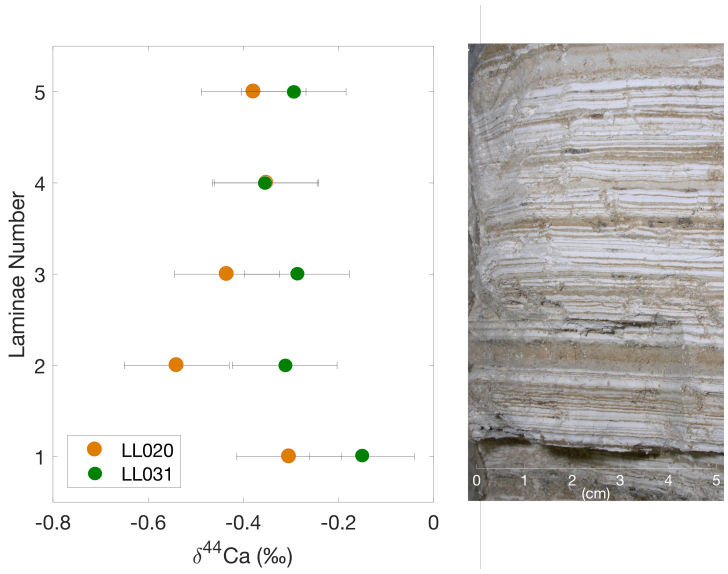

FIGURE 3.5: $\delta^{44}Ca$ VARIATIONS BETWEEN FIVE CONSECUTIVE ARAGONITE LAMINAE, AND A BLOCK OF ALTERNATING ARAGONITE AND DETRITUS ('AAD') SIMILAR TO THE ONES SAMPLED. LL_020 HAS AN AVERAGE OF -0.40 ±0.16‰ (2σ), WHEREAS LL_031 HAS AN AVERAGE OF -0.28 ±0.14‰ (2σ).

TABLE 3.1: $\delta^{44}Ca$ OF ARAGONITE, PRIMARY AND SECONDARY GYPSUM (‰ RELATIVE TO BULK SILICATE EARTH). FIVE SAMPLES WERE RUN TWICE, WITH THE AVERAGE STANDARD DEVIATION (2σ) IS 0.08‰. THE STANDARD DEVIATION (2σ) OF THE STANDARD 915B WAS 0.11‰. THE AGE UNCERTAINTY IS ±0.5KYRS UP TO 55KYRS AND ±1KYR UP TO 65KYRS (FROM TORFSTEIN ET AL., 2013).

Aragonite

Sample ID	Age (kyr)	$\delta^{44}Ca$
LL_001	14.0	-0.36
LL_004	14.5	-0.34
LL_007	15.8	-0.16
LL_008	16.1	-0.19
LL_010	16.7	-0.24
LL_012	17.3	-0.28
LL_016	18.9	-0.44
LL_017	19.6	-0.38
LL_019a	20.3	-0.58
LL_019b	20.3	-0.25
LL_019c	20.3	-0.40
LL_019d	20.3	-0.42
LL_019e	20.4	-0.28
LL_020a	20.8	-0.27
LL_020b	20.8	-0.30
LL_020c	20.8	-0.54
LL_020d	20.8	-0.43
LL_020e	20.8	-0.35
LL_020f	20.8	-0.38
LL_023	22.9	-0.45
LL_025	25.0	-0.47
LL_027	26.2	-0.38
LL_028	27.3	-0.48
LL_031a	30.9	-0.15
LL_031b	30.9	-0.31
LL_031c	30.9	-0.29
LL_031d	30.9	-0.35
LL_031e	30.9	-0.29
LL_032	39.7	-0.31
LL_033	40.6	-0.41
LL_034	40.8	-0.48
LL_036	43.3	-0.36
LL_038a	47.5	-0.35
LL_038b	47.5	-0.32
LL_038c	47.5	-0.24
LL_038d	47.5	-0.34
LL_039	49.3	-0.38
LL_041	52.0	-0.50
LL_042	52.1	-0.49
LL_043	54.0	-0.33
LL_045	56.0	-0.43
LL_046	58.1	-0.51
LL_050	61.0	-0.49
LL_051	63.5	-0.68
LL_052	64.3	-0.63

Primary Gypsum

Sample ID	Age	$\delta^{44}Ca$
LL_003	14.5	0.39
LL_005	15.7	0.71
LL_006a	15.9	0.47
LL_006b	15.9	0.65
LL_006c	15.9	0.65
LL_006d	15.9	0.60
LL_006e	15.9	0.31
LL_009	16.5	0.48
LL_011	17.0	0.41
LL_032	39.7	0.29
LL_038a	47.5	0.40
LL_038b	47.5	0.28
LL_038c	47.5	0.41
LL_038d	47.5	0.38
LL_038e	47.5	0.34
LL_038f	47.5	0.33
LL_043	54.0	0.29
LL_047	58.5	0.17
LL_048	59.2	0.24
LL_050	61.0	0.39

Secondary Gypsum

Sample ID	Age	$\delta^{44}Ca$
LL_013	17.9	-0.11
LL_017	20.0	-0.38
LL_021	21.0	-0.44
LL_022	22.8	-0.31
LL_024	24.8	-0.41
LL_026	26.2	-0.01
LL_029	29.1	-0.34
LL_030	30.8	-0.40
LL_042	52.0	-0.37

Fluid

Sample ID	Age	$\delta^{44}Ca$
Sea of Galilee	Modern	0.76
Dead Sea	Modern	0.45

3.3.2 Oxygen and carbon isotopes

The oxygen isotopes of the aragonite ranged between 1.64 and 5.92‰, with the $\delta^{18}O$ before 40ka closer to 5.5‰ and the $\delta^{18}O$ since 40ka varying with the lake level and averaging 3‰ (Figure 3.6).

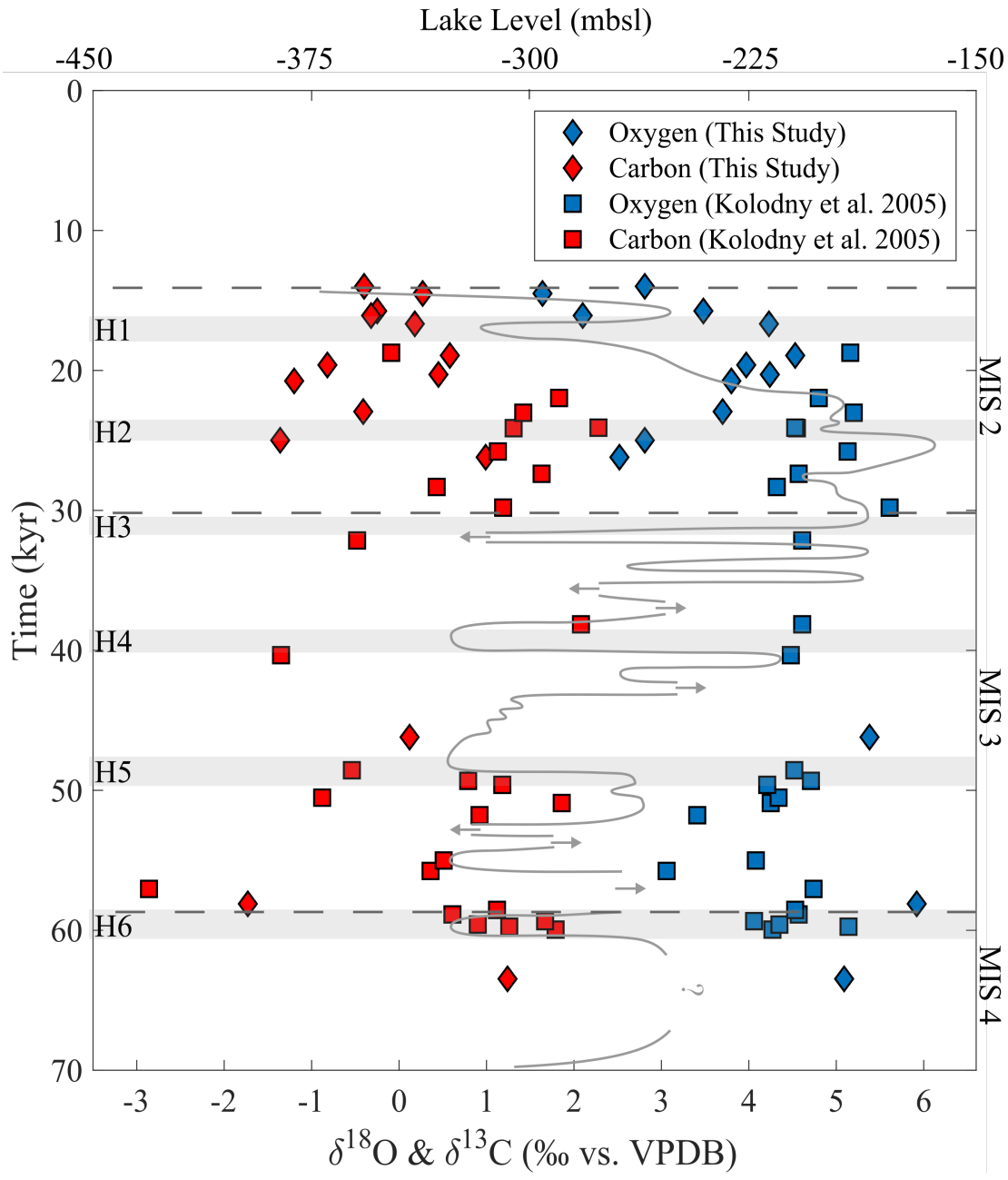

FIGURE 3.6: CARBON AND OXYGEN ISOTOPES FROM THE MASSADA SECTION 'X' (THIS STUDY) AND THE PERAZIM VALLEY SECTION 'O' (KOLODNY ET AL., 2005), ALONG WITH THE LAKE LEVEL CURVE FROM TORFSTEIN ET AL. (2013). SEE FIGURE 3.1 FOR THE LOCATIONS OF THE MEASURED SECTIONS.

The $\delta^{18}O$ measured within the aragonite is similar to previous studies of oxygen isotopes in carbonate rocks throughout the region, however there is more variation between 30 and 15ka than previously recorded in aragonite precipitated from Lake Lisan (Kolodny et al., 2005). The $\delta^{18}O$ shows a weak negative correlation (r^2=0.21) with the $\delta^{44}Ca$ of individual aragonite laminae (Figure 3.7).

Aragonite $\delta^{13}C$ ranges between –1.73 and 1.24‰ with no discernible correlation to other measured variables including lake level (Figure 3.6) and $\delta^{44}Ca$ (r^2=0.04, Figure 3.7). The $\delta^{13}C$ data agrees with previously published data of $\delta^{13}C$ in aragonite in Lake Lisan (Figure 3.6; Kolodny et al., 2005).

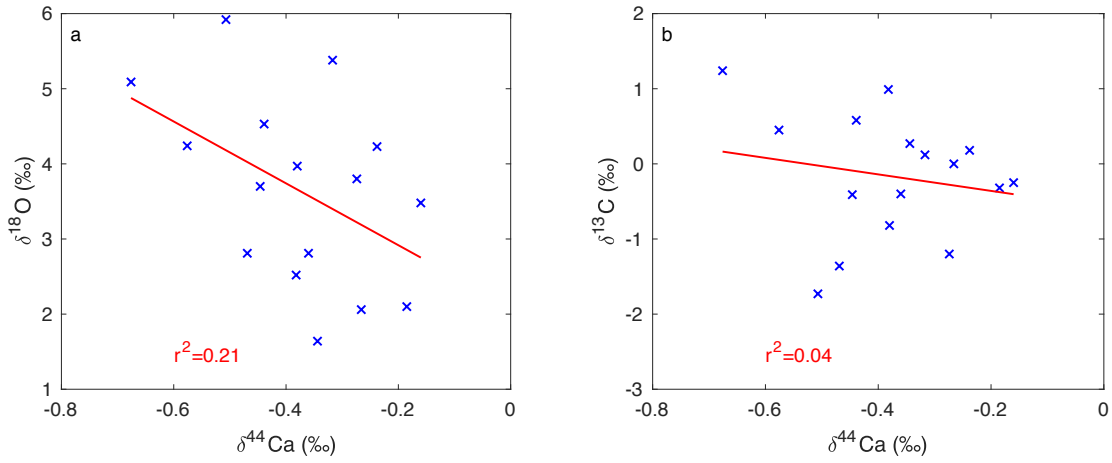

FIGURE 3.7: CROSS-PLOTS OF THE ARAGONITE $\delta^{44}Ca$ VS. $\delta^{18}O$ AND $\delta^{13}C$.

3.4 Discussion

The $\delta^{44}Ca$ of multiple calcium-bearing minerals precipitated from the same water body allows us to quantify the lake calcium mass balance and its temporal variations. Firstly, I address the water-mineral calcium isotope fractionation. In this I will consider both kinetic and equilibrium isotope fractionation and the temperature effect on this fractionation. Secondly, the use of the range of $\delta^{44}Ca$ within the calcium-bearing minerals is used to explore the changing aqueous geochemistry of Lake Lisan. Thirdly, I explore the temporal changes in the $\delta^{44}Ca$ of aragonite and gypsum, allowing the application of my two-box model to assess how the changing environmental

parameters of the lake affect the isotope composition of the precipitated aragonite and gypsum. Finally, I discuss the insight that $\delta^{44}Ca$ provides into the formation of secondary gypsum.

3.4.1 Calcium isotope fractionation

The $\delta^{44}Ca$ of calcium-bearing minerals formed in Lake Lisan depends on the composition of the lake water and the calcium isotope fractionation associated with mineral formation (ε). If ε is temporally constant, the minerals should each record the changing isotopic composition of the lake. As discussed in the introduction, there is consensus in the literature that the magnitude of ε during carbonate precipitation is dependent upon the precipitation rate, and that changes in this mineral precipitation rate have been linked quantitatively to temperature. The aragonite $\delta^{44}Ca$ varies over the studied interval by close to 0.5‰, which is well outside analytical error. One possibility is that the variability in the aragonite $\delta^{44}Ca$ is due to changes in ε controlled by temperature variations over the glacial-interglacial cycle. However, in the case of Lake Lisan, modelled temperature over the last 70kyr suggest variations of 7.5°C (Rohling, 2013), which would alter ε by 0.11‰. Therefore, it is unlikely that the aragonite $\delta^{44}Ca$ record is controlled by temperature variations but rather, that it directly records changes in the $\delta^{44}Ca$ of the lake.

The other factor that could impact ε temporally is changes in aragonite precipitation rate due to changes in salinity. It has previously been shown in laboratory experiments that increasing the ionic strength of a solution leads to more rapid precipitation of aragonite (Zuddas and Mucci, 1998). There are unlikely to be large changes in the salinity on an annual basis when the majority of aragonite precipitation occurs, however there will be large changes in salinity during lake overturn. If this were the case, the calcium isotope fractionation during aragonite precipitation might decrease, and the $\delta^{44}Ca$ of the aragonite increase during the lake overturn events. Previous measurements of the effect of different salinities on the calcium isotope fractionation factor during carbonate precipitation, however, have been conducted over a range of salinities between 1.8‰ and 49‰ (Tang et al.,

2012), whereas the salinity in Lake Lisan as a whole was thought to be between 100-150‰, with the dead sea brine around 315‰ (Katz et al., 1981; Krumgalz and Millero, 1983; Kolodny et al., 2005). Tang et al. (2012) observed a 1‰ change in calcium isotopic fractionation when varying both precipitation rate and salinity, of which out of a correlation coefficient of 0.67, 0.56 of the variability in the calcium isotopic fractionation was attributed to rate, and 0.11 to salinity. However, as the salinity in the Lisan brine is far beyond the experimental range the measured relationship is likely no longer valid. There are other competing factors, such as when combining the brine and the freshwater, the presence of magnesium and sulfate ions within the solution may inhibit carbonate mineral growth and possibly lead to a decrease in carbonate precipitation rate (Reddy and Nancollas, 1976). It may be that the confluence of these factors cancels out, but without independent controls on ionic strength and composition, it is not possible to comment further.

I conclude that neither temperature nor precipitation rate change systematically over the studied interval so the 0.5‰ changes in the aragonite $\delta^{44}Ca$ must be attributed to changes in the lake water $\delta^{44}Ca$. Assuming that ε is –1.6‰, the kinetic limit (Gussone et al., 2003), then the average Lake Lisan water $\delta^{44}Ca$ was +1.2‰ over the studied interval, but varied between +1.1 and +1.4‰. Knowing the average lake water $\delta^{44}Ca$ allows for the estimation that ε was 0.8‰ during gypsum precipitation, where the gypsum is more enriched in the ^{40}Ca-isotope relative to the lake. The calcium isotope fractionation factor for gypsum precipitation measured here is comparable to a suite of laboratory experiment results. Harouaka et al. (2014) reported calcium isotope fractionation between 0.8 and 2.25‰ in gypsum precipitated under a range of experimental conditions. This is a wider range for ε than reported by Blättler and Higgins (2014) (~1‰) and Hensley (2006) (~0.9‰) who also used a variety of starting solutions and temperatures. There have been relatively few measurements of the $\delta^{44}Ca$ of gypsum in natural environments. In a cave system in Italy, the calcium isotope fractionation during microbially-induced gypsum precipitation was narrower at 0.3 to 0.9‰ with the ^{40}Ca-isotope favoured in the mineral (Harouaka et al., 2016).

The work of Harouaka et al. (2014) hypothesised that the calcium isotopic fractionation factor during gypsum precipitation depends on the crystal face of growth, specifically that lower calcium isotopic fractionation occurs when the gypsum precipitation occurs on the 010 face of the crystals. The calculated calcium isotope fractionation factor for gypsum precipitation in Lake Lisan (0.8‰) is low; this suggests slow crystal growth, which would have occurred primarily on the 010 faces, resulting in the formation of tabulated crystals rather than the needle-shaped crystals that occur at higher rates of precipitation. This matches well with the described morphology of the crystals within the large gypsum layers, which are primarily composed of hexagonal gypsum crystals relative to the needle shaped crystals associated with the secondary gypsum. The alternative is that gypsum precipitation occurs in isotopic equilibrium with the fluid; the equilibrium calcium isotope fractionation factor between fluid and gypsum has been suggested to be ~0.5‰, although this is a theoretical calculation (DePaolo, 2011; Harouaka et al., 2014). I prefer the explanation that the lower calcium isotope fractionation factor for gypsum precipitation is due to slower crystal growth, rather than precipitation at equilibrium.

3.4.2 Range in $\delta^{44}Ca$

The range in the measured $\delta^{44}Ca$ in both gypsum and carbonate minerals has been linked to the ratio between calcium and the dominant mineral anion within the precipitating fluid. For gypsum, this method was calibrated experimentally, suggesting that if the $Ca:SO_4$ ratio of the fluid is less than 1.5, the range of $\delta^{44}Ca$ should be larger than 0.5‰, while if the $Ca:SO_4$ ratio of the fluid is above 1.5, then the range in $\delta^{44}Ca$ in gypsum will be lower than 0.5‰ (Blättler et al., 2017). In the measured primary gypsum, the range of the samples is 0.4‰ with a single outlier (n=11, Figure 3.8). This suggests that the gypsum precipitated from a solution with a high ratio of calcium-to-sulfate.

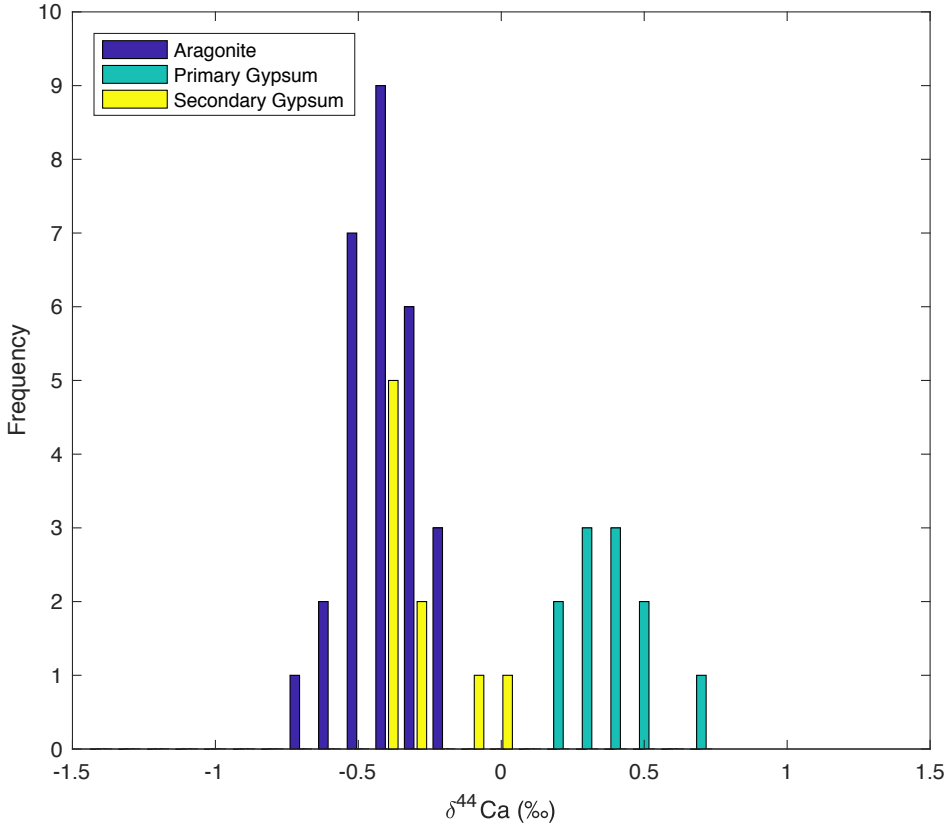

FIGURE 3.8: HISTOGRAM OF THE DISTRIBUTION OF THE δ^{44}Ca IN ARAGONITE, SECONDARY GYPSUM AND PRIMARY GYPSUM.

The same isotope distillation effect occurs with the precipitation of calcium carbonate minerals, as previously shown in the Mono Lake system, where when there is a low ratio of calcium to alkalinity (mostly as bicarbonate) within the lakewater and there is a higher range in δ^{44}Ca in the precipitated carbonate minerals (Nielsen and DePaolo, 2013). It has been suggested that when the calcium to alkalinity ratio is 0.75 or less, the calcium isotope distillation effects should be observed and the precipitating carbonate minerals will have a wide range of δ^{44}Ca (Blättler et al., 2017). In Lake Lisan, I find a range of δ^{44}Ca in aragonite of 0.7‰ with a lower range if shorter time periods are taken into account (Figure 3.4). The distribution of the δ^{44}Ca of aragonite layers that occur close to the primary gypsum layers shows the isotopic distillation effect where mineral precipitation impacts the range of calcium isotope ratios to the compared minimal δ^{44}Ca variability observed during highstand precipitation (Figure 3.8). The narrow range observed during

highstand, non-overturn, aragonite precipitation suggests that the lake water had a high ratio of calcium to alkalinity, which agrees with previous estimates of the riverine input and groundwater ($Ca:HCO_3 \sim 0.94$) (Stein et al., 1997). These observations suggest that a two box-model is required to model the changes in the $\delta^{44}Ca$ of the precipitated gypsum and aragonite within Lake Lisan due to the difference in water chemistry between the surface water and brines.

3.4.3 Box model

Typically, paleoclimate studies in lacustrine settings have focused on "traditional" stable isotopes (such as $\delta^{18}O$ and $\delta^{13}C$) to record changes in the hydrological cycle and temperature (Stuiver, 1970; Talbot, 1990; Talbot and Johannessen, 1992; Garcés et al., 1995; Fontes et al., 1996; Hammarlund et al., 2003; Leng and Marshall, 2004; Zanchetta et al., 2006). The first order, orbital- and millennial- timescale control on $\delta^{18}O$ patterns in Lake Lisan has been shown to relate to changes in the East Mediterranean source waters, with short-term (annual-timescale) $\delta^{18}O$ variations controlled by the amount of precipitation, and temperature (Kolodny et al., 2005). Carbon isotopes within Lake Lisan have been suggested to record algal blooms and changes in the primary productivity of the lake (Kolodny et al., 2005), although it has recently been argued that, in the modern Dead Sea, there is a correlation between CO_2 outgassing and aragonite precipitation that is reflected in the $\delta^{13}C$ of the precipitated aragonite (Golan et al., 2017). The correlation, albeit weak, between $\delta^{18}O$ and $\delta^{44}Ca$ reflects the fact that they both record the changing water budget of the lake (Figure 3.7). By contrast, there is no correlation between $\delta^{13}C$ and $\delta^{44}Ca$ as the biogenic processes (e.g. primary productivity) control the aragonite $\delta^{13}C$ but have no impact on the $\delta^{44}Ca$ (Figure 3.7).

By measuring the $\delta^{44}Ca$ of three isolated minerals, as has been undertaken here, I reduced the likelihood of measuring a bulk signal comprising multiple components of varying calcium isotopic composition (Leng et al., 2010). The variation in the $\delta^{44}Ca$ measured on separate laminae within a single block, as shown in Figure 3.5, is higher than the long-term error on the measurement of

calcium isotopes, and similar to the range reported over the 55kyr. This suggests that calcium isotopes could be used to investigate annual changes in the lake's calcium budget.

For Lake Lisan, there are two major inputs of calcium into the lake: the River Jordan and ground water flow, with groundwater accounting for approximately 70% of the input flux (Stein et al., 1997). The calcium content in both the River Jordan and the ground water flow is derived from dissolution of the local carbonate bedrock in the catchment. There are two removal sinks for calcium from Lake Lisan, the deposition of aragonite and gypsum. During the precipitation of aragonite and gypsum, the lakewater $\delta^{44}Ca$ will increase as the ^{40}Ca is removed into the calcium-bearing minerals. The magnitude of the shift can be related to the fraction of calcium removed from the lake during mineral precipitation as well as the residence time of calcium in the system. The systematic variability in the lakewater, and hence, aragonite $\delta^{44}Ca$, is primarily controlled by these mineral precipitation events, which can be linked back to the regional hydrological conditions.

I used the calcium box model to explore the impact of lake overturn and gypsum precipitation on the lake calcium mass balance and its calcium isotope composition (as recorded in aragonite). To explore the fundamental functioning of the system, I first ran a single box model where only the volume of the lake changes, and explored the effect of changing volume on the calcium cycle in the lake. Due to the terminal nature of Lake Lisan, the only output of water from the system is through evaporation, which depends, in this simple model, on the surface area of the lake, in itself linked to the lake volume (Bartov et al., 2002). Lake-volume-driven evaporation then imposes constraints on both regional precipitation and riverine calcium input. Thus, by changing the lake volume, the change in precipitation and river input could be calculated, and the $\delta^{44}Ca$ of the lake water and aragonite modelled. I ran this single perturbation model with four scenarios: (1) rising lake volume, (2,3) falling lake volume with and without gypsum precipitation and (4) falling lake volume with gypsum precipitation but five times the concentration of calcium

in the lake; each time the perturbation lasts 1000 years and the model was ran for 15kyr (Figure 3.9). In the Lisan Formation, the largest overturn events form 0.5m of gypsum, although most form 0.2m or less; therefore in my model we constrained the total cumulative amount of gypsum that precipitates to 0.2m.

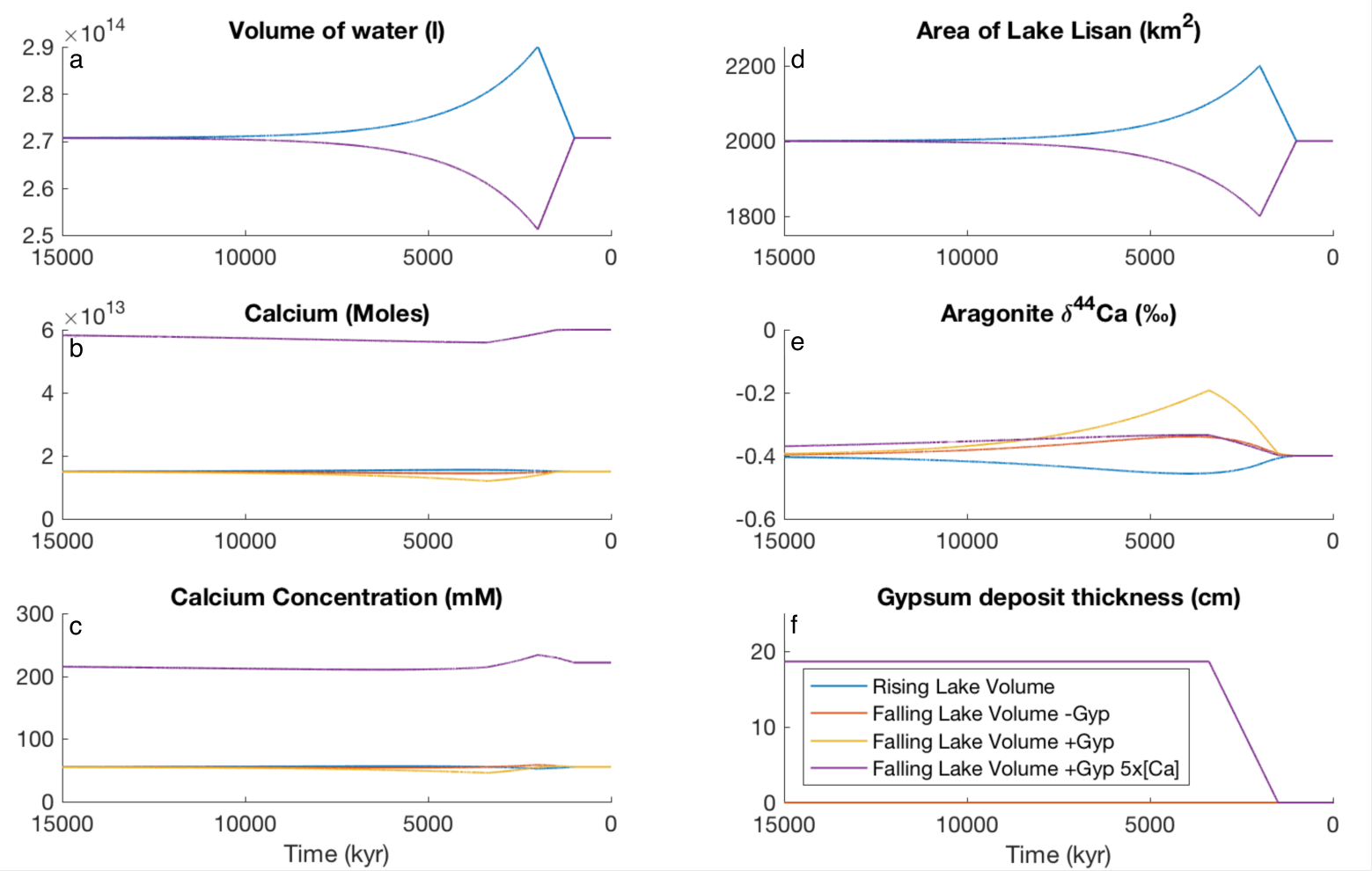

FIGURE 3.9: MODELLED LAKE PARAMETERS DEPENDING UPON THE CHANGING LAKE VOLUME OVER FOUR SCENARIOS. SCENARIO 1 DESCRIBES A RISING LAKE VOLUME, SCENARIO 2 DESCRIBES A FALLING LAKE VOLUME WITHOUT GYPSUM PRECIPITATION, SCENARIO 3 DESCRIBES A FALLING LAKE VOLUME WITH GYPSUM PRECIPITATION, SCENARIO 4 DESCRIBES A FALLING LAKE VOLUME WITH GYPSUM PRECIPITATION AND FIVE TIMES HIGHER CALCIUM CONCENTRATION. THE SCENARIOS ARE SUMMARISED IN TABLE 3.2.

According to scenario 1, where lake volume increases for 1000 years, higher input fluxes of calcium to the lake drive a decrease in the $\delta^{44}Ca$ of the lake water due to the lower $\delta^{44}Ca$ from rivers and groundwater (Figure 3.9). In Scenarios 2-4 the lake volume decreases, and we explore what happens when there is no gypsum precipitation (2), gypsum precipitation (3) and gypsum precipitation with an increased lake calcium concentration (4). The scenarios are summarised in Table 3.2. As the lake volume decreases (Scenario 2-4, Figure 3.9a), there will be an initial increase in calcium concentration (Figure 3.9c) as the ions are concentrated in the remaining lake water, which will also lead to a gradual increase in the $\delta^{44}Ca$ of the lake (Figure 3.9e). If there is no gypsum precipitation (Scenario 2, Figure 3.9) the perturbed calcium cycle will return to steady state with no further changes once lake level rises again. Because there is no gypsum precipitation in this modelled run, there is no significant change in the $\delta^{44}Ca$ of the lake (or therefore aragonite) and no real change in the calcium balance. In Scenarios 3 and 4, lake stratification breaks down and gypsum precipitates (Figure 3.9f). As the lighter ^{40}Ca-isotope is incorporated into the gypsum, the lakewater $\delta^{44}Ca$ increases further (Figure 3.9e). The perturbation to the $\delta^{44}Ca$ of the aragonite has a greater magnitude and a shorter recovery time in Scenario 3 (low lake calcium concentration) versus Scenario 4 (high calcium lake concentration) as expected when the mass of calcium varies (Figure 3.9e).

TABLE 3.2: SCENARIOS EXPLORED IN THE SINGLE BOX MODEL SHOWN IN FIGURE 3.9

Scenario 1	Rising lake volume
Scenario 2	Falling lake volume, no gypsum precipitation
Scenario 3	Falling lake volume, gypsum precipitation when the lake volume is below $2.6x10^{14}L$
Scenario 4	Falling lake volume, with 5 times higher calcium concentration, gypsum precipitation when the lake volume is below $2.6x10^{14}L$

When the concentration of calcium in the lake is low enough to be perturbed by lake overturn and mineral precipitation, this single-box model demonstrates measurable changes in the $\delta^{44}Ca$ of aragonite within the lake. However, under higher concentrations of calcium, only a small fraction of the calcium precipitates during the lake overturn, so that the overall lake $\delta^{44}Ca$ changes less or not at all. In Lake Lisan, the $\delta^{44}Ca$ measured in the aragonite varies slightly with lake overturn events, which is consistent with the calcium-chloride composition of the lake brine.

To improve the simple model, a more complex model was applied to explore the sequence of changes over the time interval studied. To do this, a longer temporal model was forced with the lake volume curve calculated using a hypsometric curve (Bartov et al., 2002) from the lake level curve of Torfstein et al. (2013b). The model was expanded to use two boxes to model both the surface water and the deeper brine. In the two-box model, aragonite precipitates from the surface waters during positive water balance periods characterized by a lake highstand, while gypsum precipitates from the mix of brine and surface waters when the stratification breaks down. The surface water box consists of mainly freshwater with a 1% brine component (Stein et al., 1997). The evaporation flux for the two-box model is calculated as described in the modelling method section, and as such is used to calculate the fluxes from the rivers and groundwater. The size of the surface and deep reservoirs are taken from the literature (Katz et al., 1977; Katz and Kolodny, 1989; Stein et al., 1997; Stein, 2001), whereas the rates of precipitation of aragonite and gypsum are calculated from the thickness of aragonite and gypsum layers that are found within the Lisan Formation. The presence of the brine box, or the deep-water body, also helps explain the earlier observation of a limited change in the $\delta^{44}Ca$ of the aragonite. As the brine box contains approximately 100 times more calcium than the surface box ($[Ca]_{brine}$ = 410mM, Stein et al., 1997), its presence helps buffer perturbations to the $\delta^{44}Ca$ during lake overturn. The model suggests the $\delta^{44}Ca$ of the primary gypsum precipitated during lake overturn should increase slightly during the precipitation, as shown in Figure 3.10a, and as shown in Figure 3.9.

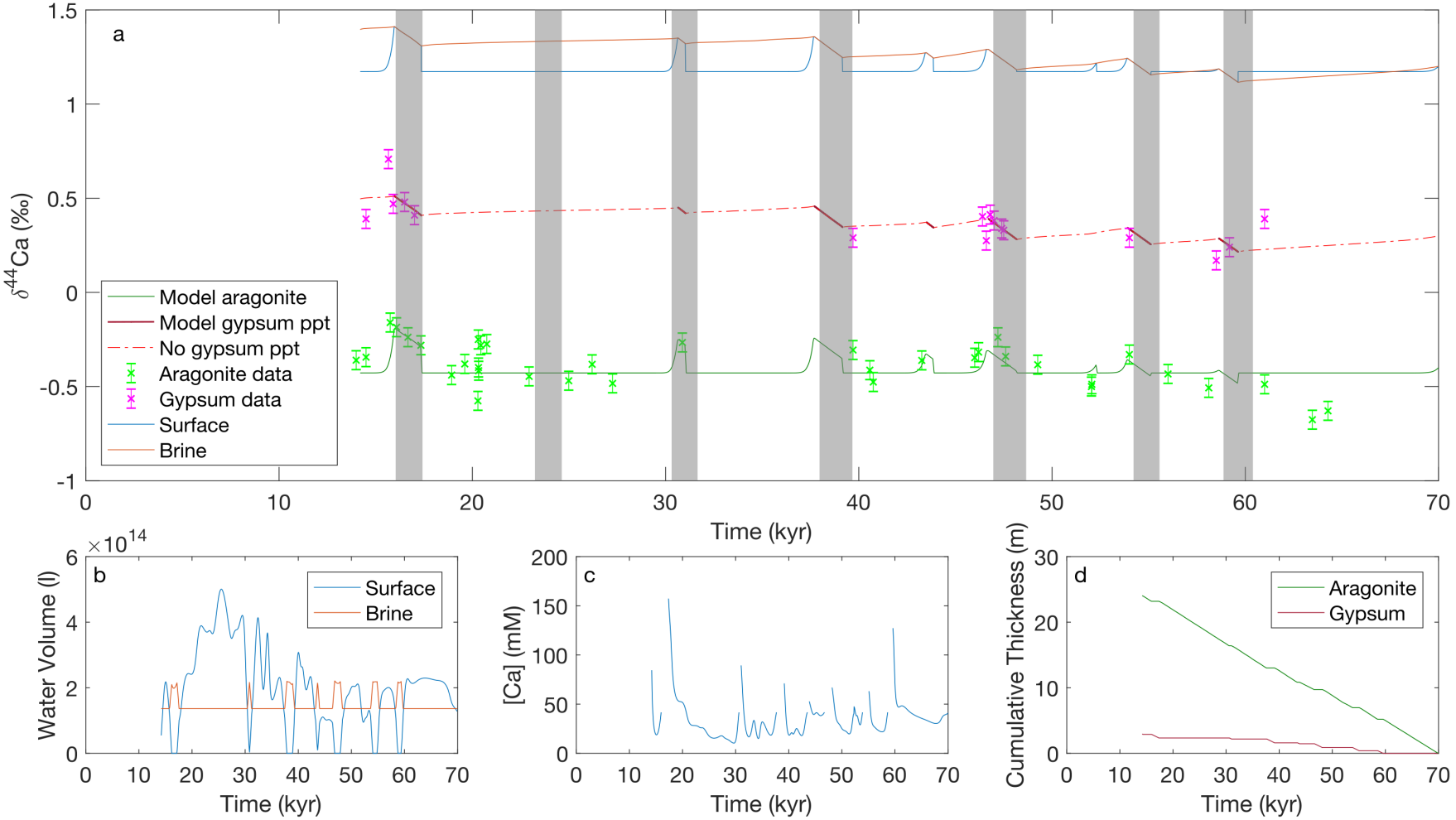

FIGURE 3.10: MODEL RESULTS FOR A LAKE LEVEL-COUPLED MODEL. PANEL (A) PRESENTS THE MEASURED ARAGONITE $\delta^{44}Ca$ AS GREEN CROSSES, MODELLED ARAGONITE $\delta^{44}Ca$ AS A BLUE LINE, MEASURED PRIMARY GYPSUM $\delta^{44}CA$ AS MAGENTA CROSSES AND MODELLED PRIMARY GYPSUM $\delta^{44}Ca$ IS PLOTTED IN RED. GREY RECTANGLES MARK THE TIMING OF NORTH ATLANTIC HEINRICH EVENTS.

The model result reproduces the temporal $\delta^{44}Ca$ aragonite data with the addition of the deep-water brine box. Although the lake overturn events produce significant changes in the concentration of the surface calcium box, the large calcium concentrations reduce the observed variability in the $\delta^{44}Ca$ recorded in the aragonite.

The model suggests that although lake evaporation changes over glacial-interglacial cycles and over millennial-scale events (e.g. Dansgaard-Oeschger cycles) these changes in evaporation are not large enough to fully explain the changes in the lake level that have been observed. When the lake reaches its highest levels ca. 25ka, my model requires that the riverine and ground water fluxes are ~5 times greater than modern day, which matches previous estimates of an increase in rainfall from 110mm $year^{-1}$ to >500mm $year^{-1}$ rainfall during this period (Barkan et al., 2001; Enzel et al., 2003; Frumkin et al., 2011; Rohling, 2013).

It has also been suggested that the changes in lake level during glacial maxima could be due to higher humidity and lower temperatures, and hence, lower evaporation during the glacial (Bar-Matthews et al., 1997; Shea, 2003; Finlayson, 2004; Robinson et al., 2006; Miebach et al., 2017). My model suggests that this is not the case; by increasing the relative humidity evaporation would decrease, leading to lake level rise. Similarly, decreasing the temperature would also reduce evaporation and cause lake level rise. Both of these would result in a dilution of the surface layer and a decrease in the calcium concentration in the surface waters. Therefore, there would be simultaneously a smaller amount of aragonite precipitated and larger variations in the $\delta^{44}Ca$ of the precipitated aragonite, which is not observed. The high control that salinity has on evaporation (Salhotra et al., 1985) suggests that when a low salinity surface layer evaporates, the rates of evaporation should be around ~2.4m $year^{-1}$ during the glacial period in the Dead Sea. Higher lake levels either require lower rates of evaporation than modern, or higher inputs in the form of precipitation. In order for the rate of evaporation from the surface layer to be lower, the relative humidity would

have to be >0.8 and the temperature increase >10°C. This is a far greater change than has been suggested in the region (Matthews et al., 2000; Arz et al., 2003; McGarry et al., 2004; Hayes et al., 2005; Affek et al., 2008; Rohling, 2013). Hence, due to the presence of the low-salinity surface layer, the model supports the hypothesis that during the glacial period there was more precipitation, rather than less, than in the current interglacial.

The present day $\delta^{44}Ca$ of the Dead Sea is 0.45‰ relative to the suggested $\delta^{44}Ca$ of Lake Lisan, which is between 1.1 and 1.4‰ (Figure 3.11). As the inputs to the lake are around -0.4‰, the previously higher $\delta^{44}Ca$ of Lake Lisan was likely due to Raleigh fractionation caused by the higher amount of precipitation of aragonite and gypsum that occurred during the Last Glacial Maximum. This higher rate of formation of calcium-bearing minerals was due to the higher input of bicarbonate and sulfate in freshwater due to the overall higher rates of precipitation during the Last Glacial Maximum.

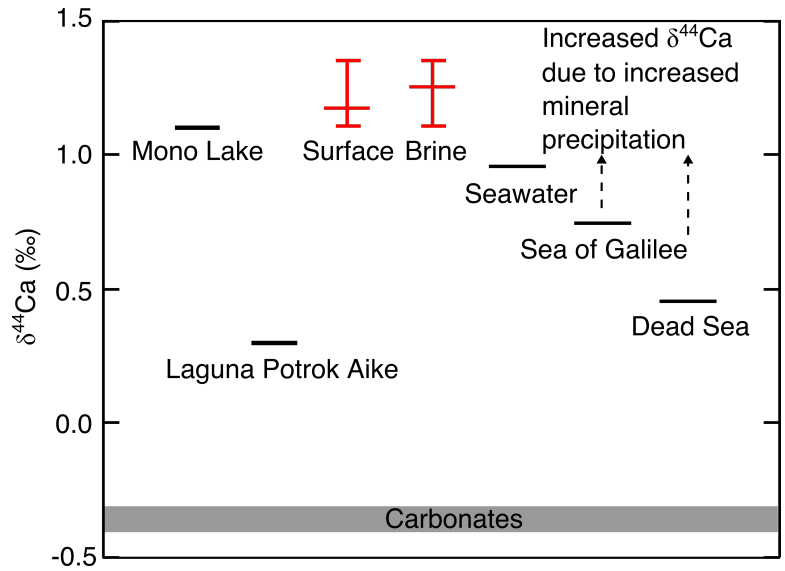

FIGURE 3.11: COMPILATION OF $\delta^{44}Ca$ VALUES IN SEDIMENT AND WATER OF THE DEAD SEA BASIN. THE RECONSTRUCTED $\delta^{44}Ca$ OF THE SURFACE AND BRINE BOXES FROM THE MODEL ARE DISPLAYED IN RED. THE AVERAGE MONO LAKE AND LAGUNA POTROK AIKE $\delta^{44}Ca$ RATIOS ARE DISPLAYED ON THE LEFT (NIELSEN AND DEPAOLO, 2013; OEHLERICH ET AL., 2015),

3.4.4 Secondary Gypsum

The secondary gypsum typically occurs as fine-crystalline or radial aggregates, within AAD sequences, where the gypsum crystals are often associated with the detrital laminae.

The calcium isotope composition of the secondary gypsum, compared to the primary gypsum, should provide further insight into its formation. If the primary and secondary gypsum form due to similar processes (precipitating from the lake water) then the $\delta^{44}Ca$ of the two gypsum phases will be similar. However, the $\delta^{44}Ca$ of the aragonite and the $\delta^{44}Ca$ of the secondary gypsum are similar (–0.3‰ for secondary gypsum, n=9, and –0.4‰ for surrounding aragonite, n=33), but differ from that of the primary gypsum (average +0.42‰, n=11).

This suggests that either that the secondary gypsum forms from waters which have a much lower $\delta^{44}Ca$, or that the calcium isotope ratio recorded in the secondary gypsum is from a second source rather than the original lake water. This would occur if there has been localised near quantitative conversion of aragonite to secondary gypsum, hence the original $\delta^{44}Ca$ of the aragonite is recorded in the $\delta^{44}Ca$ of the secondary gypsum. The second process appears more likely than a large secondary reservoir of water with a lower $\delta^{44}Ca$.

Although it was proposed initially that this fine-crystalline gypsum was also primary, due to an apparent mismatch between the calculated sulfate budget of Lake Lisan and the massive gypsum layers (Stein et al., 1997), its relatively light $\delta^{34}S$ and $\delta^{18}O_{(SO4)}$ unequivocally shows that its formation stems from the oxidation of sedimentary sulfides in response to the lake level drop and exposure of the Lisan Formation (Torfstein et al., 2005; Torfstein et al., 2008; Torfstein and Turchyn, 2017). Subsequently, sulfide minerals were oxidized in contact with meteoric water and the sulfate re-precipitated to form gypsum. Further evidence of the secondary nature of the secondary gypsum comes from the fact that it has not been found within the recent Dead Sea Drilling Project core, where sedimentary sulfide minerals are found. As the deepest

part of the Dead Sea has not been exposed to oxic meteoric water, secondary gypsum has not formed here (Torfstein et al., 2015; Torfstein and Turchyn, 2017).

In order for near quantitative conversion of the calcium sourced from the dissolution of the aragonite into gypsum the system must have been closed. This at first appears to be incompatible with the exposure of the Lisan formation and the flushing of meteoric water thought to dissolve the aragonite. However the calcium is likely to be the limiting ion during the precipitation of gypsum due to sulfate excess caused by the rapid oxidation of sulfide to sulfate. Hence, the precipitation would occur rapidly and consume the total calcium available. The needle-shape of the gypsum crystal concurs with the suggested mechanism for precipitation as these needle crystals form during rapid precipitation (Harouaka et al., 2014).

3.5 Conclusions

The measurement of the $\delta^{44}Ca$ of three calcium-bearing minerals within the Massada section of the Lisan Formation yields new insights about Lake Lisan's configuration, geochemical composition and regional hydrology. The $\delta^{44}Ca$ of the Lisan Formation at the Massada section reflects the combined effects of the water source compositions, Lake Lisan water column stratification and mixing, and precipitation of primary gypsum and aragonite from the lake. The $\delta^{44}Ca$ of both the primary gypsum and aragonite (-0.4‰ and 0.4‰, respectively) when corrected for fractionation suggested the average $\delta^{44}Ca$ of Lake Lisan was ~1.2‰, which is higher than that of the modern Dead Sea waters (0.45‰) and the Sea of Galilee (0.75‰). As these are assumed to represent the two water source end members for Lake Lisan, the actual $\delta^{44}Ca$ of Lake Lisan strongly reflects the isotopic fractionation that occurred during the precipitation of both minerals from the lake waters. In itself, this process was strongly modulated by regional hydrological conditions, which therefore allows the $\delta^{44}Ca$ to reconstruct the quantitative sources and sinks of calcium in the lake. A box model was developed to describe the

evolution of $\delta^{44}Ca$ in Lake Lisan. The results show that the observed $\delta^{44}Ca$ of aragonite and gypsum require at least a 5-fold increase in precipitation in the Dead Sea watershed during the last glacial relative to present. This increase is required in order to balance the higher rates of evaporation from the low salinity surface layer found in the stratified Lake Lisan, even with the lower glacial temperatures and potentially higher humidity suggested in previous studies.

The secondary gypsum $\delta^{44}Ca$ supports the conclusion that the precipitation occurred due to the dissolution of primary aragonite during the oxidation of sulfide minerals. The observations from the range in $\delta^{44}Ca$ observed in the individual minerals fits with the calcium chloride lakewater composition of Lake Lisan.

The oxygen and carbon isotopes measured on the aragonite laminae measured correlate well with previous studies in the area. The oxygen isotopes record decadal variations in the amount of precipitation and ratio of precipitation to evaporation. As such, they need to be sampled at a higher resolution to remove the short-term variability and to observe the long-term trends in lake level that have been observed in oxygen isotopes from speleothems in the region.

In summary, the measurement of the $\delta^{44}Ca$ of three calcium-bearing minerals of the Lisan Formation provides new constraints on Lake Lisan's configuration, geochemical composition and regional hydrology, and can be applied to reconstruct the limnological-hydrological history of additional past cycles of the Dead Sea, as well as other, comparable, environments.

CHAPTER 4

CALCIUM ISOTOPE FRACTIONATION IN SEDIMENTARY PORE FLUIDS FROM ODP LEG 175: RESOLVING CARBONATE RECRYSTALLIZATION

4.1 Introduction

Calcium isotopes can be applied to determine the precipitation and dissolution rates of carbonate sediments, as discussed in Chapter 1. The recrystallization of carbonate minerals in marine sediments, as well as the addition of carbonate through the precipitation of authigenic carbonate, impacts the carbon isotope mass balance of Earth's surface environment as well as the preservation of carbonate mineral-based proxies for paleoceanography (Berner, 1980; Schrag et al., 1995; Berner, 2003; Fantle and DePaolo, 2005; Fantle and DePaolo, 2006; Fantle and DePaolo, 2007; Fantle and Tipper, 2014; Fantle and Higgins, 2014; Fantle, 2015; Griffith et al., 2015). By studying the process of carbonate precipitation, dissolution and recrystallization within marine sediments I can explore the impact of sedimentary diagenesis on the surface carbon cycle.

The two major tools used within this chapter to determine the locus of authigenic carbonate precipitation are calcium isotopes and strontium concentrations in the pore fluid. Both the strontium concentration and the calcium isotope composition of sedimentary pore fluid are both determined by a range of processes. The strontium concentration in the pore fluid is controlled by the dissolution and precipitation of strontium-bearing minerals beneath the sediment-water interface. During the recrystallization of biogenic carbonates, strontium is released into the pore fluid during the dissolution, and included to a lesser extent into the reprecipitated minerals. Hence, the

strontium concentration can be used to calculate the recrystallization rate of the carbonate (Baker et al., 1982; Gieskes et al., 1986; Richter and DePaolo, 1987; Richter and DePaolo, 1988; Richter and Liang, 1993; Rudnicki et al., 2001; etc.). The $\delta^{44}Ca$ of the pore fluid is controlled by the dissolution and recrystallization of the carbonate as discussed in the introduction of this thesis. By combining these two models for the recrystallization, any further effect on the $\delta^{44}Ca$ of the pore fluid due to precipitation of authigenic carbonate can be established, allowing for the identification of the locus of authigenic carbonate precipitation.

There are a couple of possible complications to this approach for assessing carbonate dissolution and precipitation. The amount of strontium released during carbonate dissolution depends strongly on the dissolved mineral; for example, biogenic carbonate has higher strontium concentrations than micritized carbonate. Furthermore, if the assumption that calcium isotopes are impacted only by the dissolution and precipitation of carbonate is incorrect, and if calcium was being released from silicates or clays, then it is possible that the $\delta^{44}Ca$ of the fluid could change without a concurrent change in strontium concentrations or conversely the $\delta^{44}Ca$ of the fluid could stay the same while the strontium concentrations changed (Turchyn and DePaolo, 2011; Fantle and Tipper, 2014).

In this chapter, I present calcium isotope measurements of two geographically close but chemically different Ocean Drilling Program sites. Site 1081 is organic-rich (~5wt%) with a carbonate content of around 30%, compared to Site 1086, which contains less organic matter (~1%) and has a higher carbonate content within the sediment (~80%) (Wefer et al., 1998). By modelling the calcium isotope composition, calcium concentration and strontium concentration within the pore fluid a discrete solution in terms of carbonate dissolution and authigenic carbonate precipitation can be obtained. I use a reactive transport model of the calcium concentrations to resolve the ratio of dissolution to precipitation within the pore fluid as well as a reactive transport model of the strontium concentrations to determine an estimate for

the dissolution rates. Having determined the depth range of carbonate mineral precipitation, I then use the previously published $\delta^{13}C$ profiles to explore the $\delta^{13}C$ composition of the authigenic carbonate at these sites.

4.1.1 Sample locations and description

Sites 1081 and 1086 are located off the west coast of Africa (Figure 4.1a), and were drilled during Leg 175 of the Ocean drilling program (Lange et al., 1999; Ravelo and Andreasen, 2000; Marlow et al., 2000; Anderson et al., 2001; Dupont et al., 2001; Berger et al., 2002; Berger and Wefer, 2002; Christensen et al., 2002; Christensen and Giraudeau, 2002; Diester-Haass et al., 2002; Giraudeau et al., 2002; Gorgas and Wilkens, 2002; Lin and Chen, 2002; Murray et al., 2002; Robinson et al., 2002; Vidal et al., 2002; Uliana et al., 2002; Holtvoeth et al., 2003; Diester-Haass et al., 2004; Kuhlmann et al., 2004; Schefuß et al., 2004; Farmer et al., 2005; McClymont et al., 2005; Dupont, 2006; Lazarus et al., 2006; Dekens et al., 2007; Hayward et al., 2007). Site 1081 is at 805m water depth, at a location of intense upwelling leading to organic-rich sediments.

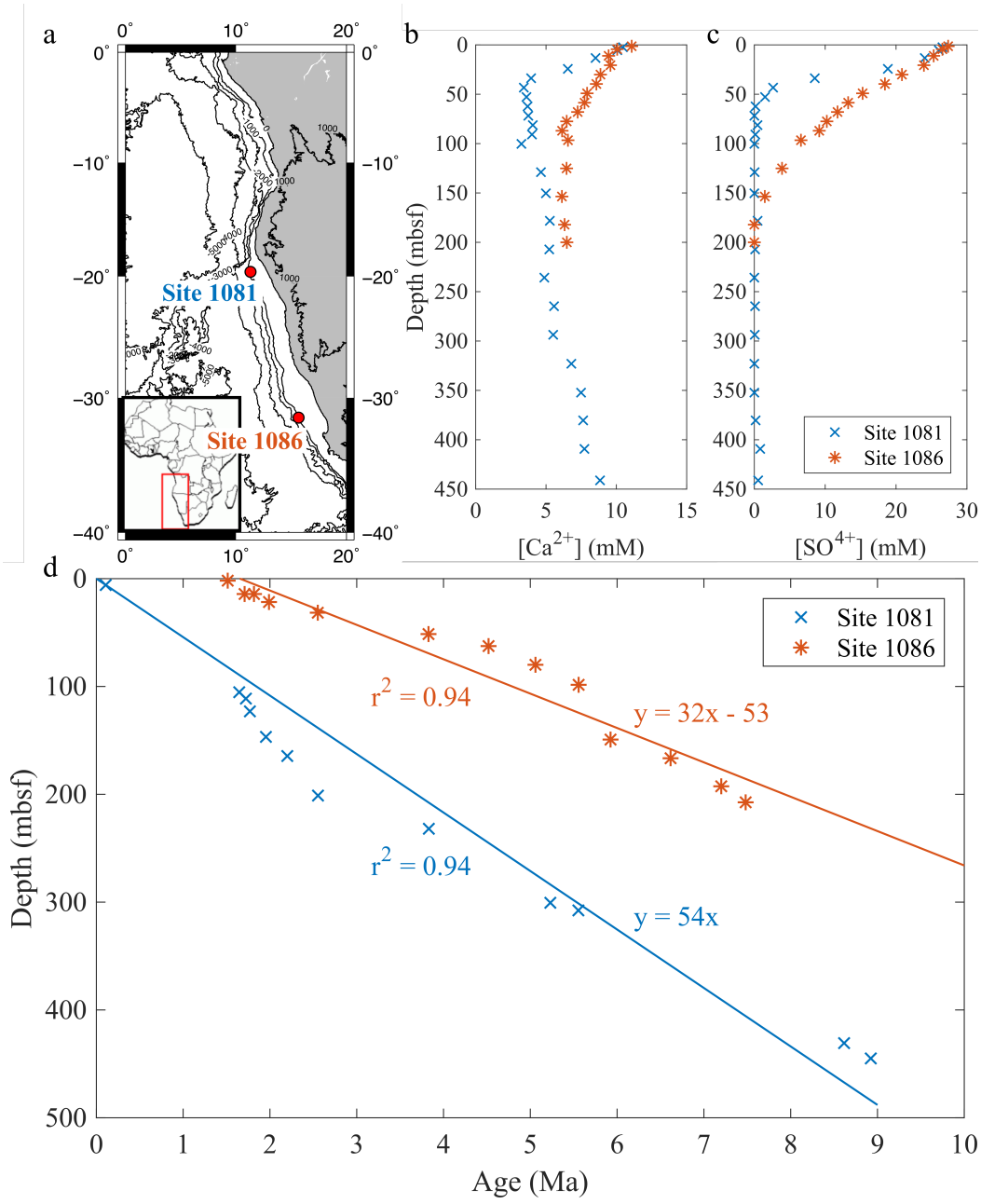

FIGURE 4.1: (A) LOCATION MAP (B) PORE FLUID CALCIUM AND SULFATE CONCENTRATIONS (WEFER ET AL., 1998).

Site 1081 comprises nanofossil and foraminifer-rich clay (upper 77m), diatom-rich clay (77-237mbsf) and nanofossil-rich clay (237-399mbsf), with the base of the core being composed mainly of nanofossil ooze with a clay fraction (Berger et al., 1998; Pufahl et al., 1998). Sedimentation rates vary between 25m/Myr to 185m/Myr calculated from spectral analyses and bulk density profiles, although biostratigraphic estimates suggest sedimentation rates as high as 345m/Myr (Gorgas and Wilkens, 2002). Sedimentation rates are

higher over the upper 200m of sediment, before decreasing to 25-65m/Myr below this (Wefer et al., 1998). The sediment ranges in age from modern to 8.5Ma. Carbonate content in the sediment decreases from around 40 wt% to around 5 wt% over the top 100m of the sediment column and is constant between 5 and 10 wt% below this depth (Figure 4.2) (Wefer et al., 1998). Organic carbon content is high, averaging around 5 wt% throughout the sediment column, but reaching as high as 8 wt% between 120 and 150mbsf (Wefer et al., 1998). High sedimentation rates and high rates of organic matter deposition lead to a rapid reduction of sulfate over the top 55m of sediment (Figure 4.1c). Below this methanogenesis occurs, leading to sulfate-driven anaerobic oxidation of methane at the sulfate-methane transition zone at 55mbsf (Sivan et al., 2007). Key pore fluid profiles referred to including calcium, strontium, magnesium, alkalinity, fraction carbonate, porosity and organic matter content are given in Figure 4.2 (Wefer et al., 1998).

Site 1086 is located off the west coast of South Africa in the Cape basin at a water depth of 794m (Figure 4.1a). The upwelling in this region is seasonal and less intense than in the waters over Site 1081. Site 1086 is composed entirely of nanofossil-foraminifera ooze over the top 200m of the sediment column, which ranges in age from modern to 7.5Ma. The sedimentation rate has been relatively constant at around 40m/Myr (Wefer et al., 1998). The carbonate content is also relatively constant at around 80 wt%, with the organic carbon content around 1 wt% throughout the sediment (Wefer et al., 1998). With the lower organic carbon content, the rates of microbial sulfate reduction are much slower with measurable sulfate concentrations still being present at the base of the core at 200mbsf (Figure 4.1c).

In both cores the calcium concentrations decrease through the zone of microbial sulfate reduction (Figure 4.1b), where the concentrations of sulfate are decreasing and the alkalinity is increasing (Figure 4.1c).

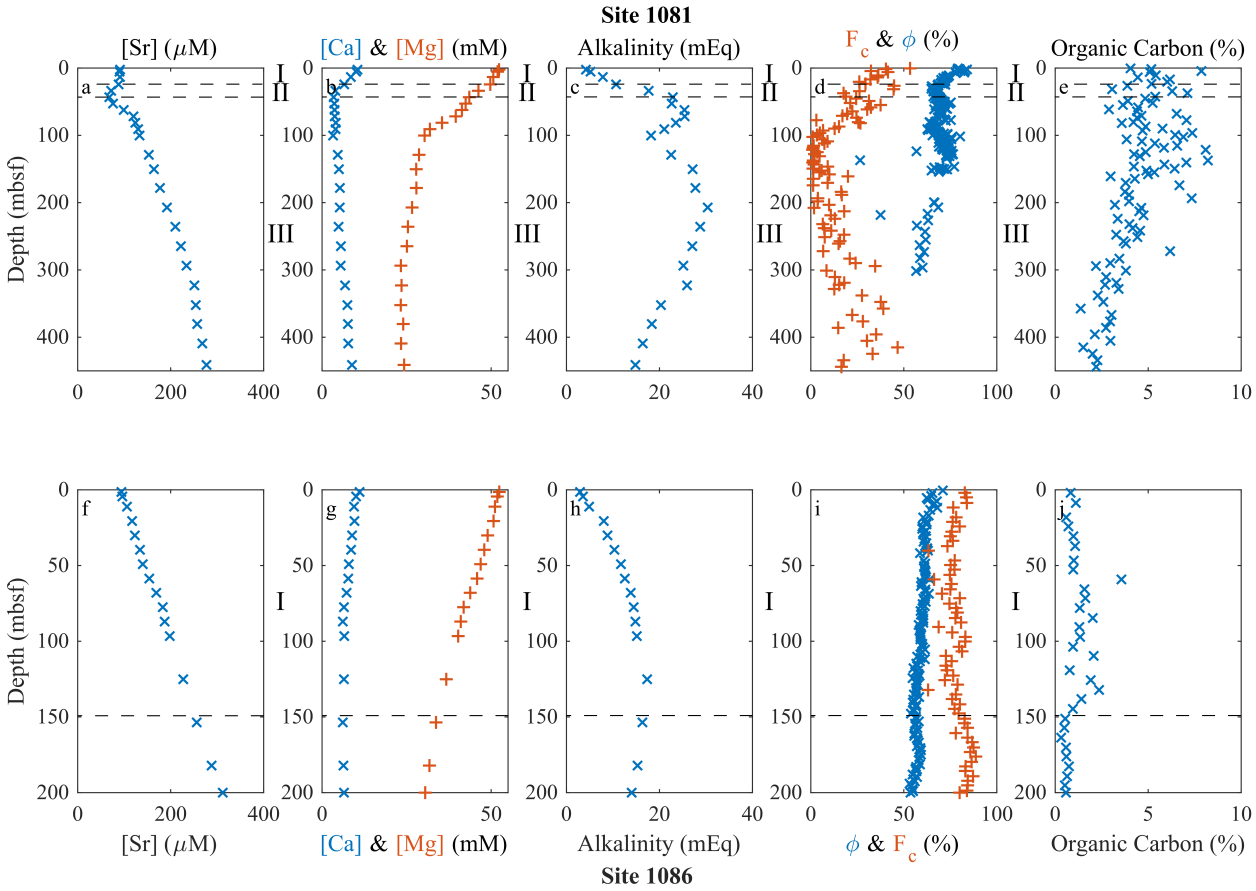

FIGURE 4.2: MEASURED PORE FLUID PROFILES FROM SITE 1081 (A-E) AND SITE 1086 (F-J) (WEFER ET AL., 1998). (A,F) STRONTIUM CONCENTRATIONS [SR], (B,G) CALCIUM [CA] (X) AND MAGNESIUM [MG] (+) CONCENTRATIONS, (C,H) ALKALINITY, (D,I) POROSITY (ϕ) (X) AND FRACTION CARBONATE (F_C) (+) AND (E,J) ORGANIC MATTER CONTENT. THE DASHES LINES SEPARATED ZONES I, II AND III, WHICH ARE THE BACTERIAL SULFATE REDUCTION ZONE, ZONE OF ANAEROBIC OXIDATION OF METHANE AND ZONE OF METHANOGENESIS RESPECTIVELY, AS DETERMINED FROM PORE FLUID CONCENTRATIONS AND PREVIOUS WORK ON THE SITES (WEFER ET AL., 1998; SIVAN ET AL., 2007). THE SULFATE-METHANE TRANSITION ZONE IS SITUATED BETWEEN ZONES I AND II.

4.2 Methods

4.2.1 Analytical methods

Shipboard measurements were conducted during Leg 175 as described by Wefer et al. (1998) and summarised below.

Calcium, magnesium and sulfate concentrations were analysed using a Dinoex DX-100, with 1σ standard deviation of <3% for calcium and magnesium and <4% for sulfate. Alkalinity was determined by Gran titration using a Brinkmann pH electrode and a Metrohm autotitrator. Strontium concentrations were quantified using flame atomic absorption (AA) spectrometry on a Varian SpectrAA-20. Carbonate carbon concentrations were determined using a Coulometric 5011 carbonate carbon analyser. Total organic carbon was determined using a Carlo Erba 1500 carbon-nitrogen-sulfur analyser. 5mg of freeze-dried, ground sediment was combusted at 1000^{o}C in a stream of oxygen. Total organic carbon was then determined by the difference between carbonate carbon and total carbonate concentrations. The error on the measurement of organic carbonate content can be as much as 2% as shown in Fig. 4.2. Porosity was computed from the wet and dry masses of the sample and the dry volume of the sediment, as determined using Method C (Blum, 1997).

Methane concentrations were measured on gases collected from a headspace method, and run on a Hewlett Packard 589- II Plus gas chromatograph equipped with a 2.4m x 3.2mm stainless steel column packed with HaySep S (80-100mesh) and a flame ionization detector.

Calcium isotope ($^{44}Ca/^{40}Ca$) analysis was conducted at the University of Cambridge as described in Chapter 2.

Sediment strontium and calcium concentrations were measured on a Varian Vista Axial ICP-OES at the University of Cambridge using the 315.887nm calcium and 421.552nm strontium emission lines (Langer et al., 2016).

4.2.2 Modelling methods

The reactive-transport model uses the changing strontium and calcium concentrations and calcium isotope composition of the pore fluid. Strontium concentrations and calcium isotopes in the pore fluid offer complementary information on the depth distribution of carbonate dissolution, precipitation and recrystallization. Within sedimentary pore fluids, strontium concentrations increase due to carbonate dissolution releasing strontium to the pore fluid while carbonate reprecipitation takes less pore fluid strontium during mineral formation (although this is mineral-dependant); thus the depth, or length, over which strontium concentrations increase is a function of the rate of carbonate dissolution and reprecipitation, or recrystallization (Richter and DePaolo, 1988; Richter and Liang, 1993). The strontium concentration in the pore fluid is determined by the strontium concentration in seawater (91μM), the amount of strontium in the sedimentary carbonate, and the partition coefficient during carbonate precipitation. As introduced earlier, the calcium isotopes in the pore fluid decrease during carbonate dissolution (towards the bulk carbonate value) and increase during carbonate precipitation due to calcium isotope fractionation during precipitation, as long as kinetic calcium isotope fractionation is occurring.

I use a model approach based originally on the work of Berner (1980), and subsequently developed in multiple other studies (Baker et al., 1982; Richter and DePaolo, 1987; Schrag et al., 1995; Fantle and DePaolo, 2006) to simulate the evolution of the concentration of an element dissolved in the pore fluid. To do this, I am modelling a system consisting of a solid that is dissolving and reprecipitating such that there is no net change in the solid mass. The evolution of the pore fluid can be described by equation (3):

$$\frac{\partial C_f}{\partial t} = D\frac{\partial^2 C_f}{\partial z^2} - v\frac{\partial C_f}{\partial z} + RM(C_s - KC_f)$$

EQUATION 4.1

In Equation 4.1 D is the diffusion coefficient of the species in solution with units of m^2/Myr, v is the pore fluid advective velocity (m/Myr), C_s is the

concentration in the solid (molal), C_f is the concentration in the fluid (molal), R is the recrystallization rate of the solid in terms of reciprocal time (Myr^{-1}), M ($= \rho_s(1-\phi)/\rho_f\phi$) is the solid/fluid mass ratio of the sediment, where ρ is the density and ϕ is the porosity, and K is the distribution coefficient between the solid and fluid (C_s/C_f) that applies for the precipitation of solid carbonate from the pore fluid. As such Equation 4.1 contains terms that describe the diffusion, advection and reaction of the element in the pore fluid with the coexisting solid. The one dimensional spatial reference frame is defined with $z = 0$ at the sediment-water interface with z increasing with depth. Another founding assumption is that of steady state: all observed changes with depth in the pore fluid profiles are due to diagenesis (Figure 4.3).

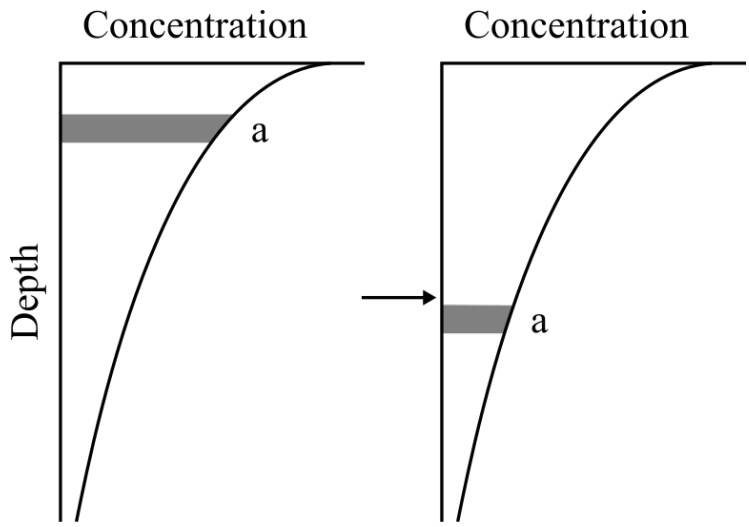

FIGURE 4.3: DIAGRAMMATIC REPRESENATION OF STEADY STATE DIAGENESIS. WITH INCREASING TIME (LEFT TO RIGHT) THE CONCENTRATION DOES NOT CHANGE FOR A FIXED DEPTH, BUT DOES CHANGE FOR A GIVEN LAYER (a). (MODIFIED AFTER BERNER, 1980)

I modify Equation 4.1 similar to Turchyn and DePaolo (2011) to separate the rate of precipitation from dissolution to account for the fact that calcium concentrations decrease in the sedimentary pore fluids, suggesting there are depths where carbonate precipitation exceeds carbonate dissolution in the sediment column. A term is also included to account for the fraction of carbonate (f_c) within the sediment, as the carbonate content is variable in the measured sites (Figure 4.2). The modified equation (Turchyn and DePaolo, 2011), is:

$$\frac{\partial C_f}{\partial t} = D\frac{\partial^2 C_f}{\partial z^2} - v\frac{\partial C_f}{\partial z} + f_c M C_s (R_d - R_p)$$

EQUATION 4.2

Where terms are the same as Equation 4.1 with the addition of R_p and R_d, which are the rates of precipitation and dissolution (Myr^{-1}). Following the sensitivity analysis of Turchyn and DePaolo (2011), it was concluded that the adsorption of aqueous calcium was unlikely to be impacting the calculated dissolution rates at either of their measured sites, and hence, it was not included in the model here.

4.1.1.1 Strontium concentrations

I can estimate the rate of carbonate dissolution within the sediment column by modelling pore fluid strontium concentrations (Richter and DePaolo, 1987; Fantle and DePaolo, 2006). There are several assumptions that need to be made to find a steady state solution for strontium to Equation 4.1. I assume that the solid does not change strontium concentration with time, the upper boundary is fixed to modern seawater values of (~91µM), the porosity, the partition coefficient of strontium into reprecipitated carbonate (K_{Sr}) and recrystallization rate are constant with time (but not necessarily with depth) and there is no advection. The steady-state solution to Equation 4.1 is:

$$C_f(z) = \frac{C_s}{nK_{Sr}} + \left(C_{sw} - \frac{C_s}{nK_{Sr}}\right) e^{-z/L}$$

EQUATION 4.3

Where K_{Sr} is the strontium distribution coefficient, *n* is the ratio of precipitation to dissolution (R_p/R_d), z is the depth below the seafloor and C_x refers to the concentration of strontium in either the solid or pore fluid. The concentration of the solid was measured using ICP-OES and has an average of 2200ppm at Site 1081 and 1800ppm at Site 1086. *L* is the diffusive reaction length, L_{Sr} (Berner, 1980; Phillips, 1991; DePaolo and Getty, 1996), which is the depth over which the concentration of strontium in the pore fluid evolves from seawater to concentration in equilibrium with the solid and is defined as:

$$L_{Sr} = \sqrt{\left(\frac{D_{Sr}}{f_c R_d M n K_{Sr}}\right)}$$

EQUATION 4.4

Where D_{Sr} is the diffusion coefficient of strontium in solution with units of m^2/Myr, f_c is the fraction of carbonate, R_d is dissolution rate, M is the solid/fluid ratio as defined earlier, n is the ratio of precipitation to dissolution and K_{Sr} is the strontium distribution coefficient. The value for K_{Sr} used within the following models is 20, which follows the work of Fantle and DePaolo (2006). As the pore fluid strontium concentrations do not reach equilibrium with the solid phase, the approach followed by Richter and DePaolo (1987; 1988) to estimate K_{Sr} cannot be applied.

The solid phase strontium concentration is also related to the recrystallization rate of the carbonate and is described by:

$$\frac{\partial C_s}{\partial t} = -V\frac{\partial C_s}{\partial z} - R(C_s - K_{Sr}C_f)$$

EQUATION 4.5

Where V is the compaction velocity, C_s and C_f are the concentrations of strontium in the solid and fluid respectively and K_{Sr} is the strontium distribution coefficient discussed above. In the reference frame used within these models *V* refers only to compaction, and can furthermore be assumed to be negligible, which simplifies Equation 4.5 so that the concentration in the solid is solely controlled by the recrystallization term.

4.1.1.2 Calcium concentrations

Previous work modelling calcium concentration in marine pore fluids suggests that the diffusive reaction length (L_{Ca}) is very short, and thus calcium quickly reaches equilibrium with the carbonate phase in sediments. Therefore, similar to strontium, I can make the assumption that the system is in steady state (Fantle and DePaolo, 2007). With similar assumptions, the steady state solution for Equation 4.2 for calcium is:

$$\frac{\partial^2[Ca]_f}{\partial z^2} = \frac{f_c M[Ca]_s}{D_{Ca}}(R_p - R_d)$$

EQUATION 4.6

Changes in the concentration of calcium in the pore fluid give a qualitative sense of the relative proportions of Rp (rate of carbonate precipitation) and Rd (rate of carbonate dissolution), although the difference between them is proportional to the curvature of the calcium concentration pore fluid profile (Equation 4.6). Over the top part of the measured Sites, the concentration of calcium decreases until it reaches the minimum calcium concentration at depth z_{min}. The decrease in the concentration of calcium in the pore fluid can be determined using the boundary conditions of seawater concentrations at the top of the profile:

$$[Ca]_f(z) = [Ca]_{sw} + \frac{f_c M[Ca]_s}{2D}\left(R_p - R_d\right)z(z - 2z_{min})$$

EQUATION 4.7

This equation gives a steady state solution for the calcium concentration in pore fluid at a depth below the sea floor and allows for the calculation of the rate of precipitation when the rate of dissolution is calculated using the strontium concentrations as described previously.

4.1.1.3 Calcium isotopes

Turchyn and DePaolo (2011) previously modified equation 4.2 to model calcium isotopes in pore fluids by deriving a steady state solution to Equation 4.6 for calcium isotopes:

$$\frac{\partial^2 \delta^{44}Ca_f}{\partial z^2} = \frac{f_c M[Ca]_s R_d}{D_{Ca}[Ca]_f}\left(\delta^{44}Ca_s - \delta^{44}Ca_f\right)$$

EQUATION 4.8

Where $\delta^{44}Ca_s$ and $\delta^{44}Ca_f$ refer to the calcium isotope composition of the solid and pore fluid, D_{Ca} is the aqueous calcium diffusion coefficient, which I

assume is the same for both ^{40}Ca and ^{44}Ca, and all other terms are the same as defined above.

To find an analytical solution to Equation 4.8, the assumption must be made that that f_c, M, $[Ca]_s$, R_d, D_{Ca}, $\delta^{44}Ca_s$ and $[Ca]_f$ are constant with depth such that the ex-parenthesis term is a constant (Fantle and DePaolo, 2007; Turchyn and DePaolo, 2011). On the whole, the $\delta^{44}Ca$ of the solid always can be assumed to be constant given the relatively small changes in measured $\delta^{44}Ca$ at these sites (Figure 4.3) and furthermore at a range of previously studied sites (Fantle and DePaolo, 2007; Turchyn and DePaolo, 2011). If I assume the other ex-parenthesis terms are constant as well (f_c, M, $[Ca]_s$, R_d, D_{Ca}, and $[Ca]_f$), the analytical solution suggests an exponential decay of the calcium isotope composition of the pore fluid to match the solid:

$$\delta^{44}Ca_{FLUID}(z) = \delta^{44}Ca_{SOLID} + (\delta^{44}Ca_{SW} - \delta^{44}Ca_{SOLID})e^{-z/L_{Ca}}$$

EQUATION 4.9

Where the calcium isotope composition of the pore fluid is related to the length scale for calcium:

$$L_{Ca} = \sqrt{\frac{D_{Ca}[Ca]_f}{f_c R_d M [Ca]_s}}$$

EQUATION 4.10

Different rates of dissolution cause the length scale over which the calcium isotopes in the pore fluid reach equilibrium with the solid phase to vary. To solve the equations above various rates of dissolution are compared with the measured $\delta^{44}Ca$ of the pore fluid, and, as such a rate of dissolution within the pore fluid is determined (Figure 4.4).

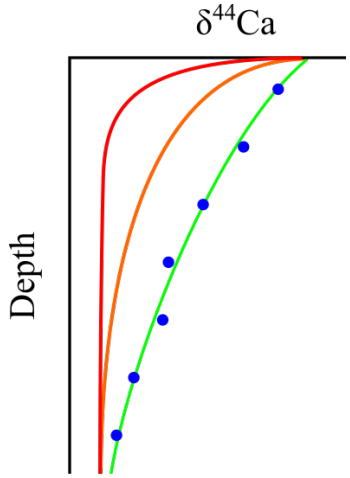

FIGURE 4.4: THREE PORE FLUID δ^{44}CA PROFILES WITH DECREASING RATES OF DISSOLUTION (RED TO GREEN) FIT AGAINST AN IDEALISED DATASET (BLUE DOTS)

This is a reasonable analytical solution for modelling the approach of the pore fluid calcium isotope composition to isotopic equilibrium with the solid-phase calcium, because over the depth where the pore fluids are moving towards calcium isotope equilibrium with the solid, the ex-parenthesis terms in Equation 4.8 can be assumed to be more-or-less constant (Fantle and DePaolo, 2007). As has been shown in previous studies, and discussed earlier, the depth over which the pore fluid aqueous calcium approaches isotopic equilibrium with the solid is a function of the recrystallization rate of the solid, which in Equation 4.8 is given as R_d with the assumption that R_p is equal to R_d.

In the upper part of many sediment columns that are undergoing active authigenic carbonate precipitation, however, the founding assumption behind the analytical solution to Equation 4.8 is invalid; the ex-parenthesis term is not constant with depth. If I consider the generic form of Equation 4.8:

$$\frac{d^2y}{dz^2} = A + By$$

EQUATION 4.11

If A=0, then the general solution for Equation 4.11 is:

$$y(z) = c1e^{B/2z} + c2e^{-B/2z}$$

EQUATION 4.12

where c1 and c2 are constants. Equation 10 is derived from this general solution. When B (Equation 4.12) is a function of depth (z) then this solution is no longer applicable. Some parameters ex-parenthesis in Equation 9 can be assumed to be constant with depth, such as the diffusion coefficient for calcium (D_{Ca}), or the concentration of calcium in the solid ($[Ca]_s$), and others I can take as a constant because they don't vary enough to impact the outcome, as shown for the mass-fluid ratio (M) or the fraction of carbonate (fc) (See section 4.4.1). However, there is a depth-variant change in the calcium concentration in the fluid $[Ca]_f$ that itself is a function of Rd and which means the analytical solution given in Equation 4.9 isn't valid. Unfortunately there is no analytical solution for Equation 4.8, and a numerical solution must be used.

This suggests that a sediment column undergoing active authigenic carbonate precipitation may need to be considered in two parts: the depth over which authigenic carbonate is precipitating and calcium concentrations are dropping (the rate of precipitation exceeds the rate of dissolution), and the depth over which the pore fluid calcium is approaching isotopic equilibrium with the solid phase (and where the rates of precipitation and dissolution are equal). In the upper part of the sediment column, Equation 4.8 must be solved numerically. Below the porefluid calcium minimum as calcium concentrations increase, the analytical solution derived in past work and given in Equations 4.9 and 4.10 is valid.

The model equations for strontium, calcium and calcium isotopes as summarised here were adapted from multiple previous studies, which describe in greater detail the derivation of the model equations (Berner, 1980; Baker et al., 1982; Richter and DePaolo, 1987; Richter and DePaolo, 1988; Richter and Liang, 1993; Richter, 1993; Schrag et al., 1995; Richter, 1996; Rudnicki et al., 2001; Fantle and DePaolo, 2006; Fantle and DePaolo, 2007; Turchyn and DePaolo, 2011).

4.3 Results

The calcium concentrations and $\delta^{44}Ca$ of the pore-fluid calcium, as well as the $\delta^{44}Ca$ of the solid phase for Sites 1081 and 1086 are summarized in Table 4.1 and Table 4.2 and plotted in Figure 4.5. At Site 1081, the calcium concentrations in the pore fluid decrease rapidly over the top 45m of the sediment column to 3.5mM, before gradually increasing over the measured depth interval, approaching 9mM at 450mbsf (Figure 4.5). The $\delta^{44}Ca$ of the pore fluids increases from 0.86‰ at 5mbsf to just over 1‰ at 45mbsf. Beneath 45mbsf the $\delta^{44}Ca$ of the pore fluid decreases to a minimum of -0.1‰ at 450mbsf. The solid phase $\delta^{44}Ca$ is constant throughout the core, with an average of -0.3‰.

At Site 1086, the pore fluid calcium concentration also decreases over the top 80m of the core, however below this depth the concentrations stay constant at 6mM. The $\delta^{44}Ca$ of the pore-fluid decreases from 0.8‰ at the top of the core to 0.2‰ by 100mbsf, where it stays relatively constant, with a slight decrease to 0.1‰ by the base of the core at just under 200mbsf. The $\delta^{44}Ca$ of the solid phase averages -0.35‰ and is constant throughout the core.

TABLE 4.1: PORE FLUID $\delta^{44}Ca$ DATA

Identifier	Depth (mbsf)	[Ca] (mM)	$\delta^{44}Ca$ (‰ vs. BSE)	Std Dev. (2σ)	n
1081_2H	5.4	10.47	0.86	0.03	2
1081_3H	13.3	10.07	0.91	0.09	3
1081_4H	24.3	8.52	0.87	0.12	3
1081_5H	33.8	6.55	1.04	0.13	3
1081_6H	43.3	3.94	1.01	0.01	2
1081_7H	52.8	3.42	1.03	0.07	2
1081_8H	62.3	3.61	0.92	0.06	3
1081_9H	71.8	3.69	0.99	0.01	2
1081_10H	81.3	3.74	0.78	0.07	2
1081_11H	90.8	4.06	0.53	0.09	3
1081_12H	100.3	4	0.62	0.01	2
1081_15H	128.94	3.25	0.41	0.10	3
1081_18H	150.35	4.64	0.49	0.02	2
1081_21X	178.2	4.99	0.37	0.19	3
1081_24X	207.2	5.27	0.33	0.18	2
1081_27X	235.8	5.23	0.10	-	1
1081_30X	264.75	4.88	0.12	-	1
1081_33X	293.65	5.57	0.12	-	1
1081_36X	323	5.51	-0.02	0.02	2
1081_39X	352.27	6.8	0.00	0.01	2
1081_42X	380.38	7.49	-0.05	0.02	2
1081_45X	409.28	7.64	0.11	0.03	2
1081_48X	441.15	7.73	-0.08	0.05	2
1086_1H1W	1.4	11.09	0.73	0.12	2
1086_1H3W	4.4	10.06	0.78	0.05	2
1086_2H	11.1	9.45	0.66	0.09	2
1086_4H	30.1	8.87	0.61	0.03	2
1086_6H	49.1	7.92	0.39	0.02	2
1086_8H	68	7.25	0.32	0.14	2
1086_10H	87	6.14	0.24	0.14	2
1086_11H	96.6	6.56	0.18	0.17	2
1086_14H	125.1	6.46	0.17	0.07	2
1086_20H	182.1	6.32	0.11	0.03	2

TABLE 4.2: SOLID $\delta^{44}Ca$ DATA

Identifier	Depth (mbsf)	% $CaCO_3$	$\delta^{44}Ca$ (‰ vs. BSE)	Std Dev. (2σ)	n
1081_2H	1.5	40.4	-0.25	-	1
1081_4H	20.5	26.1	-0.42	0.06	2
1081_5H	31.5	44.5	-0.25	-	1
1081_6H	42.5	18.9	-0.32	0.05	2
1081_7H	49.0	31.3	-0.35	0.06	2
1081_8H	58.5	32.3	-0.21	-	1
1081_9H	68.0	19.5	-0.25	0.04	2
1081_27X	146.5	9.1	-0.21	-	1
1081_33X	289.8	24.1	-0.32	0.09	2
1086_1H	2.0	82.8	-0.25	-	1
1086_3H	18.2	78.2	-0.33	-	1
1086_7H	56.2	74.8	-0.38	-	1
1086_11H	94.2	76.0	-0.36	-	1
1086_20H	179.7	86.4	-0.42	-	1

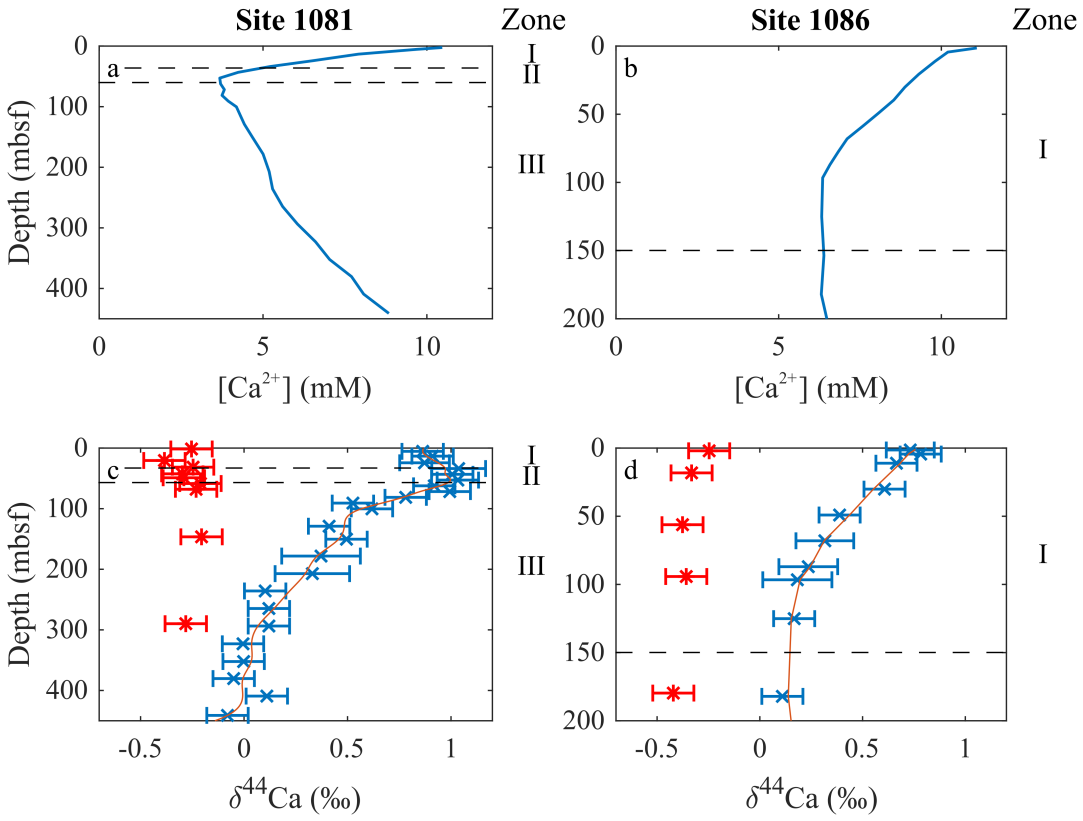

FIGURE 4.5: (A-B) PORE FLUID CALCIUM CONCENTRATION (WEFER ET AL., 1998) AND (C-D) PORE FLUID (BLUE X) AND SOLID (RED ∗) δ^{44}Ca. THE PORE FLUID δ^{44}CA MEASUREMENTS HAVE BEEN INTERPOLATED TO CREATE THE BEST-FIT LINE (ORANGE). ZONES I, II AND III ARE THE BACTERIAL SULFATE REDUCTION ZONE, ZONE OF ANAEROBIC OXIDATION OF METHANE AND ZONE OF METHANOGENESIS RESPECTIVELY, AS DETERMINED FROM PORE FLUID CONCENTRATIONS AND PREVIOUS WORK ON THE SITES (WEFER ET AL., 1998; SIVAN ET AL., 2007). THE SULFATE-METHANE TRANSITION ZONE IS SITUATED BETWEEN ZONES I AND II. THE ERROR REPORTED IS THE LONG-TERM 2σ OF 915B OR THE 2σ OF THE MEASURED SAMPLE REPLICATES, WHICHEVER IS LARGER.

4.4 Discussion

The discussion is divided into four parts. Firstly, I use the strontium concentrations, calcium concentrations and calcium isotopes in the pore fluid to model both the rates of carbonate dissolution and the depth distribution of carbonate precipitation and dissolution. To do this, I initially use the pore fluid strontium concentrations to determine the rates of carbonate dissolution because strontium concentrations are controlled by the release of strontium from biogenic calcite during dissolution. The rate of carbonate dissolution thus

calculated is compared with the calcium isotopic composition of pore fluids for an independent estimate of carbonate dissolution. Estimates of carbonate precipitation rates are derived from the calcium concentrations before calcium isotopes are used to combine carbonate dissolution and precipitation. Secondly, I explore the possibility of non-unity fractionation at Site 1086, where the pore fluid $\delta^{44}Ca$ is offset from the solid $\delta^{44}Ca$. Thirdly, I explore the relative importance of carbonate precipitation and dissolution in sediments using cross-plots of pore fluid calcium isotopes and strontium concentrations to expand our conclusions to a wider range of sedimentary environments. Finally, I use measured carbon isotopes of the DIC with the model to ascertain what the carbon isotope composition of the added authigenic phases would be.

4.4.1 Carbonate dissolution and precipitation

My first approach to determine rates of carbonate dissolution and precipitation at Sites 1081 and 1086 was to use pore fluid strontium concentrations (Equation 4.3). For Site 1081, I modelled the dissolution rates from 60mbsf to the base of the core because of the likely locus of carbonate precipitation in the zone of anaerobic methane oxidation; 30-50m (Sivan et al., 2007), which impacts the pore fluid strontium concentrations (discussed below). For Site 1086 the entire profile was modelled as there is no increase in the $\delta^{44}Ca$ of the pore fluid from seawater values and sulfate reduction zone extends to almost the base of the measured section, with no evidence for methanogenesis below (Sivan et al., 2007). The best fit using Equation 4.3 and 4.4 gives rates of carbonate dissolution within these sediments of $5*10^{-10}$ $year^{-1}$ (Site 1081) and $4*10^{-10}$ $year^{-1}$ (Site 1086). The carbonate mineral dissolution rates are higher at Site 1081 than Site 1086 due to the lower carbonate content at Site 1081. The strontium concentration within the solid is assumed to be constant in the pore fluid models. This is a valid assumption as at these two sites the strontium concentrations barely change due to the recrystallization of carbonate, as the recrystallization rate is very low (Figure 4.6).

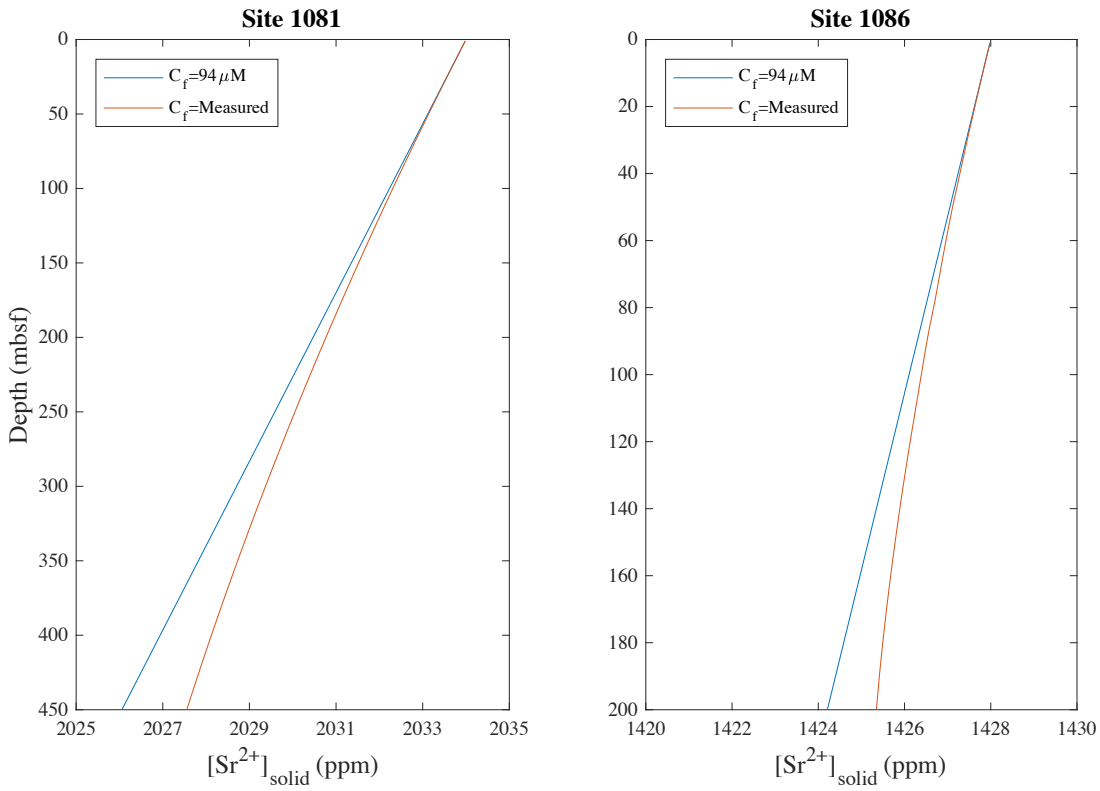

FIGURE 4.6: MODEL FOR THE CHANGE IN CONCENTRATION OF THE STRONTIUM IN THE SOLID PHASE DUE TO CARBONATE RECRYSTALLIZATION.

Carbonate dissolution supplies calcium to the pore fluid that has a $\delta^{44}Ca$ similar to that of the solid (-0.3‰). It has previously been suggested that the dominant process that impacts the calcium isotope composition of pore fluid calcium is carbonate dissolution (Fantle and DePaolo, 2007; Fantle, 2015). Therefore, my next step was to explore the effect of this carbonate dissolution on the $\delta^{44}Ca$ of the pore fluid. As discussed above in the modelling methods section, the approach taken by Turchyn and DePaolo (2011) uses an analytical solution from Equation 4.8 to form Equation 4.9. To find an analytical solution to Equation 4.8, the assumption was made that that f_c, M, $[Ca]_s$, R_d, D_{Ca}, $\delta^{44}Ca_s$ and $[Ca]_f$ are constant with depth (Turchyn and DePaolo, 2011). In the analytical solution presented in Equation 4.9, I could explore changing various variables ex-parenthesis in Equation 4.8, on the exponential decay of the pore fluid $d^{44}Ca$. For example, by decreasing Rd from $1*10^{-6}$ $year^{-1}$ to $1*10^{-9}$ $year^{-1}$ (Figure 4.7a) the pore fluid reaches equilibrium with $\delta^{44}Ca$ of the solid at 15m (faster dissolution rate) to below

200m (slower dissolution rate). If I held the dissolution rate constant but vary the fraction of carbonate the pore fluid reaches the solid $\delta^{44}Ca$ faster if there is a higher percentage of carbonate in the sediment than if there is a lower percentage (Figure 4.7b). A similar sensitivity analysis also showed that the fluid to mass ratio (M) has a much smaller effect on the pore fluid $\delta^{44}Ca$ over the range of M seen in the natural environment (Figure 4.7c). These calculations show, as previous studies have suggested, that the exponential decay form of the analytical solution for Equation 4.8 adequately explains the behaviour seen in the $\delta^{44}Ca$ of pore fluid calcium in deep-sea sediments resulting from the recrystallization of carbonate minerals. My sensitivity analysis also demonstrated that while variations in carbonate dissolution, or recrystallization rate, have a large impact on the length scale over which $\delta^{44}Ca$ in the porefluid equilibrates with $\delta^{44}Ca$ in the carbonate, changes in the fraction of carbonate and the fluid to mass ratio (M) have a smaller effect on this length scale.

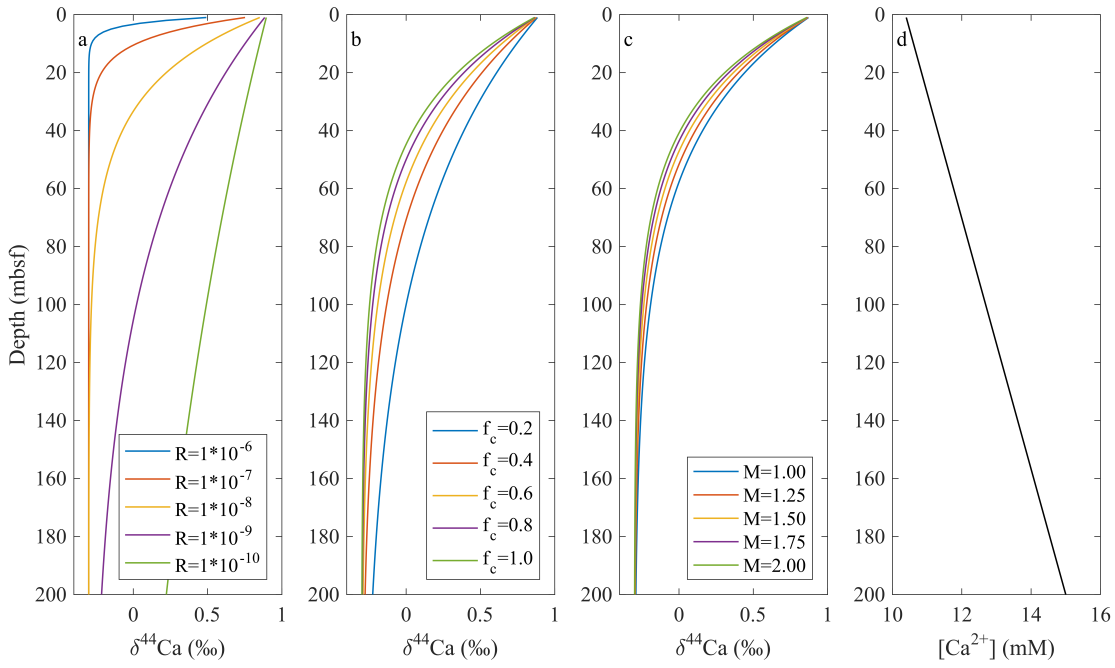

FIGURE 4.7: SENSITIVITY ANALYSIS FOR THE RATE OF RECRYSTALLIZATION (A), FRACTION OF CARBONATE (B), MASS TO FLUID RATIOS (C) AND IDEALISED CALCIUM CONCENTRATION DURING THE RECRYSTALLIZATION (D).

Having explored the various parameters that might impact the $\delta^{44}Ca$ of the pore fluid calcium, I returned to the strontium-derived carbonate dissolution

rates to model the calcium isotope composition of the pore fluid using Equation 4.9. As a start, I modelled the $\delta^{44}Ca$ pore fluid profile that would occur from simply the calculated rates of carbonate dissolution from strontium concentrations, assuming all other ex-parenthesis terms in Equation 4.8 are constant (solid and dotted line, Figure 4.8b, solid line, Figure 4.8d). For Site 1081, the modelled $\delta^{44}Ca$ pore fluid profile fits the data from 60mbsf to the base well (solid line, Figure 4.8b). On the other hand, at Site 1086, there is an offset between the modelled and measured pore fluid $\delta^{44}Ca$ below 100m, with the modelled profile being lower in $\delta^{44}Ca$ than the measured $\delta^{44}Ca$ (solid line, Figure 4.8d).

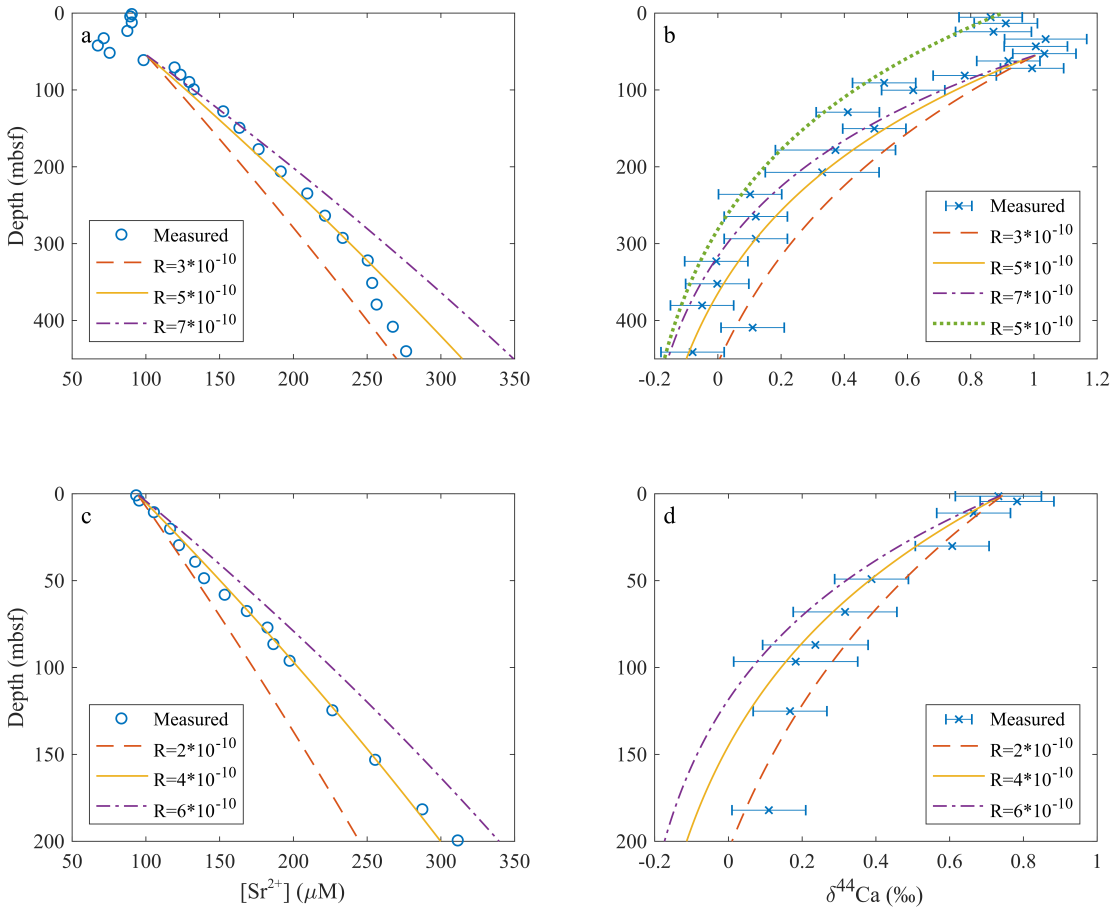

FIGURE 4.8: MEASURED STRONTIUM PORE FLUID CONCENTRATIONS (O) COMPARED TO MODEL FITS FOR RECRYSTALLIZATION RATES FROM $3*10^{-10}$ $year^{-1}$ TO $7*10^{-10}$ $year^{-1}$ FOR SITE 1081 (A). MEASURED $\delta^{44}Ca$ PORE FLUID VALUES (X) COMPARED TO THE MODEL PROFILES FOR THE SAME RATES OF RECRYSTALLIZATION FROM THE STRONTIUM CONCENTRATIONS FROM SITE 1081 (B). MEASURED STRONTIUM PORE FLUID CONCENTRATIONS (O) COMPARED TO MODEL FITS FOR RECRYSTALLIZATION RATES FROM $2*10^{-10}$ $year^{-1}$ TO $6*10^{-10}$ $year^{-1}$ FOR SITE 1086 (C). MEASURED $\delta^{44}Ca$ PORE FLUID VALUES (X) COMPARED TO THE MODEL PROFILES FOR THE SAME RATES OF RECRYSTALLIZATION FROM THE STRONTIUM CONCENTRATIONS FROM SITE 1086 (D).

The importance of sedimentary carbonate precipitation on the pore fluid $\delta^{44}Ca$ is shown when I try to model Site 1081 from the sediment-water interface assuming only carbonate dissolution impacts the $\delta^{44}Ca$ of the pore fluid. In this case, the modelled pore fluid $\delta^{44}Ca$ is too low relative to the measured $\delta^{44}Ca$ ("$R=5*10^{-10}$", dotted line, Figure 4.8b). This suggests that at the top of Site 1081 there must be carbonate precipitation that transiently raises the $\delta^{44}Ca$ of the pore fluid (Teichert et al., 2009).

The fact that at both sites the modelled $\delta^{44}Ca$ of the pore fluid calcium is lower than the measured $\delta^{44}Ca$ of the pore fluid, when modelling the whole column, is most likely due to the fact that in this initial model pass I have assumed that there is only carbonate dissolution occurring within the sediment column. However, in the upper part of the sediment column at both sites the pore fluid calcium concentrations are decreasing, suggesting there is carbonate precipitation removing calcium from the pore fluid (Figure 4.2b,g). Previous work on the calcium isotope fractionation during carbonate recrystallization in deep-sea sediments has suggested at the (slow) rates of precipitation occurring within marine sediments there is no calcium isotope fractionation between the solid and the fluid from which it is formed (Fantle and DePaolo, 2007; DePaolo, 2011; Turchyn and DePaolo, 2011; Fantle and Higgins, 2014; Fantle, 2015). The model mismatch between the pore fluid $\delta^{44}Ca$ and the 'dissolution only' modelled $\delta^{44}Ca$ suggests that there can be calcium isotope fractionation occurring during the sedimentary precipitation of carbonate, which leaves ^{44}Ca behind in the pore fluid. A distinct increase in the calcium isotope composition of the pore fluid, similar to that reported in Teichert et al. (2009), is only observed in Site 1081 in the upper 50m of the core, which correlates with the base of the sulfate reduction zone and the zone of anaerobic oxidation of methane. Over these zones, there is a rapid increase in alkalinity (Fig. 4.2c), which could drive relatively rapid precipitation of sedimentary carbonate minerals. At higher carbonate precipitation rates calcium isotope fractionation occurs, which would allow for the partitioning of calcium isotopes that my data suggest (Tang et al., 2008a; Tang et al., 2012; AlKhatib and Eisenhauer, 2016).

The rate of this sedimentary carbonate precipitation can be calculated from the change in the calcium concentrations as described by Equation 4.8. This solution is applicable over the upper part of the sediment column where calcium concentrations are decreasing, from the top of the column to the minimum calcium concentration within the profile (z_{min}). Using the dissolution rate (R_d) as calculated from strontium (Figure 4.8a,c) the best-fit profile suggests rates of carbonate precipitation of $2.35*10^{-8}$ $year^{-1}$, which is ~50

times higher than the dissolution rate at the top of this site (Figure 4.9a). At Site 1086 the model suggests carbonate precipitation is occurring at a rate of $9*10^{-10}$ $year^{-1}$, which is ~2 times higher than the carbonate dissolution rate. The modelled calcium concentration profiles confirms the qualitative reading of the pore fluid profile that the carbonate precipitation is concentrated in a relatively narrow zone in Site 1081, whereas in Site 1086 it continues to a greater depth, but at a much slower rate.

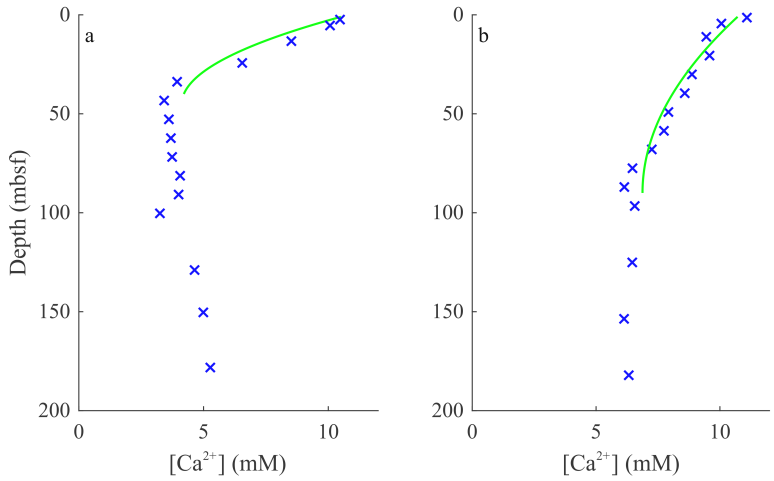

FIGURE 4.9: BEST-FIT PROFILES AS DETERMINED BY THE ROOT MEAN SQUARE ERROR (SOLID LINE) OF THE CALCIUM CONCENTRATION MODELS OF SITE 1081 (A) AND SITE 1086 (B) COMPARED WITH THE MEASURED CALCIUM CONCENTRATIONS (X) (WEFER ET AL., 1998).

As previously described in the modelling methods in order to model the calcium isotopic composition of the pore fluid where there is authigenic carbonate precipitation, Equation 4.8 has to be solved numerically. To determine the numerical solution to the top of the sediment column, I fit the ex-parenthesis term using a 2-term exponential fit. The boundary value solver BVP4C in Matlab is then used to find the numerical solution using a finite difference method, which depends on the two boundary values: the initial $\delta^{44}Ca$ of the fluid (seawater) and the $\delta^{44}Ca$ at the minimum calcium concentration (where the $\delta^{44}Ca$ of the pore fluid is at its highest). The $\delta^{44}Ca$ at the minimum pore fluid calcium concentration is determined by the ratio of carbonate precipitation (R_p) to dissolution (R_d). When $R_p >> R_d$ then there will be an increase in the $\delta^{44}Ca$ of the porefluid. As the difference between R_p and

R_d decreases, the increase in the pore fluid $\delta^{44}Ca$ becomes smaller, and eventually the $\delta^{44}Ca$ in the pore fluid calcium will only decrease, as seen in Site 1086. This can be visualised in numerically modelled sediment columns as shown in Figure 4.10.

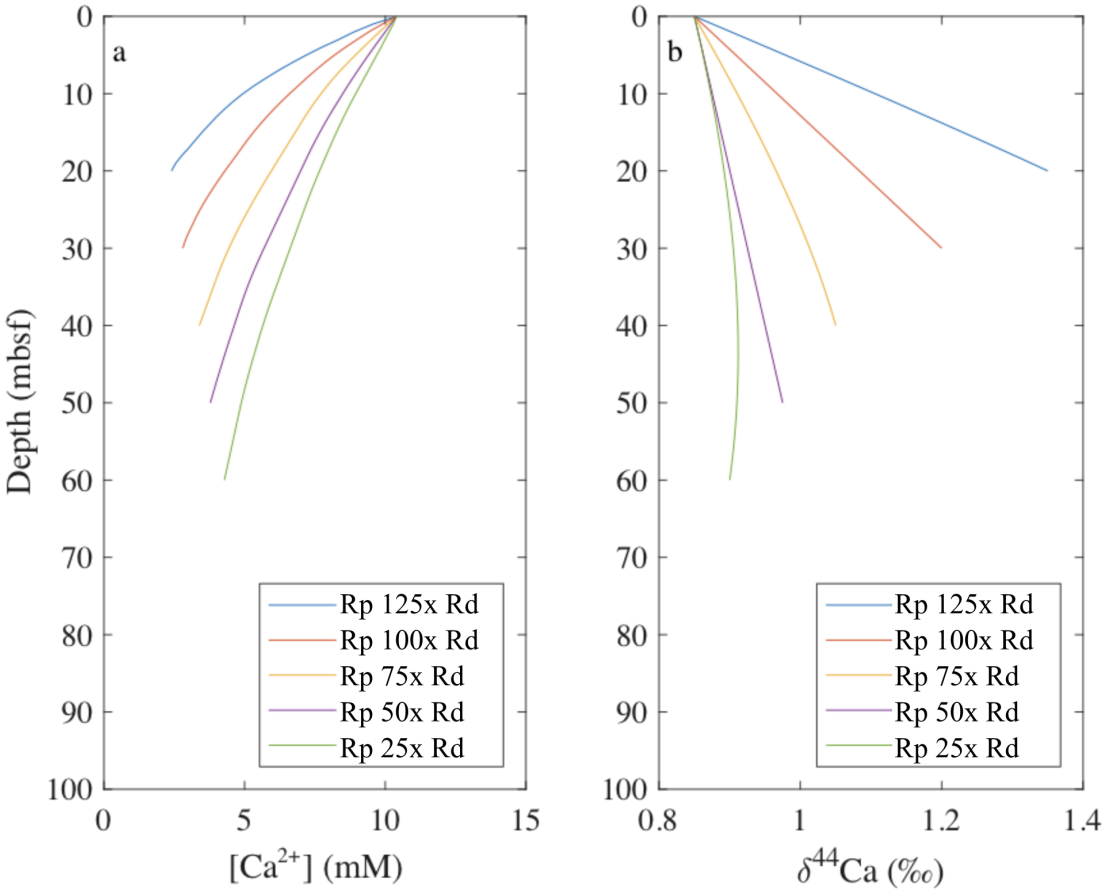

FIGURE 4.10: FIVE CALCIUM CONCENTRATION SCENARIOS WITH VARYING RATIOS OF PRECIPITATION TO DISSOLUTION (A), AND THE MODELLED $\delta^{44}Ca$ PRODUCED USING THE NUMERICAL SOLUTION FROM EQUATION 9 (B).

I used the numerical solution for the top of Site 1081, and an analytical solution for the depth range where the approach to isotopic equilibrium occurs. For Site 1086, the numerical solution is used over the upper part of the sediment column where the calcium concentrations are decreasing. The numerical solutions for the upper portion of Site 1081 and Site 1086 were compared to the measured $\delta^{44}Ca$ of the pore fluid in Figure 4.11. The numerical solution is valid where precipitation is occurring, and as such allows for determination of the impact that precipitation is having on the $\delta^{44}Ca$ of the pore fluid.

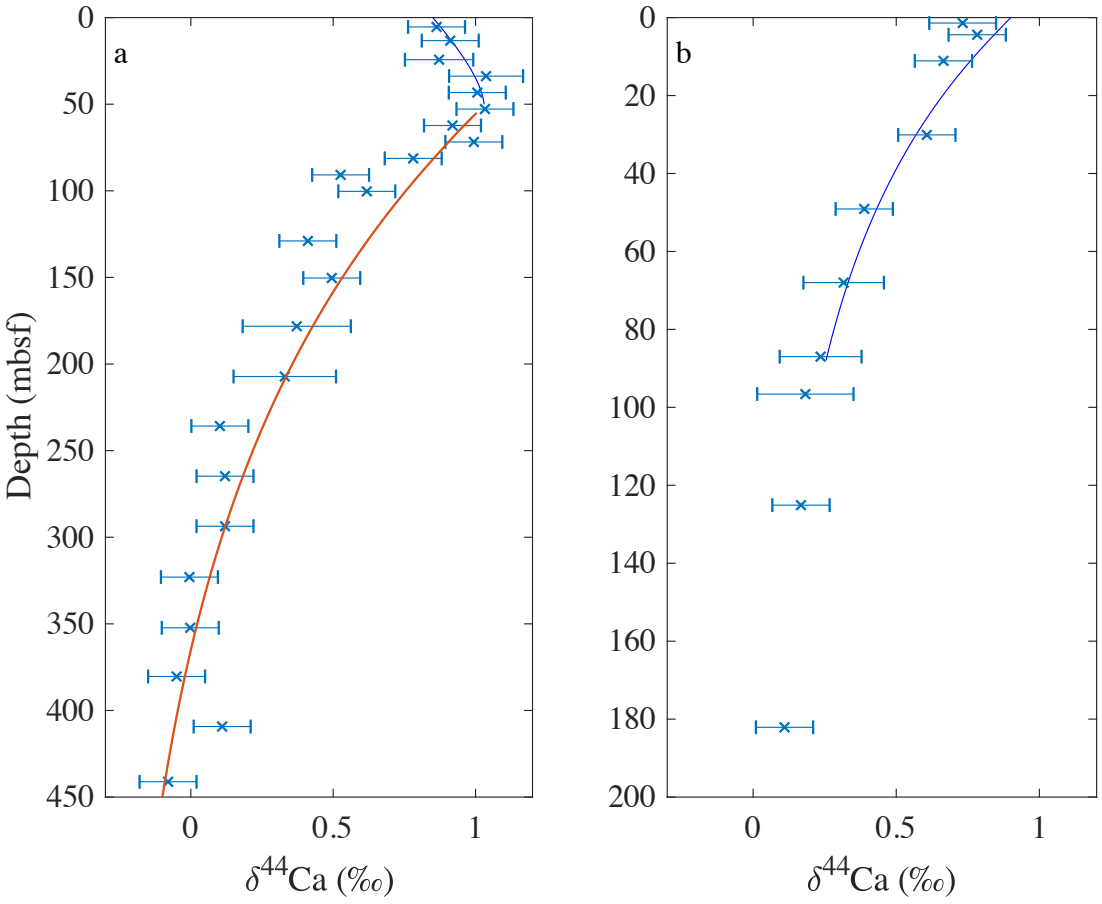

FIGURE 4.11: NUMERICAL MODELS FOR THE $\delta^{44}Ca$ OF THE PORE FLUID FROM THE SEDIMENT-WATER INTERFACE TO THE MINIMUM CALCIUM CONCENTRATION AT SITE 1081 (A) AND SITE 1086 (B). AT SITE 1081 BELOW THE MINIMUM CALCIUM CONCENTRATION THE RECRYSTALLIZATION MODEL FOR THE $\delta^{44}Ca$ IS SHOWN. THE CHANGE IN $\delta^{44}Ca$ BELOW THE MINIMUM CALCIUM CONCENTRATION AT SITE 1086 IS DISCUSSED BELOW.

4.4.2 Non-unity calcium isotope fractionation in Site 1086

At Site 1086, the $\delta^{44}Ca$ of the porewater tends towards between 0.1 and 0.2‰, approximately 0.5‰ higher than the $\delta^{44}Ca$ of the solid from 100 meters to the base of the core. This suggests that at this site, below 100 meters, there must be no carbonate recrystallization, extremely slow recrystallization, or calcium isotope fractionation between the solid and the fluid phases. I will consider each of these in turn. It is possible that carbonate recrystallization rates become so low below this depth there is no change in the calcium isotope composition (or calcium concentration) of the pore fluid, however it seems unlikely as the strontium concentrations in the pore fluid continue to

increase. A similar option is if there were a marginal difference between the rates of carbonate precipitation (R_p) and dissolution (R_d) and a constant calcium isotope fractionation factor during this precipitation; the difference in the rate of carbonate precipitation and dissolution would have to be small enough not to change the calcium concentrations. If there was such a marginal difference between the rate of carbonate precipitation and dissolution and a calcium isotope fractionation during this precipitation, this would lead to the pore fluid staying at a higher $\delta^{44}Ca$ relative to the pore fluid $\delta^{44}Ca$ that decreases towards the solid value during pure recrystallization. Equation 4.14 can be used to calculate the rates of carbonate precipitation relative to dissolution to achieve this non-unity condition (i.e. when there is a constant offset between the pore fluid and solid $\delta^{44}Ca$) using the rates of dissolution calculated from strontium concentrations and a $\delta^{44}Ca_s$ of -0.3‰.

$$\Delta^{44}Ca = \delta^{44}Ca_s - \left(\left(\frac{R_p}{R_d}\right) \times \left(\varepsilon \times \frac{R_p - R_d}{R_p}\right)\right)$$

EQUATION 4.14

In Equation 4.14, $\Delta^{44}Ca$ is the offset between the solid $\delta^{44}Ca$ ($\delta^{44}Ca_s$) and the measured pore fluid $\delta^{44}Ca$, which changes depending on the depth (Figure 4.12a). R_p and R_d are the rates of precipitation and dissolution respectively and ε is the calcium isotope fractionation during precipitation which I take as 1.4‰. The rates of carbonate precipitation that would result in calcium isotopic disequilibrium between pore fluid calcium and solid calcium is shown in Figure 4.12, (note the rate of carbonate dissolution remains as derived from the strontium concentration model above).

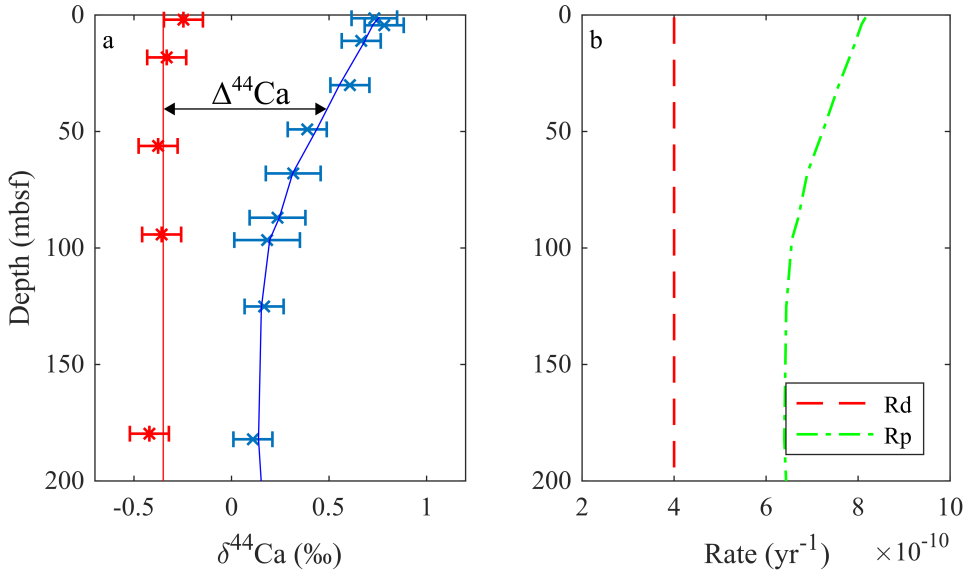

FIGURE 4.12: (A) MEASURED $\delta^{44}Ca$ OF PORE FLUID (X) AND CARBONATE SOLID (*) AND (B) MODELLED RATES OF DISSOLUTION (--) AND PRECIPITATION (-.-) FOR SITE 1086.

This calculated rate of carbonate precipitation over the top 100m can be compared with the rate of carbonate precipitation calculated from the change in the calcium concentration described above ($9*10^{-10}$ $year^{-1}$, Fig. 9b). The carbonate precipitation rate at the top of Site 1086 from the calcium isotope non-unity formulation (Equation 4.14) is $8.1*10^{-10}$ $year^{-1}$ and declines to $6.5*10^{-10}$ $year^{-1}$ at 100mbsf, with an average of $7.3*10^{-10}$ $year^{-1}$ (Fig 4.12b). Thus, the non-unity equilibrium fractionation model (Equation 4.14) and the changes in the pore fluid calcium concentration suggest similar rates of carbonate precipitation, provided there is calcium isotope fractionation during this precipitation.

Unfortunately, the difference between the rates of carbonate precipitation and dissolution below 100mbsf (Figure 4.12b) suggest that the pore fluid calcium concentration would continue to decrease, which is not observed in the data. The model suggests that the difference between R_p and R_d would have to be below 5% so as not to impact the calcium concentration in the pore fluid, and at such a low carbonate precipitation rates the calcium isotope fractionation factor during carbonate precipitation would need to approach 20‰ to keep the fluid out of isotopic equilibrium with the solid (Figure 4.13a).

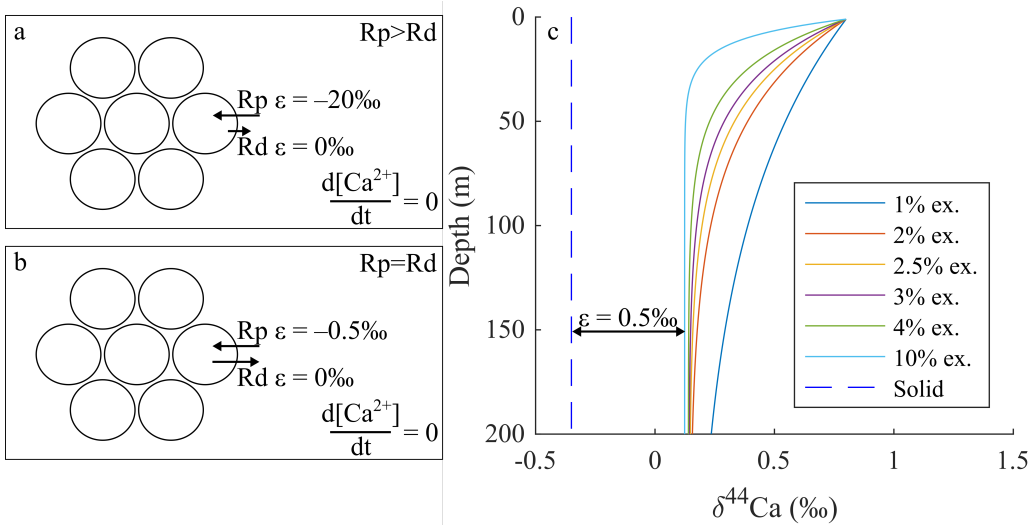

FIGURE 4.13: (A,B) SCHEMATIC DIAGRAMS OF RELATIVE PRECIPITATION AND DISSOLUTION RATES AND ASSOCIATED FRACTIONATION AND (C) MODELLED $\delta^{44}Ca$ OF THE PORE FLUID WITH PERCENTAGE OF FLUID EXCHANGED PER METER DEPTH.

Another explanation for the offset between the $\delta^{44}Ca$ of the pore fluid and $\delta^{44}Ca$ solid in the lower part of Site 1086 is that there is a calcium isotope equilibrium fractionation factor on carbonate precipitation but none on dissolution (Fig. 4.13b). Assuming a constant $\delta^{44}Ca$ of the solid and that the carbonate precipitation and dissolution rates are equal (n=1) then the calcium isotopic composition of the fluid will decrease to a $\delta^{44}Ca$ that is offset from the solid $\delta^{44}Ca$ by the magnitude of the calcium isotope fractionation during precipitation. If this equilibrium calcium isotope fractionation were 0.5‰ then this would explain why there is a 0.5‰ difference between the $\delta^{44}Ca$ of the solid and the $\delta^{44}Ca$ of the pore fluid at depth. Equally, a calcium isotope fractionation during carbonate dissolution would produce the same results. However, there are multiple studies suggesting a range of calcium isotope fractionation during carbonate precipitation but none suggesting calcium isotope fractionation during dissolution (De La Rocha and DePaolo, 2000; Gussone et al., 2003; Fantle and DePaolo, 2005; Gussone et al., 2005; Fantle and DePaolo, 2007; Teichert et al., 2009; Fantle, 2015). The best-fit surface kinetic model created by DePaolo (2011) to explain the data of Tang et al., (2008a) suggested that at very low precipitation rates the equilibrium calcium isotope fractionation factor (α_{eq}) could be 0.9995, which equates to a solid-fluid offset of -0.5‰. In this case, DePaolo (2011) suggested that the model

did not match the previously published data due to the large mismatch between the precipitation rates of the experimental and natural systems.

A simple model output of this type of equilibrium isotope exchange between the fluid and solid reservoirs is shown in Figure 4.13c, with the greater the percentage of pore fluid exchanged at each depth, the quicker the fluid will isotopically move from seawater $\delta^{44}Ca$ towards a $\delta^{44}Ca$ that is offset from the solid carbonate by the magnitude of the calcium isotope fractionation during carbonate precipitation. This calculation assumes that R_p and R_d are equal throughout the core, with a certain fraction exchanged between the solid and fluid at each depth. Therefore, it serves simply to illustrate how pore fluid $\delta^{44}Ca$ would evolve to the solid $\delta^{44}Ca$ with the calcium isotope offset imposed by an assumed calcium isotope fractionation, and the rate of evolution from seawater at the top of the sediment pile to the equilibrated values (with the isotope offset) is a function of the amount of carbonate recrystallized, or turned over, at each depth (e.g. Fantle and DePaolo, 2007)

This study is the first to suggest a calcium isotope fractionation during deep-sea carbonate diagenesis. If I assume that there must be small amounts of carbonate dissolution to explain the increase in the strontium concentrations at Site 1086, then my data require a small calcium isotope fractionation during either carbonate precipitation or carbonate dissolution, or both.

4.4.3 Strontium concentration vs. calcium isotopes

As both the strontium concentration and calcium isotopes are controlled by the relative amount of carbonate precipitation and dissolution within the sediment column, another way to visualise sedimentary carbonate precipitation and dissolution is a cross-plot of the two variables. This removes the effect of fluid transport via diffusion and advection within the sediment column and allows us to explore the relative change in one variable versus the other. At the top of the sediment column, the pore fluid has a strontium concentration of 91µM and a calcium isotope composition of 0.94‰ (both seawater values). During pure carbonate dissolution, the fluid strontium

concentration will increase and concurrently the fluid calcium isotopic composition will decrease leading to migration towards the upper left in the strontium versus $\delta^{44}Ca$ cross-plot (Figure 4.14).

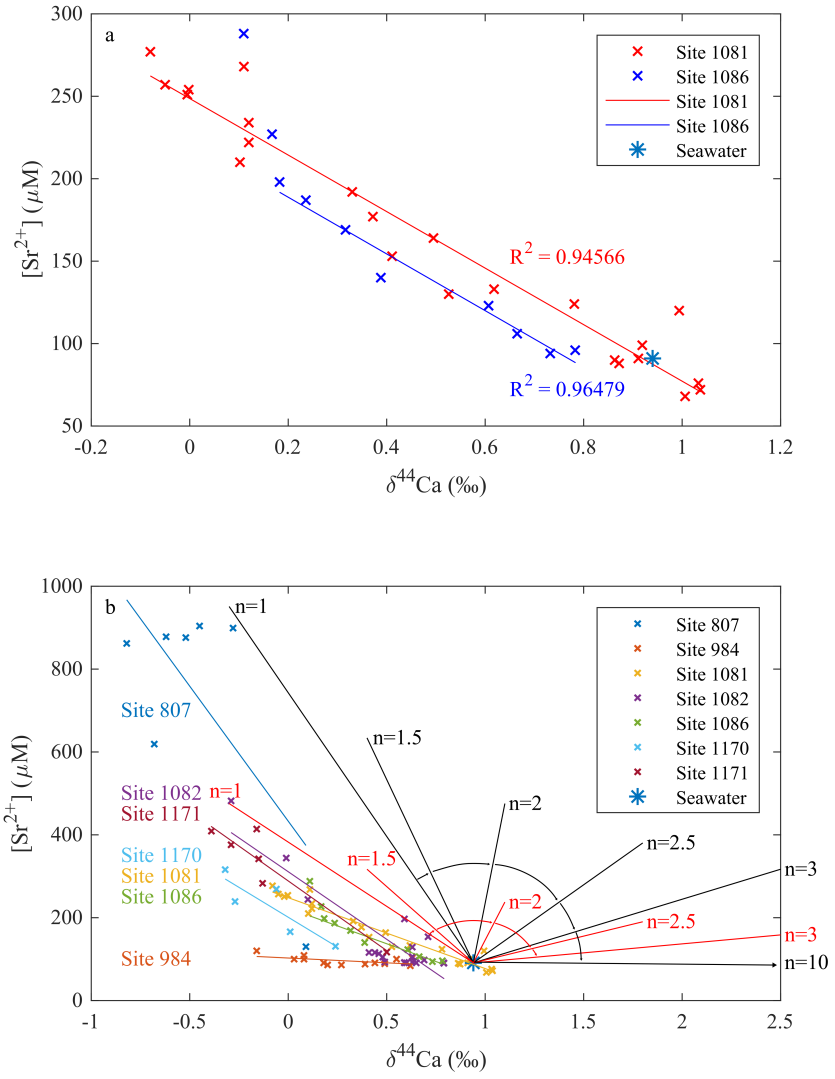

FIGURE 4.14: (A) CROSS-PLOT OF PORE FLUID $\delta^{44}Ca$ AND STRONTIUM CONCENTRATIONS FOR SITE 1081 (RED) AND SITE 1086 (BLUE) AND (B) A COMPILATION OF 7 SITES WITH LINEAR BEST FIT LINES COMPARED TO A SIMPLE MODEL WITH PLOTTED VECTORS (BLACK) RELATING TO THE EVOLUTION OF PORE FLUID WITH DIFFERING VALUES OF RELATIVE PRECIPITATION AND DISSOLUTION ($n=R_p/R_d$) THE COMPILATION CONSISTS OF SITE 807 (FANTLE AND DEPAOLO, 2007), SITES 984 & 1082 (TURCHYN AND DEPAOLO, 2011), SITES 1081 & 1086 (THIS STUDY) AND SITES 1170 & 1171 (FANTLE, 2015).

On the other hand, during pure carbonate precipitation, the fluid strontium concentrations will decrease, although this depends upon the strontium concentrations of the original and precipitated carbonate, and the fluid calcium isotopic composition will increase, plotting to the bottom right in the strontium versus $\delta^{44}Ca$ cross-plot (Figure 4.14). As fluid strontium concentrations are dominated by carbonate dissolution, there could also be situations where the carbonate dissolution overwrites any change in strontium concentrations from carbonate precipitation but the carbonate precipitation is still evident from changes in the calcium isotope composition of the pore fluid if there are no other factors influencing the calcium isotopic composition (see next paragraph). Depending on the ratio of carbonate precipitation to dissolution, the final composition of the pore fluid in a cross-plot of the strontium versus $\delta^{44}Ca$ should plot on a mixing line between the modelled value and the original seawater composition. The modelled value depends upon the strontium composition of the original and precipitated carbonate and the ratio of precipitation to dissolution (n).

There are a couple of possible complications to this approach for assessing carbonate dissolution and precipitation. The amount of strontium released during carbonate dissolution depends strongly on what is being dissolved; for example, some biogenic carbonates have higher strontium concentrations than inorganically precipitated carbonates. Furthermore, if the assumption that calcium isotopes are impacted only by the dissolution and precipitation of carbonate is incorrect, and if calcium was being released from silicates or clays, then it is possible that the $\delta^{44}Ca$ of the fluid could change without a concurrent change in strontium concentrations or conversely the $\delta^{44}Ca$ of the fluid could stay the same while the strontium concentrations changed. This process can occur during silicate weathering or when calcium is released from clay minerals

At Sites 1081 and 1086, the pore fluid concentrations of strontium and $\delta^{44}Ca$ show a strong correlation with a near-identical slope (Figure 4.14). It is possible that the offset between the two sites is due to boundary layer

processes, which leads to a lower initial $\delta^{44}Ca$ of the pore fluid at Site 1086 compared to Site 1081; this lowering of the initial $\delta^{44}Ca$ could be due to shallow carbonate dissolution close to the sediment-water interface that is not occurring in the organic-rich Site 1081. Silicate weathering or release from clay would release calcium into the pore fluid, which would account for the upper site having a lower initial $\delta^{44}Ca$ than seawater. It is possible at Site 1081 that shallow sediment carbonate dissolution isn't captured, as the first pore fluid sample is already five meters below the sediment-water interface.

A compilation of some of the currently measured sites (five, plus the two from this paper) where there are published pore fluid $\delta^{44}Ca$ and strontium concentrations is shown in Figure 4.14b. Three of the sites have similar slopes to the Sites 1081 and 1086. In theory, the ratio of carbonate precipitation-to-dissolution (n=Rp/Rd) suggests all data should plot on the black vectors (Figure 4.14b, Equations 4.5 and 4.14). What I observe is that the existing data plot to the left of the modelled vectors, even where rates of carbonate dissolution and precipitation are equal. Also, plotted on Figure 4.14b are red vectors, which represent the same equations as previously described, but with a lower carbonate strontium concentrations of 500ppm, half that of pure biogenic calcite (1000ppm). These vectors show a closer fit to the data from all sites other than Site 807, which suggests that the strontium concentrations of the bulk carbonate may be lower than previously assumed. Site 984 shows changing fluid $\delta^{44}Ca$ with very little change in strontium concentrations, which is likely due to the dissolution of silicates contributing to the $\delta^{44}Ca$ (Maher et al., 2004). Hence, changes in the ratio between the dissolution of silicate and carbonate will lead to a change in the slope.

As shown in Figure 4.14b in a closed system, if the rate of carbonate precipitation is over 10 times greater than the rate of carbonate dissolution, the strontium concentration in the pore fluids should evolve to concentrations lower than seawater. This matches well with the model for 1081 and 1086; Site 1081 has a carbonate precipitation rate 22 times higher than the carbonate dissolution rate in the upper 40m and shows a decrease in

strontium concentrations from seawater values by around 10%. Site 1086 conversely has a carbonate precipitation rate only twice as high as the carbonate dissolution rate; therefore although there is carbonate precipitation at Site 1086, the strontium concentrations are primarily controlled by the dissolution of biogenic carbonate minerals.

4.4.4 Authigenic carbonate precipitation during AOM or sulfate reduction?

It has previously been suggested that authigenic carbonate precipitation would be unlikely to occur in the zone of microbial sulfate reduction, as the pH tends towards a value of 6.7, which is considered below the critical pH for carbonate precipitation (Soetaert et al., 2007). In contrast, in the zone of anaerobic oxidation of methane (AOM), the pH tends towards 7.8 and further alkalinity is produced, leading to ideal conditions for the sedimentary precipitation of carbonate (Soetaert et al., 2007). Below where AOM occurs within the zone of methanogenesis, it has previously been reported the pH will tend towards a value of 5.6, possibly leading to carbonate dissolution (Soetaert et al., 2007). At Site 1081, the geochemistry of the pore fluids and the model suggests carbonate precipitation is happening towards the base of the zone of sulfate reduction and into the zone of anaerobic oxidation of methane (Sivan et al., 2007). The strontium concentration decreases between 20 and 50mbsf at Site 1081, which would occur during extremely rapid precipitation of carbonate or potentially celestite, and this decrease correlates with the most rapid drop in calcium concentrations. From the calcium isotopes, the most ^{44}Ca-enriched pore fluids are between 40 and 60mbsf although higher resolution pore fluids would help resolve this. At Site 1086 although there is no sulfate minimum zone in the measured profile and no methane (Wefer et al., 1998), the model requires twice as much carbonate precipitation as dissolution at the top of the sediment column to account for the decrease in the calcium concentrations in the pore fluid.

The combination of strontium concentrations and calcium isotopes suggests that the zone of carbonate precipitation at Site 1081 is between 30 and

50mbsf. The $\delta^{13}C$ of the DIC between these two depths ranges from -15‰ at 25mbsf to -22‰ at 53mbsf (Figure 4.15) (Sivan et al., 2007, O Sivan, personal communication, November 11, 2016). This suggests that any precipitated authigenic carbonate would have a $\delta^{13}C$ around these two values, with the average being -18.5‰. It should also be recalled that there is a small carbon isotope fractionation during calcite precipitation (~1‰, Romanek et al., 1992). In any case, a $\delta^{13}C$ for sedimentary carbonate of -18.5‰ is significantly lower than the $\delta^{13}C$ of biogenic carbonates (~ -2 to +2‰ Ravelo and Hillaire-Marcel, 2007). However at Site 1086, the zone of authigenic carbonate precipitation is within the entire sulfate-reducing zone (Figure 4.2), between 1.4 and 90mbsf. In this region, the $\delta^{13}C$ of the DIC varies from -2.4‰ at 1.4mbsf to -5.8‰ at 20mbsf where it remains constant (Figure 4.15). This suggests that the authigenic carbonate that formed within this region would have a $\delta^{13}C$ of around -5.0‰, which is lower than biogenic carbonate $\delta^{13}C$, but much higher than the authigenic carbonate suggested to precipitate at Site 1081.

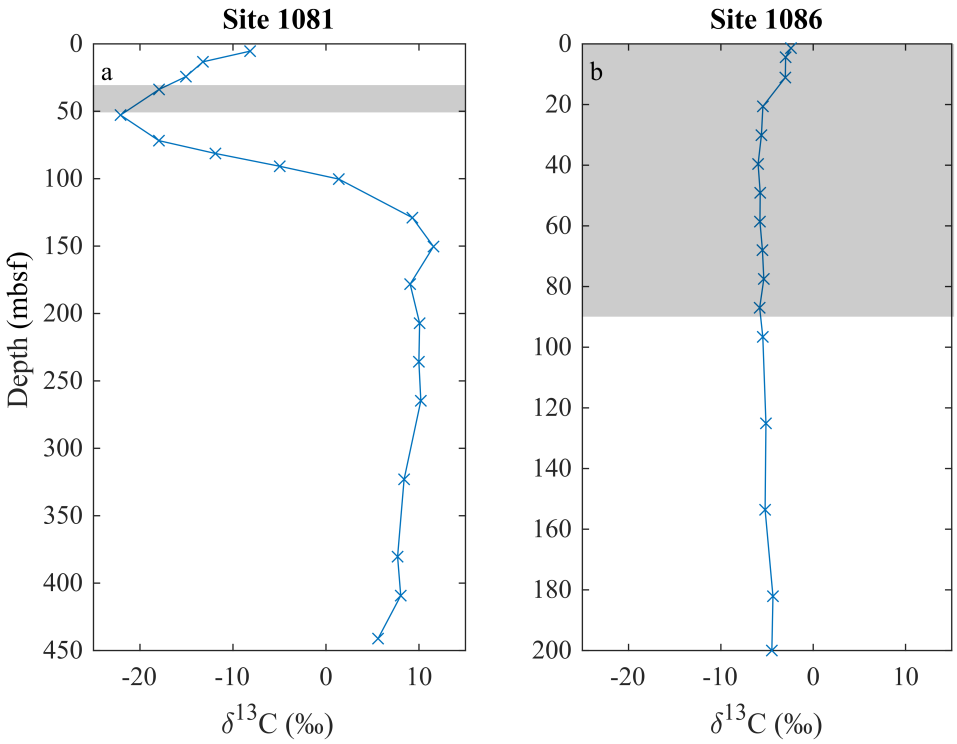

FIGURE 4.15: $\delta^{13}C$ RELATIVE TO PDB OF THE DISSOLVED INORGANIC CARBON (DIC) FROM SITE 1081 (A) AND SITE 1086 (B) (SIVAN ET AL., 2007), WITH THE ZONES OF PRECIPITATION OF CARBONATE AS SUGGESTED BY THE NUMERICAL MODELS SHADED IN GREY.

Both of these sites suggest that authigenic precipitation of carbonate is depleted in ^{13}C but that its $\delta^{13}C$ may vary depending on the rate of supply of alkalinity caused by sulfate reduction and anaerobic oxidation of methane, versus the rate of depletion of calcium in the pore fluid caused by carbonate precipitation. Further work could determine the global $\delta^{13}C$ of this authigenic carbonate sink through further modelling the controls on the depth distribution of sedimentary carbonate precipitation relative to the oxidation of organic matter.

4.5 Conclusions

The data presented within this chapter complements previous work on the extremely low rates of carbonate dissolution in organic/clay rich sites. The calcium isotope data when combined with the model and other pore fluid data constrains the zone of authigenic carbonate precipitation: at Site 1081 to the

base of the zone of sulfate reduction and into the zone of anaerobic oxidation of methane, and at Site 1086 in the upper part of the zone of sulfate reduction. Both of the measured sites require a calcium isotope fractionation during carbonate precipitation to explain the measured data, with a clear enrichment in the $\delta^{44}Ca$ of pore fluids over what would be modelled without calcium isotopic fractionation during precipitation, in the zone of precipitation at the top of Site 1081. The data from Site 1086 supports calcium isotope fractionation during recrystallization at depth in carbonate-rich marine sediments. The depth at which precipitation of authigenic carbonate is occurring within these two sites suggests that the $\delta^{13}C$ of the authigenic carbonate phase is depleted in ^{13}C but to varying degrees.

CHAPTER 5

PREDICTING AUTHIGENIC CARBONATE PRECIPITATION USING ARTIFICAL NEURAL NETWORKS

5.1 Introduction

Through this thesis, I have shown how calcium isotopes can be applied to a range of geological problems: I have demonstrated how calcium isotopes from lacustrine deposits can be used, in tandem with a box model, to determine the calcium budget of a past lake, and hence ascertain changes in regional climate. I have shown that calcium isotopes are extremely sensitive to dissolution and precipitation of carbonate minerals in marine sediments, which sheds light on the precipitation of authigenic carbonate and the rates of dissolution of primary carbonate phases. In this chapter, I will turn global, and explore the implications the processes that control the precipitation of authigenic carbonate and how this can improve our knowledge of the global carbon cycle.

Although authigenic carbonate precipitation has been proposed as a key third sink in the global carbon cycle at various points in Earth history, there is a relatively poor understanding of the modern amount of authigenic carbonate and controls on this authigenic carbonate precipitation (Schrag et al., 2013). The current estimate of authigenic carbonate precipitation on a global scale was conducted by Sun and Turchyn (2014). The Sun and Turchyn (2014) study used the calcium concentration profiles from 672 Deep Sea Drilling Program, Ocean Drilling Program, and Integrated Ocean Drilling Program (DSDP, ODP and IODP) sites to find the magnitude of the flux of calcium into and out of the sediments using Fick's first law (Equation 5.1):

$$F = -\varphi \times D_{Ca} \times \left(\frac{dC}{dz}\right)$$

EQUATION 5.1

where φ is the porosity of the sediment, *dC/dz* is the change in concentration of calcium with depth and D_{ca} is the diffusion coefficient of calcium in pore fluids, which is corrected for sediment tortuosity using:

$$D_{Ca} = D^{SW}/(1 - \ln(\varphi^2)$$

EQUATION 5.2

where D^{SW} = 4.41 x 10^{-6} cm^2s^{-1}, the diffusion coefficient of calcium in seawater at a temperature of 4^{o}C (Ullman and Aller, 1982; Boudreau, 1997).

Using Equations 5.1 and 5.2, in Sun and Turchyn (2014) the diffusive flux of calcium was calculated from the sediment-water interface to the calcium minimum, which occurs some 10 to 100 meters below the sediment-water interface in most deep-sea drill cores. Often in sedimentary pore fluids, calcium concentrations increase again below the minima, deeper in the sediment, either from the release of calcium from basalt under the sediment or from deeper carbonate dissolution. It is possible the diffusion of calcium up from deeper in the sediment column could mean that the Sun and Turchyn (2014) calculation is a minimum estimate and the actual amount of authigenic carbonate precipitation is higher. Furthermore, in the Sun and Turchyn (2014) work, the calcium flux at the individual sites was extrapolated to global rates of authigenic carbonate precipitation using an inverse distance-weighted technique. However, due to relatively large areas of the ocean floor with poor data coverage (for example, most of the Southern Ocean), this interpolation technique covered a significant area of the globe based on only a couple of measured sites.

The key driver of authigenic carbonate precipitation, as discussed in the introduction is anaerobic organic carbon oxidation. It has previously been suggested that metal oxide reduction (iron and manganese) will lead to a large increase in pH, and hence be the key driver of sedimentary carbonate

precipitation (Aller and Rude, 1988; Soetaert et al., 2007). However, the concentrations of iron and manganese oxides are low in many marine sedimentary environments; calculations have suggested that iron reduction may account for, at most, 15% of the anaerobic global organic carbon oxidation (Canfield et al., 1993; Canfield, 1994; Weber et al., 2006); bacterial iron reduction is likely a far more important process in marginal marine environments. This thesis supports the suggestion that for authigenic carbonate to form in open marine sediments, the two key microbially-mediated processes are microbial sulfate reduction (Equation 5.3) and the anaerobic oxidation of methane (Equation 5.4). Due to the relatively high concentration of marine sulfate relative to the other electron acceptors in the modern ocean, the upper part of the anoxic sediment column is dominated by sulfate reduction:

$$2CH_2O + SO_4^{2-} \rightarrow 2HCO_3^- + H^+ + HS^-$$

EQUATION 5.3

Organic carbon that escapes oxidation via microbial sulfate reduction can, below the zone of sulfate depletion, be converted into methane. Methane will diffuse up in the sediment column, and when it encounters sulfate, it is typically anaerobically oxidized, reducing the sulfate (Equation 5.4).

$$CH_4 + SO_4^{2-} \rightarrow HCO_3^- + HS^- + H_2O$$

EQUATION 5.4

Both microbial sulfate reduction and anaerobic methane oxidation produce bicarbonate ions and hence carbonate alkalinity as shown in Equations 5.3 and 5.4. This leads to an increase in the calcium carbonate saturation index (Ω from the introduction), which can lead to the precipitation of authigenic carbonate. Many anaerobic microbial processes also change pH of the pore fluid – the precise pH change depends on the type of organic carbon the microbial communities are consuming but the canonical values are that microbial sulfate reduction tends to a pH between 6.6 and 6.9, and anaerobic methane oxidation tends to a pH of 7.9 (Soetaert et al., 2007). However, as

discussed in Chapter 1, the electron donor that is available can alter the pH change that occurs within the sediment; if the sulfate reducing bacteria are feeding off formate, the resulting pH is much higher than if they are feeding off glucose for example. Furthermore, when iron hydroxides (FeOOH) react with hydrogen sulfide (H_2S) formed during microbial sulfate reduction, iron (II) sulfide is (FeS) is formed, and the consumption of protons during its formation can lead to an increase in pH. The pH further increases during the reaction of FeS with H_2S to precipitate iron (II) disulfide (FeS_2 – Pyrite) (Soetaert et al., 2007). The precipitation of pyrite cannot consume all of the protons released during sulfate reduction due to the low concentration of iron in marine sediments, but when combined with sulfide re-oxidation, pyrite precipitation could be important in the control of the pH of the pore fluids (Aller and Rude, 1988). The combination of the changes in pH and alkalinity within marine sediments lead to variations in the saturation index of carbonate minerals, and can lead to distinct horizons of authigenic carbonate formation (Figure 5.1 - Arndt et al., 2006; Arndt et al., 2009).

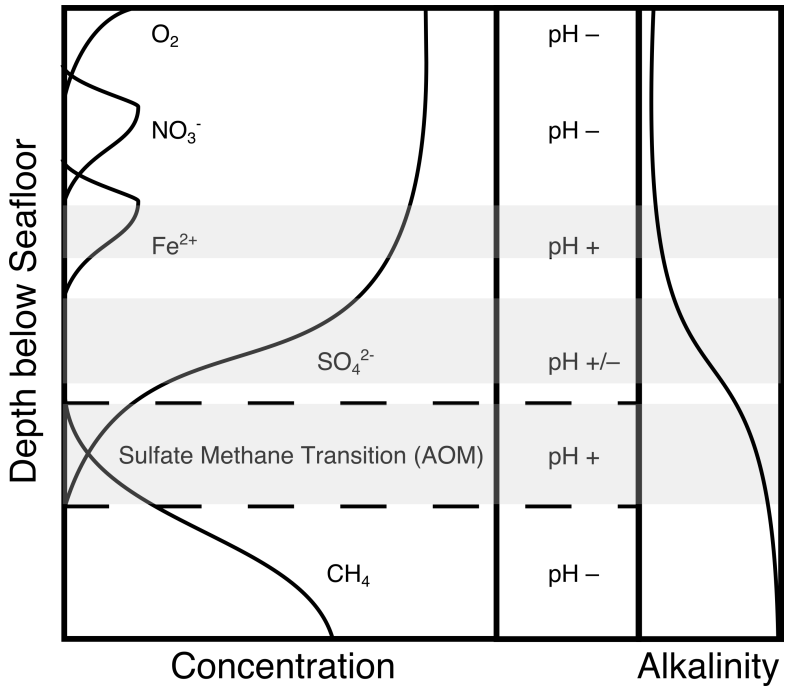

FIGURE 5.1: CONCENTRATION OF ELECTRON ACCEPTORS WITH DEPTH, AND THE ASSOCIATED CHANGES IN pH AND ALKALINITY (FROELICH ET AL., 1979; SOETAERT ET AL., 2007). POTENTIAL HORIZONS OF AUTHIGENIC CARBONATE PRECIPITATION ARE SHOWN IN GREY.

The goal of this chapter is to use the results from Chapter 4, where I determined the depth distribution of authigenic carbonate formation, to understand on a global scale where and how authigenic carbonate may be forming. I will take as an initial assumption that all authigenic carbonate forms from either microbial sulfate reduction or anaerobic methane oxidation, although the implication of this assumption will be discussed. When I have used the modern database of geochemical data to parse where and how authigenic carbonate may be forming today, then I will explore what its global carbon isotope composition might be, and then I will explore how this authigenic carbonate formation may be different when the major ion chemistry of the ocean is different.

5.2 Methods

I have utilised the ODP/IODP database of 682 sites located around the globe to identify the key geochemical parameters that indicate the precipitation of authigenic calcium carbonate, to then generate an artificial neural network (ANN) to predict the global distribution of authigenic carbonate as well as to determine how much of this authigenic is precipitating because of microbial sulfate reduction and how much is precipitating because of anaerobic methane oxidation. This has two advantages over the inverse distance weighted technique used by Sun and Turchyn (2014): the ANN predictions are based on ocean chemistry, which allows for determination of the rates of authigenic carbonate precipitation in areas of I/ODP data paucity (rather than interpolating between sites), and the classification of the microbial processes controlling authigenic carbonate precipitation enables a calculation of the global $\delta^{13}C$ of the precipitated authigenic carbonate.

Artificial Neural Networks (ANN) are computational models based upon the current understanding of the functioning of biological neural networks (Yegnanarayana, 2009). ANNs consist of inputs and outputs connected by layers of nodes or “neurons”. Each neuron is connected to the input, output or another neuron by a connection or “synapse”. The weight of importance of

each synapse depends on the training of the ANN and is given a value between 0 and 1. ANN training utilises a database of inputs, which have pre-determined output values. The ANN uses the input training database to vary the weight and sign (positive or negative) of each individual neuron and synapse to achieve the desired output, and thus establish the weight of importance of each synapse to be used for the trained ANN. The weight of each synapse determines the strength of the signal that is passed on to the next neuron. Each neuron may receive a signal from multiple synapses, and the combination of these signals determines the value (also between 0 and 1) of each individual neuron, which is fed into the following synapse. The different aspects of an ANN with 3 inputs and 2 outputs are shown below in Figure 5.2.

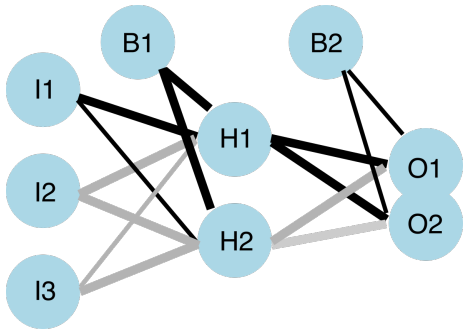

FIGURE 5.2: A SIMPLE SCHEMATIC OF AN ARTIFICIAL NEURAL NETWORK.

In Figure 5.2, the inputs are labelled I1 to I3, the neurons in the hidden layer are labelled H1 and H2, and the outputs are labelled O1 and O2. The inputs, neurons and outputs are connected by the grey and black lines, which represent the synapses. The black synapses are positive (between 0 and 1), whereas the grey synapses are negative (between -1 and 0). The thickness of the line determines the weight of the synapse. B1 and B2 are the biases that are applied to the individual neurons and outputs, which are also between -1 and 1.

The database I used to construct the artificial neural network contains information about the subsurface interstitial water and gas concentrations of a multitude of ions at sample sites with global distribution. As explained above, changes in the concentration of various elements in the porewater can be

used both to infer and numerically model the rates of processes occurring within the subsurface. Here, I focus on the concentration of dissolved calcium and sulfate and headspace methane. The microbial processes and authigenic carbonate precipitation discussed earlier impact the concentrations of these elements and hence, should allow for the identification of the zone of microbial sulfate reduction, and presence or absence of a zone of methanogenesis below this. I will make an assumption that when there is sulfate depletion and methane present at a site, sulfate-driven anaerobic oxidation of methane (AOM) occurs at the sulfate-methane transition zone.

The primary productivity of the overlying surface ocean, and hence the supply of organic matter to the sediment, plays a large role in determining the dominant microbial processes in the sediment (Canfield, 1994; Wang and Van Cappellen, 1996). When there is a high organic matter flux to the sediment, microbial sulfate reduction occurs rapidly over the upper tens of metres, and there can be a surplus of organic carbon not consumed that lasts below the depth of sulfate depletion. This organic carbon is available for fermentation into methane, which leads to the zone of anaerobic methane oxidation as methane diffuses up and meets sulfate diffusing down. In contrast, when there is a lower flux of organic matter to the sediment, microbial sulfate reduction occurs over a greater depth at a much slower rate. Sometimes, sulfate concentrations are not fully depleted, thus methane production never begins, and sometimes the organic carbon is fully utilized by the sulfate reducing bacteria, leaving little behind for the methanogens. Thus, the primary productivity of the overlying water column is a key variable in helping to predict the organic carbon supply to the sediment and the range of microbial processes that will occur in that sediment. Therefore I will consider several variables that help determine where primary productivity is highest.

In addition to primary productivity, the water depth of the site (how far the organic carbon produced must fall through the water column to reach the sediment) and other variables such as bottom water oxygen concentrations

are also key in determining whether the organic carbon that is produced in the surface ocean is deposited on the seafloor.

I gathered primary variables about the water column and surface ocean chemistry from satellite observations and ocean water chemistry maps (Table 5.1 – NCEI, 2006; Levitus et al., 2013). This includes geographical properties as well as properties relating to ocean bottom-water and ocean surface. The geographical property of the measured sites was water depth; the ocean bottom-water properties (defined at 1m below the seafloor) were oxygen content and temperature; the four ocean surface properties were: Chlorophyll-A, particulate organic carbon (POC), and nitrate and phosphate concentrations (Bowles et al., 2014).

TABLE 5.1: INPUT PARAMATERS AND SOURCES FOR THE ANN

Variable	**Relationship to productivity**	**Source**
Bathymetry	Controls organic carbon oxidation within the water column	ETOPO2v2
Chlorophyll A	Proxy for surface ocean productivity	World Ocean Atlas 2013 v2
Surface [POC]	Terrestrial carbon input	World Ocean Atlas 2013 v2
Surface [NO_3]	Key nutrient concentration	World Ocean Atlas 2013 v2
Surface [PO_4]	Key nutrient concentration	World Ocean Atlas 2013 v2
Bottom water temperature	Controls reaction rates in the sediments and water column	World Ocean Atlas 2013 v2
Bottom water dissolved oxygen	Controls the oxidation of organic carbon in the water column.	World Ocean Atlas 2013 v2

5.2.1 Authigenic carbonate precipitation determined by an ANN

The ANN allows me to determine where there will be authigenic carbonate precipitation globally based upon the sites where I have identified authigenic carbonate precipitation occurring based on the change in calcium and sulfate concentrations in the pore fluid. The seven ocean parameters I have chosen to determine the global distribution of authigenic carbonate formation (Table

5.1), are then used to train the ANN to map a global distribution of where authigenic carbonate is precipitating (Figure 5.3).

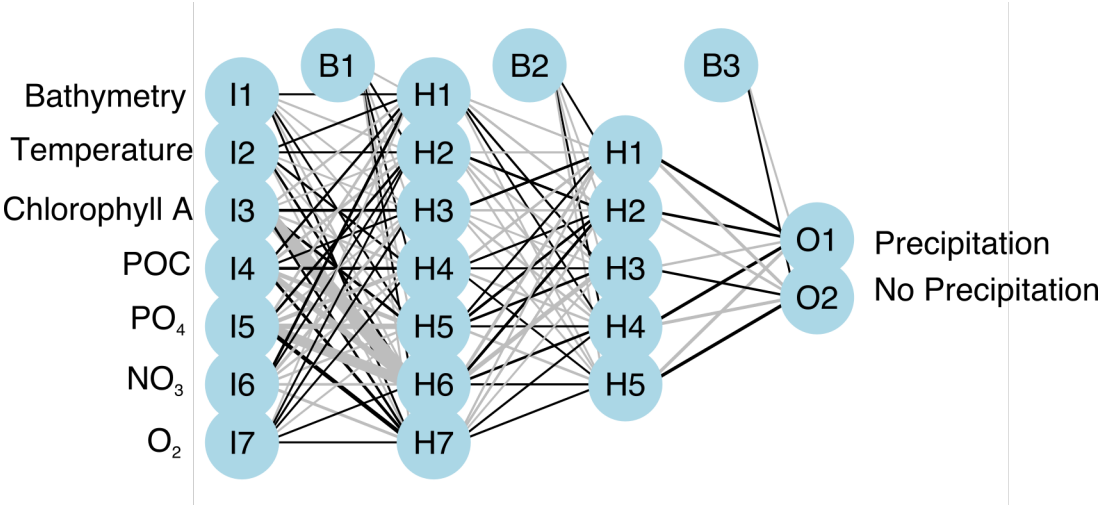

FIGURE 5.3: ANN USED TO DETERMINE SITES OF PRECIPITATION OF CARBONATE VERSUS SITES OF NO PRECIPITATION OF CARBONATE

The first stage in training an ANN to identify the precipitation of sedimentary authigenic carbonate is to create a training database as described above. The individual IODP and ODP sites where authigenic carbonate precipitation is occurring were identified on a site-by-site basis by examining the decrease in calcium concentrations over the upper part of the core, with a concurrent increase in alkalinity. In general, a decrease in calcium concentration is most likely due to the precipitation of carbonate minerals (Mozley and Burns, 1993; Fantle and DePaolo, 2005; Sun and Turchyn, 2014). This approach was conducted over 250 sites from the IODP/ODP database that had reported both pore fluid calcium and alkalinity concentrations. I identified 103 of these sites as ones where authigenic carbonate precipitation is occurring (Figure 5.4).

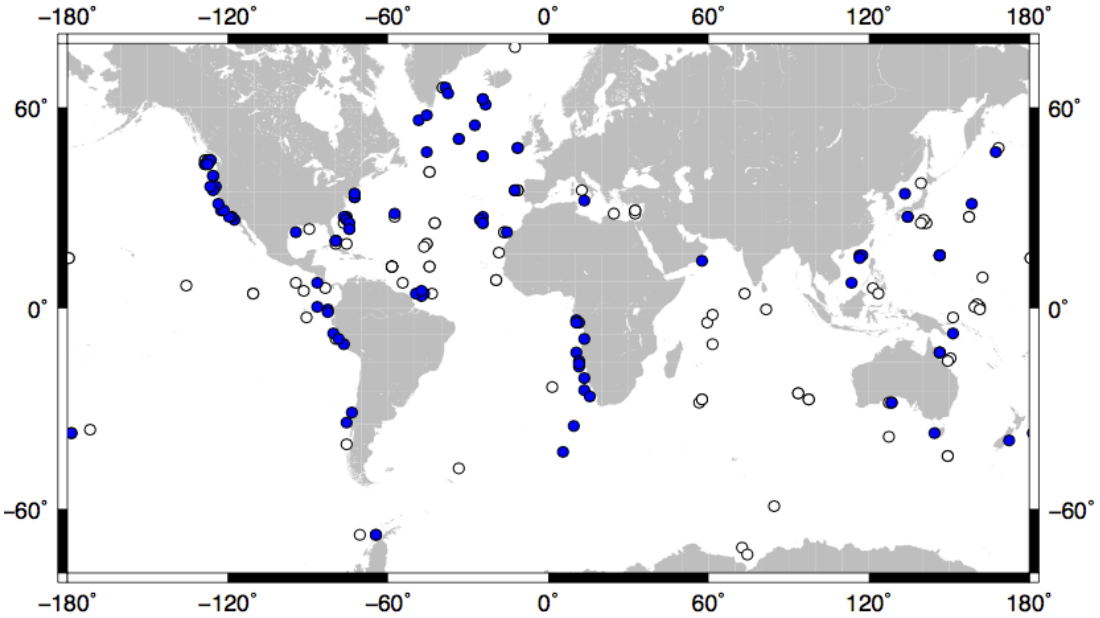

FIGURE 5.4: DISTRIBUTION OF CLASSIFIED SITES WHERE AUTHIGENIC CARBONATE PRECIPITATION OCCURS (BLUE) VERSUS SITES WITH NO AUTHIGENIC CARBONATE PRECIPITATION (WHITE).

The ANN was then created and trained using the independent seven variables at the 250 identified sites, of which 103 have pore fluid evidence for authigenic carbonate precipitation and 147 do not. The output of the ANN was whether or not authigenic carbonate precipitation was occurring at each given site. The ANN achieved a 92% correct identification of the training database. This means that when the trained ANN is reapplied to the original training database it correctly identifies carbonate precipitation at 92% of the Sites. In order to assess the true validity of the model, however, cross-validation is required. Cross-validation is conducted by splitting the training database into a training and validation database using a 95:5 ratio. The ANN is then trained on the training database and tested on the validation database. This process is conducted 10 times and the average error determines the accuracy of the model. The average cross validation score was 80% accuracy. Although ideally this would be higher, the low grid spacing requires that a weighted average be taken of multiple sites in order to plot the distribution, which reduces the error. A global grid of the seven training variables (bathymetry, bottom water temperature, chlorophyll A, particulate organic carbon,

phosphate, nitrate and bottom water oxygen concentrations) at 1° resolution was then input to the ANN in order to calculate the areal extent of authigenic carbonate precipitation globally.

5.2.2 Application of an ANN to determine the microbial drivers for authigenic carbonate precipitation

A second ANN was then used to determine whether the authigenic carbonate precipitation occurring at a site was due to microbial sulfate reduction or AOM. The sites that had been previously been identified as locations of authigenic carbonate precipitation (103 of the 250 sites mentioned above) had to be linked to either microbial sulfate reduction or AOM. The microbial driver of authigenic carbonate precipitation could be identified by using a combined approach of examining the curvature of the sulfate concentration profile, the presence or absence of methane at the site, and the rate and magnitude of change in the calcium concentration profile. I decided to focus on these three criteria based on the results from the two sites reported in Chapter 4: At Site 1081, where the precipitation of carbonate was due to AOM, that there was a linear decrease in sulfate concentrations, with a concurrent rapid decrease in calcium concentrations to below 4mM and the presence of methane. At Site 1086 there was a gradual exponential decrease in sulfate concentration, with a concurrent drop in calcium concentration to 6mM. I also explored the sulfate concentration when the calcium concentration reached its minimum. Where sulfate concentrations were higher than 5mM when calcium was at its minimum, I linked this to authigenic carbonate precipitation due to microbial sulfate reduction. If carbonate precipitation is due to AOM, the calcium minima typically coincides with sulfate concentrations of <1mM as AOM is the depth where sulfate is consumed. A combination of these approaches led to my being able to classify all 103 sites originally identified into sites with authigenic carbonate formation driven by AOM or by microbial sulfate reduction (Figure 5.5, Table 5.2).

TABLE 5.2: PORE FLUID CHARACTERISTICS USED TO IDENTIFY AUTHIGENIC CARBONATE PRECIPITATION AS DUE TO AOM OR SULFATE REDUCTION.

AOM	Sulfate reduction
Linearly decreasing [SO_4] profile	Exponentially decreasing [SO_4] profile
[SO_4] at calcium minimum <5mM	[SO_4] at calcium minimum >5mM
CH_4 present below [SO_4] minima	No CH_4 present below [SO_4] minima

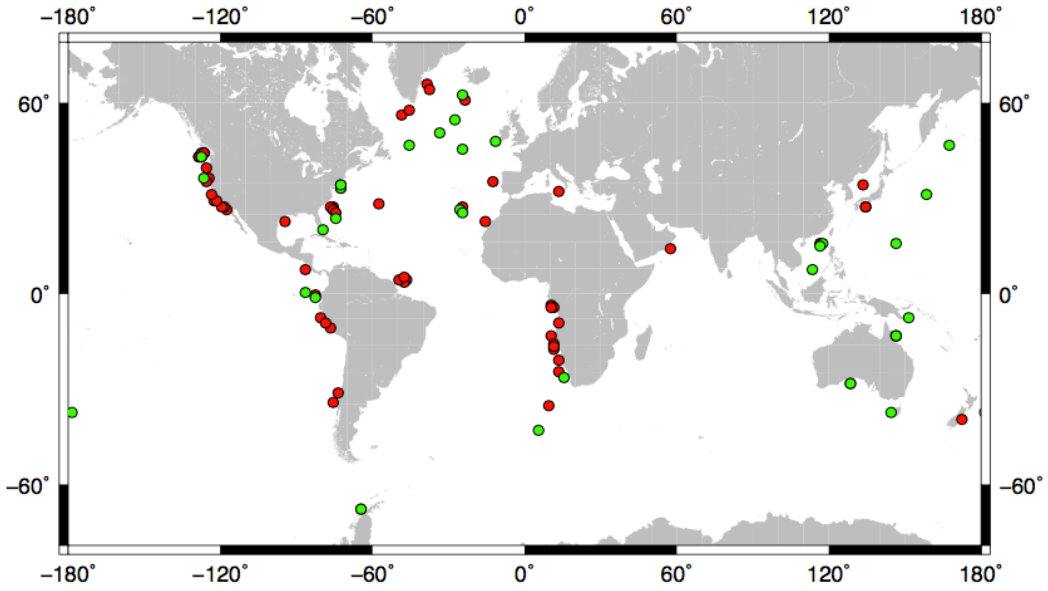

FIGURE 5.5: ODP SITES WHERE CARBONATE PRECIPITATION IS DRIVEN BY SULFATE REDUCTION (GREEN) OR AOM (RED).

The individual grid points that the first ANN predicted have authigenic carbonate precipitation were then input through the second neural network, which had been trained using the 103 ODP sites in which the carbonate precipitation had been defined as due to AOM or microbial sulfate reduction. A schematic of the second ANN is given in Figure 5.6.

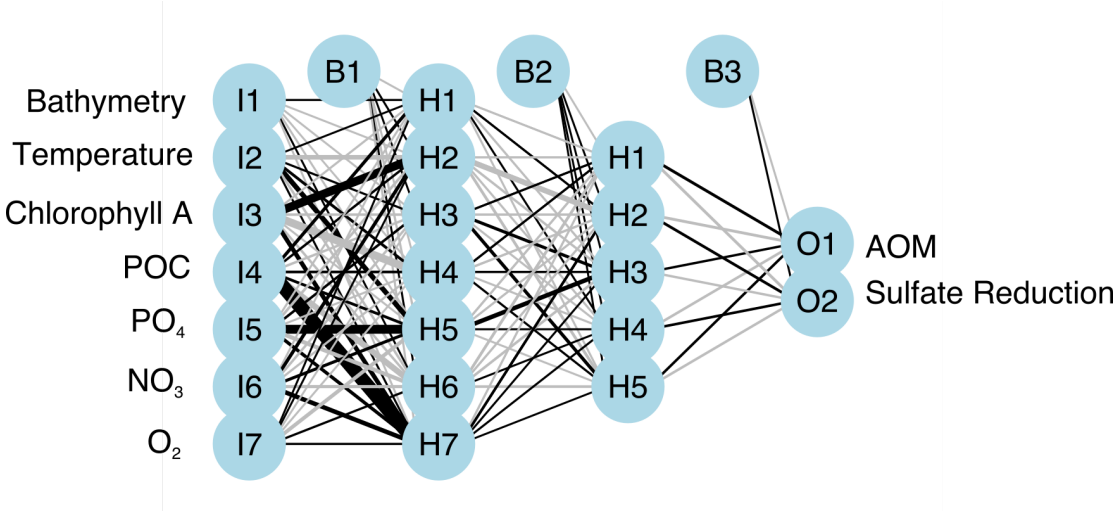

FIGURE 5.6: ANN USED TO DETERMINE WHETHER CARBONATE PRECIPITATION WAS DUE TO AOM OR SULFATE REDUCTION

The second ANN used to determine authigenic carbonate precipitation due to microbial sulfate reduction or AOM had a training accuracy of 94%, and a cross-validation score of 80%.

5.3 Results and discussion

In this section I will firstly discuss the distribution of authigenic carbonate precipitation predicted by the Artificial Neural Network, and how this compares to distribution determined by Sun and Turchyn (2014). I will secondly examine the distribution of the two microbial processes driving authigenic carbonate precipitation in the modern ocean and discuss the impact this has on a global budget for authigenic carbonate precipitation. Thirdly, I will determine whether the sites measured in Chapter 4 are representative. Fourthly, I will run a sensitivity analysis to study the impact that changing the input parameters can have on the predictions of the ANN before applying the ANN to a specific time period, the Miocene Climatic Optimum. Finally, I will discuss how temporal changes in the ocean major ion concentrations might have affected the saturation state of carbonate minerals and hence, the precipitation of authigenic carbonate.

5.3.1 Where does authigenic carbonate precipitation occur globally?

The first ANN predicted that in the modern ocean, 37% of the ocean floor has authigenic carbonate precipitating in the sediment using the methodology discussed in 5.2.1 (Figure 5.7). This ANN prediction provides an estimate for the areal extent of the ocean floor where there is active authigenic carbonate precipitation in the sediment. The distribution is plotted using a “nearest-neighbour” gridding algorithm, with a grid radius of 150km. The distribution of authigenic carbonate precipitation can be compared between the ANN and the inverse-weighted mean approach taken in Sun and Turchyn 2014 (Figures 5.7 and 5.8). Both methods predict a similar distribution of authigenic carbonate precipitation in the southern Atlantic Ocean, Indian Ocean and the west Pacific Ocean, although the ANN predicts a wider extent of authigenic carbonate precipitation in the Southern Ocean than in the inverse-weighted extrapolation (Figures 5.7 and 5.8).

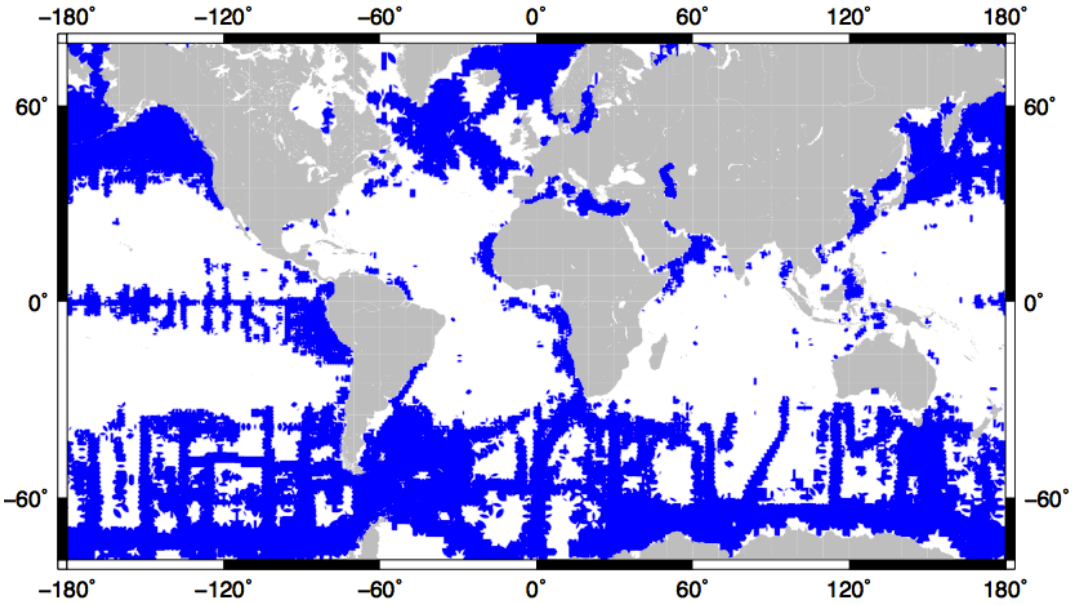

FIGURE 5.7: AREAL EXTENT OF AUTHIGENIC CARBONATE PRECIPITATION (IN BLUE) DETERMINED BY THE ANN.

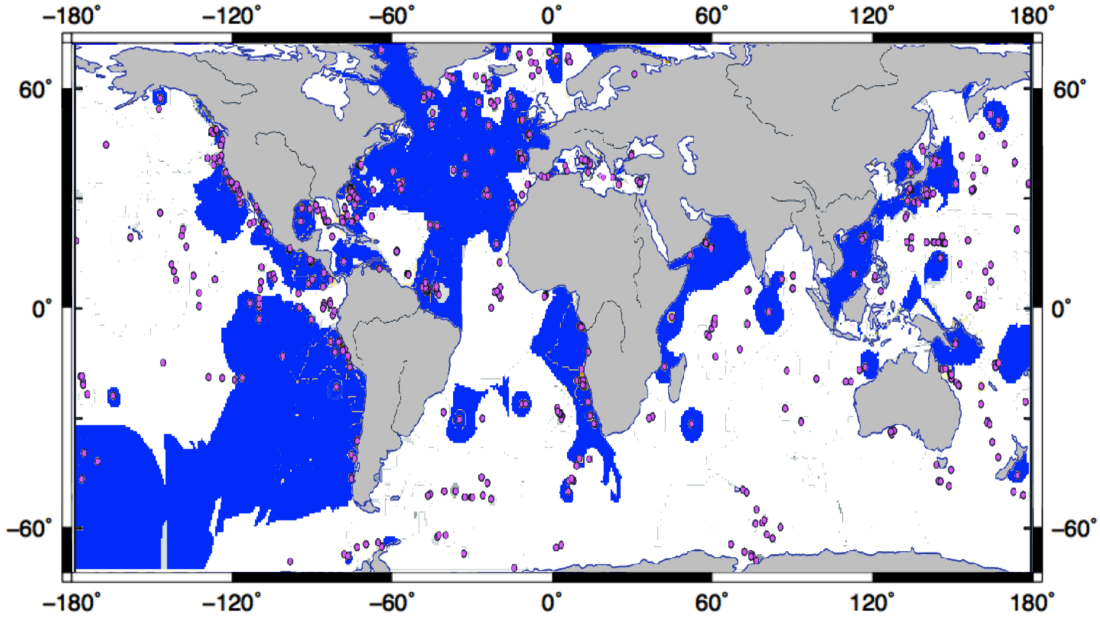

FIGURE 5.8: AUTHIGENIC CARBONATE PRECIPITATION AREAL EXTENT (IN BLUE) EXTRAPOLATED USING AN INVERSE DISTANCE WEIGHTING TECHNIQUE FROM 672 IODP SITES (SHOWN BY RED DOTS; SUN AND TURCHYN, 2014).

Understanding the areal extent of sediment where authigenic carbonate may be precipitating does not, however, give a rate for global authigenic carbonate precipitation. In order to estimate a global rate for authigenic carbonate precipitation the areal extent has to be combined with an understanding of the

flux of calcium into the sediment. Fick's first law (Equation 5.1) allows for the determination the flux of calcium into sediment due to authigenic carbonate precipitation. I used an average estimate of a decrease in calcium concentration from seawater to 5mM over the top 40m with a porosity of 0.8 in the sediment column. This gives an average flux of 1mM/m^2/year, which, when multiplied by the areal extent of authigenic carbonate precipitation determined by the ANN suggests the global flux of carbon due to authigenic carbonate precipitation is $1.4x10^{11}$mol/C/year ± $1x10^{11}$mol/C/year. The reason that this calculation is so unconstrained is that it is very inaccurate to make the assumptions of the change in calcium concentration and depth described. As such, it should be emphasized that this is a very rough calculation to allow me to take the areal extent of authigenic carbonate formation and calculate a useful rate for this process to consider against other estimates of the global flux of authigenic carbonate formation. Section 5.3.2 discusses how we can improve this estimation to make it more realistic on a global scale.

This estimation of the total global authigenic carbonate flux is almost an order of magnitude lower than the flux calculated by Sun and Turchyn (2014) - $1x10^{12}$mol/C/year. Their estimate took into account the flux of calcium at each individual site, which meant some sites had much higher rates of authigenic carbonate precipitation than others, which partially accounts for the lower flux calculated by my first estimate.

There are multiple estimates of marine calcium carbonate burial from production in the water column and deposition in sediments, but many are in the ballpark of $32x10^{12}$ moles C/year (Milliman, 1993; Lerman et al., 2007). The first back-of-the envelope authigenic carbonate precipitation rate suggests that authigenic carbonate precipitation would only be between 0.1-1% of the global total accumulation of carbonate.

5.3.2 Microbial drivers of authigenic carbonate precipitation

Having determined the global areal extent of authigenic carbonate precipitation, I then turn to figuring out what percentage of it is driven by

anaerobic methane oxidation and what percentage is through microbial sulfate reduction. It has previously been shown in Chapter 4 that microbial sulfate reduction and AOM lead to different rates of authigenic carbonate precipitation, likely linked to the fact that the two processes increase alkalinity in the pore fluids at different rates. My work suggests that the rate of authigenic carbonate precipitation occurring due to AOM is approximately 25 times higher than that due to microbial sulfate reduction at the sites I studied (although precipitation occurred over a greater depth when linked to microbial sulfate reduction).

As described in the methods, a second ANN was trained, using the sites determined to have AOM or microbial sulfate reduction. The modern global distribution of authigenic carbonate precipitation driven by AOM (red) and microbial sulfate reduction (green) is displayed in Figure 5.9. My results suggest that 47% of the authigenic carbonate precipitation in the modern ocean is driven by microbial sulfate reduction and 53% is driven by AOM.

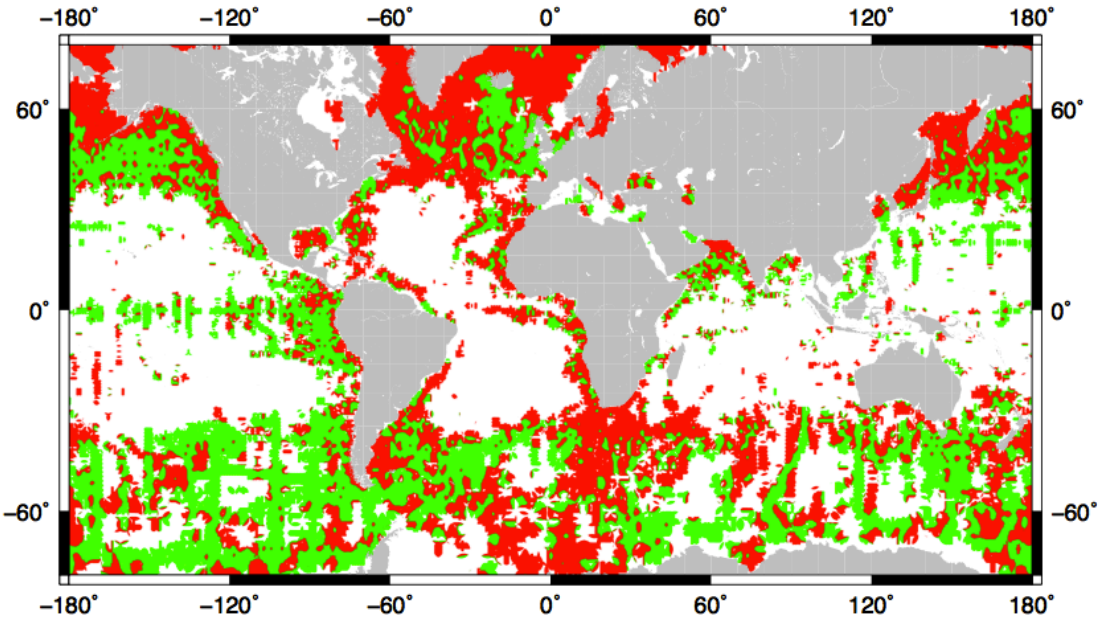

FIGURE 5.9: DISTRIBUTION OF CARBONATE PRECIPITATION IN THE MODERN OCEAN DUE TO AOM (RED) OR SULFATE REDUCTION (GREEN) AS DETERMINED BY THE ANN.

The authigenic carbonate precipitation driven AOM correlates with areas of high productivity, such as on the western coast of Africa and the Americas, where there is strong seasonal upwelling. The model suggests microbial

sulfate reduction drives authigenic carbonate precipitation in the Pacific Ocean, with a relatively equal distribution of authigenic carbonate precipitation driven by AOM and microbial sulfate reduction in the Southern Ocean.

Having determined a modelled global distribution of authigenic carbonate precipitation driven by AOM versus microbial sulfate reduction, I can now redo the back-of-the envelope calculation for the global flux of authigenic carbonate precipitation that I did with the first ANN where I just determined the areal extent of authigenic carbonate precipitation. For this, I use the depth and rate of authigenic carbonate precipitation as determined in Chapter 4, assuming that Site 1081 is a good representative for sediments that have authigenic carbonate precipitation driven by AOM and Site 1086 is a good representative for sediments that have authigenic carbonate precipitation driven by microbial sulfate reduction. With this assumption, microbial sulfate reduction gives a per-area flux of calcium into the sediment to make authigenic carbonate of 2mM/m^2/year whereas AOM sites have a calcium flux of 15mM/m^2/year. The estimate of the per-area precipitation due to microbial sulfate reduction compares favourably to a previously determined estimate for the calcium flux into the seafloor due to authigenic carbonate precipitation of between 0-10mM/m^2/year. The estimate of the per-area flux for AOM is higher (Sun and Turchyn, 2014).

These per-area rates can then be used to calculate a new estimate for the global amount of authigenic carbonate precipitation by multiplying the per-area rates by the areal extent of the two processes. The global flux is calculated from authigenic carbonate precipitation is 1.22×10^{12} moles/year. The global flux as calculated is of a similar magnitude to the Sun and Turchyn (2014) estimate of 1×10^{12} moles/year, and suggests that authigenic carbonate precipitation accounts for 4% of the global total accumulation of carbonate minerals in the modern ocean.

5.3.3 Are Sites 1081 and Sites 1086 globally representative?

One of the important considerations when extrapolating studies of a limited number of sites to global processes is whether or not the studied sites are globally representative. In order to assess this I compiled 10 sites in which AOM or sulfate reduction were identified (Figure 5.10). The sites where AOM is occurring are more and less similar: The average depth of the sulfate-methane transition zone is 30m; relative to 50m at Site 1081. The average calcium concentration at the sulfate-methane transition zone was 3.55mM, relative to 3.5mM at Site 1081. As such, Site 1081 appears to be representative of sites where authigenic carbonate mineral precipitation is due to the AOM. However, as can be seen in Figure 5.10, the sites where there is authigenic carbonate precipitation due to microbial sulfate reduction are more disparate.

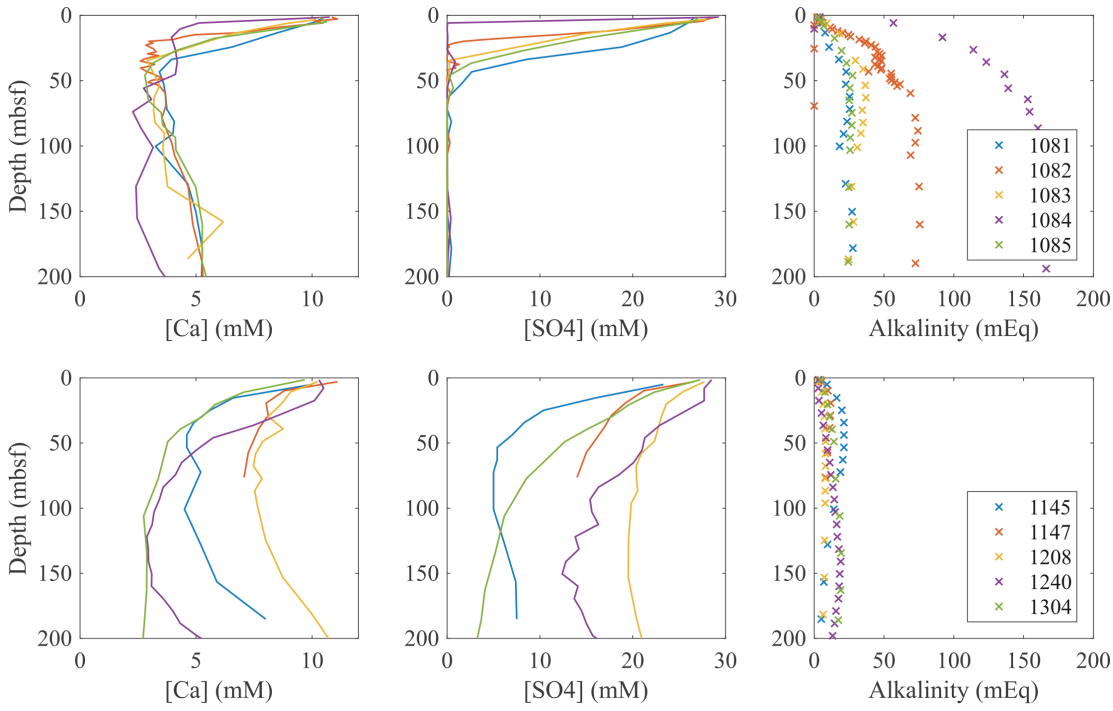

FIGURE 5.10: COMPARISON OF 5 REPRESENTATIVE SITES OF AOM (UPPER ROW) AND SULFATE REDUCTION (LOWER ROW).

Site 1086 appears to be a good first pass; however there would be significant benefit of completing a more significant modelling study, such as Chapter 4, on a wide variety of Sites where there is no AOM. Where there is no AOM occurring within the sediment (Figure 5.10, bottom row), there is much lower

alkalinity (up to 30mM) relative to the sites where AOM is occurring (30-170mM – Figure 5.10, top row). This accounts for the lower rates of authigenic carbonate precipitation, as the saturation state of the carbonate minerals will be lower, even if the pH is similar. The high alkalinity values at these sites are still unexplained, and require further study.

5.3.4 Carbon isotopic composition of the authigenic carbonate

The ANN allows me to determine that 88% of the authigenic carbonate precipitation is driven by AOM and 12% is caused by microbial sulfate reduction, which is reasonable due to the higher rates of authigenic carbonate precipitation observed during AOM. The carbon isotope composition of the authigenic carbonate created by microbial sulfate reduction versus AOM differs widely. In Chapter 4, I discussed how the authigenic carbonate that precipitated due to microbial sulfate reduction had a $\delta^{13}C$ of -4.5‰ assuming that there is a 1‰ fractionation of carbon isotopes during the precipitation of calcite (Romanek et al., 1992). However, during AOM, there is a lower $\delta^{13}C$ of the DIC in the pore fluids. At Site 1081 the minimum $\delta^{13}C$ of the DIC (-22‰) occurs in the sulfate-methane transition zone at 50mbsf. The average throughout the sulfate methane transition zone is around -20‰, similar to the average $\delta^{13}C$ of the ten sites shown below (Figure 5.11, left panel). This suggests that the precipitation of authigenic carbonates that occur within this zone will lead to carbonates minerals with a $\delta^{13}C$ of around -19‰. By multiplying the carbon isotopic composition of each process by the percentage that precipitates due to sulfate reduction and AOM the global $\delta^{13}C$ of the authigenic carbonate is -17‰.

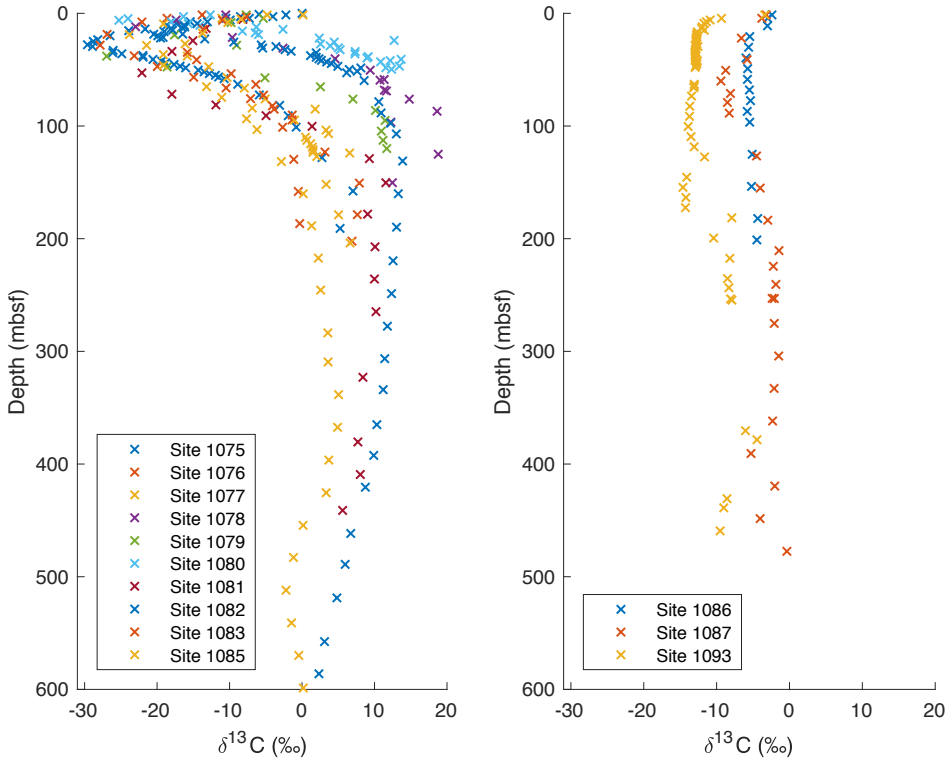

FIGURE 5.11: CARBON ISOTOPIC COMPOSITION OF THE DIC MEASURED AT SITES WHERE AOM IS OCCURING (LEFT PANEL), AND SITES WHERE AOM IS NOT OCCURING (RIGHT PANEL) (SIVAN ET AL., 2007).

5.3.5 Sensitivity analysis of the predictive capacity of the ANN

In order to explore the use of the ANN as a predictive tool for investigating authigenic carbonate formation, I tested how authigenic carbonate precipitation would change when there were changes in the conditions in the ocean that serve as training variables for the ANN. This also serves as a sensitivity analysis for the training variables for the ANN. A summary of the four scenarios I have explored and the modern values are displayed in Table 5.3.

TABLE 5.3: COMPARISON OF THE AREAL EXTENT OF AUTHIGENIC CARBONATE PRECIPITATION AND THE PROPORTION OF AOM AND SULFATE REDUCTION

Scenario	Areal extent of carbonate precipitation	AOM v. Sulfate Reduction
Modern	37%	47:53
Nutrients x5	51%	71:29
1/5th Oxygen	25%	55:45
Temp +10^{o}C	40%	48:52
Productivity x5	55%	62:38

The first scenario involves a 5x increase in nutrient concentrations (nitrate and phosphate) in the oceans surface (Figure 5.12).

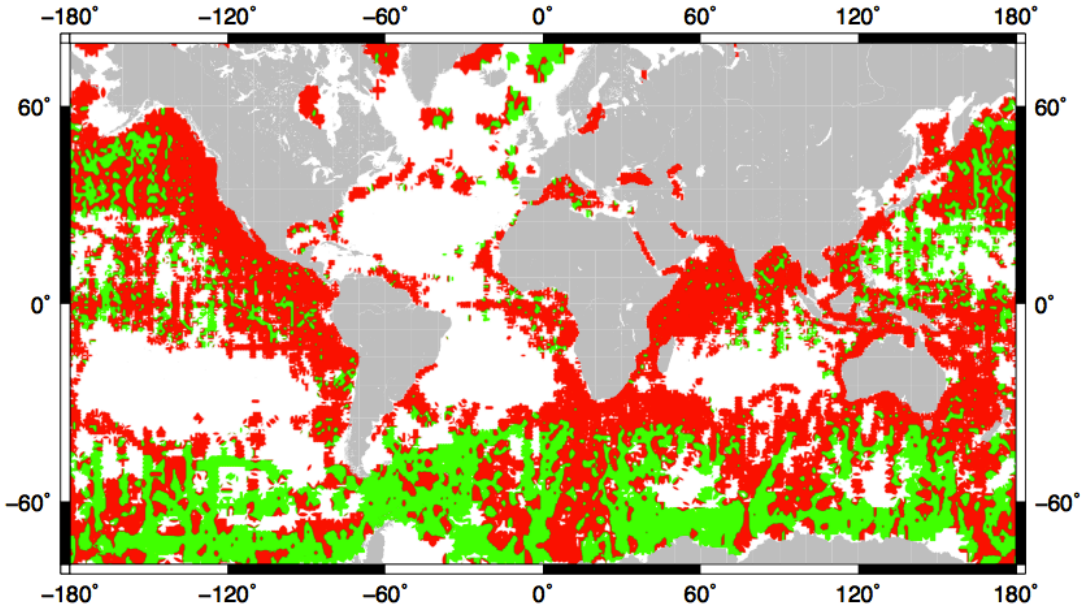

FIGURE 5.12: DISTRIBUTION OF AOM AND SULFATE REDUCTION WITH A FIVE-FOLD INCREASE IN THE SURFACE NUTRIENT CONCENTRATIONS

This should lead to far higher organic carbon production in the oceans. The areal extent over which authigenic carbonate precipitates increased from 37% to 51% of the seafloor, with much of the increase in carbonate precipitation

occurring in the Southern and Pacific Ocean. The northern Atlantic Ocean however sees a decrease in authigenic carbonate precipitation. This decrease is likely explained by the higher concentrations of nutrients causing the ANN to predict that the north Atlantic is similar to the modern Southern Ocean, where there is very little authigenic carbonate precipitation. The increase in nutrient concentrations also leads to an increase in the relative proportion of AOM to sulfate reduction to 71% AOM and 29% sulfate reduction. This is expected, as the higher nutrient concentrations should lead to higher production of organic carbon, and hence where there is a very high flux of organic carbon to the sediment AOM should dominate. The higher production of organic carbon also explains the increase in the areal extent of authigenic carbonate precipitation, as both sulfate reduction and AOM require organic carbon.

The second scenario involved decrease in the bottom-water oxygen concentrations to 1/5th of modern values (Figure 5.13).

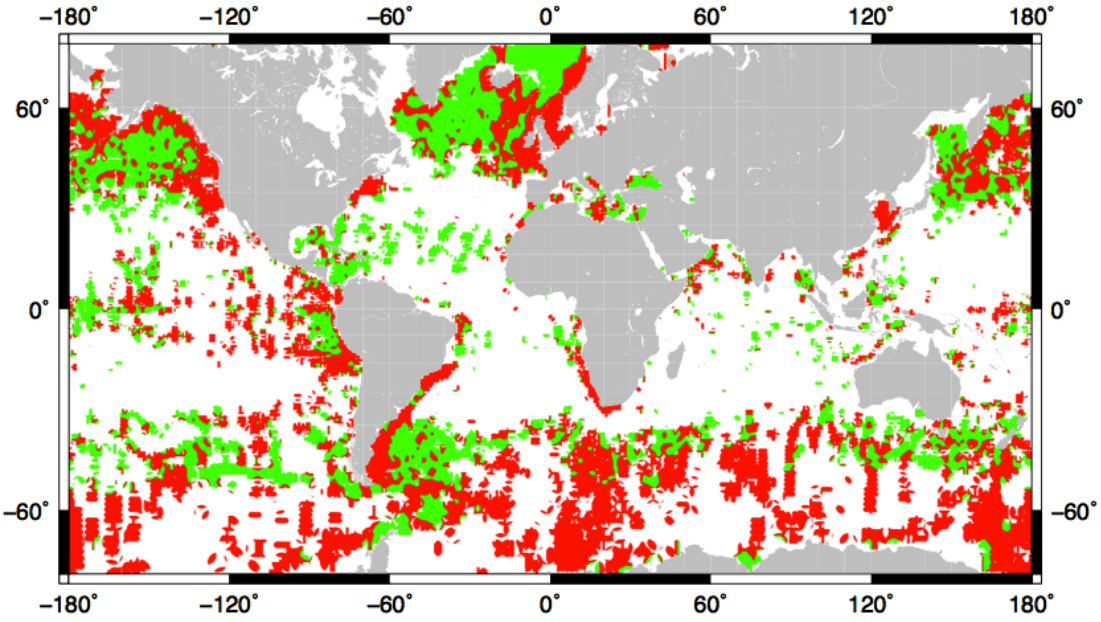

FIGURE 5.13: DISTRIBUTION OF AOM AND SULFATE REDUCTION WITH 1/5TH MODERN BOTTOM WATER OXYGEN CONCENTRATIONS.

The change in oxygen concentration in the bottom waters significantly affected the areal extent of authigenic carbonate precipitation, with a decrease down to 25% of the ocean floor. The relative proportions of AOM and sulfate

reduction are similar to modern values at 55% areal extent of AOM and 45% due to sulfate reduction. It should be noted that a decrease in the bottom water oxygen concentration in the ocean would normally be expected to increase the amount of organic matter that reaches the sea floor, and hence, to drive an increase in authigenic carbonate precipitation. It may be, that in the modern ocean, the sites where there is lower oxygen concentration in the bottom water are in the deep Pacific, where the model is trained that there is no authigenic carbonate precipitation. Hence, in this scenario the ANN is limited as in the modern ocean it appears that oxygen concentrations may not be significantly controlling authigenic carbonate precipitation. Instead, the low oxygen concentrations in the bottom waters correlate with other factors such as water depth, which limit the precipitation of authigenic carbonate, leading to the apparent relationship of lower oxygen concentrations decreasing authigenic carbonate precipitation.

The third scenario involved a 10°C global increase in bottom water temperatures, similar to early Cenozoic oceans (Figure 5.14).

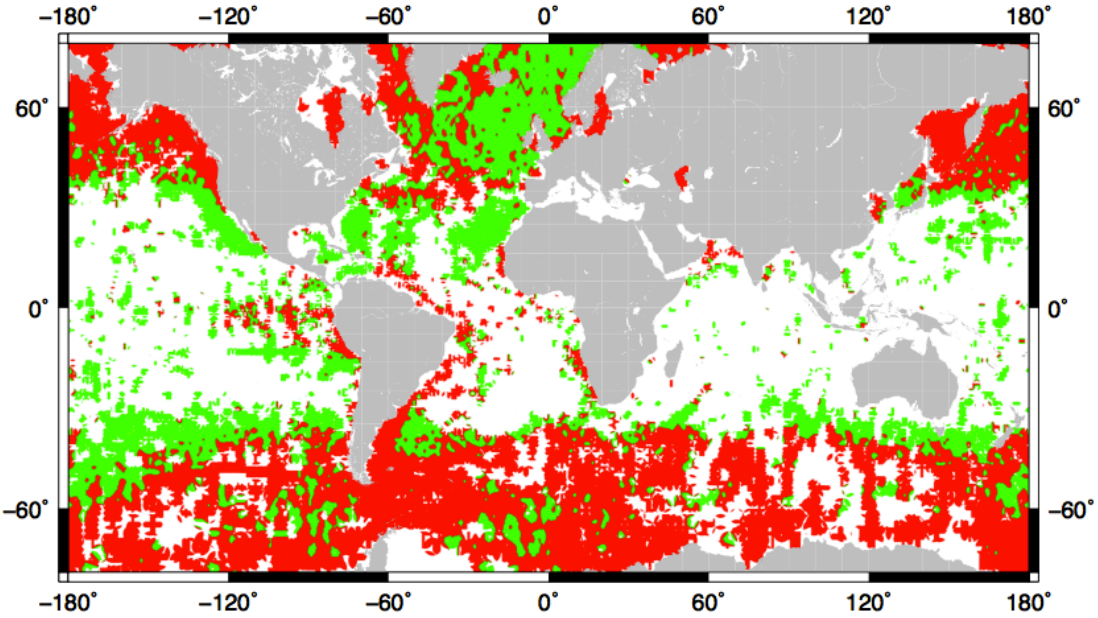

FIGURE 5.14: DISTRIBUTION OF AOM AND SULFATE REDUCTION WITH A 10°C INCREASE IN BOTTOM WATER TEMPERATURES

When I test this change in temperature, the ANN predicts that there is not a significant change in the proportion of authigenic carbonate precipitation driven by microbial sulfate versus AOM (48:52, versus 47:53 today) although the areal extent of authigenic carbonate with higher bottom water temperatures increases by 3% (Table 5.3). What I notice, however is the distribution of authigenic carbonate precipitation driven by AOM versus microbial sulfate reduction around the oceans is significantly different, with the largest changes in the North Atlantic, which switches mainly from AOM to microbial sulfate reduction, and the Southern Ocean, which switches from a mix of microbial sulfate reduction and AOM to almost entirely AOM. It should be noted that the change in temperature is just imposed independently on the neural network – the model does not consider the change in the saturation state of carbonate minerals that would also occur with increased temperature so it is certain that this is not an accurate calculation of the change in authigenic carbonate precipitation as a result of a change in global bottom water temperatures.

The final scenario was an increase in global chlorophyll concentrations in the surface ocean (Figure 5.15).

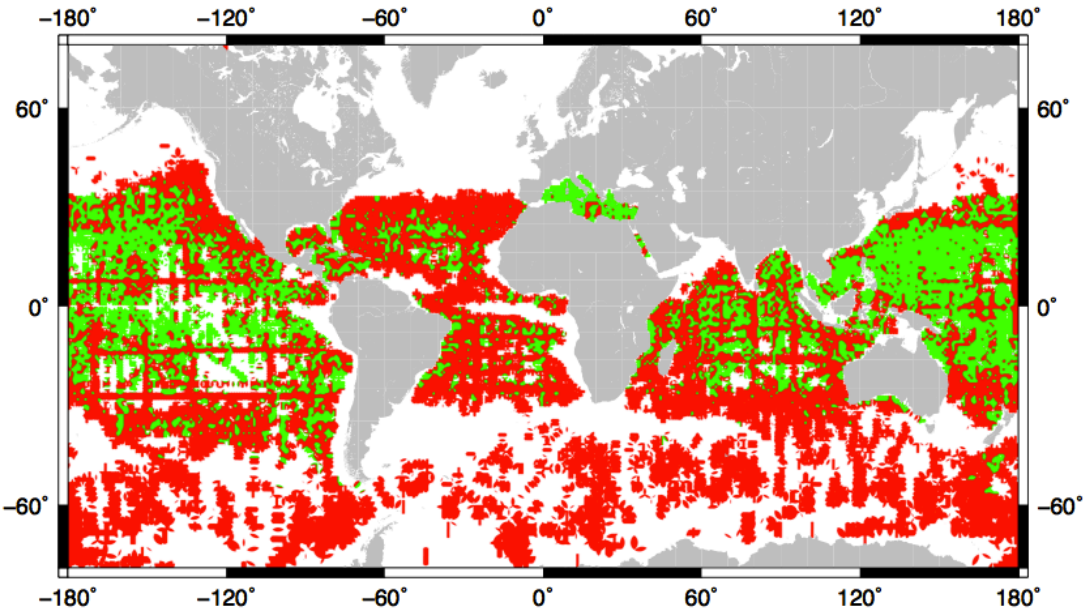

FIGURE 5.15: DISTRIBUTION OF AOM AND SULFATE REDUCTION WITH A FIVE-FOLD INCREASE IN SURFACE CHLOROPHYLL CONCENTRATIONS

This scenario led to the most significant change in the distribution of authigenic carbonate precipitation over the four scenarios. The significant increase in chlorophyll concentrations led to an increase in the areal extent of precipitation to 55%, however the distribution is almost the inverse of the modern day authigenic carbonate precipitation distribution, with no authigenic carbonate precipitation in the northern Atlantic Ocean or near the coasts. This scenario also shows the limitations of the ANN: where the chlorophyll concentrations were already high (such as the northern Atlantic Ocean, or off the west coast of Africa), the further increase in productivity reached concentrations where the ANN had been trained that there was no authigenic carbonate precipitation occurring. However, the sites where there was originally low productivity and no authigenic carbonate precipitation occurring reached the modern levels of productivity found in areas where there is authigenic carbonate precipitation occurring today, which led to the inverse distribution displayed.

5.3.6 Miocene case study

In order to test the predictive capacity of the ANNs, I applied them to a specific climate event where I could explore the functioning of the ANN: the middle Miocene Climatic Optimum (MCO), 15 million years ago. The MCO is thought to be the warmest period in the past 22 Ma, with mid-latitude warming of around 6^{o}C (Flower and Kennett, 1993). This period was characterised by with deep ocean temperatures around 5^{o}C warmer than modern (Lear et al., 2000; Zachos et al., 2001). The cause of the warming during the MCO has been debated, as has the link with atmospheric carbon dioxide. Estimates of pCO_2 range from almost twice modern values (700ppmv) to pre industrial levels (180ppmv) (Cerling et al., 1991; Pagani et al., 1999; Pearson and Palmer, 2000; Royer et al., 2001; Kürschner et al., 2008).

During the MCO there is a peak in the $\delta^{13}C$ recorded in carbonate minerals, leading to the suggestion of higher primary productivity and more organic carbon burial occurred at this interval (see introduction for the discussion of the carbon isotope mass balance). It was originally proposed that enhanced

organic matter burial along the Pacific margin could be used to explain the $\delta^{13}C$ peak, and the concurrent cooling of the planet after the MCO, as the burial of organic carbon removes carbon from the surface (Vincent and Berger, 1985). However, it has more recently been shown that the organic matter accumulation in the Pacific Margin (specifically the Monterey formation) is not high enough to be responsible for the global $\delta^{13}C$ excursion, and geochemical box models suggest that marine productivity changes leading to enhanced organic carbon burial are unlikely to be the cause of the $\delta^{13}C$ peak (Föllmi et al., 2005; Diester-Haass et al., 2009). As well as the long-term $\delta^{13}C$ peak there are also smaller positive excursions of benthic forminiferal $\delta^{13}C$, the so called carbonate isotope maxima, or "CM events" (Woodruff and Savin, 1991). The CM events are linked to the eccentricity cycle, which in turn has been coupled to organic matter burial (Pälike et al., 2006; Holbourn et al., 2007). Recent estimates of paleo-productivity during CM events, using the accumulation rate of benthic foraminiferal tests, are up to twice modern productivity (Diester-Haass et al., 2004; Diester-Haass et al., 2009; Diester-Haass et al., 2011; Diester-Haass et al., 2013).

I wanted to test whether changing the input parameters to match the Miocene seawater chemistry would have an effect on the precipitation of authigenic carbonate and the microbial processes controlling the precipitation. The advantage of the MCO over other periods is that the bathymetry and other geographical parameters are more or less the same. The input for the ANNs was compiled using 1.5 times modern ocean chlorophyll concentrations to mimic a 50% increase in productivity (to match the average paleo-productivity estimates discussed above) and a global increase in bottom water temperatures of 5 degrees (Lear et al., 2000) (Figure 5.16).

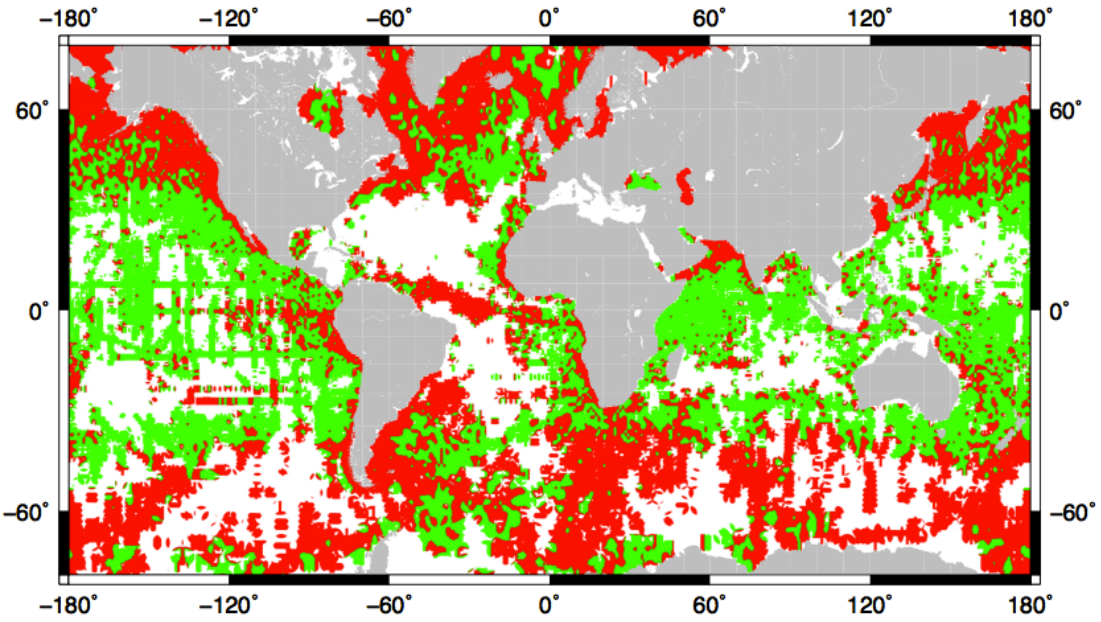

FIGURE 5.16: DISTRIBUTION OF AOM AND SULFATE REDUCTION WITH A 15^{O}C INCREASE IN BOTTOM WATER TEMPERATURES AND 1.5 TIMES CHLOROPHYLL A CONCENTRATIONS.

The distribution of AOM and microbial sulfate reduction does not change significantly with the Miocene parameters, however there is significantly more authigenic carbonate precipitation driven by microbial sulfate reduction occurring in the mid-latitudes. This leads to the balance of authigenic carbonate precipitation driven by microbial sulfate reduction versus AOM shifting to a ratio of 52:48, compared to 47:53 in the modern ocean. The increased productivity also leads to the prediction of a significant increase in the area over which authigenic carbonate precipitation occurs, as both microbial processes need a supply of organic carbon to produce the alkalinity required for authigenic carbonate precipitation. The areal extent of authigenic carbonate precipitation increased to 58% of the seafloor precipitating authigenic carbonate compared to 37% in the modern ocean. This is almost doubles the area of authigenic carbonate precipitation in the modern ocean, leading to a flux of carbon into the seafloor of $1.77*10^{12}$, which is 50% higher than our modern estimate. However, as the model is currently only forced using changes in productivity and temperatures a more complete global model including nutrient concentration changes due to continent arrangement would

need to be applied for a more constrained estimate of authigenic carbonate precipitation during the Miocene, and further into Earth's history.

5.3.7 Temporal variations in ocean chemistry

The ANN is trained using modern seawater major ion concentrations, so while the training of the neural network can be varied (e.g. chlorophyll, bottom water oxygen, etc), the other aspects of ocean chemistry, such as salinity, or concentration of various ions, are constant. This becomes an issue when applying the ANN to past oceans, as changes in the major ion balance of the ocean will impact the processes discussed throughout this seawater. The saturation index depends on the concentration of calcium in seawater (and therefore pore fluid) and the concentration of the carbonate ion. Both the concentration of seawater calcium and the total concentration of DIC and pH (and thus the carbonate ion concentration) certainly changed in the past. Furthermore, one of the major microbial processes discussed in this thesis that drives authigenic carbonate formation is microbial sulfate reduction, and sulfate concentrations in the ocean have also varied in the past.

Calcium has a long residence time in the ocean of ~1 Ma relative to an ocean mixing time of 1500 years (Broecker et al., 1982), and, as such, is responds only to significant variations in the calcium cycle. It has been proposed that the calcium concentration within seawater is currently the lowest it has been in the past 100 million years, although the concentration over Earth history is poorly constrained (Broecker et al., 1982; Opdyke and Wilkinson, 1988; Farkaš et al., 2007). Previous work on fluid inclusions in evaporite minerals has suggested there has been a decrease in calcium concentrations in seawater from 30mM to 10mM over the past 100 million years but the precise timing of this change is unclear (Kovalevich et al., 1998; Zimmermann, 2000; Lowenstein et al., 2001). When seawater calcium concentration increases, the amount of calcium available for pore fluid authigenic carbonate precipitation will necessarily increase as well. The higher the concentration of calcium in the pore fluid, the higher the overall saturation state of carbonate minerals in the sediment pile.

Sulfate concentrations in seawater have increased over the past 60 million years (Kurtz et al., 2003; Turchyn and Schrag, 2004). The lower sulfate concentrations in the past should have led to lower overall alkalinity generated within the pore fluid. Furthermore if there were lower sulfate concentrations in the past, all else being equal, more organic carbon would escape oxidation and be potentially converted into methane. More methane would lead to more overall sulfate being consumed by AOM. The lower alkalinity, and thus lower overall concentration of DIC, at the sulfate-methane transition zone would in theory decrease the carbonate mineral saturation state as the overall carbonate ion concentration would be much lower.

In order to examine the effect that the change in sulfate and calcium concentrations will have on the carbonate mineral saturation index, I created a simple sediment column model. Within the model the main driver for alkalinity generation is the reduction of sulfate, which occurs as an exponential decay from seawater concentrations to 0. The pH is modelled to converge towards the steady state values for microbial sulfate reduction (6.7) and AOM (7.9) as previously discussed (Soetaert et al., 2007).

The temperature and pressure within the sediment column also impact the saturation index of carbonate minerals within the sediment. To determine the saturation index, the temperature within the sediment column was defined to follow the average temperature gradient of 207 IODP sites determined using least squares linear fit (Malinverno and Martinez, 2015). The pressure is defined as the depth in metres below the sediment plus 800m to simulate a sediment column at 800m water depth, similar to the measured sites in Chapter 4. Then the stoichiometric solubility product (Ksp*) of calcite, with its pressure and temperature dependence, was calculated following (Mucci, 1983) and the carbonate equilibrium was calculated using Csys package in Matlab (Zeebe and Wolf-Gladrow, 2001).

I have conducted sensitivity analyses for both the sulfate and calcium concentrations to show the proposed effect that changing the concentration may have on the saturation index of calcite (Figures 5.17 and 5.18).

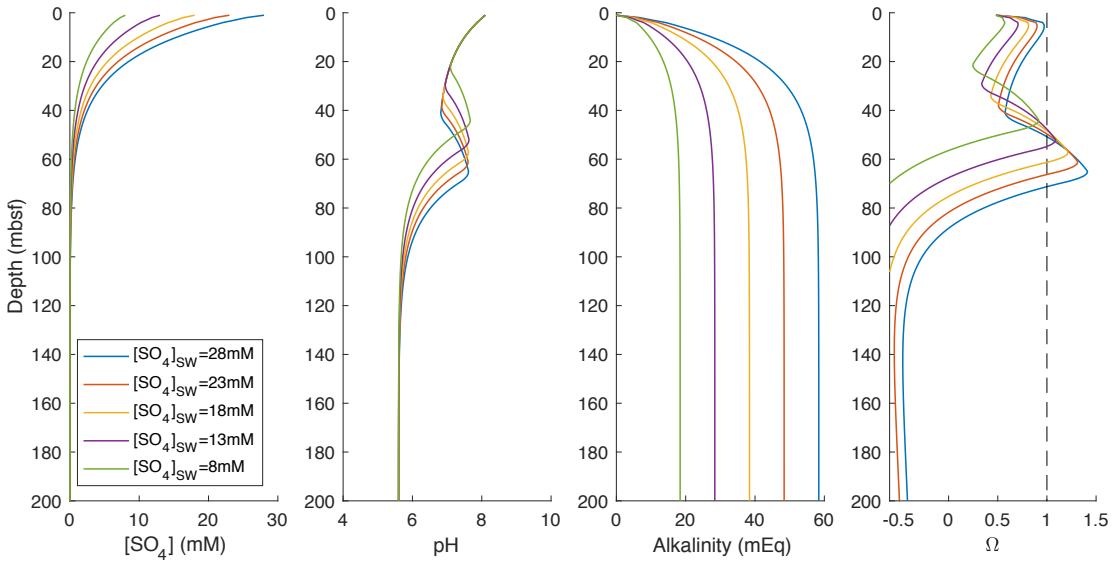

FIGURE 5.17: SATURATION INDEX (Ω) OF PORE FLUID WITH CHANGES IN THE SULFATE CONCENTRATION OF SEAWATER DURING SULFATE REDUCTION AND AOM

Figure 5.17 suggests that when the concentration of marine sulfate is lower, the AOM zone shifts higher in the sediment. When marine sulfate concentrations are below 13mM, the pore fluid no longer reaches saturation with respect to calcium carbonate, suggesting there would be minimal sedimentary precipitation.

In Figure 5.18, the saturation index of calcite is shown to increase with increasing calcium concentration in seawater.

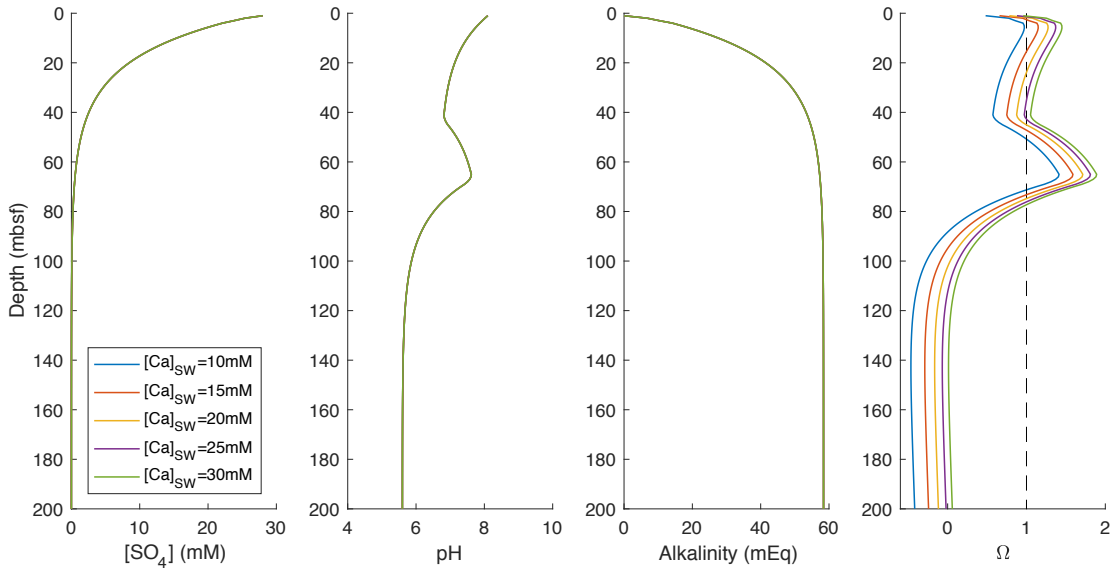

FIGURE 5.18: SATURATION INDEX (Ω) OF PORE FLUID WITH CHANGES IN THE CALCIUM CONCENTRATION OF SEAWATER DURING SULFATE REDUCTION AND AOM

The combined effect that the decrease in seawater sulfate concentrations to 22mM and increase in calcium concentrations to 15mM, similar to hypothesised global ocean chemistry during the Mid-Miocene, would have had on the saturation state of calcite within the sediment is shown in Figure 5.19.

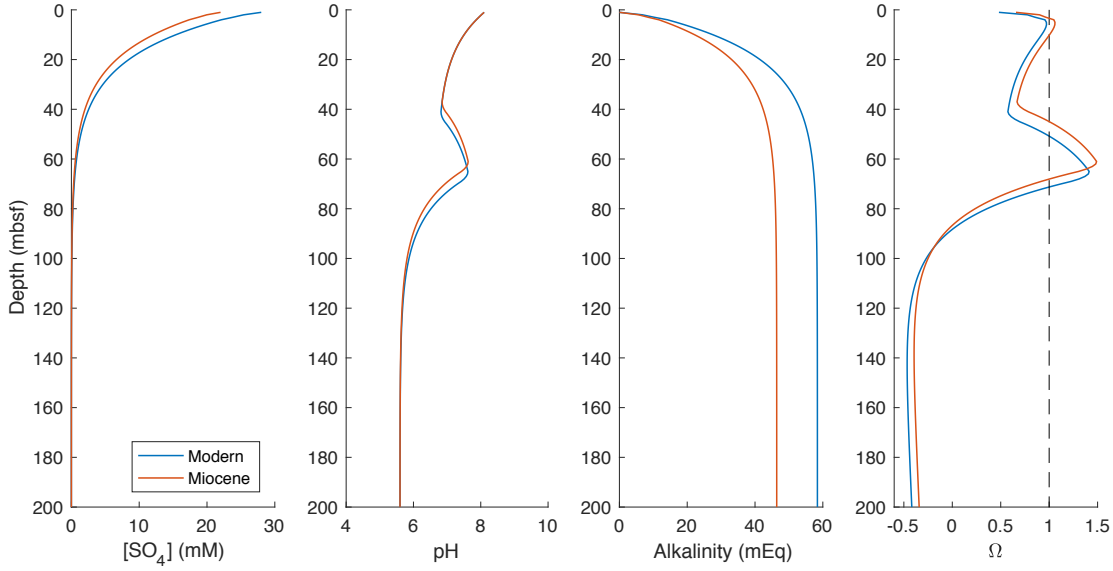

FIGURE 5.19: SATURATION INDEX (Ω) OF PORE FLUID DERIVED FROM MODERN AND MIOCENE SEAWATER DURING SULFATE REDUCTION AND AOM

The combination of the lower sulfate concentrations and higher calcium concentrations suggests that there would have been a higher calcite

saturation state during AOM in the Mid-Miocene relative to modern AOM. Hence, the ANN approach to authigenic carbonate precipitation described above is valid, and the 50% increase in authigenic carbonate precipitation could be even higher when ocean chemistry changes are accounted for.

5.4 Conclusions

During this chapter, I have shown that the understanding gained into the precipitation of authigenic carbonate at Sites 1081 and 1086 can be applied to further the understanding of authigenic carbonate precipitation on a global scale. This has been achieved by the use of Artificial Neural Networks to predict the location of the precipitation of authigenic carbonate, and to link the precipitation with the microbial process of either microbial sulfate reduction or the Anaerobic Oxidation of Methane. By mapping the global distribution of sulfate reduction and AOM an estimate of the flux of carbon due to the precipitation of authigenic carbonate can be made, which is $1.22*10^{12}$g of carbon per year. This makes up ~4% of the estimated global carbon deposition of the $32x10^{12}$ moles/year. In the Miocene using simple changes in ocean productivity and temperature, the ANNs predict that authigenic carbonate precipitation would be 50% higher, and would make up almost 10% of modern carbon deposition on the sea floor. This application of the ANN approach to mapping global distribution of authigenic carbonate precipitation shows the potential for future applications of this novel tool.

CHAPTER 6

CONCLUSIONS

In this thesis, I have explored the application of calcium isotopes to the carbon cycle from the smaller scale (lacustrine settings and regional climate), through to sedimentary systems, and to the global scale in understanding the rate and global extent of authigenic carbonate deposition. Authigenic carbonate precipitates from bicarbonate that is released during the oxidation of organic matter from the sediment-water interface to hundreds of meters below the seafloor. In the latter part of this thesis, I have looked at how the carbon isotopic composition of authigenic carbonate can vary during its formation. These various projects are linked together in order to determine the effect that variations in the amount of authigenic carbonate formation can have on the $\delta^{13}C$ of marine carbonate and thus the impact of authigenic carbonate formation on our interpretation of the past carbon cycle.

In the hypothesis put forward by Schrag et al. (2013) exploring the role that an expanding the authigenic carbonate sink might have on the global carbon cycle, the suggestion was that as authigenic carbonate precipitation increases, the $\delta^{13}C$ of the ocean will increase, as more ^{12}C-enriched carbon is removed from the ocean during authigenic carbonate precipitation. In their model, the suggestion was that for a $\delta^{13}C$ of marine DIC that is +5‰ comparable to the modern value (Swart and Eberli, 2005), and thus marine carbonate is +5‰, this could be achieved either through a fractional organic carbon burial that is 40% or a modern fractional organic carbon burial of 20% with a fraction of authigenic carbonate burial that is between 29-37%. Their model was predicated on the $\delta^{13}C$ of authigenic carbonate being between -15 and -20‰.

Most of the authigenic carbonate that precipitates in the modern ocean is formed from the anaerobic oxidation of methane, my modelling work suggests this could be as much as 90% of the total sedimentary carbonate formation in

deep sea sediments. During this formation the organic matter ($\delta^{13}C$ = ~-25‰) is converted first into methane ($\delta^{13}C$ = ~-50‰) leaving a pool of ^{13}C enriched DIC within pore fluid, and then this methane is oxidized, mixing with standard pore fluid DIC, and converted into authigenic carbonate with a carbon isotope ratio of around -19‰. We can consider the implications of this in several ways. A mass balance of carbon isotopes in sedimentary systems requires that if all the carbon deposited at the sediment-water interface is ultimately buried, then the bulk $\delta^{13}C$ of what is removed is the same as what is deposited. From the perspective of the burial of electrons, clearly whether the carbon is buried in reduced or oxidized form matters, but from a global carbon isotope mass balance perspective, it matters less so. Thus, if the formation of authigenic carbonate is to impact the global carbon cycle and the $\delta^{13}C$ of the global ocean and marine carbonate, as suggested by Higgins et al. (2009) and Schrag et al (2013), some of the oxidized carbon, or methane, must escape the sediment pile and return to the overlying ocean.

If sedimentary organic matter (-25‰) is oxidised and converted into sedimentary authigenic carbonate (-20‰), there must be also be the release of ^{12}C-enriched carbon to somewhere else in the system. This is because the $\delta^{13}C$ of organic matter is more enriched in ^{12}C than pore fluid DIC or than any modern authigenic carbonate. In theory, the ^{12}C-enriched carbon should diffuse (either as DIC or as methane) into the base of the ocean as alkalinity; the methane will presumably be oxidized along the way or at the sediment-water interface. Therefore, if there is an increase in the flux of organic matter to the seafloor, there should be an increase in the flux of ^{12}C-enriched alkalinity from the seafloor into the oceans unless all organic matter deposited is buried or all oxidized organic matter is trapped as authigenic carbonate in marine sediments. Both of these end member scenarios are unlikely; organic matter will be oxidized as long as it is chemical possible in sediments, and there are very few places where there is no net flux of alkalinity out of marine sediments; that is there is never enough calcium to precipitate all the DIC in modern marine sediments (Figure 6.1).

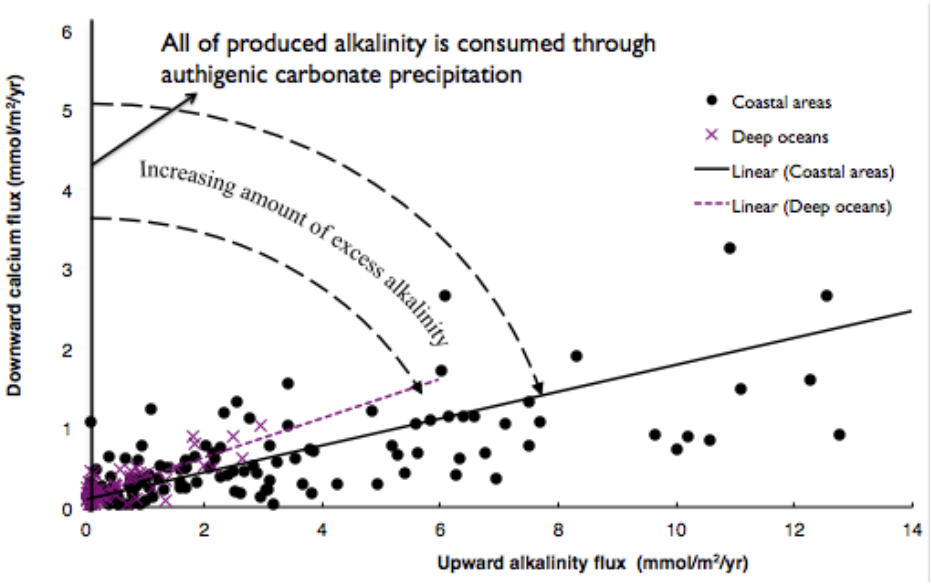

FIGURE 6.1: FLUX OF CALCIUM INTO THE SEDIMENTS DUE TO AUTHIGENIC CARBONATE PRECIPITATION VERSUS THE FLUX OF ALKALINITY OUT OF THE SEDIMENT (REDRAWN FROM SUN AND TURCHYN, 2014)

Therefore, an interesting way to consider the impact of the authigenic carbonate flux is to consider what impacts the flux of alkalinity from marine sediments back into the overlying ocean. Any increased flux of ^{12}C-enriched alkalinity from the sea floor would reduce the $\delta^{13}C$ of the oceans, and leading to a negative excursion in the $\delta^{13}C$ of seawater. There are many possible factors that can influence the flux of alkalinity from the sediment to seafloor. These include the calcium concentration and saturation state of carbonate minerals within the sediment pile, permeability and porosity of the sediment, and the availability of electron acceptors to fuel the microbial deep biosphere.

In the Miocene case study described at the end of Chapter 5, I suggested that during the CM intervals there would have been more global authigenic carbonate precipitation, linked to the increased productivity and higher calcium concentrations in seawater. This suggests that there would have been a decrease in the flux of ^{12}C-enriched alkalinity from the seafloor, due to the increased precipitation of authigenic carbonate, which could have been partially responsible for the increase in the $\delta^{13}C$ observed during CM events.

The simple mass balance described above makes the assumption that all of the organic carbon is oxidised, and that not all of the DIC produced is

precipitated as authigenic carbonate. The other controlling factor in the volume of authigenic carbonate precipitation, and the amount of DIC that will escape from the sediments, is the calcium concentrations in the pore fluid. When the calcium concentration is higher the saturation state of calcium carbonate will be higher, and hence, the more of the alkalinity that is produced during the reduction of organic matter will be consumed (Chapter 5).

This suggests that the calcium concentration within seawater could have a long-term effect on the global carbon cycle as interpreted through the global $\delta^{13}C$ of marine carbonates. When the calcium concentrations in seawater are higher, there will be a lower flux of ^{12}C-enriched alkalinity into the oceans, and hence, all else being equal, the $\delta^{13}C$ of the oceans would be higher. When marine calcium concentrations are lower then there will be a higher flux of ^{12}C-enriched alkalinity from the seafloor due to the lower saturation state of calcium carbonate, leading to the $\delta^{13}C$ of the oceans being lower. Unfortunately, a firm control on changes in the calcium concentration of the ocean over time is enigmatic.

Although provocative, I suggest that some variations in the global carbon cycle in the past can be explore by linking marine calcium concentrations to authigenic carbonate formation and the flux of alkalinity from the seafloor (Figure 6.2; Veizer et al., 1999; Lowenstein et al., 2001).

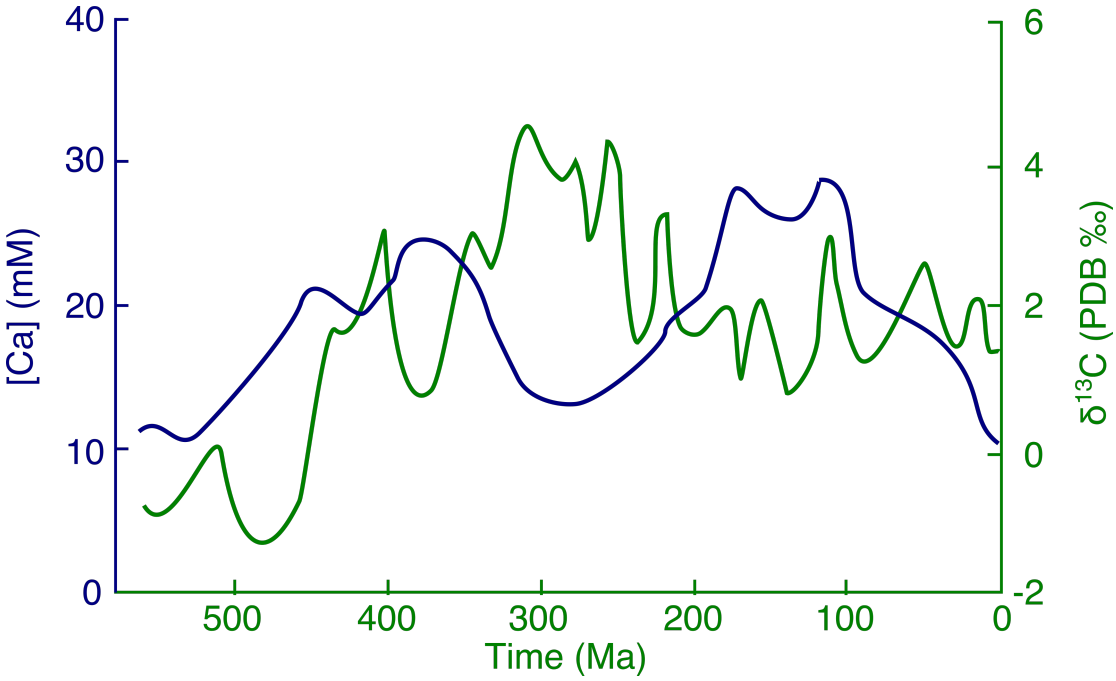

FIGURE 6.2: $\delta^{13}C$ OF SEAWATER THROUGH THE PHANEROZOIC (GREEN, VEIZER ET AL., 1999) COMPARED TO THE CALCIUM CONCENTRATION OF SEAWATER (BLUE, LOWENSTEIN ET AL., 2001)

There is potential co-variation between the calcium concentration and $\delta^{13}C$ between 400 and 150Ma. This would fit with my theory that the higher the calcium concentration within the pore fluid, the lower the flux of ^{12}C-enriched alkalinity that escapes from the sediments, and the higher the overall $\delta^{13}C$. However, over much of the Phanerozoic record, there is a decoupling of the calcium and the carbon isotopes (Veizer et al., 1999). This is likely because the system isn't as simple and there are multiple controls on the $\delta^{13}C$ of the ocean, including the much interpreted evolution of land plants in the late Palaeozoic, as well as changes in the fractional organic carbon burial, the standard interpretation of the paleo-$\delta^{13}C$ record. Furthermore, there are changes in marine sulfate concentrations, which my work suggests will play a large role in the saturation state of calcium carbonate minerals within the sediments independent of calcium concentrations (Figure 6.3). However, further research would be needed to apply it on a global scale temporally.

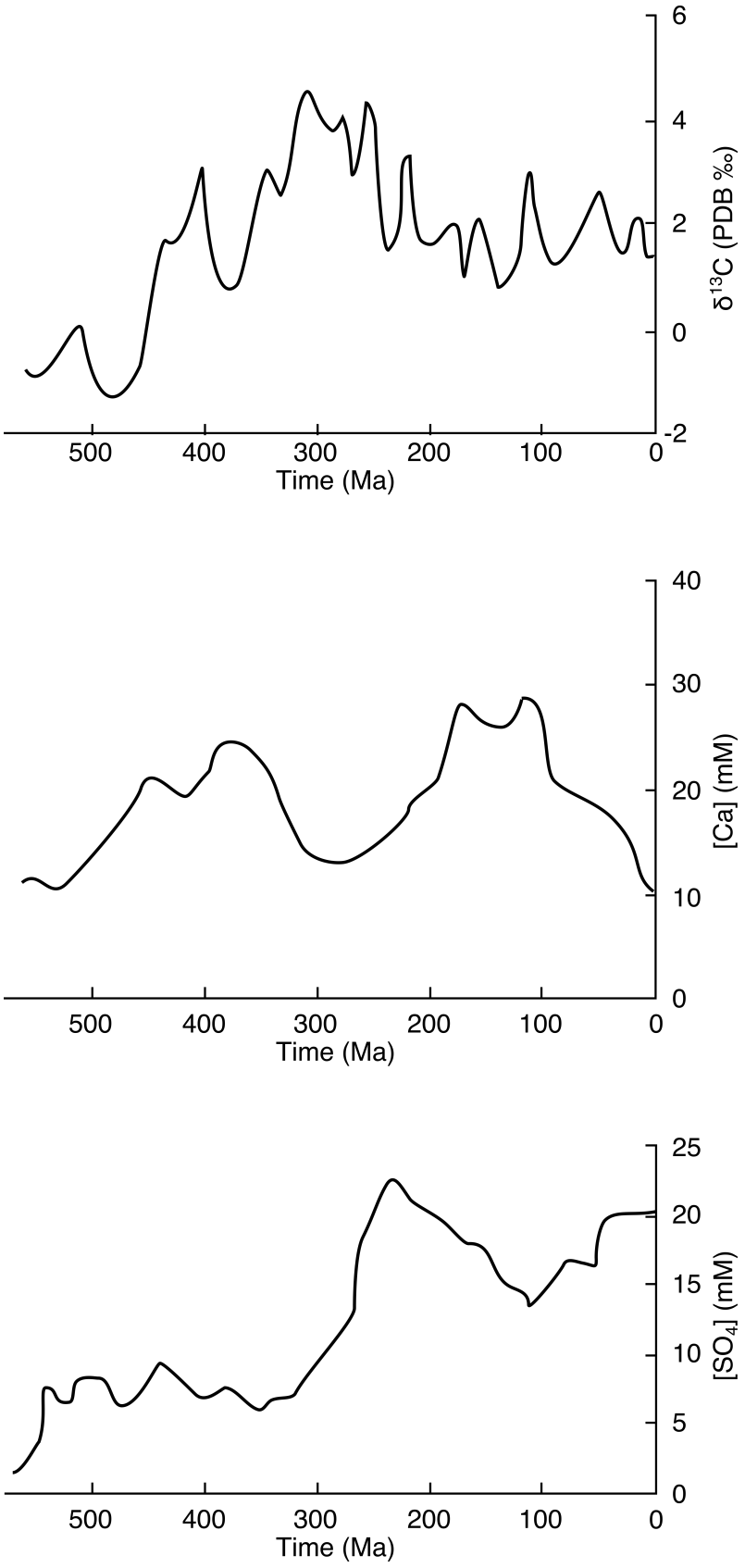

FIGURE 6.3: VARITATIONS IN THE $\delta^{13}C$, CALCIUM CONCENTRATION AND SULFATE CONCENTRATION IN SEAWATER THROUGH THE PHANEROZOIC (VEIZER ET AL., 1999; LOWENSTEIN ET AL., 2001; ALGEO ET AL., 2015)

BIBLIOGRAPHY

Abdollahi H. and Wimpenny J. W. T. (1990) Effects of oxygen on the growth of Desulfovibrio desulfuricans. *J Gen Microbiol* **136**, 1025–1030.

Affek H. P., Bar-Matthews M., Ayalon A., Matthews A. and Eiler J. M. (2008) Glacial/interglacial temperature variations in Soreq cave speleothems as recorded by 'clumped isotope' thermometry. *Geochimica et Cosmochimica Acta* **72**, 5351–5360.

Algeo T. J., Luo G. M., Song H. Y., Lyons T. W. and Canfield D. E. (2015) Reconstruction of secular variation in seawater sulfate concentrations. *Biogeosciences* **12**, 2131–2151.

AlKhatib M. and Eisenhauer A. (2016) Calcium and Strontium Isotope Fractionation in Aqueous Solutions as a Function of Temperature and Reaction Rate; I. Calcite. *Geochimica et Cosmochimica Acta*. Available at: http://www.sciencedirect.com/science/article/pii/S0016703716305609 [Accessed October 13, 2016].

Aller R. C. and Rude P. D. (1988) Complete oxidation of solid phase sulfides by manganese and bacteria in anoxic marine sediments. *Geochimica et Cosmochimica Acta* **52**, 751–765.

Andersen K. K., Azuma N., Barnola J.-M., Bigler M., Biscaye P., Caillon N., Chappellaz J., Clausen H. B., Dahl-Jensen D., Fischer H., Flückiger J., Fritzsche D., Fujii Y., Goto-Azuma K., Grønvold K., Gundestrup N. S., Hansson M., Huber C., Hvidberg C. S., Johnsen S. J., Jonsell U., Jouzel J., Kipfstuhl S., Landais A., Leuenberger M., Lorrain R., Masson-Delmotte V., Miller H., Motoyama H., Narita H., Popp T., Rasmussen S. O., Raynaud D., Rothlisberger R., Ruth U., Samyn D., Schwander J., Shoji H., Siggard-Andersen M.-L., Steffensen J. P., Stocker T., Sveinbjörnsdóttir A. E., Svensson A., Takata M., Tison J.-L., Thorsteinsson T., Watanabe O., Wilhelms F. and White J. W. C. (2004) High-resolution record of Northern Hemisphere climate extending into the last interglacial period. *Nature* **431**, 147–151.

Anderson D. M., Mauk E. M., Wahl E. R., Morrill C., Wagner A. J., Easterling D. and Rutishauser T. (2013) Global warming in an independent record of the past 130 years. *Geophys. Res. Lett.* **40**, 189–193.

Anderson L. D., Delaney M. L. and Faul K. L. (2001) Carbon to phosphorus ratios in sediments: Implications for nutrient cycling. *Global Biogeochem. Cycles* **15**, 65–79.

Antler G., Turchyn A. V., Herut B., Davies A., Rennie V. C. F. and Sivan O. (2014) Sulfur and oxygen isotope tracing of sulfate driven anaerobic

methane oxidation in estuarine sediments. *Estuarine, Coastal and Shelf Science* **142**, 4–11.

Arndt S., Brumsack H.-J. and Wirtz K. W. (2006) Cretaceous black shales as active bioreactors: A biogeochemical model for the deep biosphere encountered during ODP Leg 207 (Demerara Rise). *Geochimica et Cosmochimica Acta* **70**, 408–425.

Arndt S., Hetzel A. and Brumsack H.-J. (2009) Evolution of organic matter degradation in Cretaceous black shales inferred from authigenic barite: A reaction-transport model. *Geochimica et Cosmochimica Acta* **73**, 2000–2022.

Arndt S., Jørgensen B. B., LaRowe D. E., Middelburg J. J., Pancost R. D. and Regnier P. (2013) Quantifying the degradation of organic matter in marine sediments: A review and synthesis. *Earth-Science Reviews* **123**, 53–86.

Arz H. W., Lamy F., Pätzold J., Müller P. J. and Prins M. (2003) Mediterranean Moisture Source for an Early-Holocene Humid Period in the Northern Red Sea. *Science* **300**, 118–121.

Ayalon A., Bar-Matthews M. and Kaufman A. (2002) Climatic conditions during marine oxygen isotope stage 6 in the eastern Mediterranean region from the isotopic composition of speleothems of Soreq Cave, Israel. *Geology* **30**, 303–306.

Baker P. A., Gieskes J. M. and Elderfield H. (1982) Diagenesis of Carbonates in Deep-Sea Sediments--Evidence From SR/CA Ratios and Interstitial Dissolved SR2+ Data. *Journal of Sedimentary Research* **52**. Available at: http://archives.datapages.com/data/sepm/journals/v51-54/data/052/052001/0071.htm [Accessed March 23, 2016].

Barkan E., Luz B. and Lazar B. (2001) Dynamics of the carbon dioxide system in the Dead Sea. *Geochimica et Cosmochimica Acta* **65**, 355–368.

Bar-Matthews M., Ayalon A., Gilmour M., Matthews A. and Hawkesworth C. J. (2003) Sea–land oxygen isotopic relationships from planktonic foraminifera and speleothems in the Eastern Mediterranean region and their implication for paleorainfall during interglacial intervals. *Geochimica et Cosmochimica Acta* **67**, 3181–3199.

Bar-Matthews M., Ayalon A. and Kaufman A. (1997) Late Quaternary Paleoclimate in the Eastern Mediterranean Region from Stable Isotope Analysis of Speleothems at Soreq Cave, Israel. *Quaternary Research* **47**, 155–168.

Bar-Matthews M., Ayalon A. and Kaufman A. (2000) Timing and hydrological conditions of Sapropel events in the Eastern Mediterranean, as evident

from speleothems, Soreq cave, Israel. *Chemical Geology* **169**, 145–156.

Barnes R. O. and Goldberg E. D. (1976) Methane production and consumption in anoxic marine sediments. *Geology* **4**, 297–300.

Bartov Y., Goldstein S. L., Stein M. and Enzel Y. (2003) Catastrophic arid episodes in the Eastern Mediterranean linked with the North Atlantic Heinrich events. *Geology* **31**, 439–442.

Bartov Y., Stein M., Enzel Y., Agnon A. and Reches Z. (2002) Lake Levels and Sequence Stratigraphy of Lake Lisan, the Late Pleistocene Precursor of the Dead Sea. *Quaternary Research* **57**, 9–21.

Begin Z. B., Ehrlich A. and Nathan Y. (1974) Lake Lisan: the Pleistocene precursor of the Dead Sea. *Minisrey of Commerce and Industry, Geological Survey*.

Berger W. H., Lange C. B. and Pérez M. E. (2002) The early Matuyama Diatom Maximum off SW Africa: a conceptual model. *Marine Geology* **180**, 105–116.

Berger W. H. and Wefer G. (2002) On the reconstruction of upwelling history: Namibia upwelling in context. *Marine Geology* **180**, 3–28.

Berger W. H., Wefer G., Richter C., Lange C. B., Giraudeau J., Hermelin O. and Party S. S. (1998) 17. THE ANGOLA-BENGUELA UPWELLING SYSTEM: PALEOCEANOGRAPHIC SYNTHESIS OF SHIPBOARD RESULTS FROM LEG 1751. In *Proceedings Ocean Drilling Program, Initial Reports* pp. 505–531. Available at: http://www.iodp.tamu.edu/publications/175_IR/VOLUME/CHAPTERS/CHAP_17.PDF [Accessed March 9, 2016].

Berner R. A. (1980) *Early Diagenesis: A Theoretical Approach*., Princeton University Press.

Berner R. A. (2009) Phanerozoic atmospheric oxygen: New results using the GEOCARBSULF model. *Am J Sci* **309**, 603–606.

Berner R. A. (2003) The long-term carbon cycle, fossil fuels and atmospheric composition. *Nature* **426**, 323–326.

Berner R. A. (1992) Weathering, plants, and the long-term carbon cycle. *Geochimica et Cosmochimica Acta* **56**, 3225–3231.

Birck J. L. (1986) Precision K瑇Rb瑇Sr isotopic analysis: Application to Rb瑇Sr chronology. *Chemical Geology* **56**, 73–83.

Blättler C. L. and Higgins J. A. (2014) Calcium isotopes in evaporites record variations in Phanerozoic seawater SO4 and Ca. *Geology* **42**, 711–714.

Blättler C. L., Jenkyns H. C., Reynard L. M. and Henderson G. M. (2011) Significant increases in global weathering during Oceanic Anoxic Events 1a and 2 indicated by calcium isotopes. *Earth and Planetary Science Letters* **309**, 77–88.

Blättler C. L., Kump L. R., Fischer W. W., Paris G., Kasbohm J. J. and Higgins J. A. (2017) Constraints on ocean carbonate chemistry and pCO2 in the Archaean and Palaeoproterozoic. *Nature Geosci* **10**, 41–45.

Blättler C. L., Miller N. R. and Higgins J. A. (2015) Mg and Ca isotope signatures of authigenic dolomite in siliceous deep-sea sediments. *Earth and Planetary Science Letters* **419**, 32–42.

Blum P. (1997) Physical properties handbook: a guide to the shipboard measurement of physical properties of deep-sea cores. *ODP Tech. Note* **26**.

Boetius A., Ravenschlag K., Schubert C. J., Rickert D., Widdel F., Gieseke A., Amann R., Jorgensen B. B., Witte U. and Pfannkuche O. (2000) A marine microbial consortium apparently mediating anaerobic oxidation of methane. *Nature* **407**, 623–627.

Böhm F., Gussone N., Eisenhauer A., Dullo W.-C., Reynaud S. and Paytan A. (2006) Calcium isotope fractionation in modern scleractinian corals. *Geochimica et Cosmochimica Acta* **70**, 4452–4462.

Bohrmann G., Greinert J., Suess E. and Torres M. (1998) Authigenic carbonates from the Cascadia subduction zone and their relation to gas hydrate stability. *Geology* **26**, 647–650.

Bookman R., Bartov Y., Enzel Y. and Stein M. (2006) Quaternary lake levels in the Dead Sea basin: Two centuries of research. *Geological Society of America Special Papers* **401**, 155–170.

Boulyga S. F. (2010) Calcium isotope analysis by mass spectrometry. *Mass Spectrom. Rev.* **29**, 685–716.

Bowles M. W., Mogollón J. M., Kasten S., Zabel M. and Hinrichs K.-U. (2014) Global Rates of Marine Sulfate Reduction and Implications for Sub–Sea-Floor Metabolic Activities. *Science*, 1249213.

Brazier J.-M., Suan G., Tacail T., Simon L., Martin J. E., Mattioli E. and Balter V. (2015) Calcium isotope evidence for dramatic increase of continental weathering during the Toarcian oceanic anoxic event (Early Jurassic). *Earth and Planetary Science Letters* **411**, 164–176.

Broecker W. S., Beng Z. and Lamont-Doherty Geological Observatory (1982) *Tracers in the sea*., Lamont-Doherty Geological Observatory, Columbia University, Palisades, N.Y.

Bryant M. P., Campbell L. L., Reddy C. A. and Crabill M. R. (1977) Growth of Desulfovibrio in Lactate or Ethanol Media Low in Sulfate in Association with H2-Utilizing Methanogenic Bacteria. *Appl. Environ. Microbiol.* **33**, 1162–1169.

Canfield D. E. (1994) Factors influencing organic carbon preservation in marine sediments. *Chemical Geology* **114**, 315–329.

Canfield D. E., Jørgensen B. B., Fossing H., Glud R., Gundersen J., Ramsing N. B., Thamdrup B., Hansen J. W., Nielsen L. P. and Hall P. O. J. (1993) Marine Sediments, Burial, Pore Water Chemistry, Microbiology and Diagenesis Pathways of organic carbon oxidation in three continental margin sediments. *Marine Geology* **113**, 27–40.

Cerling T. E., Solomon D. K., Quade J. and Bowman J. R. (1991) On the isotopic composition of carbon in soil carbon dioxide. *Geochimica et Cosmochimica Acta* **55**, 3403–3405.

Chatterjee S., Dickens G. R., Bhatnagar G., Chapman W. G., Dugan B., Snyder G. T. and Hirasaki G. J. (2011) Pore water sulfate, alkalinity, and carbon isotope profiles in shallow sediment above marine gas hydrate systems: A numerical modeling perspective. *Journal of Geophysical Research: Solid Earth* **116**, n/a–n/a.

Christensen B. A. and Giraudeau J. (2002) Neogene and Quaternary evolution of the Benguela upwelling system. *Marine Geology* **180**, 1–2.

Christensen B. A., Kalbas J. L., Maslin M. and Murray R. W. (2002) Paleoclimatic changes in southern Africa during the intensification of Northern Hemisphere glaciation: evidence from ODP Leg 175 Site 1085. *Marine Geology* **180**, 117–131.

Compston W. and Oversby V. M. (1969) Lead isotopic analysis using a double spike. *J. Geophys. Res.* **74**, 4338–4348.

Curtis C. D. (1978) Possible links between sandstone diagenesis and depth-related geochemical reactions occurring in enclosing mudstones. *Journal of the Geological Society* **135**, 107–117.

Dansgaard W., Johnsen S. J., Clausen H. B., Dahl-Jensen D., Gundestrup N. S., Hammer C. U., Hvidberg C. S., Steffensen J. P., Sveinbjörnsdottir A. E., Jouzel J. and Bond G. (1993) Evidence for general instability of past climate from a 250-kyr ice-core record. *Nature* **364**, 218–220.

De La Rocha C. L. and DePaolo D. J. (2000) Isotopic evidence for variations in the marine calcium cycle over the cenozoic. *Science* **289**, 1176–8.

Dekens P. S., Ravelo A. C. and McCarthy M. D. (2007) Warm upwelling regions in the Pliocene warm period. *Paleoceanography* **22**, PA3211.

DePaolo D. J. (2004) Calcium Isotopic Variations Produced by Biological, Kinetic, Radiogenic and Nucleosynthetic Processes. *Reviews in Mineralogy and Geochemistry* **55**, 255–288.

DePaolo D. J. (2011) Surface kinetic model for isotopic and trace element fractionation during precipitation of calcite from aqueous solutions. *Geochimica et Cosmochimica Acta* **75**, 1039–1056.

DePaolo D. J. and Getty S. R. (1996) Models of isotopic exchange in reactive fluid-rock systems: Implications for geochronology in metamorphic rocks. *Geochimica et Cosmochimica Acta* **60**, 3933–3947.

Diester-Haass L., Billups K. and Emeis K. (2011) Enhanced paleoproductivity across the Oligocene/Miocene boundary as evidenced by benthic foraminiferal accumulation rates. *Palaeogeography, Palaeoclimatology, Palaeoecology* **302**, 464–473.

Diester-Haass L., Billups K., Gröcke D. R., François L., Lefebvre V. and Emeis K. C. (2009) Mid-Miocene paleoproductivity in the Atlantic Ocean and implications for the global carbon cycle. *Paleoceanography* **24**, PA1209.

Diester-Haass L., Billups K., Jacquemin I., Emeis K. C., Lefebvre V. and François L. (2013) Paleoproductivity during the middle Miocene carbon isotope events: A data-model approach. *Paleoceanography* **28**, 334–346.

Diester-Haass L., Meyers P. A. and Bickert T. (2004) Carbonate crash and biogenic bloom in the late Miocene: Evidence from ODP Sites 1085, 1086, and 1087 in the Cape Basin, southeast Atlantic Ocean. *Paleoceanography* **19**, PA1007.

Diester-Haass L., Meyers P. A. and Vidal L. (2002) The late Miocene onset of high productivity in the Benguela Current upwelling system as part of a global pattern. *Marine Geology* **180**, 87–103.

Dupont L. M. (2006) Late Pliocene vegetation and climate in Namibia (southern Africa) derived from palynology of ODP Site 1082. *Geochem. Geophys. Geosyst.* **7**, Q05007.

Dupont L. M., Donner B., Schneider R. and Wefer G. (2001) Mid-Pleistocene environmental change in tropical Africa began as early as 1.05 Ma. *Geology* **29**, 195–198.

Enzel Y., Amit R., Dayan U., Crouvi O., Kahana R., Ziv B. and Sharon D. (2008) The climatic and physiographic controls of the eastern Mediterranean over the late Pleistocene climates in the southern

Levant and its neighboring deserts. *Global and Planetary Change* **60**, 165–192.

Enzel Y., Bookman (Ken Tor) R., Sharon D., Gvirtzman H., Dayan U., Ziv B. and Stein M. (2003) Late Holocene climates of the Near East deduced from Dead Sea level variations and modern regional winter rainfall. *Quaternary Research* **60**, 263–273.

Fantle M. S. (2015) Calcium isotopic evidence for rapid recrystallization of bulk marine carbonates and implications for geochemical proxies. *Geochimica et Cosmochimica Acta* **148**, 378–401.

Fantle M. S. and Bullen T. D. (2009) Essentials of iron, chromium, and calcium isotope analysis of natural materials by thermal ionization mass spectrometry. *Chemical Geology* **258**, 50–64.

Fantle M. S. and DePaolo D. J. (2007) Ca isotopes in carbonate sediment and pore fluid from ODP Site 807A: The Ca2+(aq)–calcite equilibrium fractionation factor and calcite recrystallization rates in Pleistocene sediments. *Geochimica et Cosmochimica Acta* **71**, 2524–2546.

Fantle M. S. and DePaolo D. J. (2006) Sr isotopes and pore fluid chemistry in carbonate sediment of the Ontong Java Plateau: Calcite recrystallization rates and evidence for a rapid rise in seawater Mg over the last 10 million years. *Geochimica et Cosmochimica Acta* **70**, 3883–3904.

Fantle M. S. and DePaolo D. J. (2005) Variations in the marine Ca cycle over the past 20 million years. *Earth and Planetary Science Letters* **237**, 102–117.

Fantle M. S. and Higgins J. (2014) The effects of diagenesis and dolomitization on Ca and Mg isotopes in marine platform carbonates: Implications for the geochemical cycles of Ca and Mg. *Geochimica et Cosmochimica Acta* **142**, 458–481.

Fantle M. S. and Tipper E. T. (2014) Calcium isotopes in the global biogeochemical Ca cycle: Implications for development of a Ca isotope proxy. *Earth-Science Reviews* **129**, 148–177.

Farkaš J., Böhm F., Wallmann K., Blenkinsop J., Eisenhauer A., van Geldern R., Munnecke A., Voigt S. and Veizer J. (2007) Calcium isotope record of Phanerozoic oceans: Implications for chemical evolution of seawater and its causative mechanisms. *Geochimica et Cosmochimica Acta* **71**, 5117–5134.

Farmer E. C., deMenocal P. B. and Marchitto T. M. (2005) Holocene and deglacial ocean temperature variability in the Benguela upwelling region: Implications for low-latitude atmospheric circulation. *Paleoceanography* **20**, PA2018.

Finlayson C. (2004) *Neanderthals and Modern Humans: An Ecological and Evolutionary Perspective*., Cambridge University Press.

Fletcher I. R., Maggi A. L., Rosman K. J. R. and McNaughton N. J. (1997) Isotopic abundance measurements of K and Ca using a wide-dispersion multi-collector mass spectrometer and low-fractionation ionisation techniques. *International Journal of Mass Spectrometry and Ion Processes* **163**, 1–17.

Flower B. P. and Kennett J. P. (1993) Middle Miocene ocean-climate transition: High-resolution oxygen and carbon isotopic records from Deep Sea Drilling Project Site 588A, southwest Pacific. *Paleoceanography* **8**, 811–843.

Föllmi K. B., Badertscher C., Kaenel E. de, Stille P., John C. M., Adatte T. and Steinmann P. (2005) Phosphogenesis and organic-carbon preservation in the Miocene Monterey Formation at Naples Beach, California—The Monterey hypothesis revisited. *GSA Bulletin* **117**, 589–619.

Fontes J.-C., Gasse F. and Gibert E. (1996) Environmental Changes in the Tibetan Plateau and Surrounding AreasHolocene environmental changes in Lake Bangong basin (Western Tibet). Part 1: Chronology and stable isotopes of carbonates of a Holocene lacustrine core. *Palaeogeography, Palaeoclimatology, Palaeoecology* **120**, 25–47.

Froelich P. N., Klinkhammer G. P., Bender M. L., Luedtke N. A., Heath G. R., Cullen D., Dauphin P., Hammond D., Hartman B. and Maynard V. (1979) Early oxidation of organic matter in pelagic sediments of the eastern equatorial Atlantic: suboxic diagenesis. *Geochimica et Cosmochimica Acta* **43**, 1075–1090.

Frumkin A., Bar-Yosef O. and Schwarcz H. P. (2011) Possible paleohydrologic and paleoclimatic effects on hominin migration and occupation of the Levantine Middle Paleolithic. *Journal of Human Evolution* **60**, 437–451.

Frumkin A., Ford D. C. and Schwarcz H. P. (1999) Continental Oxygen Isotopic Record of the Last 170,000 Years in Jerusalem. *Quaternary Research* **51**, 317–327.

Gallagher K. L., Kading T. J., Braissant O., Dupraz C. and Visscher P. T. (2012) Inside the alkalinity engine: the role of electron donors in the organomineralization potential of sulfate-reducing bacteria. *Geobiology* **10**, 518–530.

Garcés B. L. V., Kelts K. and Ito E. (1995) Oxygen and carbon isotope trends and sedimentological evolution of a meromictic and saline lacustrine system: the Holocene Medicine Lake basin, North American Great Plains, USA. *Palaeogeography, Palaeoclimatology, Palaeoecology* **117**, 253–278.

Garfunkel Z. and Ben-Avraham Z. (1996) Dynamics of Extensional Basins and Inversion TectonicsThe structure of the Dead Sea basin. *Tectonophysics* **266**, 155–176.

Gieskes J. M. (1975) Chemistry of Interstitial Waters of Marine Sediments. *Annual Review of Earth and Planetary Sciences* **3**, 433.

Gieskes J. M., Elderfield H. and Palmer M. R. (1986) Strontium and its isotopic composition in interstitial waters of marine carbonate sediments. *Earth and Planetary Science Letters* **77**, 229–235.

Gieskes J. M. and Lawrence J. R. (1981) Alteration of volcanic matter in deep sea sediments: evidence from the chemical composition of interstitial waters from deep sea drilling cores. *Geochimica et Cosmochimica Acta* **45**, 1687–1703.

Giraudeau J., Meyers P. A. and Christensen B. A. (2002) Accumulation of organic and inorganic carbon in Pliocene–Pleistocene sediments along the SW African margin. *Marine Geology* **180**, 49–69.

Golan R., Lazar B., Wurgaft E., Lensky N., Ganor J. and Gavrieli I. (2017) Continuous CO2 escape from the hypersaline Dead Sea caused by aragonite precipitation. *Geochimica et Cosmochimica Acta* **207**, 43–56.

Gopalan K., Macdougall D. and Macisaac C. (2006) Evaluation of a 42Ca–43Ca double-spike for high precision Ca isotope analysis. *International Journal of Mass Spectrometry* **248**, 9–16.

Gorgas T. J. and Wilkens R. H. (2002) Sedimentation rates off SW Africa since the late Miocene deciphered from spectral analyses of borehole and GRA bulk density profiles: ODP Sites 1081–1084. *Marine Geology* **180**, 29–47.

Griffith E. M., Fantle M. S., Eisenhauer A., Paytan A. and Bullen T. D. (2015) Effects of ocean acidification on the marine calcium isotope record at the Paleocene–Eocene Thermal Maximum. *Earth and Planetary Science Letters* **419**, 81–92.

Grootes P. M., Stuiver M., White J. W. C., Johnsen S. and Jouzel J. (1993) Comparison of oxygen isotope records from the GISP2 and GRIP Greenland ice cores. *Nature* **366**, 552–554.

Gussone N., Böhm F., Eisenhauer A., Dietzel M., Heuser A., Teichert B. M. A., Reitner J., Wörheide G. and Dullo W.-C. (2005) Calcium isotope fractionation in calcite and aragonite. *Geochimica et Cosmochimica Acta* **69**, 4485–4494.

Gussone N., Eisenhauer A., Heuser A., Dietzel M., Bock B., Böhm F., Spero H. J., Lea D. W., Bijma J. and Nägler T. F. (2003) Model for kinetic effects on calcium isotope fractionation (δ44Ca) in inorganic aragonite

and cultured planktonic foraminifera. *Geochimica et Cosmochimica Acta* **67**, 1375–1382.

Gussone N., Hönisch B., Heuser A., Eisenhauer A., Spindler M. and Hemleben C. (2009) A critical evaluation of calcium isotope ratios in tests of planktonic foraminifers. *Geochimica et Cosmochimica Acta* **73**, 7241–7255.

Gussone N., Nehrke G. and Teichert B. M. A. (2011) Calcium isotope fractionation in ikaite and vaterite. *Chemical Geology* **285**, 194–202.

Haase-Schramm A., Goldstein S. L. and Stein M. (2004) U-Th dating of Lake Lisan (late Pleistocene dead sea) aragonite and implications for glacial east Mediterranean climate change. *Geochimica et Cosmochimica Acta* **68**, 985–1005.

Hammarlund D., Björck S., Buchardt B., Israelson C. and Thomsen C. T. (2003) Rapid hydrological changes during the Holocene revealed by stable isotope records of lacustrine carbonates from Lake Igelsjön, southern Sweden. *Quaternary Science Reviews* **22**, 353–370.

Haouari O., Fardeau M.-L., Casalot L., Tholozan J.-L., Hamdi M. and Ollivier B. (2006) Isolation of sulfate-reducing bacteria from Tunisian marine sediments and description of Desulfovibrio bizertensis sp. nov. *Int J Syst Evol Microbiol* **56**, 2909–2913.

Harouaka K., Eisenhauer A. and Fantle M. S. (2014) Experimental investigation of Ca isotopic fractionation during abiotic gypsum precipitation. *Geochimica et Cosmochimica Acta* **129**, 157–176.

Harouaka K., Mansor M., Macalady J. L. and Fantle M. S. (2016) Calcium isotopic fractionation in microbially mediated gypsum precipitates. *Geochimica et Cosmochimica Acta* **184**, 114–131.

Hart S. R. and Zindler A. (1989) Isotope fractionation laws: a test using calcium. *International Journal of Mass Spectrometry and Ion Processes* **89**, 287–301.

Hayes A., Kucera M., Kallel N., Sbaffi L. and Rohling E. J. (2005) Glacial Mediterranean sea surface temperatures based on planktonic foraminiferal assemblages. *Quaternary Science Reviews* **24**, 999–1016.

Hayes J. M., Strauss H. and Kaufman A. J. (1999) The abundance of 13C in marine organic matter and isotopic fractionation in the global biogeochemical cycle of carbon during the past 800 Ma. *Chemical Geology* **161**, 103–125.

Hayward B. W., Kawagata S., Grenfell H. R., Sabaa A. T. and O'Neill T. (2007) Last global extinction in the deep sea during the mid-Pleistocene climate transition. *Paleoceanography* **22**, PA3103.

Hein J. R., O'neil J. R. and Jones M. G. (1979) Origin of authigenic carbonates in sediment from the deep Bering Sea. *Sedimentology* **26**, 681–705.

Henderson G. M., Chu N.-C., Bayon G. and Benoit M. (2006) δ44/42 Ca in gas hydrates, porewaters and authigenic carbonates from Niger Delta sediments. *Geochimica et Cosmochimica Acta Supplement* **70**, A244–A244.

Hensley T. M. (2006) Calcium Isotopic Variation in Marine Evaporites and Carbonates: Applications to Late Miocene Mediterranean Brine Chemistry and Late Cenozoic Calcium Cycling in the Oceans. *Scripps Institution of Oceanography*. Available at: http://escholarship.org/uc/item/3fk9j79s [Accessed July 22, 2016].

Heuser A. and Eisenhauer A. (2008) The calcium isotope composition (δ44/40Ca) of NIST SRM 915b and NIST SRM 1486. *Geostandards and Geoanalytical Research* **32**, 311–315.

Heuser A., Eisenhauer A., Gussone N., Bock B., Hansen B. T. and Nägler T. F. (2002) Measurement of calcium isotopes (δ44Ca) using a multicollector TIMS technique. *International Journal of Mass Spectrometry* **220**, 385–397.

Higgins J. A., Blättler C. L., Lundstrom E. A., Santiago-Ramos D. P., Akhtar A. A., Crüger Ahm A.-S., Bialik O., Holmden C., Bradbury H., Murray S. T. and Swart P. K. (2018) Mineralogy, early marine diagenesis, and the chemistry of shallow-water carbonate sediments. *Geochimica et Cosmochimica Acta* **220**, 512–534.

Higgins J. A., Fischer W. W. and Schrag D. P. (2009) Oxygenation of the ocean and sediments: Consequences for the seafloor carbonate factory. *Earth and Planetary Science Letters* **284**, 25–33.

Hinrichs K.-U., Hayes J., Sylva S., Brewer P. and DeLong E. F. (1999) Methane-consuming archaebacteria in marine sediments. *Nature* **398**, 802–805.

Hoehler T. M., Alperin M. J., Albert D. B. and Martens C. S. (1994) Field and laboratory studies of methane oxidation in an anoxic marine sediment: Evidence for a methanogen-sulfate reducer consortium. *Global Biogeochem. Cycles* **8**, 451–463.

Holbourn A., Kuhnt W., Schulz M., Flores J.-A. and Andersen N. (2007) Orbitally-paced climate evolution during the middle Miocene "Monterey"

carbon-isotope excursion. *Earth and Planetary Science Letters* **261**, 534–550.

Holtvoeth J., Wagner T. and Schubert C. J. (2003) Organic matter in river-influenced continental margin sediments: The land-ocean and climate linkage at the Late Quaternary Congo fan (ODP Site 1075). *Geochem. Geophys. Geosyst.* **4**, 1109.

Irwin H., Curtis C. and Coleman M. (1977) Isotopic evidence for source of diagenetic carbonates formed during burial of organic-rich sediments. *Nature* **269**, 209–213.

Jacobson A. D., Grace Andrews M., Lehn G. O. and Holmden C. (2015) Silicate versus carbonate weathering in Iceland: New insights from Ca isotopes. *Earth and Planetary Science Letters* **416**, 132–142.

Jungck M. H. A., Shimamura T. and Lugmair G. W. (1984) Ca isotope variations in Allende. *Geochimica et Cosmochimica Acta* **48**, 2651–2658.

Kasten S. and Jørgensen B. B. (2000) Sulfate Reduction in Marine Sediments. In *Marine Geochemistry* Springer, Berlin, Heidelberg. pp. 263–281. Available at: https://link.springer.com/chapter/10.1007/978-3-662-04242-7_8 [Accessed August 24, 2017].

Katz A. (1973) The interaction of magnesium with calcite during crystal growth at 25–90°C and one atmosphere. *Geochimica et Cosmochimica Acta* **37**, 1563–1586.

Katz A. and Kolodny N. (1989) Hypersaline brine diagenesis and evolution in the Dead Sea-Lake Lisan system (Israel). *Geochimica et Cosmochimica Acta* **53**, 59–67.

Katz A., Kolodny Y. and Nissenbaum A. (1977) The geochemical evolution of the Pleistocene Lake Lisan-Dead Sea system. *Geochimica et Cosmochimica Acta* **41**, 1609–1626.

Katz A., Starinsky A., Taitel-Goldman N. and Beyth M. (1981) Solubilities of gypsum and halite in the Dead Sea and in its mixtures with seawater1. *Limnol. Oceanogr.* **26**, 709–716.

Ken-Tor R. B., Enzel Y., Agnon A. and Stein M. (2004) Late Holocene lake levels of the Dead Sea. *Geological Society of America Bulletin* **116**, 555–571.

Knoll A. H., Hayes J. M., Kaufman A. J., Swett K. and Lambert I. B. (1986) Secular variation in carbon isotope ratios from Upper Proterozoic successions of Svalbard and East Greenland. *Nature* **321**, 832–838.

Kolodny Y., Stein M. and Machlus M. (2005) Sea-rain-lake relation in the Last Glacial East Mediterranean revealed by δ18O-δ13C in Lake Lisan aragonites. *Geochimica et Cosmochimica Acta* **69**, 4045–4060.

Kovalevich V. M., Peryt T. M. and Petrichenko O. I. (1998) Secular Variation in Seawater Chemistry During the Phanerozoic As Indicated By Brine Inclusions in Halite. *The Journal of Geology* **106**, 695–712.

Krumgalz B. S. and Millero F. J. (1983) Physico-chemical study of dead sea waters. III. On gypsum saturation in Dead Sea waters and their mixtures with Mediterranean Sea water. *Marine Chemistry* **13**, 127–139.

Kuhlmann H., Meggers H., Freudenthal T. and Wefer G. (2004) The transition of the monsoonal and the N Atlantic climate system off NW Africa during the Holocene. *Geophys. Res. Lett.* **31**, L22204.

Kürschner W. M., Kvaček Z. and Dilcher D. L. (2008) The impact of Miocene atmospheric carbon dioxide fluctuations on climate and the evolution of terrestrial ecosystems. *PNAS* **105**, 449–453.

Kurtz A. C., Kump L. R., Arthur M. A., Zachos J. C. and Paytan A. (2003) Early Cenozoic decoupling of the global carbon and sulfur cycles. *Paleoceanography* **18**, 1090.

Lange C. B., Berger W. H., Lin H.-L. and Wefer G. (1999) The early Matuyama Diatom Maximum off SW Africa, Benguela Current System (ODP Leg 175). *Marine Geology* **161**, 93–114.

Langer G., Sadekov A., Thoms S., Keul N., Nehrke G., Mewes A., Greaves M., Misra S., Reichart G.-J., de Nooijer L. J., Bijma J. and Elderfield H. (2016) Sr partitioning in the benthic foraminifera Ammonia aomoriensis and Amphistegina lessonii. *Chemical Geology* **440**, 306–312.

Lazarus D., Bittniok B., Diester-Haass L., Meyers P. and Billups K. (2006) Comparison of radiolarian and sedimentologic paleoproductivity proxies in the latest Miocene–Recent Benguela Upwelling System. *Marine Micropaleontology* **60**, 269–294.

Lear C. H., Elderfield H. and Wilson P. A. (2000) Cenozoic Deep-Sea Temperatures and Global Ice Volumes from Mg/Ca in Benthic Foraminiferal Calcite. *Science* **287**, 269–272.

Lehn G. O., Jacobson A. D. and Holmden C. (2013) Precise analysis of Ca isotope ratios (δ44/40Ca) using an optimized 43Ca–42Ca double-spike MC-TIMS method. *International Journal of Mass Spectrometry* **351**, 69–75.

Lein A. Y. (2004) Authigenic Carbonate Formation in the Ocean. *Lithology and Mineral Resources* **39**, 1–30.

Lemarchand D., Wasserburg G. J. and Papanastassiou D. A. (2004) Rate-controlled calcium isotope fractionation in synthetic calcite. *Geochimica et Cosmochimica Acta* **68**, 4665–4678.

Leng M. J., Jones M. D., Frogley M. R., Eastwood W. J., Kendrick C. P. and Roberts C. N. (2010) Detrital carbonate influences on bulk oxygen and carbon isotope composition of lacustrine sediments from the Mediterranean. *Global and Planetary Change* **71**, 175–182.

Leng M. J. and Marshall J. D. (2004) Palaeoclimate interpretation of stable isotope data from lake sediment archives. *Quaternary Science Reviews* **23**, 811–831.

Lerman A., Wu L. and Mackenzie F. T. (2007) CO2 and H2SO4 consumption in weathering and material transport to the ocean, and their role in the global carbon balance. *Marine Chemistry* **106**, 326–350.

Levitus S., Antonov J. I., Baranova O. K., Boyer T. P., Coleman C. L., Garcia H. E., Grodsky A. I., Johnson D. R., Locarnini R. A., Mishonov A. V., Reagan J. R., Sazama C. L., Seidov D., Smolyar I., Yarosh E. S. and Zweng M. M. (2013) The World Ocean Database. *Data Science Journal* **12**, WDS229-WDS234.

Lin H.-L. and Chen C.-J. (2002) A late Pliocene diatom Ge/Si record from the Southeast Atlantic. *Marine Geology* **180**, 151–161.

Lisker S., Vaks A., Bar-Matthews M., Porat R. and Frumkin A. (2010) Late Pleistocene palaeoclimatic and palaeoenvironmental reconstruction of the Dead Sea area (Israel), based on speleothems and cave stromatolites. *Quaternary Science Reviews* **29**, 1201–1211.

Lowenstein T. K., Timofeeff M. N., Brennan S. T., Hardie L. A. and Demicco R. V. (2001) Oscillations in Phanerozoic Seawater Chemistry: Evidence from Fluid Inclusions. *Science* **294**, 1086–1088.

Machlus M., Enzel Y., Goldstein S. L., Marco S. and Stein M. (2000) Reconstructing low levels of Lake Lisan by correlating fan-delta and lacustrine deposits. *Quaternary International* **73–74**, 137–144.

Maher K., DePaolo D. J. and Lin J. C.-F. (2004) Rates of silicate dissolution in deep-sea sediment: In situ measurement using 234U/238U of pore fluids. *Geochimica et Cosmochimica Acta* **68**, 4629–4648.

Malinverno A. and Martinez E. A. (2015) The effect of temperature on organic carbon degradation in marine sediments. *Scientific Reports* **5**, srep17861.

Marlow J. R., Lange C. B., Wefer G. and Rosell-Melé A. (2000) Upwelling Intensification As Part of the Pliocene-Pleistocene Climate Transition. *Science* **290**, 2288–2291.

Marriott C. S., Henderson G. M., Belshaw N. S. and Tudhope A. W. (2004) Temperature dependence of δ7Li, δ44Ca and Li/Ca during growth of calcium carbonate. *Earth and Planetary Science Letters* **222**, 615–624.

Marschall C., Frenzel P. and Cypionka H. (1993) Influence of oxygen on sulfate reduction and growth of sulfate-reducing bacteria. *Arch. Microbiol.* **159**, 168–173.

Martens C. S. and Berner R. A. (1974) Methane Production in the Interstitial Waters of Sulfate-Depleted Marine Sediments. *Science* **185**, 1167–1169.

Matthews A., Ayalon A. and Bar-Matthews M. (2000) D/H ratios of fluid inclusions of Soreq cave (Israel) speleothems as a guide to the Eastern Mediterranean Meteoric Line relationships in the last 120 ky. *Chemical Geology* **166**, 183–191.

McClymont E. L., Rosell-Melé A., Giraudeau J., Pierre C. and Lloyd J. M. (2005) Alkenone and coccolith records of the mid-Pleistocene in the south-east Atlantic: Implications for the U37K′ index and South African climate. *Quaternary Science Reviews* **24**, 1559–1572.

McDuff R. E. and Gieskes J. M. (1976) Calcium and magnesium profiles in DSDP interstitial waters: Diffusion or reaction? *Earth and Planetary Science Letters* **33**, 1–10.

McGarry S., Bar-Matthews M., Matthews A., Vaks A., Schilman B. and Ayalon A. (2004) Constraints on hydrological and paleotemperature variations in the Eastern Mediterranean region in the last 140ka given by the δD values of speleothem fluid inclusions. *Quaternary Science Reviews* **23**, 919–934.

Melim L. A., Swart P. K. and Maliva R. G. (1995) Meteoric-like fabrics forming in marine waters: Implications for the use of petrography to identify diagenetic environments. *Geology* **23**, 755–758.

Melim L. A., Westphal H., Swart P. K., Eberli G. P. and Munnecke A. (2002) Questioning carbonate diagenetic paradigms: evidence from the Neogene of the Bahamas. *Marine Geology* **185**, 27–53.

Miebach A., Chen C., Schwab M. J., Stein M. and Litt T. (2017) Vegetation and climate during the Last Glacial high stand (ca. 28–22 ka BP) of the Sea of Galilee, northern Israel. *Quaternary Science Reviews* **156**, 47–56.

Migowski C., Stein M., Prasad S., Negendank J. F. W. and Agnon A. (2006) Holocene climate variability and cultural evolution in the Near East from the Dead Sea sedimentary record. *Quaternary Research* **66**, 421–431.

Milliman J. D. (1993) Production and accumulation of calcium carbonate in the ocean: Budget of a nonsteady state. *Global Biogeochem. Cycles* **7**, 927–957.

Milucka J., Ferdelman T. G., Polerecky L., Franzke D., Wegener G., Schmid M., Lieberwirth I., Wagner M., Widdel F. and Kuypers M. M. M. (2012) Zero-valent sulphur is a key intermediate in marine methane oxidation. *Nature* **491**, 541–546.

Mozley P. S. and Burns S. J. (1993) Oxygen and carbon isotopic composition of marine carbonate concretions; an overview. *Journal of Sedimentary Research* **63**, 73–83.

Mucci A. (1983) The solubility of calcite and aragonite in seawater at various salinities, temperatures, and one atmosphere total pressure. *Am J Sci* **283**, 780–799.

Murray R. W., Christensen B. A., Kalbas J. L. and Kryc K. A. (2002) Pliocene export production and terrigenous provenance of the Southern Cape Basin, southwest African margin. *Marine Geology* **180**, 133–150.

NCEI N. C. for E. I. (2006) 2-minute Gridded Global Relief Data (ETOPO2) v2. Available at: https://data.nodc.noaa.gov/cgi-bin/iso?id=gov.noaa.ngdc.mgg.dem:301 [Accessed September 9, 2017].

Neev D. and Emery K. O. (1967) The Dead Sea. Available at: http://afrilib.odinafrica.org/handle/0/3907 [Accessed July 25, 2016].

Nielsen L. C. and DePaolo D. J. (2013) Ca isotope fractionation in a high-alkalinity lake system: Mono Lake, California. *Geochimica et Cosmochimica Acta* **118**, 276–294.

Nielsen L. C., DePaolo D. J. and De Yoreo J. J. (2012a) Self-consistent ion-by-ion growth model for kinetic isotopic fractionation during calcite precipitation. *Geochimica et Cosmochimica Acta* **86**, 166–181.

Nielsen L. C., Druhan J. L., Yang W., Brown S. T. and DePaolo D. J. (2012b) Calcium Isotopes as Tracers of Biogeochemical Processes. In *Handbook of Environmental Isotope Geochemistry* (ed. M. Baskaran). Springer Berlin Heidelberg, Berlin, Heidelberg. pp. 105–124. Available at: http://link.springer.com/10.1007/978-3-642-10637-8_7 [Accessed March 15, 2016].

Niemann H., Losekann T., De Beer D., Elvert M., Nadalig T., Knittel K., Amann R., Sauter E., Schluter M., Klages M., Foucher J.-P. and Boetius A. (2006) Novel microbial communities of the Haakon Mosby mud volcano and their role as a methane sink. *Nature (depuis 1997)* **443**, 854–858.

Oehlerich M., Mayr C., Gussone N., Hahn A., Hölzl S., Lücke A., Ohlendorf C., Rummel S., Teichert B. M. A. and Zolitschka B. (2015) Lateglacial and Holocene climatic changes in south-eastern Patagonia inferred from carbonate isotope records of Laguna Potrok Aike (Argentina). *Quaternary Science Reviews* **114**, 189–202.

Okabe S., Nielsen P. H., Jones W. L. and Characklis W. G. (1995) Sulfide product inhibition of Desulfovibrio desulfuricans in batch and continuous cultures. *Water Research* **29**, 571–578.

Opdyke B. N. and Wilkinson B. H. (1988) Surface area control of shallow cratonic to deep marine carbonate accumulation. *Paleoceanography* **3**, 685–703.

Orphan V. J., House C. H., Hinrichs K.-U., McKeegan K. D. and DeLong E. F. (2001) Methane-Consuming Archaea Revealed by Directly Coupled Isotopic and Phylogenetic Analysis. *Science* **293**, 484–487.

Orphan V. J., House C. H., Hinrichs K.-U., McKeegan K. D. and DeLong E. F. (2002) Multiple archaeal groups mediate methane oxidation in anoxic cold seep sediments. *PNAS* **99**, 7663–7668.

Pagani M., Arthur M. A. and Freeman K. H. (1999) Miocene evolution of atmospheric carbon dioxide. *Paleoceanography* **14**, 273–292.

Pälike H., Norris R. D., Herrle J. O., Wilson P. A., Coxall H. K., Lear C. H., Shackleton N. J., Tripati A. K. and Wade B. S. (2006) The Heartbeat of the Oligocene Climate System. *Science* **314**, 1894–1898.

Pearson P. N. and Palmer M. R. (2000) Atmospheric carbon dioxide concentrations over the past 60 million years. *Nature* **406**, 695–699.

Phillips O. M. (1991) *Flow and Reactions in Permeable Rocks.*, Cambridge University Press.

Postgate J. R. and Campbell L. L. (1966) Classification of Desulfovibrio species, the nonsporulating sulfate-reducing bacteria. *Bacteriol Rev* **30**, 732–738.

Price R. I., Neil Kent G., Rosman K. J. B., Gutteridge D. H., Reeve J., Allen J. P., Stuckey B. G. A., Smith M., Guelfi G., Hickling C. J. and Blakeman S. L. (1990) Kinetics of intestinal calcium absorption in humans measured using stable isotopes and high-precision thermal ionization mass spectrometry. *Biol. Mass Spectrom.* **19**, 353–359.

Pufahl P. K., Maslin M. A., Anderson L., Brüchert V., Jansen F., Lin H., Perez M., Vidal L. and Party10 S. S. (1998) 18. LITHOSTRATIGRAPHIC SUMMARY FOR LEG 175: ANGOLA-BENGUELA UPWELLING SYSTEM1. In *Proceedings Ocean Drilling Program, Initial Reports* pp. 533–542. Available at:

http://www.iodp.tamu.edu/publications/175_IR/VOLUME/CHAPTERS/CHAP_18.PDF [Accessed March 9, 2016].

Quennell A. M. (1958) The Structural and Geomorphic Evolution of the Dead Sea Rift. *Quarterly Journal of the Geological Society* **114**, 1–24.

Ravelo A. C. and Andreasen D. H. (2000) Enhanced circulation during a warm period. *Geophys. Res. Lett.* **27**, 1001–1004.

Ravelo A. C. and Hillaire-Marcel C. (2007) Chapter Eighteen The Use of Oxygen and Carbon Isotopes of Foraminifera in Paleoceanography. In *Developments in Marine Geology* (ed. C. H. and A. D. Vernal). Proxies in Late Cenozoic Paleoceanography. Elsevier. pp. 735–764. Available at: http://www.sciencedirect.com/science/article/pii/S1572548007010238 [Accessed January 16, 2017].

Reddy M. M. and Nancollas G. H. (1976) The crystallization of calcium carbonate: IV. The effect of magnesium, strontium and sulfate ions. *Journal of Crystal Growth* **35**, 33–38.

Reeburgh W. S. and Heggie D. T. (1977) Microbial methane consumption reactions and their effect on methane distributions in freshwater and marine environments1. *Limnol. Oceanogr.* **22**, 1–9.

Reynard L. M., Henderson G. M. and Hedges R. E. M. (2010) Calcium isotope ratios in animal and human bone. *Geochimica et Cosmochimica Acta* **74**, 3735–3750.

Richter F. M. (1993) Fluid flow in deep-sea carbonates: estimates based on porewater Sr. *Earth and Planetary Science Letters* **119**, 133–141.

Richter F. M. (1996) Models for the coupled Sr-sulfate budget in deep-sea carbonates. *Earth and Planetary Science Letters* **141**, 199–211.

Richter F. M. and DePaolo D. J. (1988) Diagenesis and Sr isotopic evolution of seawater using data from DSDP 590B and 575. *Earth and Planetary Science Letters* **90**, 382–394.

Richter F. M. and DePaolo D. J. (1987) Numerical models for diagenesis and the Neogene Sr isotopic evolution of seawater from DSDP Site 590B. *Earth and Planetary Science Letters* **83**, 27–38.

Richter F. M. and Liang Y. (1993) The rate and consequences of Sr diagenesis in deep-sea carbonates. *Earth and Planetary Science Letters* **117**, 553–565.

Rickard D. T. (1975) Kinetics and mechanism of pyrite formation at low temperatures. *Am J Sci* **275**, 636–652.

Robinson R. S., Meyers P. A. and Murray R. W. (2002) Geochemical evidence for variations in delivery and deposition of sediment in Pleistocene light–dark color cycles under the Benguela Current Upwelling System. *Marine Geology* **180**, 249–270.

Robinson S. A., Black S., Sellwood B. W. and Valdes P. J. (2006) A review of palaeoclimates and palaeoenvironments in the Levant and Eastern Mediterranean from 25,000 to 5000 years BP: setting the environmental background for the evolution of human civilisation. *Quaternary Science Reviews* **25**, 1517–1541.

Rohling E. J. (1999) Environmental control on Mediterranean salinity and δ18O. *Paleoceanography* **14**, 706–715.

Rohling E. J. (2013) Quantitative assessment of glacial fluctuations in the level of Lake Lisan, Dead Sea rift. *Quaternary Science Reviews* **70**, 63–72.

Romanek C. S., Grossman E. L. and Morse J. W. (1992) Carbon isotopic fractionation in synthetic aragonite and calcite: Effects of temperature and precipitation rate. *Geochimica et Cosmochimica Acta* **56**, 419–430.

Royer D. L., Berner R. A. and Beerling D. J. (2001) Phanerozoic atmospheric CO2 change: evaluating geochemical and paleobiological approaches. *Earth-Science Reviews* **54**, 349–392.

Rudge J. F., Reynolds B. C. and Bourdon B. (2009) The double spike toolbox. *Chemical Geology* **265**, 420–431.

Rudnicki M. D., Wilson P. A. and Anderson W. T. (2001) Numerical models of diagenesis, sediment properties, and pore fluid chemistry on a paleoceanographic transect: Blake Nose, Ocean Drilling Program Leg 171B. *Paleoceanography* **16**, 563–575.

Russell W. A. and Papanastassiou D. A. (1978) Calcium isotope fractionation in ion-exchange chromatography. *Anal. Chem* **50**, 1151–1154.

Russell W. A., Tombrello T. A. and Papanastassiou D. A. (1978) Ca isotope fractionation on the Earth and other solar system materials. *Geochimica et Cosmochimica Acta* **42**, 1075–1090.

Salhotra A. M., Adams E. E. and Harleman D. R. F. (1985) Effect of Salinity and Ionic Composition on Evaporation: Analysis of Dead Sea Evaporation Pans. *Water Resour. Res.* **21**, 1336–1344.

Schefuß E., Sinninghe Damsté J. S. and Jansen J. H. F. (2004) Forcing of tropical Atlantic sea surface temperatures during the mid-Pleistocene transition. *Paleoceanography* **19**, PA4029.

Schiller M., Paton C. and Bizzarro M. (2012) Calcium isotope measurement by combined HR-MC-ICPMS and TIMS. *Journal of Analytical Atomic Spectrometry* **27**, 38–49.

Schmitt A.-D., Chabaux F. and Stille P. (2003) The calcium riverine and hydrothermal isotopic fluxes and the oceanic calcium mass balance. *Earth and Planetary Science Letters* **213**, 503–518.

Schmitt A.-D., Gangloff S., Cobert F., Lemarchand D., Stille P. and Chabaux F. (2009) High performance automated ion chromatography separation for Ca isotope measurements in geological and biological samples. *J. Anal. At. Spectrom.* **24**, 1089–1097.

Schrag D. P., DePaolo D. J. and Richter F. M. (1995) Reconstructing past sea surface temperatures: Correcting for diagenesis of bulk marine carbonate. *Geochimica et Cosmochimica Acta* **59**, 2265–2278.

Schrag D. P., Higgins J. A., Macdonald F. A. and Johnston D. T. (2013) Authigenic Carbonate and the History of the Global Carbon Cycle. *Science* **339**, 540–543.

Schramm A., Stein M. and Goldstein S. L. (2000) Calibration of the 14C time scale to >40 ka by 234U–230Th dating of Lake Lisan sediments (last glacial Dead Sea). *Earth and Planetary Science Letters* **175**, 27–40.

Shackleton N. (1967) Oxygen Isotope Analyses and Pleistocene Temperatures Re-assessed. *Nature* **215**, 15–17.

Shea J. J. (2003) The Middle Paleolithic of the East Mediterranean Levant. *Journal of World Prehistory* **17**, 313–394.

Shea J. J. (2008) Transitions or turnovers? Climatically-forced extinctions of Homo sapiens and Neanderthals in the east Mediterranean Levant. *Quaternary Science Reviews* **27**, 2253–2270.

Sivan O., Schrag D. P. and Murray R. W. (2007) Rates of methanogenesis and methanotrophy in deep-sea sediments. *Geobiology* **5**, 141–151.

Skulan J. and DePaolo D. J. (1999) Calcium isotope fractionation between soft and mineralized tissues as a monitor of calcium use in vertebrates. *PNAS* **96**, 13709–13713.

Skulan J., DePaolo D. J. and Owens T. L. (1997) Biological control of calcium isotopic abundances in the global calcium cycle. *Geochimica et Cosmochimica Acta* **61**, 2505–2510.

Soetaert K., Hofmann A. F., Middelburg J. J., Meysman F. J. R. and Greenwood J. (2007) The effect of biogeochemical processes on pH. *Marine Chemistry* **105**, 30–51.

Stakes D. S., Orange D., Paduan J. B., Salamy K. A. and Maher N. (1999) Cold-seeps and authigenic carbonate formation in Monterey Bay, California. *Marine Geology* **159**, 93–109.

Stein M. (2001) The sedimentary and geochemical record of Neogene-Quaternary water bodies in the Dead Sea Basin - inferences for the regional paleoclimatic history. *Journal of Paleolimnology* **26**, 271–282.

Stein M., Starinsky A., Katz A., Goldstein S. L., Machlus M. and Schramm A. (1997) Strontium isotopic, chemical, and sedimentological evidence for the evolution of Lake Lisan and the Dead Sea. *Geochimica et Cosmochimica Acta* **61**, 3975–3992.

Street-Perrott F. A. and Roberts N. (1983) Fluctuations in Closed-Basin Lakes as An Indicator of Past Atmospheric Circulation Patterns. In *Variations in the Global Water Budget* (eds. A. Street-Perrott, M. Beran, and R. Ratcliffe). Springer Netherlands. pp. 331–345. Available at: http://link.springer.com/chapter/10.1007/978-94-009-6954-4_26 [Accessed July 25, 2016].

Stuiver M. (1970) Oxygen and carbon isotope ratios of fresh-water carbonates as climatic indicators. *J. Geophys. Res.* **75**, 5247–5257.

Sun X. and Turchyn A. V. (2014) Significant contribution of authigenic carbonate to marine carbon burial. *Nature Geoscience* **7**, 201–204.

Swart P. K. (1979) The effect of seawater calcium concentrations on the growth and skeletal composition of a Scleractinian coral: Acropora squamosa. *Journal of Sedimentary Research* **49**. Available at: http://archives.datapages.com/data/sepm/journals/v47-50/data/049/049003/0951.htm [Accessed September 8, 2017].

Swart P. K. (2015) The geochemistry of carbonate diagenesis: The past, present and future. *Sedimentology* **62**, 1233–1304.

Swart P. K., Berier D., McNeill D., Guzikowski M., Harrison S. A. and Dedick E. (1989) Interstitial water geochemistry and carbonate diagenesis in the sub-surface of a Holocene mud island in Florida Bay. *Bulletin of Marine Science* **44**, 490–514.

Swart P. K. and Burns S. J. (1990) Pore-water chemistry and carbonate diagenesis in sediments from Leg 115: Indian Ocean. In *Proc., scientific results, ODP, Leg 115, Mascarene Plateau* ODP, Texas A&M University, College Station; UK distributors, IPOD Committee, NERC, Swindon. Available at: https://miami.pure.elsevier.com/en/publications/pore-water-chemistry-and-carbonate-diagenesis-in-sediments-from-l [Accessed September 8, 2017].

Swart P. K. and Eberli G. (2005) The nature of the δ13C of periplatform sediments: Implications for stratigraphy and the global carbon cycle. *Sedimentary Geology* **175**, 115–129.

Swart P. K. and Melim L. A. (2000) The origin of dolomites in Tertiary sediments from the margin of Great Bahama Bank. *Journal of Sedimentary Research* **70**, 738–748.

Swart P. K., Oehlert A. M., Mackenzie G. J., Eberli G. P. and Reijmer J. J. G. (2014) The fertilization of the Bahamas by Saharan dust: A trigger for carbonate precipitation? *Geology* **42**, 671–674.

Talbot M. R. (1990) A review of the palaeohydrological interpretation of carbon and oxygen isotopic ratios in primary lacustrine carbonates. *Chemical Geology: Isotope Geoscience section* **80**, 261–279.

Talbot M. R. and Johannessen T. (1992) A high resolution palaeoclimatic record for the last 27,500 years in tropical West Africa from the carbon and nitrogen isotopic composition of lacustrine organic matter. *Earth and Planetary Science Letters* **110**, 23–37.

Tang J., Dietzel M., Böhm F., Köhler S. J. and Eisenhauer A. (2008a) Sr2+/Ca2+ and 44Ca/40Ca fractionation during inorganic calcite formation: II. Ca isotopes. *Geochimica et Cosmochimica Acta* **72**, 3733–3745.

Tang J., Köhler S. J. and Dietzel M. (2008b) Sr2+/Ca2+ and 44Ca/40Ca fractionation during inorganic calcite formation: I. Sr incorporation. *Geochimica et Cosmochimica Acta* **72**, 3718–3732.

Tang J., Niedermayr A., Köhler S. J., Böhm F., Kısakürek B., Eisenhauer A. and Dietzel M. (2012) Sr2+/Ca2+ and 44Ca/40Ca fractionation during inorganic calcite formation: III. Impact of salinity/ionic strength. *Geochimica et Cosmochimica Acta* **77**, 432–443.

Teichert B. M. A., Gussone N., Eisenhauer A. and Bohrmann G. (2005) Clathrites: Archives of near-seafloor pore-fluid evolution (δ44/40Ca, δ13C, δ18O) in gas hydrate environments. *Geology* **33**, 213–216.

Teichert B. M. A., Gussone N. and Torres M. E. (2009) Controls on calcium isotope fractionation in sedimentary porewaters. *Earth and Planetary Science Letters* **279**, 373–382.

Teichert B. M. A., Johnson J. E., Solomon E. A., Giosan L., Rose K., Kocherla M., Connolly E. C. and Torres M. E. (2014) Composition and origin of authigenic carbonates in the Krishna–Godavari and Mahanadi Basins, eastern continental margin of India. *Marine and Petroleum Geology* **58**, **Part A**, 438–460.

Torfstein A., Gavrieli I., Katz A., Kolodny Y. and Stein M. (2008) Gypsum as a monitor of the paleo-limnological–hydrological conditions in Lake Lisan and the Dead Sea. *Geochimica et Cosmochimica Acta* **72**, 2491–2509.

Torfstein A., Gavrieli I. and Stein M. (2005) The sources and evolution of sulfur in the hypersaline Lake Lisan (paleo-Dead Sea). *Earth and Planetary Science Letters* **236**, 61–77.

Torfstein A., Goldstein S. L., Kagan E. J. and Stein M. (2013a) Integrated multi-site U–Th chronology of the last glacial Lake Lisan. *Geochimica et Cosmochimica Acta* **104**, 210–231.

Torfstein A., Goldstein S. L., Kushnir Y., Enzel Y., Haug G. and Stein M. (2015) Dead Sea drawdown and monsoonal impacts in the Levant during the last interglacial. *Earth and Planetary Science Letters* **412**, 235–244.

Torfstein A., Goldstein S. L., Stein M. and Enzel Y. (2013b) Impacts of abrupt climate changes in the Levant from Last Glacial Dead Sea levels. *Quaternary Science Reviews* **69**, 1–7.

Torfstein A., Haase-Schramm A., Waldmann N., Kolodny Y. and Stein M. (2009) U-series and oxygen isotope chronology of the mid-Pleistocene Lake Amora (Dead Sea basin). *Geochimica et Cosmochimica Acta* **73**, 2603–2630.

Torfstein A. and Turchyn A. V. (2017) Rates and Cycles of Microbial Sulfate Reduction in the Hyper-Saline Dead Sea over the Last 200 kyrs from Sedimentary δ34S and δ18O(SO4). *Front. Earth Sci.* **5**. Available at: http://journal.frontiersin.org/article/10.3389/feart.2017.00062/full [Accessed September 11, 2017].

Turchyn A. V. and DePaolo D. J. (2011) Calcium isotope evidence for suppression of carbonate dissolution in carbonate-bearing organic-rich sediments. *Geochimica et Cosmochimica Acta* **75**, 7081–7098.

Turchyn A. V. and Schrag D. P. (2004) Oxygen Isotope Constraints on the Sulfur Cycle over the Past 10 Million Years. *Science* **303**, 2004–2007.

Uliana E., Lange C. B. and Wefer G. (2002) Evidence for Congo River freshwater load in Late Quaternary sediments of ODP Site 1077 (5°S, 10°E). *Palaeogeography, Palaeoclimatology, Palaeoecology* **187**, 137–150.

Vaks A., Bar-Matthews M., Ayalon A., Schilman B., Gilmour M., Hawkesworth C. J., Frumkin A., Kaufman A. and Matthews A. (2003) Paleoclimate reconstruction based on the timing of speleothem growth and oxygen and carbon isotope composition in a cave located in the rain shadow in Israel. *Quaternary Research* **59**, 182–193.

Veizer J., Ala D., Azmy K., Bruckschen P., Buhl D., Bruhn F., Carden G. A. F., Diener A., Ebneth S., Godderis Y., Jasper T., Korte C., Pawellek F., Podlaha O. G. and Strauss H. (1999) 87Sr/86Sr, δ13C and δ18O evolution of Phanerozoic seawater. *Chemical Geology* **161**, 59–88.

Vidal L., Bickert T., Wefer G. and Röhl U. (2002) Late Miocene stable isotope stratigraphy of SE Atlantic ODP Site 1085: Relation to Messinian events. *Marine Geology* **180**, 71–85.

Vincent E. and Berger W. H. (1985) Carbon dioxide and polar cooling in the Miocene: The Monterey hypothesis. *Washington DC American Geophysical Union Geophysical Monograph Series* **32**, 455–468.

Waldmann N., Starinsky A. and Stein M. (2007) Primary carbonates and Ca-chloride brines as monitors of a paleo-hydrological regime in the Dead Sea basin. *Quaternary Science Reviews* **26**, 2219–2228.

Wang Y. and Van Cappellen P. (1996) A multicomponent reactive transport model of early diagenesis: Application to redox cycling in coastal marine sediments. *Geochimica et Cosmochimica Acta* **60**, 2993–3014.

Weber K. A., Achenbach L. A. and Coates J. D. (2006) Microorganisms pumping iron: anaerobic microbial iron oxidation and reduction. *Nat Rev Micro* **4**, 752–764.

Wefer G., Berger W. H. and Richter C. (1998) *Proceedings of the Ocean Drilling Program, Initial Reports*., Ocean Drilling Program, College Station, Tex.

Woodruff F. and Savin S. (1991) Mid-Miocene isotope stratigraphy in the deep sea: High-resolution correlations, paleoclimatic cycles, and sediment preservation. *Paleoceanography* **6**, 755–806.

Yegnanarayana B. (2009) *Artificial Neural Networks*., PHI Learning Pvt. Ltd.

Zachos J., Pagani M., Sloan L., Thomas E. and Billups K. (2001) Trends, Rhythms, and Aberrations in Global Climate 65 Ma to Present. *Science* **292**, 686–693.

Zanchetta G., Borghini A., Fallick A. E., Bonadonna F. P. and Leone G. (2006) Late Quaternary palaeohydrology of Lake Pergusa (Sicily, southern Italy) as inferred by stable isotopes of lacustrine carbonates. *J Paleolimnol* **38**, 227–239.

Zeebe R. E. and Wolf-Gladrow D. (2001) *CO2 in Seawater: Equilibrium, Kinetics, Isotopes: Equilibrium, Kinetics, Isotopes*., Elsevier.

Zhu P. and Macdougall J. D. (1998) Calcium isotopes in the marine environment and the oceanic calcium cycle. *Geochimica et Cosmochimica Acta* **62**, 1691–1698.

Zimmermann H. (2000) Tertiary seawater chemistry; implications from primary fluid inclusions in marine halite. *Am J Sci* **300**, 723–767.

Zuddas P. and Mucci A. (1998) Kinetics of Calcite Precipitation from Seawater: II. The Influence of the Ionic Strength. *Geochimica et Cosmochimica Acta* **62**, 757–766.

APPENDIX 1

TABLE A1.1: TABLE OF THE OUTPUT FROM THE MATLAB SCRIPT TO DETERMINE WHETHER CARBONATE PRECIPITATION WAS DUE TO AOM OR SULFATE REDUCTION (BSR) AT THE ODP SITES

Site	Latitude	Longitude	Depth of Ca min	$[Ca^{2+}]$ depth 0	Ca depth min	Sulfate depth 0	Sulfate depth min	Alkalinity depth min
682	-11.27	-79.07	23.70	9.14	5.31	24.70	12.20	29.60
720	16.13	60.75	23.45	7.85	4.73	21.40	8.50	6.73
731	16.47	59.70	25.25	8.06	6.96	22.00	21.00	7.83
823	-16.62	146.78	32.25	9.30	3.10	26.80	6.90	9.88
882	50.37	167.60	124.35	10.25	6.45	28.01	20.24	6.65
906	38.97	-72.77	22.95	9.39	4.21	24.01	5.60	24.06
919	62.67	-37.47	78.95	10.45	3.19	24.90	4.30	17.38
981	55.48	-14.65	87.65	0.00	4.20	0.00	9.06	6.33
983	60.40	-23.63	79.85	9.70	2.90	27.60	4.10	13.06
993	32.97	-75.90	21.25	9.97	5.41	26.62	5.97	21.71
1064	32.55	-57.08	18.40	9.45	7.33	20.17	14.37	12.01
1086	-31.55	15.67	77.50	11.09	6.47	27.35	10.23	14.46
1091	-47.10	5.92	182.30	11.03	7.34	28.06	22.61	9.51
1145	19.58	117.63	34.35	10.00	4.90	23.30	8.30	21.30
1148	18.83	116.57	71.75	8.79	6.84	21.60	13.70	8.79
1200	13.78	146.00	11.20	0.38	0.87	29.02	25.72	31.78
1208	36.13	158.20	67.65	10.25	7.47	27.73	20.38	8.17
1240	0.02	-86.47	93.34	10.30	3.42	28.50	15.40	14.42
1303	50.20	-45.68	39.85	8.08	4.65	22.45	11.35	10.44
1304	53.05	-33.53	77.45	9.68	3.37	27.25	8.52	15.46
1306	58.23	-45.65	57.25	10.20	4.00	27.90	4.58	15.50
1314	56.37	-27.88	74.35	10.31	5.23	23.18	6.84	7.46
686	-13.48	-76.88	22.45	9.09	5.11	19.11	0.00	27.12
798	37.03	134.80	70.67	8.22	3.36	0.00	0.00	69.17
799	39.22	133.87	161.15	9.12	3.38	19.60	0.00	36.96
861	-45.85	-75.70	7.45	4.08	1.43	11.60	0.30	28.28
890	48.67	-126.88	43.62	6.90	1.44	14.29	0.00	30.43
892	44.67	-125.12	3.79	3.27	3.27	0.62	0.62	20.48
908	78.38	1.37	88.80	11.04	7.17	29.00	1.50	11.72
909	78.58	3.07	33.95	9.84	3.60	22.72	0.00	14.09
910	80.27	6.58	22.45	5.34	3.88	26.73	0.23	0.00
911	80.47	8.23	35.95	7.30	3.19	11.80	1.30	17.14
912	79.97	5.45	32.60	10.40	2.40	26.40	0.00	12.19
933	5.10	-46.82	95.60	8.80	4.40	11.61	0.34	10.22
939	4.72	-47.50	59.07	10.70	4.09	21.00	0.50	6.38

941	5.37	-48.03	112.27	6.40	4.20	11.30	0.50	8.64
942	5.75	-49.08	35.25	10.60	5.20	25.30	0.60	11.07
944	5.93	-47.75	18.70	9.80	4.40	20.40	0.40	9.22
946	6.95	-47.92	11.50	10.10	5.40	20.70	0.50	13.51
963	37.03	13.18	154.40	8.32	5.14	15.60	0.35	7.01
1002	10.70	-65.17	157.12	4.87	2.79	7.24	0.18	17.41
1013	32.80	-118.90	38.05	10.17	3.45	26.80	1.00	48.55
1014	32.83	-119.98	26.55	10.22	3.47	27.70	0.00	56.62
1015	33.72	-118.82	19.84	5.96	3.88	0.00	0.00	13.68
1016	34.53	-122.28	78.55	10.03	5.15	25.70	0.00	15.52
1017	34.53	-121.10	28.75	8.92	2.37	23.90	1.00	44.59
1018	36.98	-123.28	9.35	8.68	4.21	23.70	1.30	41.49
1019	41.68	-124.93	41.25	8.10	0.97	20.60	0.50	46.74
1022	40.08	-125.35	27.95	9.09	4.49	23.45	3.26	14.35
1057	32.03	-76.08	24.40	7.32	2.25	18.80	0.16	19.05
1057	32.03	-76.08	24.40	7.32	2.25	18.80	0.16	19.05
1059	31.67	-75.42	22.25	9.81	2.37	24.45	0.39	31.40
1059	31.67	-75.42	22.25	9.81	2.37	24.45	0.39	31.40
1060	30.77	-74.47	25.90	9.65	3.23	25.10	0.11	27.17
1061	29.98	-73.60	26.46	3.91	3.10	0.00	0.00	22.57
1062	28.25	-74.42	47.60	10.38	4.40	27.50	3.46	19.61
1063	33.68	-57.62	33.20	10.84	3.43	25.90	2.29	22.31
1073	39.25	-72.32	26.90	9.09	3.31	21.31	0.42	8.29
1075	-4.78	10.08	31.40	10.27	5.31	27.76	0.08	37.03
1076	-5.07	11.10	123.10	9.99	3.45	25.90	0.04	20.85
1077	-5.18	10.43	28.40	10.84	5.02	27.22	0.67	34.54
1079	-11.93	13.32	57.20	10.21	3.45	28.38	0.00	34.76
1080	-16.57	10.82	25.54	8.80	2.23	26.17	0.08	36.75
1081	-19.62	11.32	43.30	10.47	3.42	26.54	2.65	22.89
1082	-21.10	11.82	19.95	10.85	2.96	29.00	1.76	37.01
1083	-20.90	11.22	34.60	10.18	2.90	27.93	0.20	29.53
1084	-25.52	13.03	73.80	10.76	2.27	29.27	0.00	154.24
1085	-29.37	13.98	36.60	10.30	3.14	27.18	2.60	23.16
1087	-31.47	15.32	60.10	9.91	4.31	27.55	3.84	28.39
1089	-40.93	9.90	49.75	7.86	1.86	22.68	0.38	42.06
1099	-64.95	-64.32	9.77	7.90	3.30	11.10	0.80	40.70
1118	-9.58	151.57	257.81	2.56	2.56	0.49	0.49	13.06
1119	-44.75	172.40	20.15	10.84	3.49	28.64	0.00	27.73
1144	20.05	117.42	20.85	0.00	3.40	0.00	0.00	32.29
1171	-48.50	149.12	934.25	10.30	5.60	26.80	0.00	0.00
1178	32.73	134.48	29.80	9.96	3.29	27.69	1.45	18.25
1232	-39.88	-75.90	88.43	6.96	3.49	8.40	0.68	30.88
1233	-41.00	-74.45	75.76	5.92	1.37	12.49	0.00	47.69
1235	-36.17	-73.57	45.24	10.27	1.25	25.49	0.00	56.63
1255	9.65	-86.18	133.94	4.66	4.66	0.22	0.22	0.00
1255	9.65	-86.18	133.94	4.66	4.66	0.22	0.22	0.00

1305	57.48	-48.53	48.35	7.81	3.21	21.52	1.49	18.48
1307	58.50	-46.40	79.15	10.11	5.27	29.06	1.58	10.08
1329	48.78	-126.68	23.45	9.40	2.40	16.90	0.00	16.50

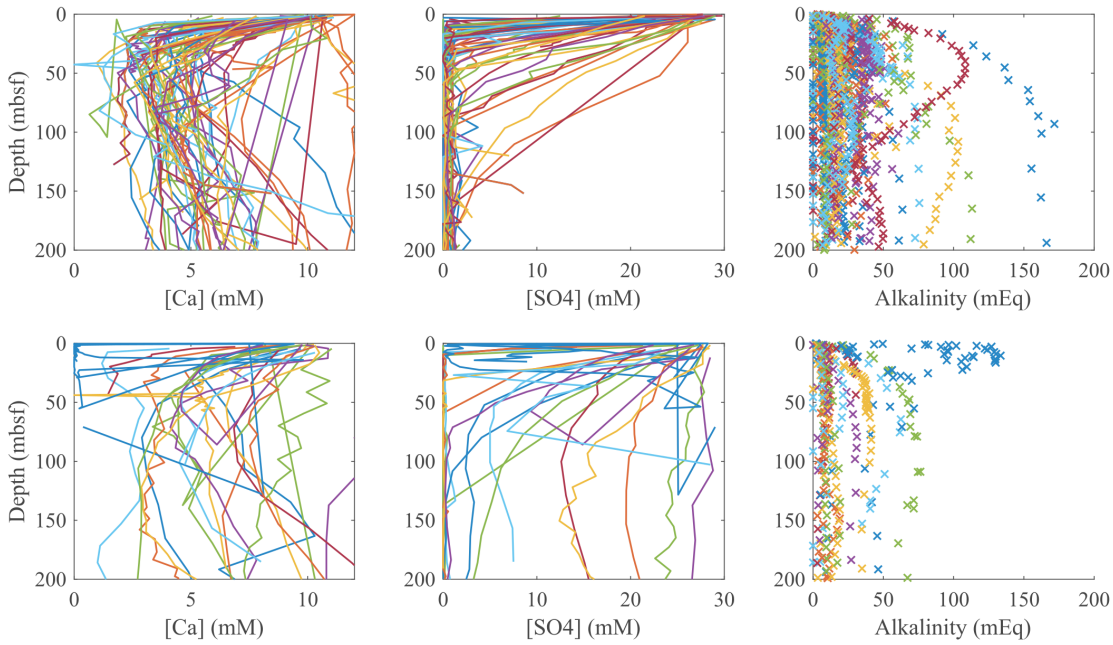

FIGURE A1.1: PLOT OF THE CALCIUM, SULFATE AND ALKALINITY VALUES FOR THE SITES DETERMINED TO BE SULFATE REDUCTION OR AOM BY THE MATLAB SCRIPT AS LISTED IN TABLE A1.1

APPENDIX 2

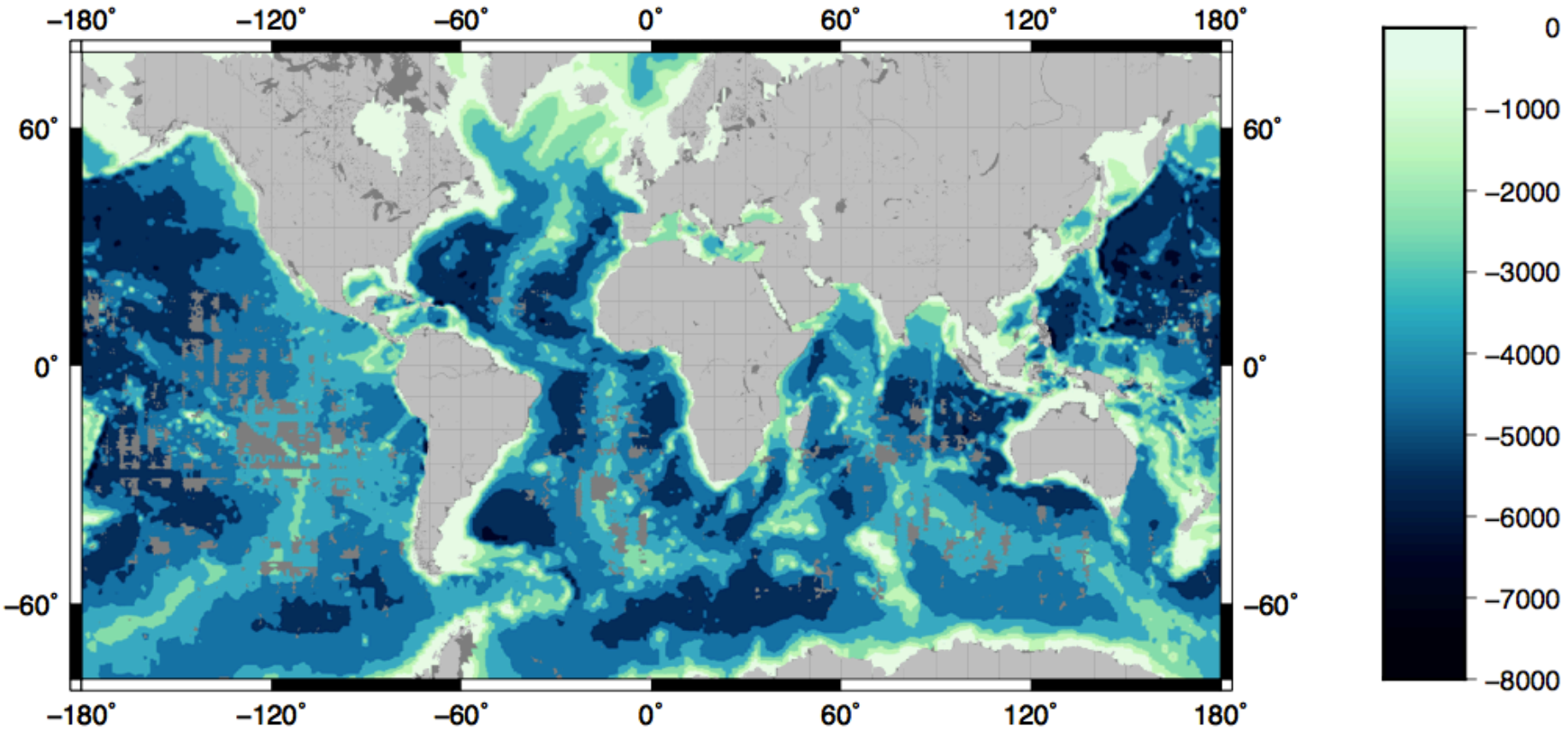

FIGURE A2.1: BATHYMETRIC INPUT MAP (SCALE IN M)

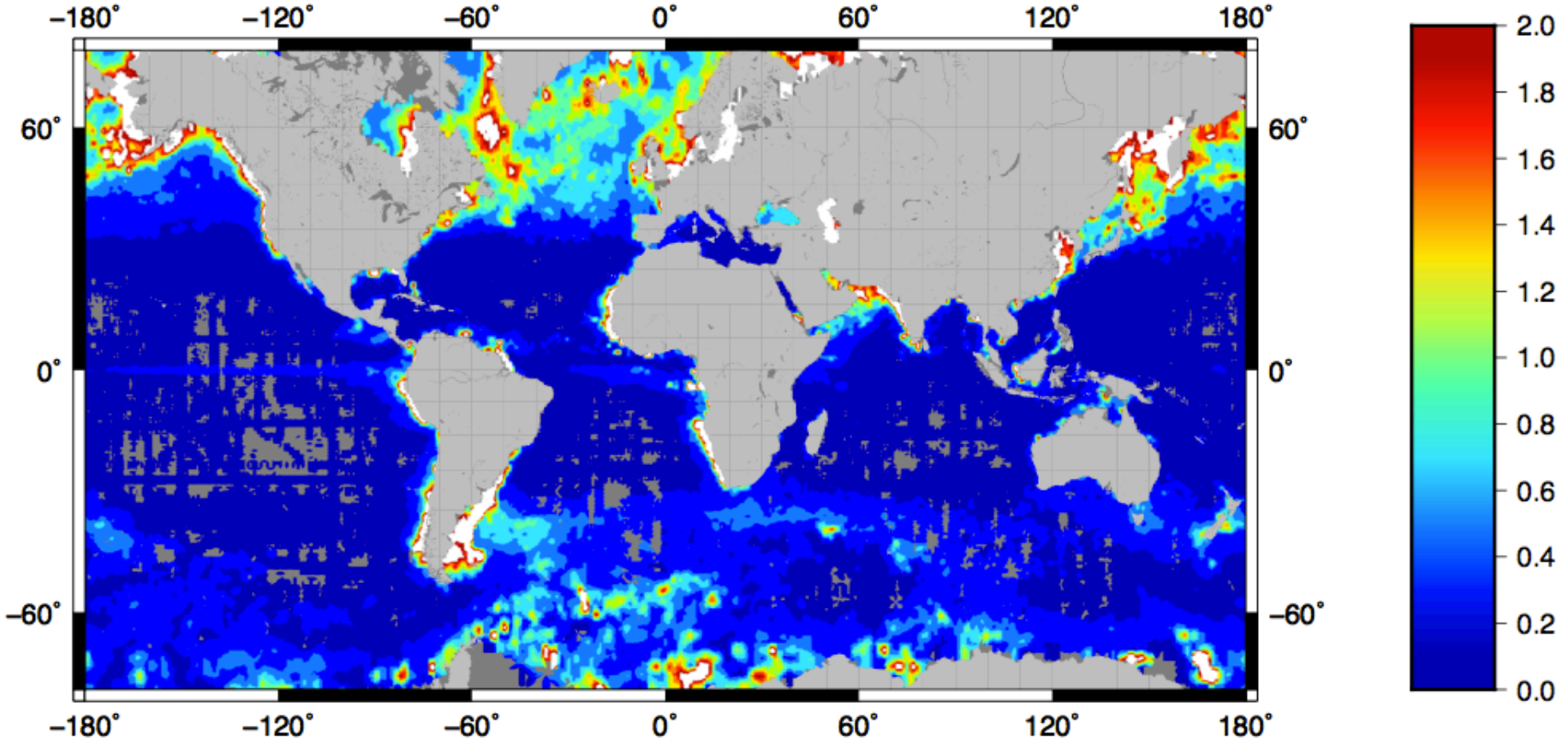

FIGURE A2.2: CHLOROPHYLL A SURFACE CONCENTRATIONS (SCALE IN mg/m^3)

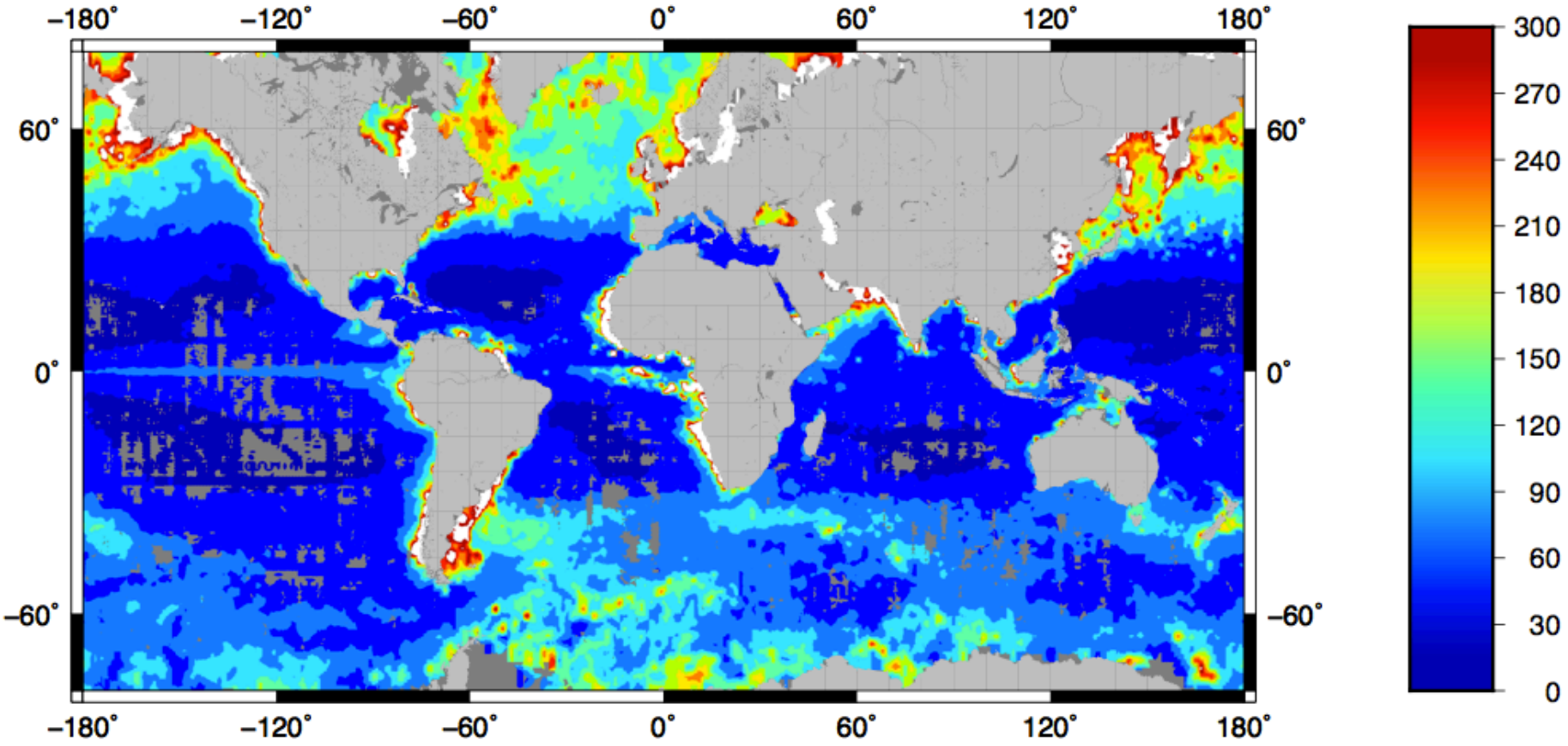

FIGURE A2.3: POC SURFACE CONCENTRATIONS INPUT MAP (SCALE IN mg/m^3)

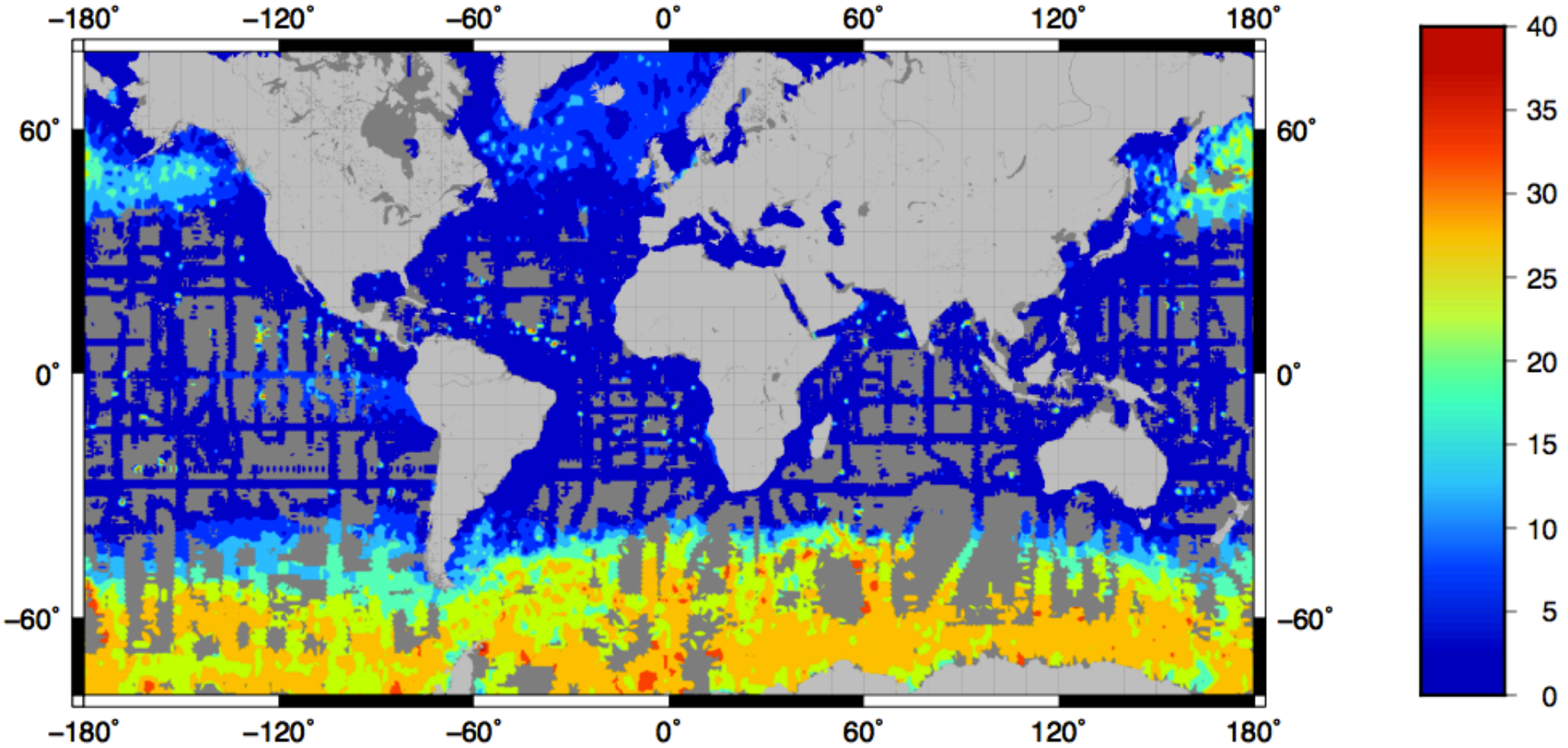

FIGURE A2.4: NITRATE SURFACE CONCENTRATIONS INPUT MAP (SCALE IN mmol/m^3)

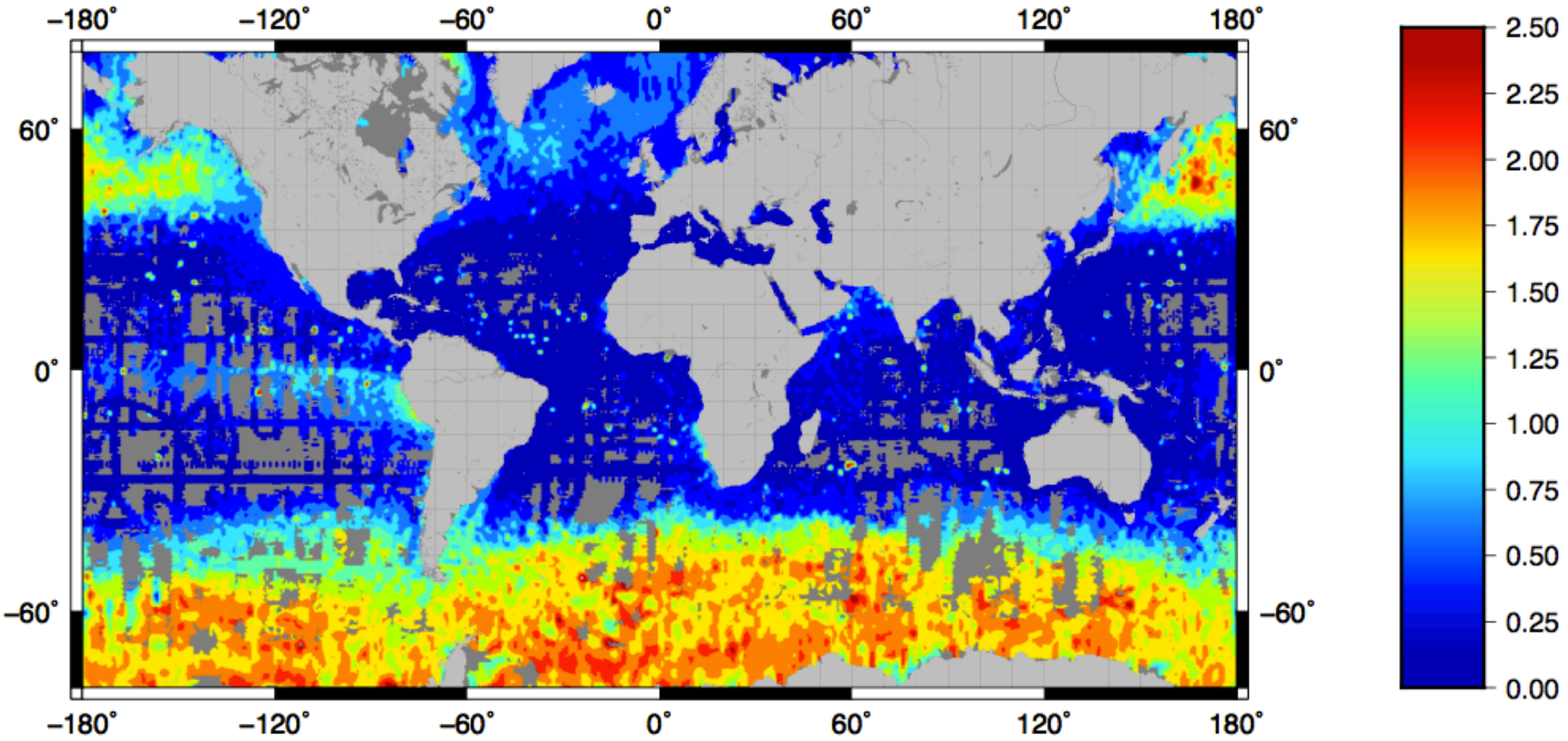

FIGURE A2.5: PHOSPHATE SURFACE CONCENTRATIONS INPUT MAP (SCALE IN mmol/m^3)

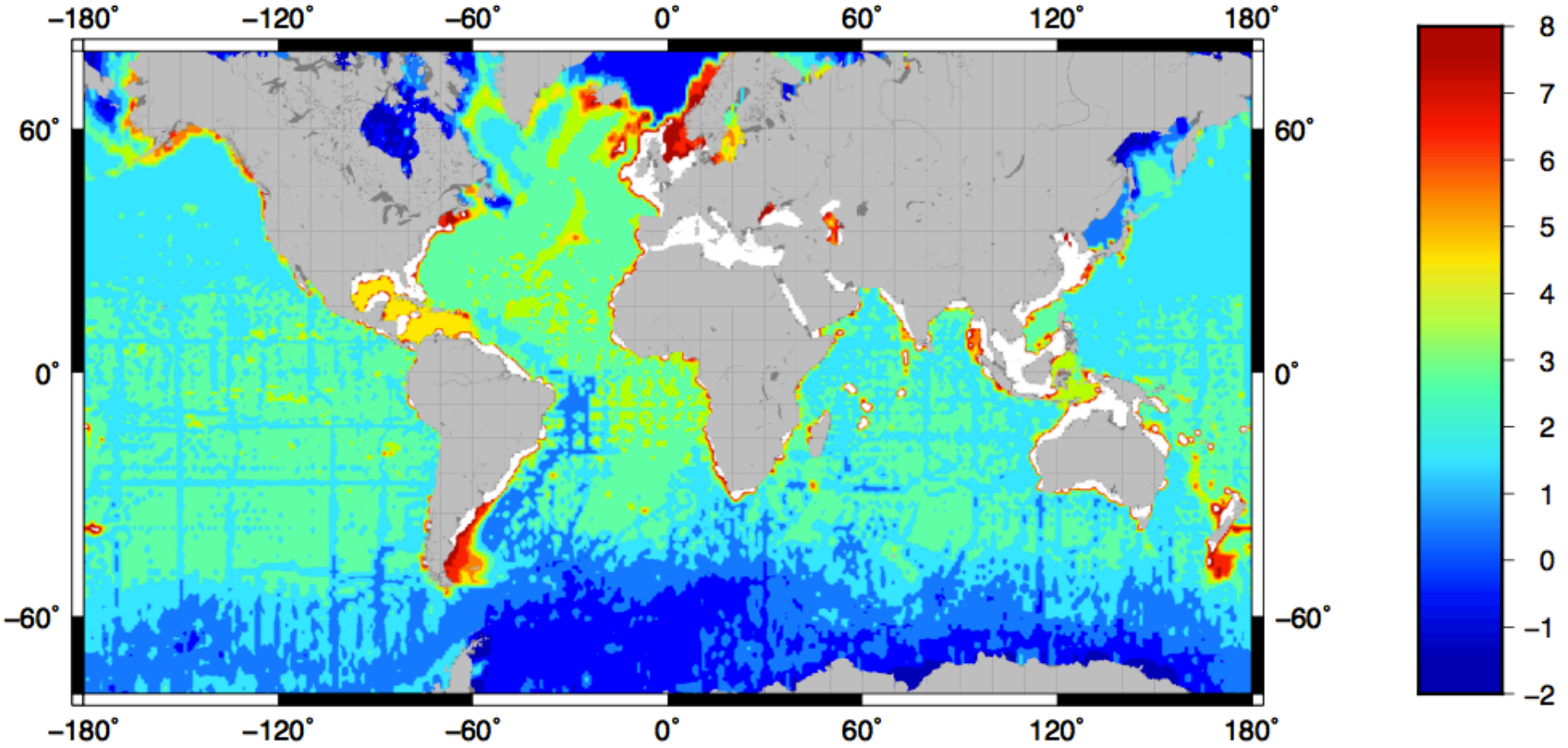

FIGURE A2.6: BOTTOM WATER TEMPERATURE INPUT MAP (SCALE IN ^{O}C)

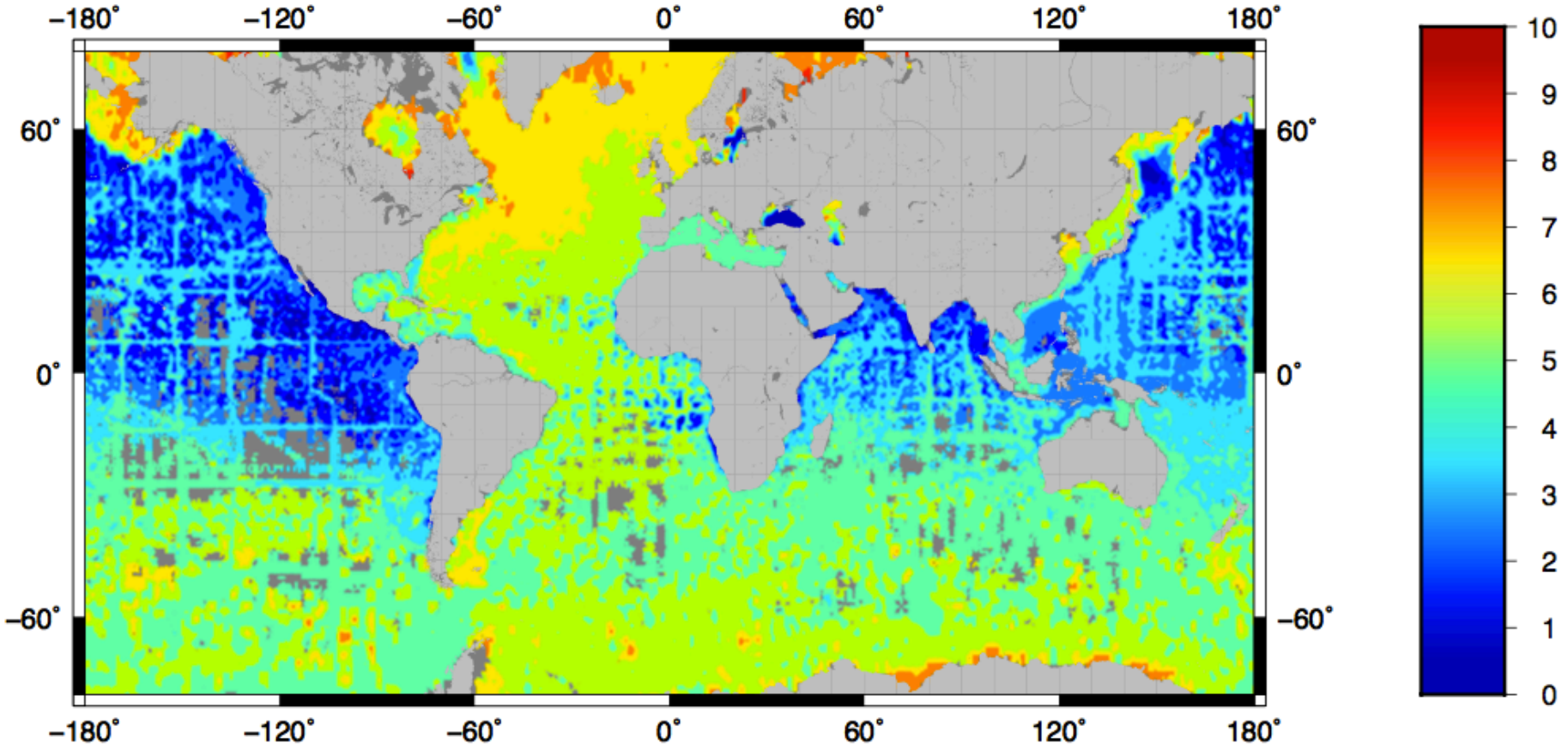

FIGURE A2.7: BOTTOM WATER DISSOLVED OXYGEN INPUT MAP (SCALE IN ml/l)